NASA Technical Memorandum 88213

Proceedings of the Second Infrared Detector Technology Workshop

1986

National Aeronautics and Space Administration

Held at Ames Research Center
Moffett Field, California
August 13-14, 1985

NASA Technical Memorandum 88213

Proceedings of the Second Infrared Detector Technology Workshop

Compiled by Craig R. McCreight, Ames Research Center, Moffett Field, California

1986

National Aeronautics and
Space Administration

Ames Research Center
Moffett Field, California 94035

Held at Ames Research Center
Moffett Field, California
August 13-14, 1985

TABLE OF CONTENTS

Foreword

The summer of 1985 marked the time of the second Infrared Detector Technology Workshop for space astronomy sponsored by NASA. It is remarkable that in just the 2 years since the first Workshop was held such important advances have been made. It has become clear that this is a field of fast-moving technologies. The large attendance by the scientific community, industry, and government is indicative of the keen interest and need for an open forum where there can be a good exchange of information and discussion. The individual papers are presented here, unedited, as submitted by the authors.

The Workshop was organized to be a review of the status and progress of astronomical infrared detector research supported by NASA within the Office of Space Science and Applications (OSSA) and the Office of Aeronautics and Space Technology (OAST). The coordinated program between OAST and OSSA is a primary reason for such excellent progress. From the points of view of both offices, this coordination is important. In times of budgetary constraints, it is necessary to ensure that the most important technologies are studied in a timely manner for high-priority space missions, so that during the development phase there is no impact on the mission schedule.

Since the Space Infrared Telescope Facility (SIRTF) is a premiere scientific space mission now under study, a large portion of this Workshop addressed those technologies useful for the cryogenically cooled telescope of SIRTF. The Workshop also included technologies which could be used with an ambient-temperature telescope in space, such as the Hubble Space Telescope (HST) for its second-generation instruments.

At the close of the Workshop, invited summary statements were given by Drs. J. Houck of Cornell University, E. Wright of the University of California at Los Angeles, F. Gillett of the National Optical Astronomy Observatories, and L. Greenberg of The Aerospace Corporation. The summaries concluded that very significant and encouraging progress has been made, but that vigorous research and development are needed for arrays to attain background-limited performance on SIRTF.

The Workshop made clear that SIRTF and other future space opportunities present tremendous technological challenges for scientific instrumentation to capitalize fully on the potential of telescopes in space. Intellectual resources combined with financial support are required to meet these challenges, and should help increase our understanding of basic phenomena throughout our universe.

Nancy W. Boggess
NASA Headquarters

Craig R. McCreight
Ames Research Center

AGENDA

Infrared Detector Technology Workshop
NASA Ames Research Center
Auditorium, Building N201
Message Phone: (415) 694-5256 or FTS 464-5256

Tuesday, August 13, 1985

8:30	Introductory Remarks	N. W. Boggess (NASA Headquarters)
	Opening Remarks	C. R. McCreight (Ames Research Center)
8:45	"Detector Requirements for Space Astronomy"	E. L. Wright (UCLA)
	"Near Infrared Observations of the Space Shuttle and Other Orbiting Objects"	F. Witteborn, L. Caroff (Ames Research Center), D. Rank (UC Santa Cruz), G. Ashley (AVCO Everett Research Laboratory)
	"Extrinsic Detector Characterization at Ultra-Low Backgrounds"	E. T. Young, D. K. Speed (U. Arizona)
10:00	Break	
10:20	"Development of Integrating JFET Readouts"	F. J. Low, M. Alwardi (U. Arizona and Infrared Laboratories)
	"Long Wavelength Detectors for SIRTF"	P. L. Richards (UC Berkeley)
	"Transient- and Temperature-Dependent Behavior in Ge:Be Photoconductors"	N. M. Haegel, E. E. Haller (Lawrence Berkeley Laboratory)
	"Detector Systems for ISO's Photometer ISOPHOT"	J. Wolf, D. Lemke, M. Burgdorf, D. Lutz (Max Planck Institut für Astronomie)
12:10	Lunch	
1:10	"Progress Report on NTD Germanium for Low-Temperature Bolometers"	E. E. Haller (Lawrence Berkeley Laboratory)
	"Characterization of NTD Germanium and Ion-Implanted Silicon Bolometers at 0.3 K and 0.1 K"	H. Moseley, R. Kelley, A. E. Szymkowiak (Goddard Space Flight Center), M. Juda, D. McCammon, J. Zhang (U. Wisconsin), E. E. Haller (Lawrence Berkeley Lab)

Tuesday, August 13, 1985 (cont'd)

	"A Progress Report on Bolometers Operating at 0.1 K using Adiabatic Demagnetization Refrigeration"	T. Roellig, L. Lesyna, M. Werner, P. Kittel (Ames Research Center)
	"Low-Background InSb Array Development"	R. D. Thom, B. T. Yang (Santa Barbara Research Center)
2:45	Break	
3:05	"InSb Arrays: Astronomy with a 32 x 32 CCD / Development of a 58 x 62 DRO"	W. J. Forrest, J. L. Pipher (U. Rochester)
	Development of InSb and Si:x Arrays for ISO Camera	F. Sibille et al. (Observatoire de Lyon)
4:00	Discussion -- Status of SIRTF	M. W. Werner, J. P. Murphy (Ames Research Center)
	-- Status of ISO	J. Wolf (Max Planck Institut für Astronomie), F. Sibille (Observatoire de Lyon)
5:30	Adjourn	
7:30	Banquet (Chef Chu's)	

Wednesday, August 14, 1985

8:30	"Shortwave Photovoltaic HgCdTe Detector Arrays for Space Astronomy"	A. Sood, N. Hartle, J. Marciniec, P. Zimmermann (Honeywell Electro-Optics Division)
	"Characterization of 2.5 Micron HgCdTe Detectors for Ultra Low Background Applications"	D. DePoy, D. N. B. Hall (U. Hawaii)
	"Evaluation of Rockwell HgCdTe Arrays for Astronomical Use"	M. J. Lebofsky, E. F. Montgomery, W. F. Kailey (U. Arizona)
	"Tests of Rockwell HgCdTe PACE Array"	M. Hereld, D. A. Harper (U. Chicago)
10:20	Break	

Wednesday, August 14, 1985 (cont'd)

10:40	"Si:As BIB Detector Arrays"	R. Bharat, M. D. Petroff, J. J. Speer, M. G. Stapelbroek (Rockwell Science Center)
	"A Study of Si:In Hybrid Surface Channel IRCCD Device"	E. Tollestrup, R. W. Capps (U. Hawaii)
	"Imagery with a Si:Bi 16 x 16 Array"	J. H. Goebel, N. Moss, C. R. McCreight (Ames Research Center), D. Rank (UC Santa Cruz), W. Wisniewski (U. Arizona)
12:15	Lunch	
1:15	"58 x 62 Si:Sb Detector Array for Low-Background Applications"	M. S. Worley, S. D. Gaalema (Hughes Aircraft Company/IEGTC)
	"Preliminary Test Data Using the MOS DRO with Si:In Detector Material"	A. Fowler, R. Joyce (NOAO/Kitt Peak National Observatory)
	"Evaluation of Si:Ga Direct Readout Array -- Preliminary Results"	G. Lamb, P. Shu, D. Lokerson, D. Gezari, J. Bowser (Goddard Space Flight Center)
2:45	Break	
3:05	"Si:Ga and Si:As Direct Readout Detector Arrays"	J. F. Arens, M. C. Peck (UC Berkeley), S. Gaalema (Hughes Aircraft Company)
	"Development of the Unit Cell of a Ge:Ga Array"	C. A. Schnitzer, C. M. Parry (Aerojet ElectroSystems Company)
4:00	Summary and Conclusion	

ATTENDEES -- INFRARED DETECTOR TECHNOLOGY WORKSHOP

Name	Address	Telephone
George M. Anderson	Ames Research Center Mail Stop 244-10 Moffett Field, CA 94035	(415) 694-6548
Jeffrey Beeman	University of California Berkeley, CA 94720	(415) 486-5632
Chas A. Beichman	Jet Propulsion Laboratory Mail Stop 230-207 4800 Oak Grove Dr. Pasadena, CA 91109	(818) 584-1012
Gary Bernstein	Department of Physics University of California Berkeley, CA 94720	(415) 642-5721
Ramesh Bharat	Rockwell International Science Center MS 031-BA01 3370 Miraloma Dr. Anaheim, CA 92803	(714) 762-1460
J. F. Blodget	NASA Ames Research Center Mail Stop 213-8 Moffett Field, CA 94035	(415) 694-6407
Nancy W. Boggess	NASA Headquarters Code EZ Washington, DC 20546	(202) 453-1469
Walter F. Brooks	Ames Research Center Mail Stop 244-15 Moffett Field, CA 94035	(415) 694-6547
Richard W. Capps	Institute for Astronomy University of Hawaii 2680 Woodlawn Dr. Honolulu, HI 96822	(808) 948-8429
M. W. Castelaz	NASA Ames Research Center Mail Stop 245-6 Moffett Field, CA 94035	(415) 694-6849
Gordon Chin	Goddard Space Flight Center Code 697 Greenbelt, MD 20771	(301) 344-8649

Jesse Davis	Cochise Instruments P. O. Box 729 Sierra Vista, AZ 85636	(602) 458-6453
Rudolf Decher	Marshall Space Flight Center ES-61 Huntsville, AL 35812	(205) 453-5130
Darren DePoy	Institute for Astronomy University of Hawaii 2680 Woodlawn Dr. Honolulu, HI 96822	(808) 948-6756
William Duncan	Royal Observatory Blackford Hill Edinburgh EH9 3HJ Scotland	(031) 667 3321
David O. Edge	Science Studies Unit University of Edinburgh c/o 25 Gilmour Rd. Edinburgh EH16 5NS Scotland	(031) 667 3497
W. Lum Eisenman	Naval Ocean Systems Center Code 563 San Diego, CA 92152	(619) 225-6591
Benton Ellis	Department of Astronomy University of Texas Austin, TX 78712	(512) 471-4461
Don Enders	Litton Industries Electron Devices Division Tempe, AZ 85281	(602) 968-4471 (714) 835-2821
Edwin F. Erickson	Ames Research Center Mail Stop 245-6 Moffett Field, CA 94035	(415) 694-5508
Giovanni G. Fazio	Smithsonian Astrophysical Observatory 60 Garden St. Cambridge, MA 02138	(617) 495-7458
Marc Fisher	Department of Physics University of California Berkeley, CA 94720	(415) 642-5721
William J. Forrest	Department of Physics & Astronomy University of Rochester Rochester, NY 14627	(716) 275-4343

Al M. Fowler	NOAO/Kitt Peak National Observatory Box 26732 Tucson, AZ 85726	(602) 325-9339
Steven D. Gaalema	Hughes Aircraft Company 6155 El Camino Real MS 102 Carlsbad, CA 92008	(619) 931-3408
T. N. Gautier	IPAC Mail Stop 100-22 California Institute of Technology Pasadena, CA 91125	(818) 584-1012
Dan Gezari	Goddard Space Flight Center Code 697 Greenbelt, MD 20771	(301) 344-1432
C. M. Gillespie Jr.	NASA Ames Research Center Mail Stop 211-12 Moffett Field, CA 94035	(415) 694-6302
Fred C. Gillett	NOAO/Kitt Peak National Observatory Box 26732 Tucson, AZ 85726	(602) 327-5344
John H. Goebel	Ames Research Center Mail Stop 244-10 Moffett Field, CA 94035	(415) 694-6525
Lawrence T. Greenberg	Aerospace Corporation Box 92957 Los Angeles, CA 90009	(213) 416-8964
Erich Grossman	Downs Laboratory of Physics 320-47 California Insitute of Technology Pasadena, CA 91125	(818) 356-6627
Stephen Grossman	Lockheed Palo Alto Research Laboratory 3251 Hanover St. Palo Alto, CA 94304	(415) 424-2280
Nancy M. Haegel	Lawrence Berkeley Laboratory 70A/3307 University of California Berkeley, CA 94720	(415) 486-5632
John A. Hackwell	Department of Physics & Astronomy University of Wyoming Box 3905 Laramie, WY 82071	(307) 766-6296

Donald N. B. Hall	Institute for Astronomy University of Hawaii 2680 Woodlawn Dr. Honolulu, HI 96822	(307) 766-6296
Eugene E. Haller	Lawrence Berkeley Laboratory 70A/3363D University of California Berkeley, CA 94720	(415) 486-5294
William L. Hansen	Lawrence Berkeley Laboratory 70A/3307 University of California Berkeley, CA 94720	(415) 486-5632
D. A. Harper	Yerkes Observatory University of Chicago Williams Bay, WI 53191	(414) 245-5555
Paul Harvey	Department of Astronomy University of Texas Austin, TX 78712	(512) 471-4461
S. Roland Hawkins	Lockheed Palo Alto Research Laboratory Bldg. 202, Org. 95-43 3251 Hanover St. Palo Alto, CA 94304	(415) 424-2230
Mark Hereld	University of Chicago Astronomy and Astrophysics 5640 S. Ellis Ave Chicago, IL 60637	(414) 245-5555
Terry L. Herter	Department of Astronomy Cornell University Ithaca, NY 14853	(607) 256-4805
Steven M. Hing	NASA Ames Research Center Mail Stop 244-15 Moffett Field, CA 94035	(415) 694-5913
Alan Hoffman	Santa Barbara Research Center 75 Coromar Dr. Goleta, CA 93117	(805) 968-3511 x2515
Harris Honickman	Government Systems Division R&E, Dept. 339 Eastman Kodak Company 121 Lincoln Ave. Rochester, NY 14650	(716) 253-2302
William T. Hornaday	Jet Propulsion Laboratory Mail Stop 11-116 4800 Oak Grove Dr. Pasadena, CA 91109	(818) 354-3111

James R. Houck	Department of Astronomy Cornell University Ithaca, NY 14853	(607) 256-4806
Barbara Jones	CASS, C-011 University of California La Jolla, CA 92093	(619) 452-4066
Marshall Joy	Department of Astronomy University of Texas Austin, TX 78712	(512) 471-3415
Reinhard Katterloher	Max-Planck-Institut für Physik und Astrophysik 8046 Garching Federal Republic of Germany	(089) 32 99 1
Jocelyn Keene	California Institute of Technology 320-47 Pasadena, CA 91125	(818) 356-6675
George T. Keene	Government Systems Division R&E, Dept. 394 Eastman Kodak Company 121 Lincoln Ave. Rochester, NY 14650	(716) 253-2531
Randall K. Kirschman	Box 391716 Mountain View, CA 94039	(415) 369-7531
Michael K. Kiya	NASA Headquarters Code EZ Washington, DC 20546	(202) 453-1435
Alan J. Kogut	416 North St. Oakland, CA 94609	(415) 655-9466
Jeff Kuhn	Department of Physics Princeton University Princeton, NJ 08544	(609) 452-5862
John Lacy	Department of Astronomy University of Texas Austin, TX 78712	(512) 471-1469
Gerald M. Lamb	Goddard Space Flight Center Code 724.3 Greenbelt, MD 20771	(301) 344-8694
John W. Lear	P.O. Box 179 Denver, CO 80201	(303) 977-5457
Marcia J. Lebofsky	Steward Observatory University of Arizona Tucson, AZ 85721	(602) 621-2731

Kenneth E. Leibold	Government Systems Division R&E, Dept. 365 Eastman Kodak Company 121 Lincoln Ave. Rochester, NY 14650	(716) 253-2330
Chris Leidich	Ames Research Center Mail Stop 244-15 Moffett Field, CA 94035	(415) 694-5692
Dan Lester	Department of Astronomy University of Texas Austin, TX 78712	(512) 471-4461
Paul LeVan	OPI Air Force Geophysics Laboratory Hanscom AFB, MA 01731	(617) 861-4550
Larry Lesyna	NASA Ames Research Center Mail Stop 245-6 Moffett Field, CA 94035	(415) 694-5537
Frank J. Low	Steward Observatory University of Arizona Tucson, AZ 85721	(602) 621-2727
Willem Luinge	Laboratory for Space Research Groningen P. O. Box 800 9700 AV Groningen The Netherlands	(50) 116629
Paul N. Luke	Lawrence Berkeley Lab 70A/3361 University of California Berkeley, CA 94720	(415) 486-5632
David Lynch	Aerospace Corporation P.O. Box 92457 Los Angeles, CA 90009	(213) 648-6686
John C. Lyons	Goddard Space Flight Center Code 724.0 Greenbelt, MD 20771	(301) 344-8006
Mark McCaughrean	Royal Observatory Blackford Hill Edinburgh EH9 3HJ Scotland	(031) 667 3321
Craig R. McCreight	Ames Research Center Mail Stop 244-10 Moffett Field, CA 94035	(415) 694-6549

Mark E. McKelvey	Ames Research Center Mail Stop 244-10 Moffett Field, CA 94035	(415) 694-6525
Gary J. Melnick	Smithsonian Astrophysical Observatory 60 Garden St. Cambridge, MA 02138	(617) 495-7388
Harvey Moseley	Goddard Space Flight Center Code 697 Greenbelt, MD 20771	(301) 344-5018
James P. Murphy	Ames Research Center Mail Stop 244-15 Moffett Field, CA 94035	(415) 694-6643
David Nadeau	Government Systems Division R&E, Dept. 339 Eastman Kodak Company 121 Lincoln Ave. Rochester, NY 14650	(716) 253-2302
Gerry Neugebauer	Downs Laboratory of Physics 320-47 California Institute of Technology Pasadena, CA 91125	(818) 356-4284
Richard L. Nielsen	Santa Barbara Research Center 75 Coromar Dr. Goleta, CA 93117	(805) 968-3511 x2688
In-Shik Park	Lawrence Berkeley Laboratory 70A/3345 Berkeley, CA 94720	(415) 486-5632
Philip C. Parr	Government Systems Division R&E, Dept. 365 Eastman Kodak Company 121 Lincoln Ave. Rochester, NY 14650	(716) 253-2330
Michael C. Peck	University of California Space Sciences Laboratory Berkeley, CA 94720	(415) 642-8494
Michael D. Petroff	Rockwell International Science Center 3370 Miraloma Ave. Anaheim, CA 92803	(714) 632-4513
Judith L. Pipher	Department of Physics & Astronomy University of Rochester Rochester, NY 14627	(617) 275-4402

Dieter Pommerrenig	E-O Product Engineering 23866 Petrel Ct. Laguna Niguel, CA 92677	(714) 643-3319
Richard Puetter	CASS, C-011 University of California San Diego, CA 92093	(619) 452-4945
James V. Radostitz	Department of Physics University of Oregon Eugene, OR 97403	(503) 686-4226
Ruben Ramos	Ames Research Center Mail Stop 244-15 Moffett Field, CA 94035	(415) 694-5698
Harold Reitsema	Ball Aerospace Systems Division Box 1062 Boulder, CO 80306	(303) 939-5026
Paul L. Richards	Department of Physics University of California Berkeley, CA 94720	(415) 642-3027
George H. Rieke	Steward Observatory University of Arizona Tucson, AZ 85721	(602) 621-2832
Thomas P. L. Roellig	Ames Research Center Mail Stop 245-6 Moffett Field, CA 94035	(415) 694-6426
Carolyn Rossington	University of California Dept. of Materials Science Berkeley, CA 94720	(415) 486-5632
Sid Russak	Martin Marietta P.O. Box 179 Denver, CO 80201	(303) 977-4180
Ray Russell	Aerospace Corporation Mail Stop M2-266 Box 92957 Los Angeles, CA 90009	(213) 648-5528
Kandiah Shivanandan	Naval Research Laboratory Code 4138SM Washington, DC 20375	(202) 767-2749
Peter Shu	Goddard Space Flight Center Code 727.2 Greenbelt, MD 20771	(301) 344-5297

Francois Sibille	Observatoire de Lyon 69230 St. Genis Laval France	(7) 856 0705
Peter Silverglate	Perkin-Elmer Corporation Space Science Division 100 Wooster Heights Rd. Danbury, CT 06810	(203) 797-5566
David S. Smith	Cincinatti Electronics Corp. 2630 Glendale-Milford Rd. Cincinatti, OH 45241	(513) 733-6100
Robert G. Smith	Institute for Astronomy University of Hawaii 2680 Woodlawn Dr. Honolulu, HI 96822	(808) 948-6526
Robert L. Smith	Cincinatti Electronics Corp. 2630 Glendale-Milford Rd. Cincinatti, OH 45241	(513) 733-6100
Ashok K. Sood	Honeywell Electro-Optics Division 2 Forbes Road Lexington, MA 02173	(617) 863-3100
Maryn G. Stapelbroek	Rockwell International Science Center 3370 Miraloma Ave. Anaheim, CA 92803	(714) 632-4528
Donald W. Strecker	Ball Aerospace Systems Division Box 1062 Boulder, CO 80306	(303) 939-4346
Alan Tokunaga	Institute for Astronomy University of Hawaii 2680 Woodlawn Dr. Honolulu, HI 96822	(808) 948-6691
Eric Tollestrup	Institute for Astronomy University of Hawaii 2680 Woodlawn Dr. Honolulu, HI 96822	(808) 948-8701
Charles Townes	University of California Dept. of Physics Berkeley, CA 94720	(415) 642-1128
Russell G. Walker	Jamieson Science and Engineering Box F1 Felton, CA 95018	(408) 335-2591

Jian-Qing Wang	Department of Physics University of California Berkeley, CA 94720	(415) 642-5721
Robert E. Warren	Hughes Aircraft Company Bldg. E1/Mail Stop C108 Box 902 El Segundo, CA 90245	(213) 616-9530
Dan M. Watson	Downs Laboratory of Physics 320-47 California Institute of Technology Pasadena, CA 91125	(818) 356-4682
Ted Weber	Ames Research Center Mail Stop 244-10 Moffett Field, CA 94035	(415) 694-6525
Michael W. Werner	Ames Research Center Mail Stop 245-6 Moffett Field, CA 94035	(415) 694-5101
Fred C. Witteborn	Ames Research Center Mail Stop 245-6 Moffett Field, CA 94035	(415) 694-5520
Jürgen Wolf	Ames Research Center Mail Stop 245-6 Moffett Field, CA 94035	(415) 694-5522
Diane Wooden	Ames Research Center Mail Stop 245-6 Moffett Field, CA 94035	(415) 694-6151
M. Stuart Worley	Hughes Aircraft Company 6155 El Camino Real Carlsbad, CA 92008	(619) 931-3401
Edward L. Wright	Department of Astronomy University of California, Los Angeles 405 Hilgard Ave. Los Angeles, CA 90024	(213) 825-5755
B. T. Yang	Santa Barbara Research Center 75 Coromar Dr. Goleta, CA 93117	(805) 968-3511 X4369
Erick T. Young	Steward Observatory University of Arizona Tucson, AZ 85721	(602) 621-4119

Detector Requirements for Space Infrared Astronomy

N87-13705

by Edward L. Wright, UCLA Astronomy

I have been given the easy job of assigning the problems which the other speakers at this workshop must solve. In this professorial role I have decided to start my lecture with a quiz:

Why observe from space?

A. Better transmission.
B. Lower background.
C. Better "seeing"
D. Spend more $$$$
E. All of the above

The answer of course is E, all of the above. Since space infrared astronomy will be an expensive operation, I want to describe the limits of performance that can be achieved, given the low background in space, the lack of atmospheric distortion, and the availability of the entire infrared spectrum.

The natural background in space is composed of several components: the scattered zodiacal light, the diffuse galactic light, the thermal zodiacal light, the thermal radiation from galactic dust, and the 2.7 K cosmic background. Figure 1 presents the sum of these components in a fairly unconventional form: Planck brightness temperature vs. wavenumber. Any background-limited (BLIP) detector must have a temperature less than the Planck brightness temperature of the background, and practical detectors require much lower temperatures. Telescope mirrors, however, are nearly perfect devices, so the same plot on linear axes in Figure 2 shows where the Hubble Space Telescope (HST) and the Large Deployable Reflector (LDR) are capable of natural background-limited performance.

For detectors the most important aspect of the background is the number of photons falling on each pixel. Figure 3 shows a plot of the photons per second per octave per diffraction-limited pixel both from the natural background and from a warm telescope such as LDR. I have used the definition $A\Omega = \lambda^2$ for the diffraction limit, which gives the correct transition to single mode coherent systems. Thus the plotted quantity is $\nu I_\nu \lambda^2/h\nu$. There are two regions in this chart where the current state of detector array development is far from meeting the challenge of BLIP operation in space: the 3 μm region near the zodiacal light minimum, and the high background region for LDR with $\lambda > 30$ μm.

VERY LOW BACKGROUNDS

A reasonable photometric camera on SIRTF would have a transmission of 30%, including filters, and a fractional bandwidth of 1/3, leading to a flux of 1 photon/second on a diffraction-limited pixel at 3 μm. This gives a BLIP NEP of 10^{-19} W/√Hz. Clearly a BLIP detector must have a dark current < 0.5 e/sec. By comparing the shot noise current caused by dark current to the Johnson noise current from the junction resistance

$$(2I_d e)^{0.5} = (4kT/R)^{0.5} \text{ amp}/\sqrt{\text{Hz}}$$

I find that the junction resistance must be greater than

$$(R/T) > 2 * 10^{15}\ \Omega/K$$

to give $I_d < 0.5$ e/sec. For InSb or HgCdTe detectors operating near 50 K, the detector resistance must be more than $10^{17}\ \Omega$!

For detectors in an integrating array, the read noise must be less than the square root of the number of photons collected. Taking 1000 seconds as an optimistic upper limit to the possible length of an integration in low Earth orbit I find that the read noise must be less than 22 electrons.

Spectroscopy in the 3 μm region will be a very powerful tool for extragalactic and cosmological problems, but will require even better detector performance. For a resolution $\nu/\Delta\nu = 1000$, and a slightly larger than diffraction-limited aperture, a detector in a spectrograph will receive 0.01 photons/second. This application requires dark currents < 0.005 e/sec, detector impedances > $10^{19}\ \Omega$ at 50 K, and read noises < 2.2 electrons.

I have concentrated on the resistance of the detectors, and not the capacitance, because resistors generate noise and capacitors do not. The $\sqrt{kTC}$ charge noise on a capacitor is just the Johnson noise current $\sqrt{4kT/R}$ A/$\sqrt{Hz}$ of the resistor across it integrated over the effective bandwidth 1/4RC Hz of the RC circuit. Thus when a pixel in an array is reset by connecting the storage capacitor to a fixed potential through a small reset resistance, the charge after resetting has a variance of kTC. During an integration, however, thermal effects change the charge very slowly, with the time constant given by RC, which for a 0.01 pf well connected to a $10^{19}\ \Omega$ detector is longer than one day. By using a non-destructive readout to measure Q_1 just after reset and Q_2 just at the end of the integration, the variance of the signal Q_2-Q_1 is given by

$$var(Q_2-Q_1) = 2kTC(1 - e^{-t/RC})$$

Thus for integration times $t << RC$ the noise is $(2kTt/R)^{0.5}$ which is just Johnson noise. The Millikan oil drop experiments used to search for free quarks routinely achieve 0.01 electron rms noise, which is 100-1000 times smaller than $\sqrt{kTC}$.

Achieving sub-electron read noises in an integrated array presents a great challenge, but the required operations are easy to describe. Since stability over the integration time is needed, and DC circuits are not very stable, the charge must be modulated by "sloshing" it on and off the gate of a FET. This makes the unit cell of the multiplexor array a very small vibrating reed electrometer.

VERY LOW CONTRASTS

A second environment with very different requirements is the 100 μm region from a warm telescope such as LDR. Here the problem is the very large background of 10^{12} photons/second. Astronomers will want to observe sources right to the limit imposed by photon statistics, which after a 1 second exposure is a contrast of 1 part per million. The solution has been to chop the signal and have separate AC coupled amplifiers and phase sensitive

demodulators for each pixel, but this approach becomes impractical for arrays with more than a few dozen detectors. However, since the detectors for a 100 μm camera will probably be space more than 500 μm apart, one could make a multiplexor chip that includes an AC amplifier and phase sensitive demodulator for each pixel.

The detectors for this application require very high detective quantum efficiencies. A photoconductor with a high Gη but a low value of η will not be satisfactory, because its DQE is η/2. Bolometers easily achieve DQE > 70% and have NEPs less than the BLIP NEP of 10^{-15} W/√Hz, but bolometers are difficult to package in a 2 dimensional array. The blocked impurity band (BIB) detectors available for λ < 30 μm have high DQE, but have not been available for 100 μm.

REQUIRED ARRAY SIZES

The diffraction-limited cameras I have considered for SIRTF and LDR will require large numbers of pixels. If I take a reasonable pixel size of θ = λ/D, the 7' FOV of SIRTF covers 577 by 577 pixels at 3 μm. For LDR at 100 μm, the 3' FOV requires 175 by 175 pixels. Of course a truly diffraction-limited camera would have pixel spacing given by the Nyquist theorem: λ/2D, and would need 4 times as many pixels as given above.

To conclude, let me say that students who want credit for this workshop should turn in their projects to me, Ned Wright, by 5 PM tomorrow.

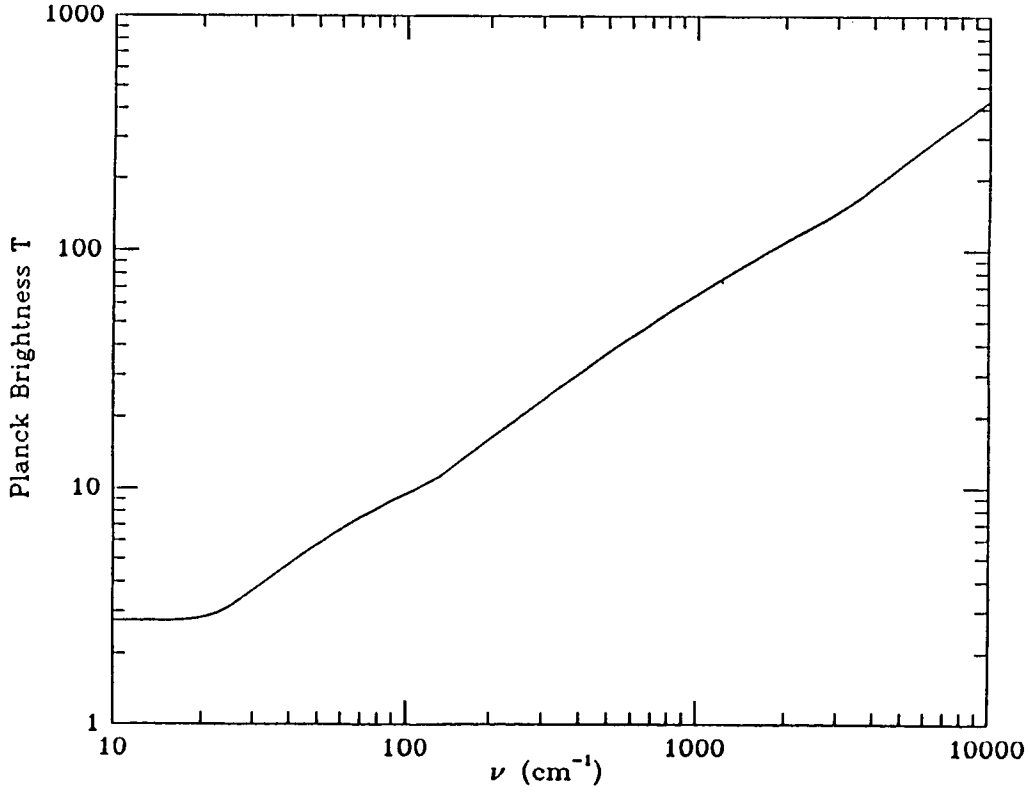

FIGURE 1: The natural background from Earth orbit, plotted as Planck brightness temperature vs. wavenumber.

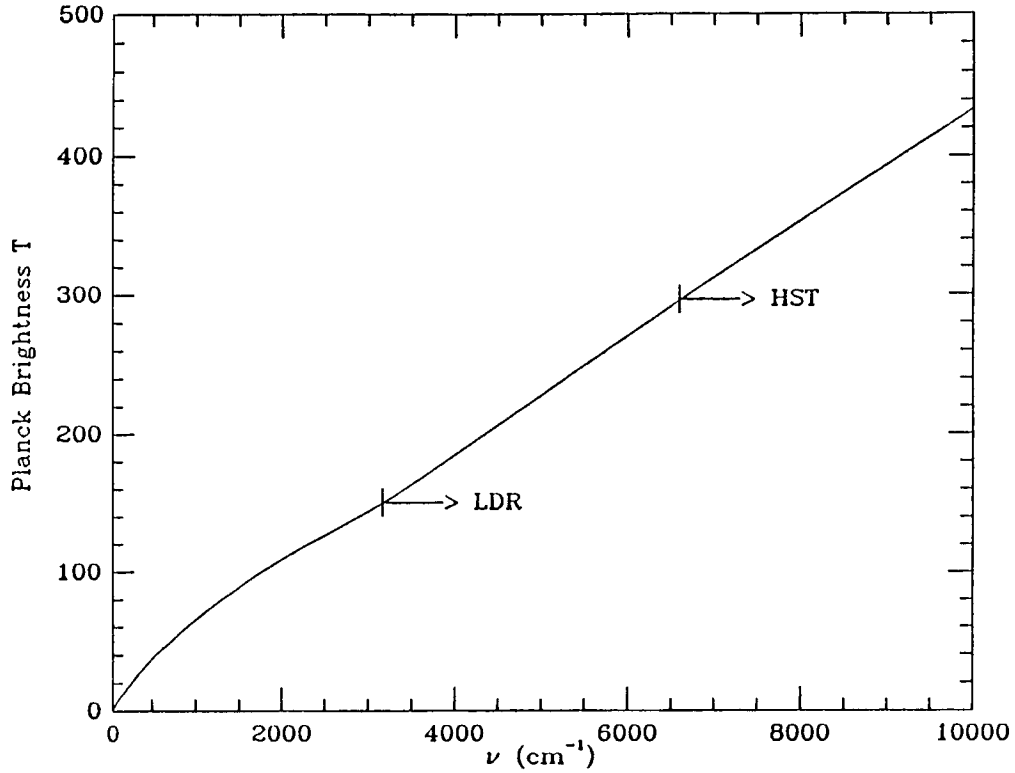

FIGURE 2: The natural background at short wavelengths, showing where HST and LDR become natural background limited.

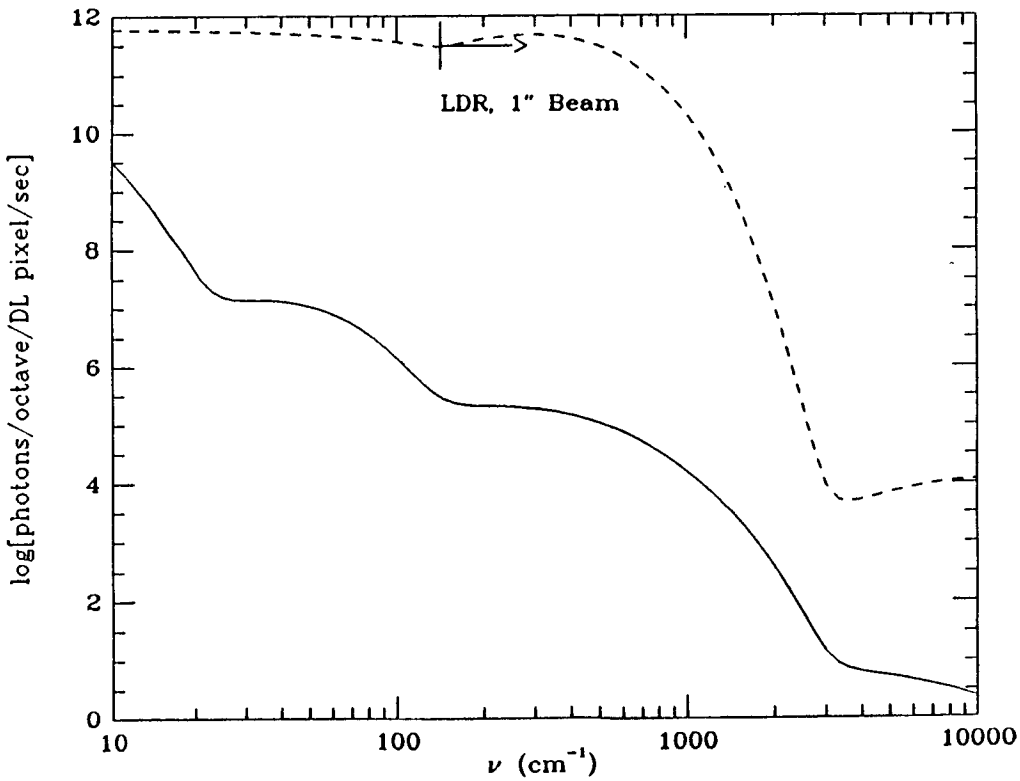

FIGURE 3: The natural background and the LDR background plotted as photons/second/DL pixel/octave = $\nu I_\nu \lambda^2/h\nu$. For LDR a 1" pixel size is used at short wavelengths, since LDR will not be diffraction-limited.

A Preliminary Assessment of Ground-based, Infrared Spectra of SpaceLab 2 During Nighttime Portions of Its Orbit

F.C. Witteborn, L.J. Caroff, Ames Research Center
D.M. Rank, Lick Observatory
G. Ashley, AVCO Everett Research Laboratory, Inc.

Abstract: The Space Shuttle Challenger was observed spectroscopically in two passes over Maui during the Spacelab 2 mission. Through most of one of the passes strong bands centered at 1.52 and 1.69 μm, tentatively identified as OH bands, were detected. The average luminosity of the Shuttle in the 1.45 to 1.75 μm range was roughly equal to that of a star of magnitude +5.5. The luminosity was much lower during part of the pass. Spectra from 0.65 to 2.4 μm were obtained during a second pass. These showed that most of the non-thermal emission is in the 1.2 to 2.2 μm range as would be expected for vibrationally excited OH.

Introduction

Observations of a visible glow emanating from the ram side of Shuttle surfaces (Banks et al. 1983), coupled with the proposal by Slanger (1983) that vibrationally excited OH could account for the glow, made clear the need for an infrared spectroscopic study of the orbiting Shuttle. The OH spectral density near 1.6μm would be at least 100 times higher than at 0.6 μm (Langhoff et al., 1983). The possibility that this glow might impair the sensitivity of infrared instruments on low orbiting platforms makes such a study particularly important. Observations from the Orbiter cabin with an objective grating device suggested that the glow could be attributed to NO_2 (Swenson, Mende, Clifton, 1984). Analysis of Atmospheric Explorer data (Yee and Abreu, 1983) and recent rocket photometer data (Lopez-Moreno, Rodrigo and Vidal, 1985) both provide strong evidence for OH glow in the vicinity of their respective spacecraft. The latter article provide a review of recent attempts to identify the contributions to the glow phenomena. A ground-based, photometric observation of Spacelab 1 showed that the Shuttle was exceptionally bright near 1.6 μm, (magnitude +6.6) consistent with OH emission (Witteborn, O'Brien and Caroff, 1985). To distinguish between these and other possibilities we proposed a spectroscopic study of Spacelab 2, again using the 1.6 meter telescope at the Advanced Research Projects Agency's Maui Optical Station (AMOS).

Method: A circular variable-interference-filter spectrometer (CVF) (Fig. 1) was mounted at the focus of the 1.6 meter AMOS tracking telescope on Mt. Haleakala. A dichroic beam splitter allowed half the visible light to reach a parfocal television camera used for fine guidance during tracking. The Shuttle was observed only at night when both it and the AMOS were in darkness. The Shuttle is made visible even in the Earth's shadow because of diffusely scattered light and, perhaps, the glow phenomena. During the first half of the second pass (August 6, 7 hr 54 min 39 sec) the Shuttle was lit by the 40 watt filament of the electron plasma gun.

As soon as the Shuttle was acquired in the CVF's field-of-view (FOV), the CVF was scanned repeatedly between 1.45 and 1.75 microns with $\lambda/\Delta\lambda=48$ during the first pass (August 1, 9 hr 56 min 56 sec to 9 hr 59 min 50 sec) and between 0.65 and 2.4 microns with $\lambda/\Delta\lambda=38$ during the second pass. The tracking was excellent, holding the Shuttle's center of luminosity constant relative to the FOV to within a few arcseconds. At closest approach the Shuttle was 22 arcseconds long. The FOV was 16 arcseconds diameter during the first pass and 24 arcseconds during the second pass. The passes lasted only about 3 minutes.

Spectra of calibration stars at two elevation angles were obtained before and after each sighting to permit corrections for atmospheric extinction. The wavelength scale was calibrated against a Xenon lamp.

An oscillating tertiary mirror moved the Shuttle's image into and out of the FOV so that the foreground radiation from the Earth's atmosphere did not contribute to the AC component of the signal. The detector was an indium antimonide photovoltaic diode cooled to about 55K. Its output signal was sent to a lock in amplifier, then digitized and stored in an Apple computer at 0.2 second intervals. A voltage corresponding to the CVF position angle (calibrated for wavelength) was simultaneously stored in the computer with the corresponding signal. Both sets of values were subsequently store on disk.

Approximate analogue displays of signal and wavelength were recorded on a strip-chart in real time.

Results: A strip-chart trace of the first useful night-time pass of Spacelab 2 over Maui is shown in Figure 2. This shows the temporal pattern of luminosity. The spectrum from 1.45 to 1.75 microns was scanned once every 8 seconds. We note that for the first 32 seconds after the object was in the FOV it was just detectable above the instantaneous noise level. (Further analysis to be carried out later will integrate the signal over various periods to provide greater photometric sensitivity.) Comparison with the AOV star BS7235 indicates a magnitude of approximately +8.5 during this part of the pass, as the Shuttle's distance decreased from 565 km to 474 km. At 9 hr 57 min 36 sec the infrared brightness began to increase rapidly reaching a magnitude of +5.5 at a distance of 324 km, 20 seconds after closest approach. The overall brightness fluctuated some but remained near this value as the range increased to 750 km.

The large, short-term variations in intensity apparent on the strip chart are emission lines. Several spectral scans representing 48 seconds of data are superimposed and plotted against a wavelength scale in Figure 3. Two bands show up repeatedly on successive scans. They are centered at 1.52 microns and 1.69 microns. The wavelength scale is accurate to 0.5%; the resolution is about 2%. These bands correspond quite closely to the positions of the strongest OH bands calculated by Langhoff et al. (1983) in their simulated spectrum of the Explorer O-glow which was made with the assumption that all vibrational states were equally excited.

During the second useful Spacelab 2 pass, we scanned the full range from 0.65 to 2.4 microns and used a larger aperture to include the entire Shuttle at closest range. Since this spectral range includes large terrestrial absorption features, these data must be corrected using stellar spectra before their appearance is meaningful. However, a preliminary glance at the raw data shows that again the magnitude near 1.6 microns reached about +5.5, this time just prior to pass overhead. The most prominant non-thermal feature appears to be the 1.1 to 2.2 μm micron band complex which we would associate with highly excited OH emission. Near 2.4 microns, thermal radiation from the payload bay may be the dominant source.

Discussion: The sudden appearance of OH lines during the first pass is evidence that the component of glow caused by OH emission is a variable phenomenon. It is expected that a review of the Spacelab 2 housekeeping data will show whether this display resulted from a water dump or from a change in attitude resulting in the exposure of hydrogen-rich surfaces to the ram direction. The relative constancy of the glow as the Shuttle moved to 750 km, where the 16 arcsecond FOV was nearly double the Shuttle's largest dimension and the projected surface area only 0.2 times that at closest range, suggests that the source of radiation was extended with a diameter of about 60 meters. An alternate explanation is that the intensity of the source was increasing at a rate that roughly cancelled its dilution with distance.

Further analysis of the data is expected to enable us to put upper limits on the glow intensity during the faint approach portion of the first pass. Unfortunately, sensitivity limitations of the instrument will put this upper limit in the range of 10 to 100 times the zodiacal background at 1.6 microns.

The CVF/AMOS system was used to obtain spectra of several other large satellites in the same wavelength ranges. No obvious infrared signal was obtained, although further analysis is required. The visible light luminosity of the Shuttle will also be determined from the co-mounted television camera. Comparison with star images is underway to quantify the faintest intensities observed.

Conclusion: The Shuttle glow is dominated by OH emission some of the time, but not necessarily all of the time. The emission appears to be variable with time and probably extended tens of meters beyond the Shuttle surface. The luminosity extremes at 1.6 microns measured for Spacelab 2 bracket the 1.6 micron measurement made for Spacelab 1.

References

1. Banks, P.M., Williamson, P.R., and Raitt, W.J.: Space Shuttle Glow Observations. Geophys, Res. Lett., vol. 10, 1983, p.118.

2. Langhoff, S.R., Jaffe, R.L., Yee, J.H., and Dalgarno, A.: The Surface Glow of the Atmospheric Explorer C and E Satellites. Geophys. Res. Lett., vol. 10, 1983, p.896.

3. Lopez-Moreno, J.J., Rodrigo, R., and Vidal, S.: Radiative Contamination in Rocket-Borne Infrared Photometric Measurements. J. of Geophys. Res., vol. 90, 1985, p.6617.

4. Slanger, T.G.: Conjectures on the Origin of the Surface Glow of Space Vehicles. Geophys. Res. Lett., vol. 10, 1983, p.130.

5. Swenson, G.R., Mende, S.B., and Clifton, K.S.: Ram Vehicle Glow Spectrum; Implication of NO_2 Recombination Continuum. Geophys. Res. Lett., vol. 12, 1985, p. 97.

6. Witteborn, F.C., O'Brien, K., Caroff, L.: Measurement of the Nighttime Infrared Luminosity of Spacelab 1 in the H- and K-Bands. NASA TM 85972, 1985.

7. Yee, J.H., and Abreu, V.J.: Visible Glow Induced by Spacecraft-Environment Interaction. Geophys. Res. Lett., vol. 10, 1983, p. 126.

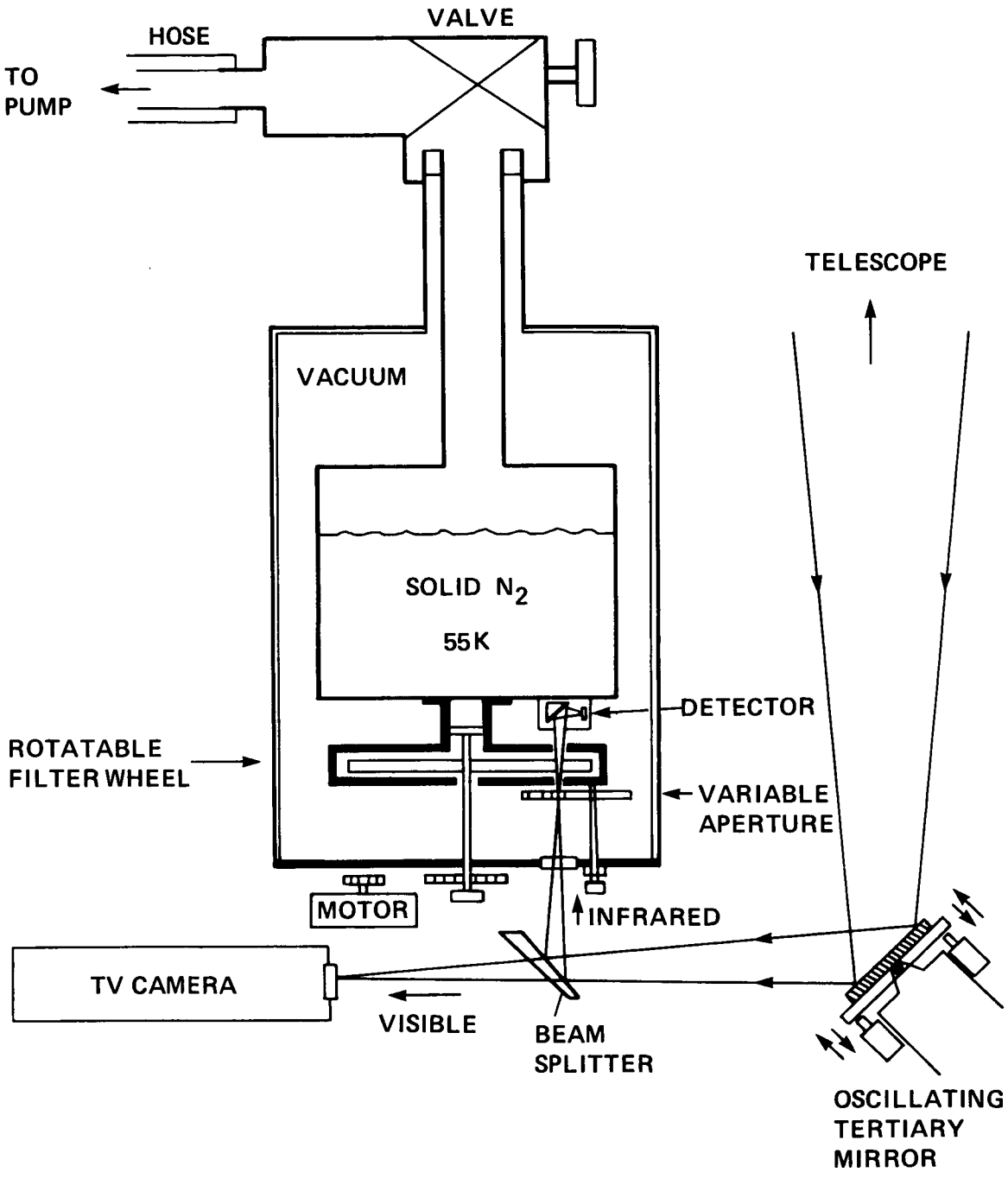

Figure 1. - Schematic diagram of focal-plane region showing cross sectional view of CVF spectrometer.

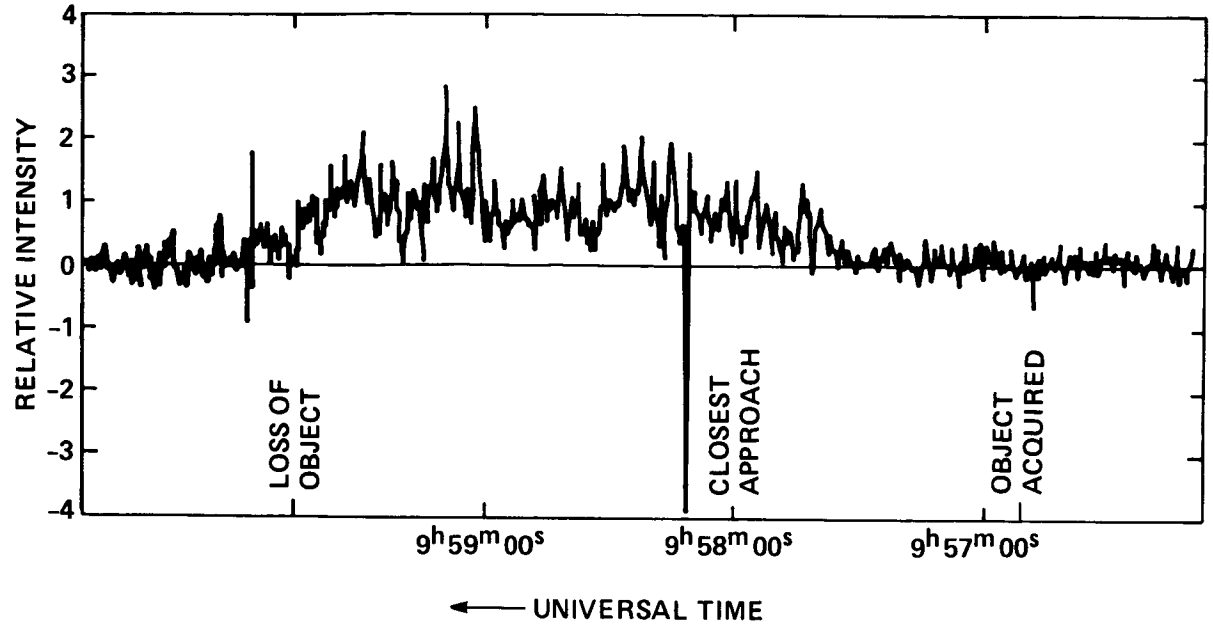

Figure 2. - Strip chart record of signal from spectrometer during Shuttle pass over Maui on August 1, 1985. Note that the spectrometer scanned from 1.45 to 1.75 μm and back again every 15.4 seconds.

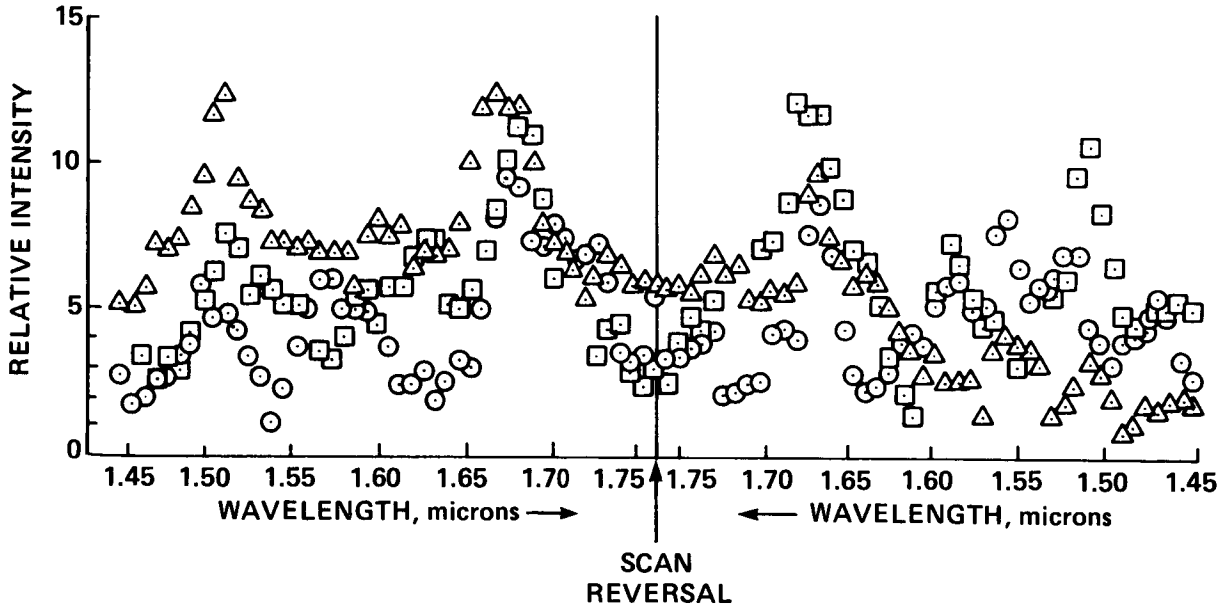

Figure 3. - Successive spectral scans are superimposed on a wavelength scale. Note that the range is covered twice so that reproducible features appear symmetrical about the scan reversal line. The time period brackets the time of closest approach. The circles denote the first scan shown, the x's, the second and the triangles, the third. More scans were obtained.

DARK CURRENT MEASURMENTS IN PHOTOCONDUCTORS

Erick T. Young
Donald Speed

Steward Observatory
University of Arizona

I. INTRODUCTION

The Space Infrared Telescope Facility (SIRTF) is envisioned as a next generation space observatory for observations between 2 and 700 um. In order to address many of the important scientific questions in areas such as cosmology, star formation, and galaxy evolution, infrared detectors of unparalleled sensitivity will be required. This paper describes measurments of one aspect of detector performance that may be of importance at the very low backgrounds expected with SIRTF.

SIRTF will be a meter-class cryogenic telescope capable of diffraction-limited performance down to 2 um. To fully exploit the potential of such a facility, it is highly desirable to have detection systems limited only by natural backgrounds, in particular, scattered and emitted radiation from the zodiacal dust. Table 1 gives some typical values for backgrounds expected at the SIRTF focal plane. The zodiacal emission is represented by a 275K graybody with an emissivity of 7.1×10^{-8}, and a telescope optical efficiencty of 50% is assumed. The pixel size used in this calculation is $\lambda/2D$, the size appropriate for superresolution observations. The column I(e/s) gives the background

TYPICAL SIRTF PHOTOMETER CONDITIONS

$\lambda(\mu m)$	$\Delta\lambda$	R(A/W)	Q(PH/S)	I(E/S)	NOISE(500)
3.5	1.75	1	0.32	0.11	14
12	2.4	2	323	67	259
20	10	3	2096	389	645
60	20	5	7042	726	1095

induced photocurrent (in electrons/second) if a responsivity of R (A/W) is realized. Finally, NOISE(500) is the maximum readout noise in a 500 second integration if the background limit is to be reached.

If the noise associated with detector dark current is not to be the limiting factor in system performance, the dark current should be less than the background current. The table shows that especially at the shorter wavelengths, exceedingly low dark currents are required. We describe dark current measurments for a number of different discrete photoconductive detectors. These materials are representative of those that might be used in a SIRTF focal plane.

II. EXPERIMENTAL SETUP

The measurments were conducted in a standard Infrared Laboratories liquid helium-cooled dewar. Consideralbe effort was required to insure a truly zero background environment for the

detectors. The arrangement used for these tests consisted of a series of three nested helium-temperature baffle boxes with hermetic electrical feedthroughs to the cold electronics. Small photon-shielded apertures were used for pump-out of the chambers.

Figure 1 is a schematic of the electronics used. The circuit is similar to the integrating JFET amplifier described by Low (1984 Appl.Opt., 23, 1308). The JFET is a 2N6483 thermally isolated from the helium-temperature work surface with a thin-wall fiberglass stalk. Roughly 1 mW of power is required to maintain a device temperature of ~60 K. The JFET is used as the input to a differential amplifier to minimize errors due to thermal drifts. A miniature RF relay is used to reset the integrator. A mechanical relay was chosen for this application since it was expected to be free of possible leakage paths that might be present in a solid-state reset device.

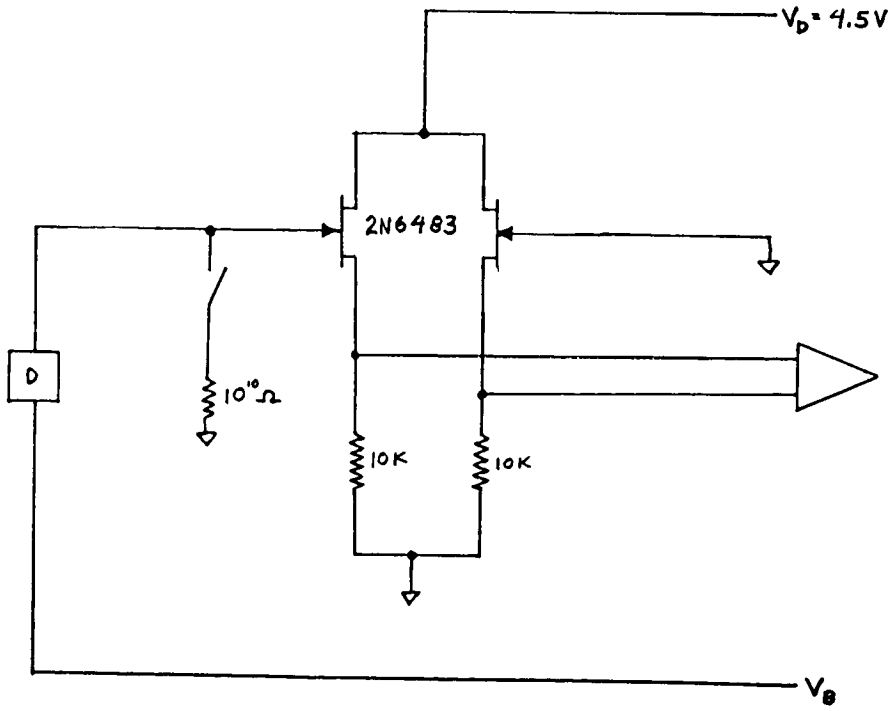

Figure 1. Electronics Schematic

The output of the integrator is given by:

$$\Delta V = \Delta Q * G / C$$

where ΔQ is the accumulated charge on the gate, G is the JFET voltage gain, and C is the effective gate capacitance (including any stray components). In order to measure G/C, we have substituted the detector with a 1.0 pF capacitor and applied a signal through the bias line. This circuit is then a capacitive divider with the gain given by the ratio of the standard capacitor to (G/C). If G is taken to be unity, the effective gate capacitance is found to be 13 pF.

The noise in this circuit has been measured with the capacitor in place of a detector. Figure 2 shows a typical 10 minute record of the differentiated integrator output. The important

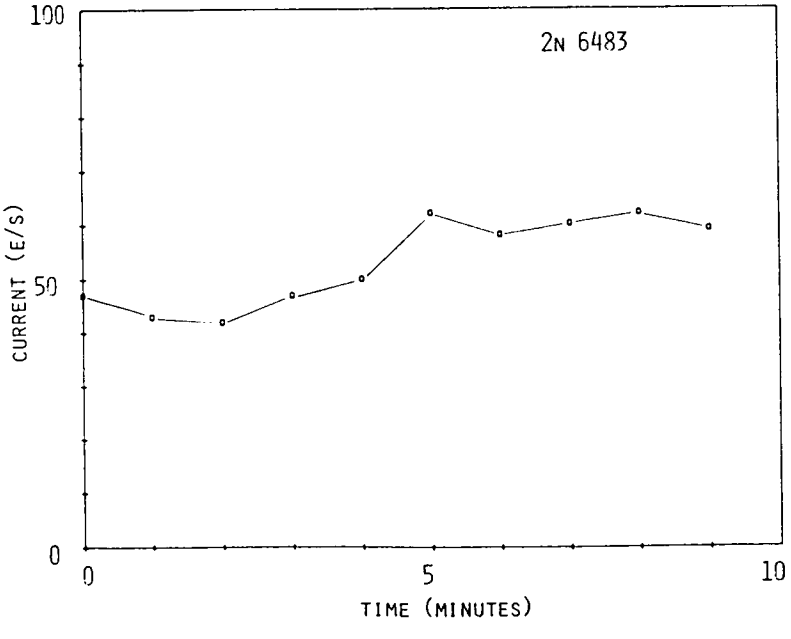

Figure 2. Integrating Amplifier Drift

point to note is that the intrinsic drift of the integrator is constant to better than +/- 10 electrons/sec. The constancy of this drift allows the JFET contribution in the dark current measurments to be removed and allows absolute current measurments to be made to a very low level.

The measurment cycle consisted of alternate readings taken at zero bias to establish the inherent amplifier drift rate and readings taken at full bias to determine the detector dark current. The bias switch was typically done every 30 - 60 minutes.

III. RESULTS

Table 2 lists the detector characteristics and bias voltages used for this series of dark current measurments. The bias values were determined independently at photon backgrounds of

DETECTOR CHARACTERISTICS

NUMBER	TYPE	SIZE (MM)	THICKNESS (MM)	BIAS(V)
UA 3-85	SI:IN	1.0x1.0	0.5	50
UA 5-01	SI:IN	1.0x1.0	0.25	18
SBRC 704	SI:GA	2.5x2.5	0.5	15
UA 101	SI:GA	1.0x1.0	0.5	15
UA 119	SI:SB	2.5x2.5	0.5	3

~10^7 ph s^{-1} cm^{-2} using a TIA amplifier. The materials are representative of high quantum efficiency extrinsic silicon photoconductors that are currently in use. The UA 3-85 Si:In sample was kindly provided by Dr. E. Haller of Lawrence Berkeley Laboratory. UA 5-01 and UA 101 were fabricated at the University of Arizona from float-zone refined crystals produced by Virginia Semiconductor. SBRC 704 is a Si:Ga detector made by Santa Barbara Research Center for the Spacelab II Infrared Telescope. Finally, UA 119 is a detector fabricated from Si:Sb produced by Rockwell for the IRAS project.

Figures 3-7 show the dark current as a function of time after application of bias. For plots with two curves, the open symbols represent data taken at 4.2K while the crosses show data taken at 2.5K.

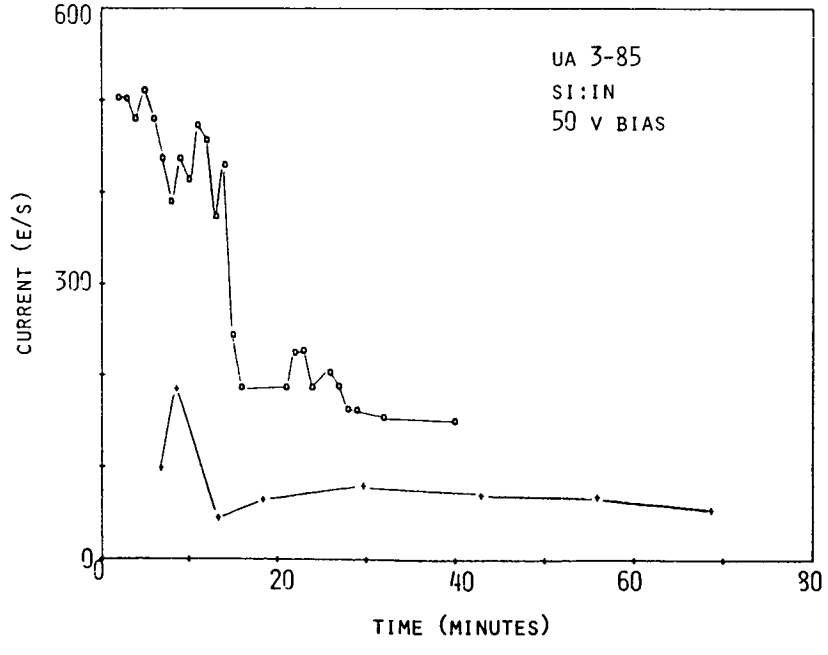

Figure 3. UA 3-85 Dark Current

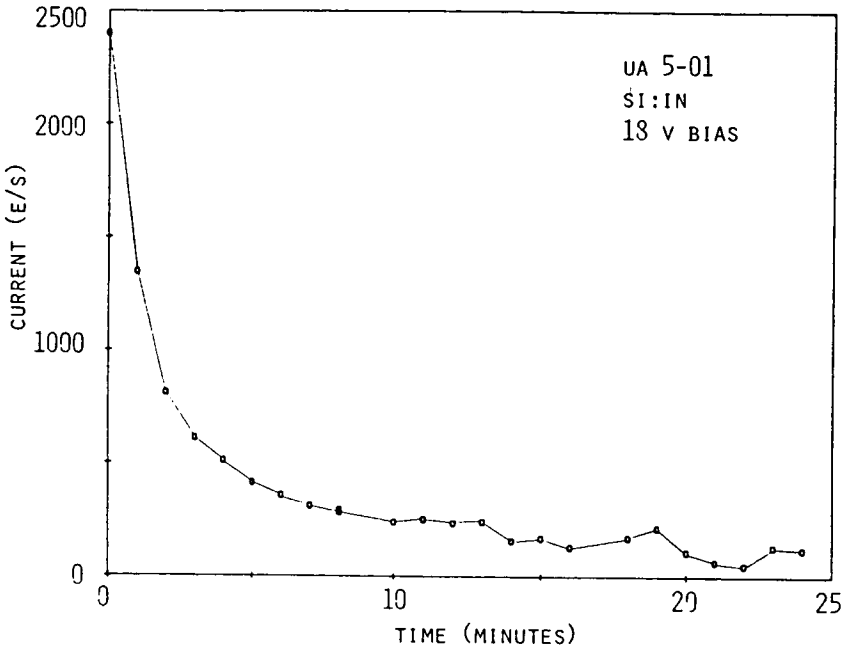

Figure 4. UA 5-01 Dark Current

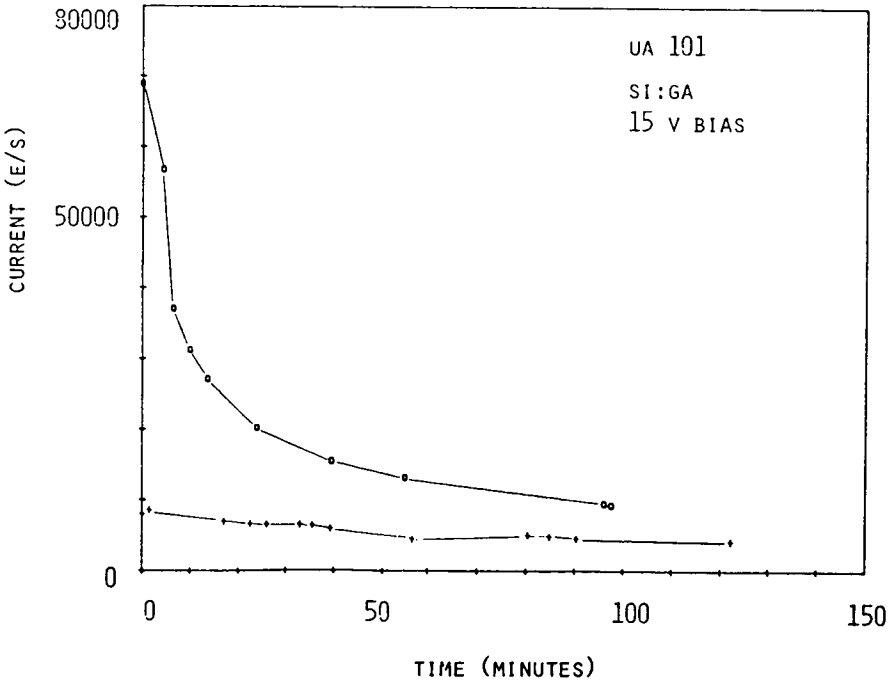

Figure 5. UA 101 Dark Current

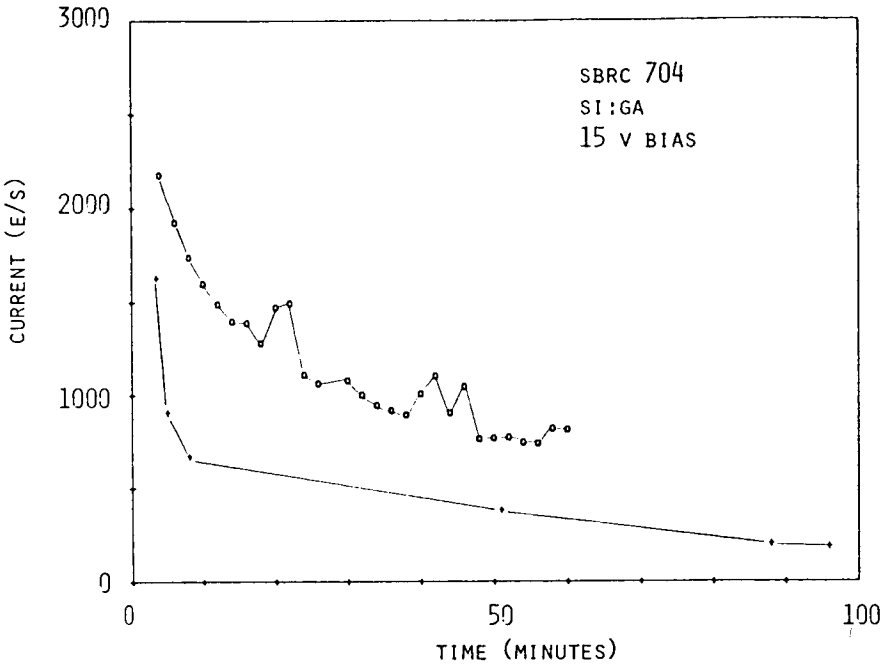

Figure 6. SBRC 704 Dark Current

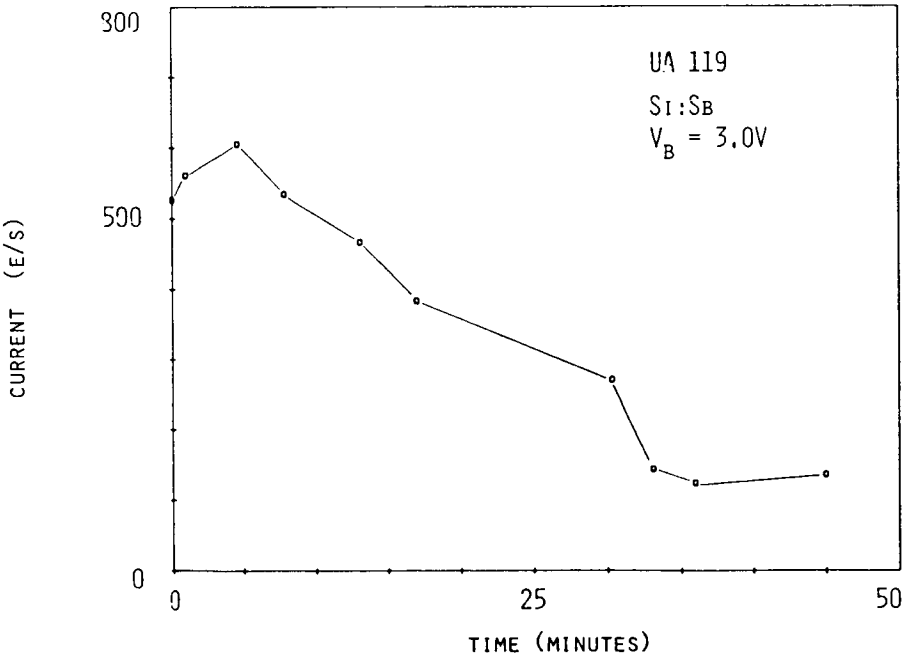

Figure 7. UA 119 Dark Current

Two conclusions can be immediately drawn from these curves. First, settling times for the detectors at zero background are very long, often approaching one hour. This result complicates the use of bias boost techniques such as were applied in IRAS to anneal radiation-induced responsivity increases. Since the recovery times are a significant fraction of the SIRTF orbital time, a simple bias boost after a passage through the South Atlantic Anomaly does not appear to be useful. Clearly, additional testing to determine the recovery time as a function of background is in order.

Second, all the detectors show a non-zero dark current. It is especially interesting to compare the two Si:Ga samples. Although the two detectors have quite comparable responsivities and quantum efficiencies, they differ in dark current by more than an order of magnitude. This result emphasizes the need to include dark current measurments as part of a complete detector characterization. The dark current in the Si:In and Si:Ga samples is temperature dependent, showing about a factor of two decrease between 4.2 and 2.5 K. This temperature dependence argues against both photon leak and surface conduction mechanisms. The most plausible explaination for this dark current is some hopping mechanism. The theory of hopping conduction, however, has not been applied to these very low levels.

How do these measured dark currents compare to the requirements for a background-limited SIRTF? The typical SIRTF application for photoconductors will be in arrays with pixel sizes of 50 - 100 um. If the dark current scales as the detector area, the measured values for these large discrete detectors can then

be scaled to a hypothetical SIRTF pixel. At 12 and 20 um existing materials appear to be adequate to reach the background limit. At the short wavelengths, where the demands are most severe, the best Si:In still falls short by almost two orders of magnitude. If the ultimate sensitivity of SIRTF is to be reached, additional materials research will probably be needed.

A number of questions remain unanswered by these dark current results. First, what is the mechanism for the dark current? The fact that very similarly performing detectors can have quite different dark currents may be an important clue. Second, what is the effect of various processing steps on the dark current? This question is especially relevant for SIRTF since array fabrication often involves many more processing steps than the manufacture of discrete detectors. Finally, is the area scaling law really valid for this dark current? We plan to investigate this question by fabricating small-pixel arrays for dark current measurments.

In the course of the dark current investigation, we discovered an additional, transient dark current that appears when the detector temperature is raised. Figure 8 shows the TIA output of detector UA 3-85 (Si:In). The detector is looking at a 500K blackbody source chopped at 2.5 Hz. The amplitude of the chopped signal is given by the thickness of the trace. The detector was warmed from 4.2K up to ~30K using an internal heater. Clearly evident are two output peaks at 19 and 25K during the warming cycle. The detector responsivity is fairly constant during these peaks since the chopped amplitude does not

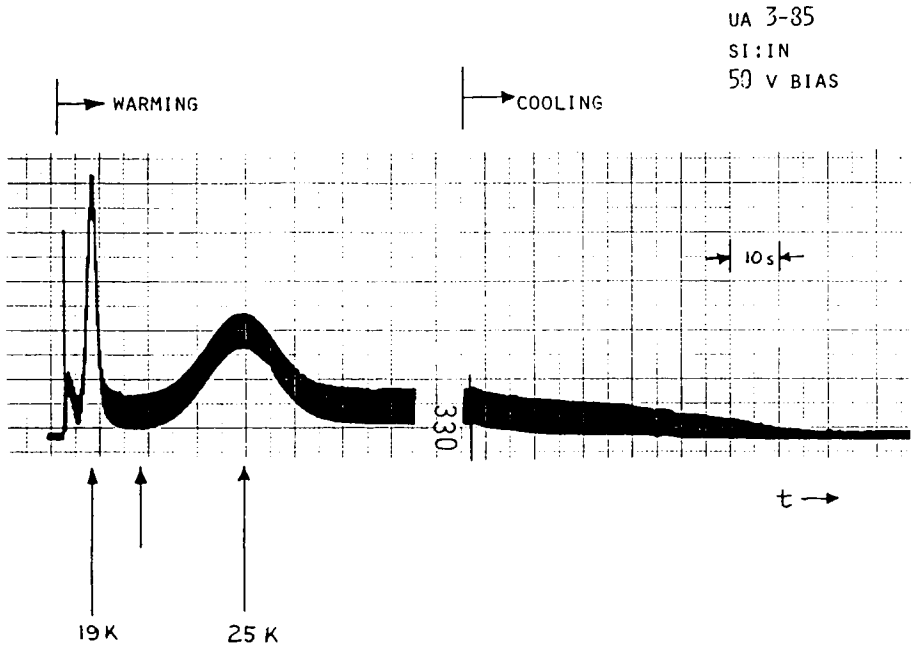

Figure 8. Transient Dark Current for UA 3-85

change significantly during these excursions. On the cooldown cycle, these dark current peaks are not present. We have found that an immediate reheating will yield peaks at a lower amplitude, but a long soak at 4.2K followed by a heating cycle will produce large amplitude peaks. We have also found that this effect is not unique to Si:In detectors, but is also present in Si:Ga samples we have tested.

The transient dark current is likely due to the thermal release of trapped charges in the detector. If so, this phenomenon may be a useful diagnostic tool for investigating the trap states in a photoconductor.

We wish to acknowledge the assistance of Frank Low in this investigation, and we thank George Rieke for the use of his SIRTF background calculations. This work was supported by NASA under an advanced detector development grant.

PROGRESS IN THE DEVELOPMENT OF INTEGRATING JFET AMPLIFIERS

F. J. Low and M. Alwardi

University of Arizona
and
Infrared Laboratories, Inc.

INTRODUCTION

A new approach to infrared detector readout has appeared with the development of integrating JFet amplifiers (Low, F.J., Applied Optics, 23, 1308, 1984). This brief progress report includes results on the operation of commerically available devices at a temperature of 40 K, on their sensitivity and on an effort to develop a new Si JFet with properties optimized for cryogenic applications. Even with presently available devices it will be shown that for applications such as the SIRTF photometer, MIPS, the most stringent sensitivity requirements of noise currents as low as 1 electron/sec in less than 100 seconds of integration can be met.

ARRAY CONCEPTS

Our current concept of a simple hybrid array is included to illustrate how the JFet integrator may be used in modest sized arrays. Our goal is a 16 x 16 element array with read noise << 10 e^-. The readout is non-destructive and permits the detector array and its associated electronic component arrays to operate at their optimum operating temperatures. This facilitates thermal annealing of radiation effects and should eliminate problems associated with free carrier freezeout in active Si devices below 30 K.

INVERTING AMPLIFIER CIRCUIT

In previous work the integrating JFet has always been operated in the source follower mode. At temperatures below about 65 K it is not possible to operate at useful current levels with this circuit. This is shown in the plots of Vs versus T. Therefore we have investigated the "inverting amplifier mode" where it is possible to optimize the operating conditions at any temperature where the device can provide useful gain. The circuit shown works well at 40 K with the parameters listed. The noise tests and integrating signal tests were carried out using this particular set of parameters. Note that we have purposely chosen to operate with only a voltage gain of 1.2. It may prove desirable to increase this to much higher values.

In order to determine the effects of 1/f noise on the read noise of the single J230 integrator at T = 40K, 800 sec. of data in 8 100 sec. blocks was analyzed in various "integration intervals" or "chopping periods", τ . The results tabulated below show both "read noise" (σ_Q) and current noise (σ_I) as measured. Note that for long integrations σ_Q increases rather than decreases. Further work is needed to explain this effect.

τ (sec)	σ_I (e/sec)	σ_Q (e)	$\sigma_I(100)$ (e/sec)
1	22	22	2.2
2.5	8.3	21	1.3
5	4.8	24	1.1
10	3.7	37	1.2
20	2.6	52	1.2
50	1.0	50	0.7

$$\sigma_I(100) \equiv \sigma_I(100/\tau)^{-\frac{1}{2}}$$

CONCLUSIONS

1. Operation of the "new" J230 manufactured by Siliconix at 40 K in the inverting amplifier mode is both feasible and advantageous. Even though the transconductance is only 100 umho both the shorted input and open gate noise levels at 1 Hz are quite low (<100 nanovolt/Hz^.5) and stable operation is achieved.

2. Our preliminary goal of rms noise current < 1 electronc/sec using integration times of < 100 seconds has been met.

3. Opportunities for significant improvements in such devices are available through improved geometries and through optimized doping of the devices.

Odd and Even Integrations

$$\bar{I}_o = \int_o^\tau I_1 + I_2 + I_3/\tau$$

$$\bar{I}_E = \int_o^\tau I_1 + I_2 + I_3 + I_4/\tau$$

I_1 = JFet leakage current + temp. drift

I_2 = Detector dark current

I_3 = Sky background photo-current

I_4 = Signal current

$$\text{Signal} = \bar{I}_E - \bar{I}_o$$

or

$$I = I_2 - (I_1 + I_3)/2$$

Fig. 1. The assumption is made that the "signal" is the difference between odd and even integrations where the even integrations include the photo-current from the object being measured, I4. Thus current noise as measured here refers to the rms scatter of a series of such current differences.

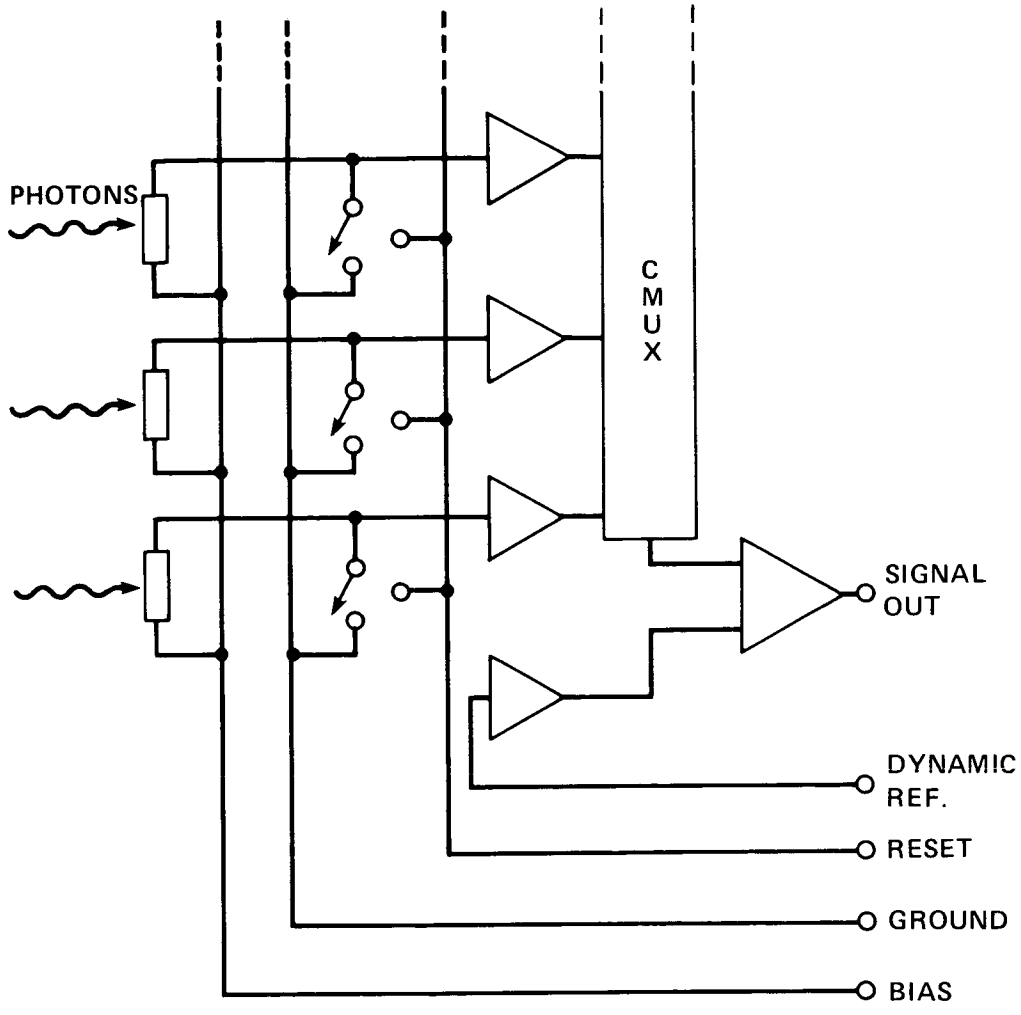

Fig. 2. Schematic diagram of multiplexed integrating preamplifier.

RESULTS:

T = 40 K

C = 10 pF OR 16 nV/e^-

$\bar{I}$ = 170 e^-/sec

$\sigma[\bar{I}_n - \bar{I}_{n-1}]$ = 2.3 e^-/sec

τ = 100 sec

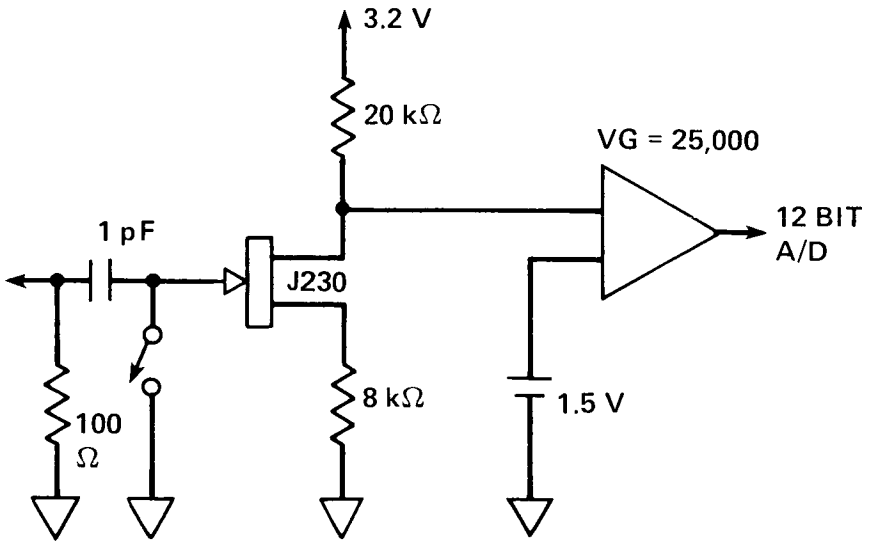

v_D = 2 V, i_D = 60 μa

p = 80 μW, VG = 1.2

Fig. 3. Circuit diagram for one channel of integrating preamplifier.

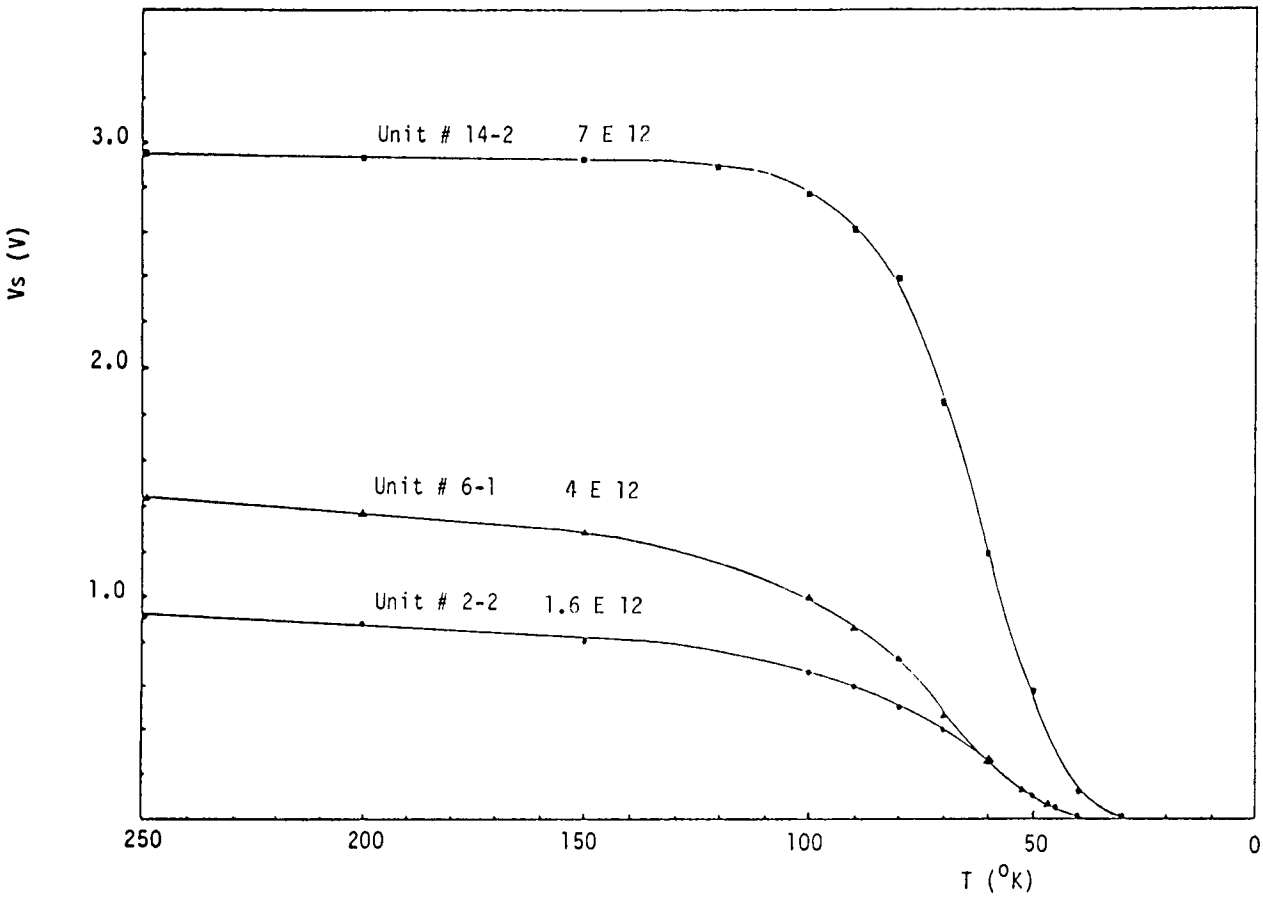

Fig. 4. Vs, source voltage, as a function of temperature for the Burr-Brown JFets with 3 different channel doping levels ranging from ∿ 1 E12 to 7 E12.

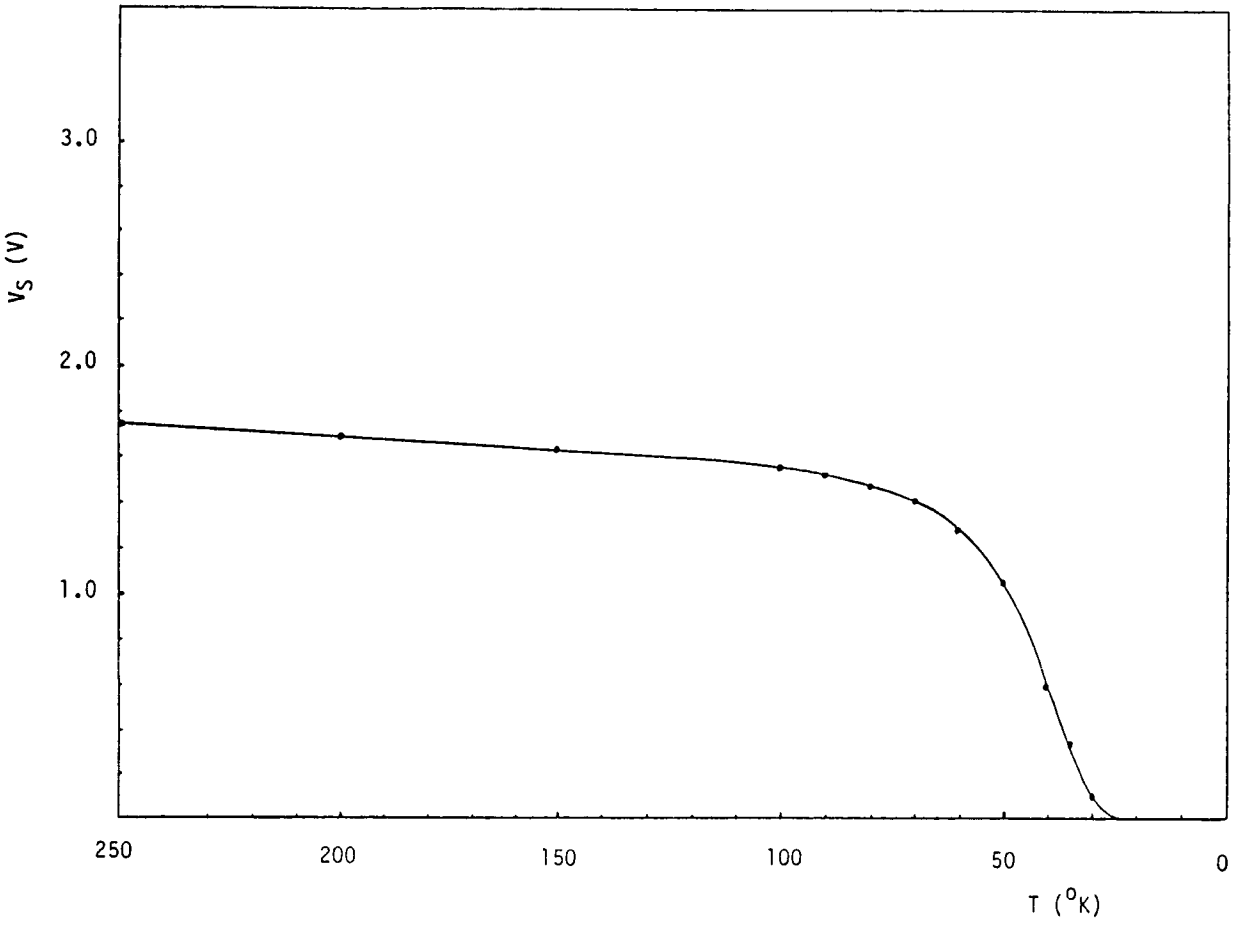

Fig. 5. Vs, source voltage, as a function of temperature for the "new" J230.

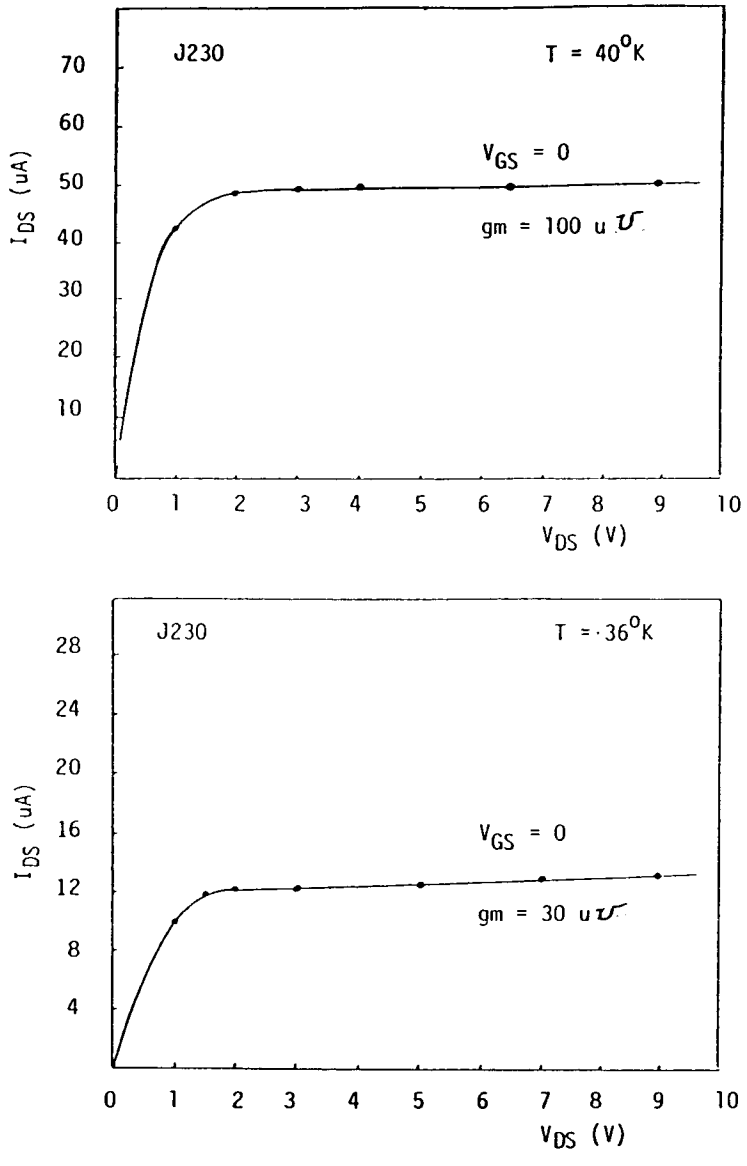

Fig. 6. I-V characteristics of the J230 at 40°K and 36°K with V_{GS} = 0.

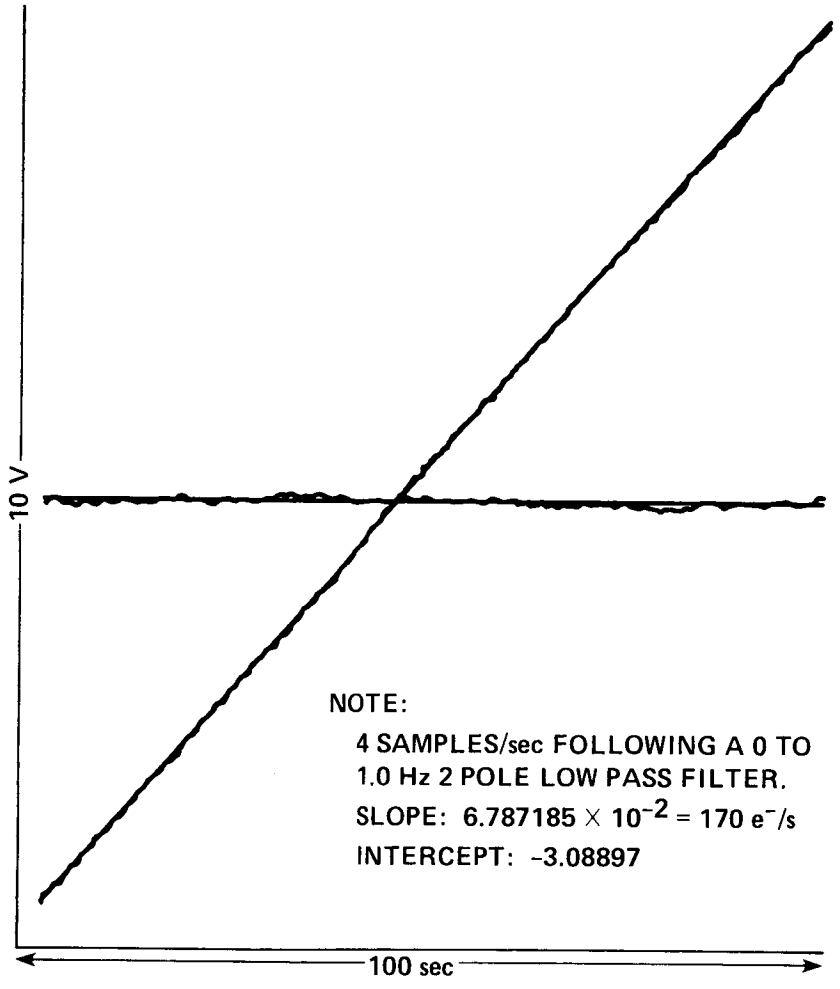

Fig. 7. Typical plot of integrated signal vs. time.

Ge:Be Far Infrared Photoconductors

N. M. Haegel and E. E. Haller
Lawrence Berkeley Laboratory and
University of California
Berkeley, CA 94720

Abstract

Ge:Be photoconductors have been optimized for the 30-50 μm wavelength range. Crystal growth of detector quality material requires good control of both the Be and residual impurity doping. Detective quantum efficiencies of η_d = 46% at 5 A/W have been achieved at a photon background of 10^8 p/s. The responsivity of Ge:Be detectors can be strongly temperature-dependent when the residual shallow levels in the material are closely compensated. Transient responses on the order of ~1 second have been observed in some materials. The role of residual shallow impurities on the performance of photoconductors doped with semi-deep and deep impurities is discussed.

Introduction

Recent development of Ge:Be photoconductor material and devices has led to the availability of optimized detectors for the 30-50 μm wavelength range. This paper will review the crystal growth, characterization, and detector performance of this material. The temperature dependence and transient behavior will be examined to illustrate some of the remaining issues concerning device behavior. Finally, a general summary of criteria for selecting multi-level material for detectors such as Ge:Be, Si:Ga, or Si:In will be presented.

Investigation of the photoconductive response of Ge:Be was first reported in 1967 (1). Be is a double acceptor in Ge and is the shallowest of the helium-like, group II impurities. Its ionization energies are 24.8 and 58 meV, corresponding to wavelength thresholds of 50 and 21 μm (2). In addition, its high solubility in the Ge lattice (3) makes it especially suitable as a dopant for an extrinsic photoconductor. A schematic response for Ge:Be is presented in Figure 1 which shows that Ge:Be photoconductors should be useful for attaining high sensitivity in the wavelength gap between the shallow levels in Si and the peak response of Ge:Ga.

Ge:Be Crystal Growth

Despite early encouraging results, however, the difficulties associated with the growth of Ge:Be have, until recently, prevented these detectors from being fully developed and utilized. Be forms a very stable oxide and can react with oxygen present in either the silica crucible or the ambient gas in the crystal puller. The oxygen content of the melt environment, therefore, is a critical factor in determining whether Be will precipitate as stable and neutral BeO or remain as an isolated dopant which is electrically active in a substitutional site.

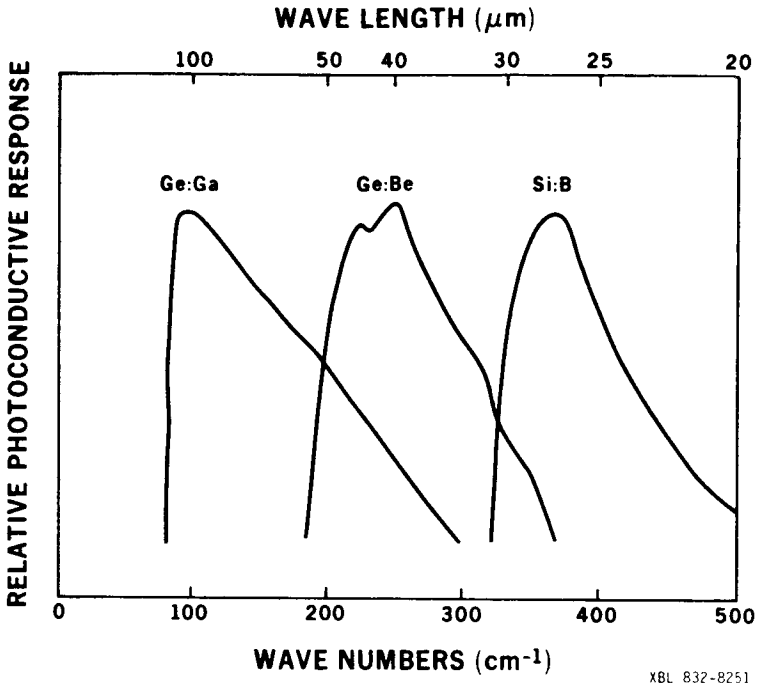

Figure 1
Schematic photoconductive response for Ge:Be

Thermodynamics calculations, based on free energy of formation data and the mass action law, can give an indication of the stability of an oxide under various conditions of temperature, concentration in the melt, and environment. Calculations done following the method used by Darken (4) indicate that stable BeO would be expected to form in equilibrium under a H_2 atmosphere when p_{H_2O}/p_{H_2} exceeds 5.5×10^{-7} for crystal growth at 1200 K with a Be concentration in the melt of 5×10^{15} cm^{-3} (5). Since the usual ratio of p_{H_2O}/p_{H_2} partial pressures attained during crystal growth is approximately 10^{-5}, the H_2 atmosphere commonly used for high-purity growth is unsuitable for growing Be-doped crystals since the formation of BeO is thermodynamically favorable. In addition, BeO is more stable, on a relative scale, than the SiO_2 which composes a silica crucible. This suggests that Be in the melt would react with a SiO_2 crucible within the limits imposed by diffusion and convection.

Thermodynamic conditions, therefore, dictate that Ge:Be be grown in a less oxygen rich environment. We have achieved reliable and reproducible Be doping using Czochralski growth from a carbon susceptor under high vacuum (10^{-6}–10^{-7} torr). Czochralski growth provides good control of residual impurities and results in low dislocation densities (< 1000 cm^{-2}) in the single crystal material (6). Doping of the melt is achieved by using a heavily doped master alloy. Use of a master alloy provides a more controlled method of doping than the direct addition of pure Be. The weight of the dopant can be determined more precisely, and a Hall effect measurement can be used to reliably determine the Be concentration in the master alloy.

Seven Ge:Be crystal have been grown for photoconductor material, both to study the effects of shallow level doping and to develop a supply of material for use in providing optimized detectors for various operating conditions. These crystals are summarized in Table 1. Optimum Be doping for maximum absorption without excessive hopping conductivity ranges from 5×10^{14} cm^{-3} to 1×10^{15} cm^{-3} depending on the residual donor concentration.

TABLE 1.

Crystal	[Be] (cm^{-3}) Seed End	Shallow Level Characterization	Growth Conditions
703	10^{15}	$N_A > N_D$	carbon susceptor, vacuum
706	5×10^{14}	$N_A > N_D$	carbon susceptor, vacuum
707	10^{14}	$N_A > N_D$	carbon susceptor, vacuum
710	5×10^{14}	$N_D > N_A$	carbon susceptor, vacuum
719	4×10^{14}	Variable	carbon susceptor, H_2
727	6×10^{14}	$N_A > N_D$	carbon susceptor, vacuum
728	10^{15}	Variable	carbon susceptor, H_2

Material Characterization

Schematic band diagrams for Si:In and Ge:Be (showing only the first ionization stage for Ge:Be) are given in Figure 2. Ge:Be, as well as Ge:Hg, Ge:Zn, Si:Ga, Si:In, etc., can be referred to as "multi-level systems" because there will be additional shallow levels (B in Si, B and Al in Ge) present in the bandgap which will affect the photoconductor performance. Variable temperature Hall effect and resistivity measurements are necessary to determine the concentration and compensation of the residual shallow levels in such materials (7).

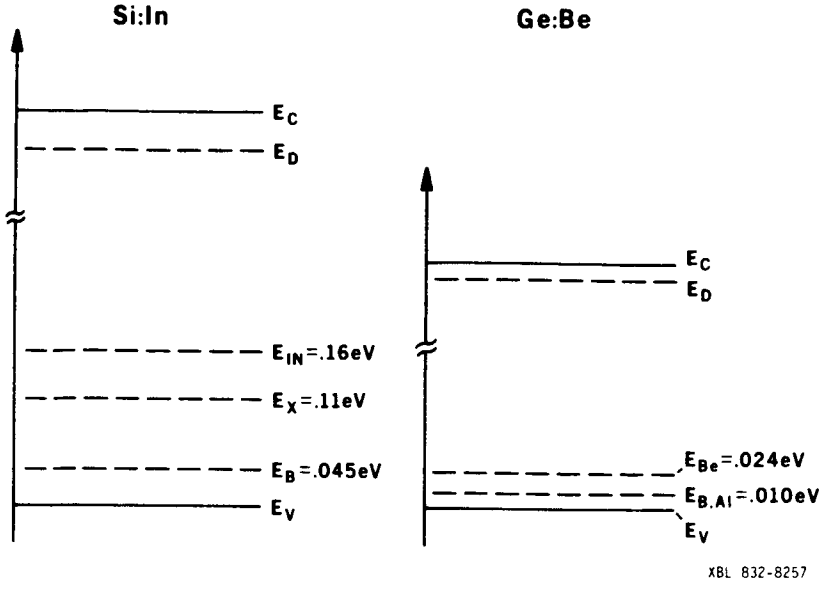

Figure 2
Schematic band diagrams for Si:In and Ge:Be
indicating the presence of residual shallow acceptors

The free carrier concentration as a function of inverse temperature and the corresponding resistivity data are plotted in Figure 3 for a number of Ge:Be samples with varying compensation and concentration of residual shallow impurities. The experimental techniques for controlling these residual shallow levels will be discussed in a later section.

Detector Performance

Ge:Be detectors have been evaluated for responsivity and NEP as a function of bias and temperature at a background flux of 1.5×10^8 photons/sec (8). Narrow-band filters, consisting of Fabry-Perot and restrahlen salt filters (9), were used to restrict the photon energy to within ± 1 μm of 42 μm, and the detectors were tested in brass integrating cavities. Results are summarized in Figures 4 and 5. The comparison to Ge:Ga was performed with each detector operating at its optimum temperature, as determined by optimum signal to noise ratio.

The best result obtained to date for Ge:Be detectors is a detective quantum efficiency $((NEP_{exp}/NEP_{blip})^2)$ of 46% with a responsivity of 5 A/W. One sees from Figure 4 that the value of NEP does not vary greatly for the different materials tested, except at the lower bias where Johnson noise of the feedback resistor becomes significant. Under these conditions, highest responsivity will result in lowest measured NEP. The difference in responsivity in the various materials is due to the difference in free carrier mobility resulting from differences in Be concentration.

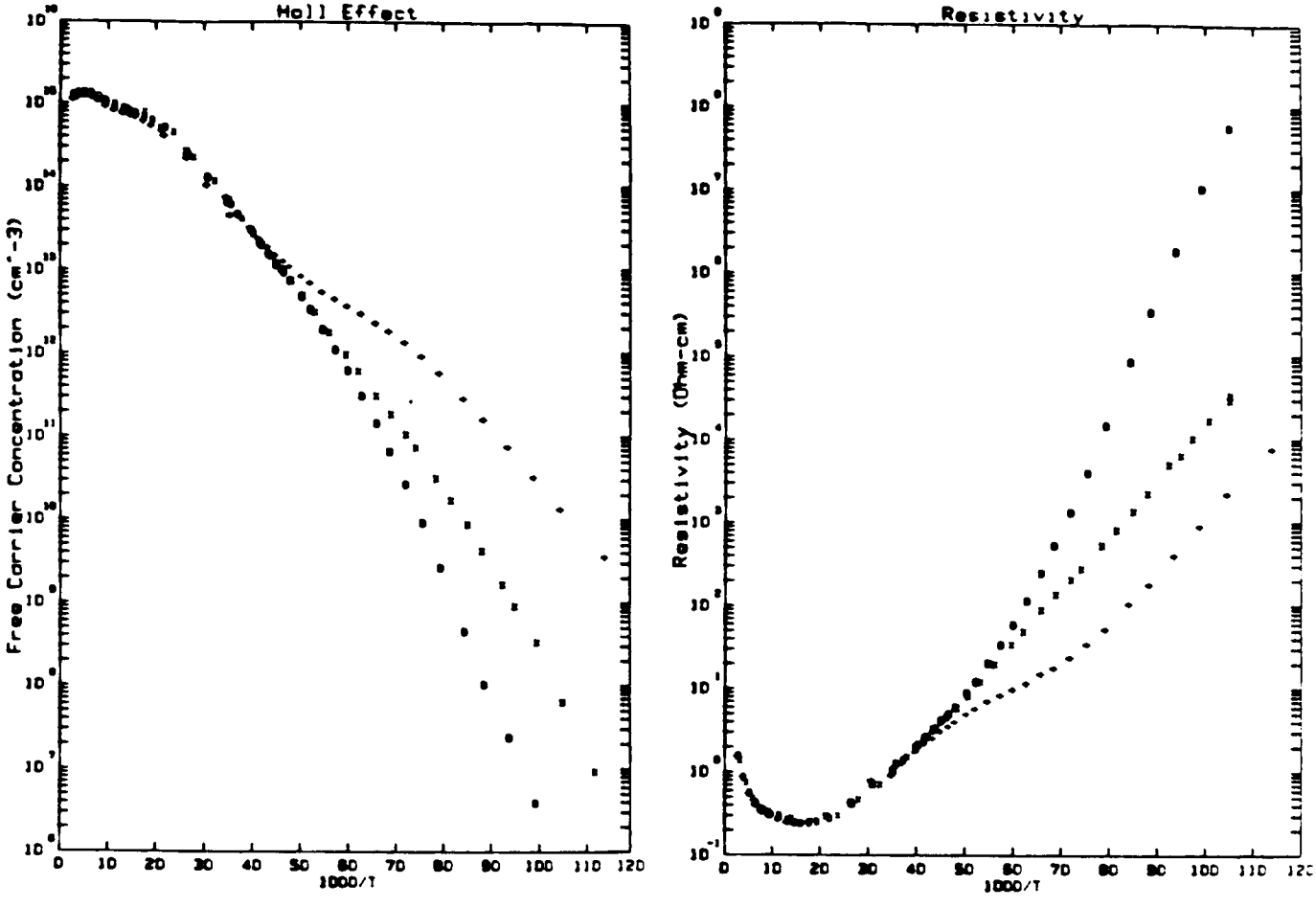

Figure 3

Free hole concentration and resistivity as a function of inverse temperature for the following Ge:Be materials:

+ Ge:Be 728-4.3 As grown
x Ge:Be 728-4.3 Annealed 75 minutes/600°C
□ Ge:Be 728-4.3 Annealed 90 minutes/660°C

Note the increase in resistivity of the fully annealed material.

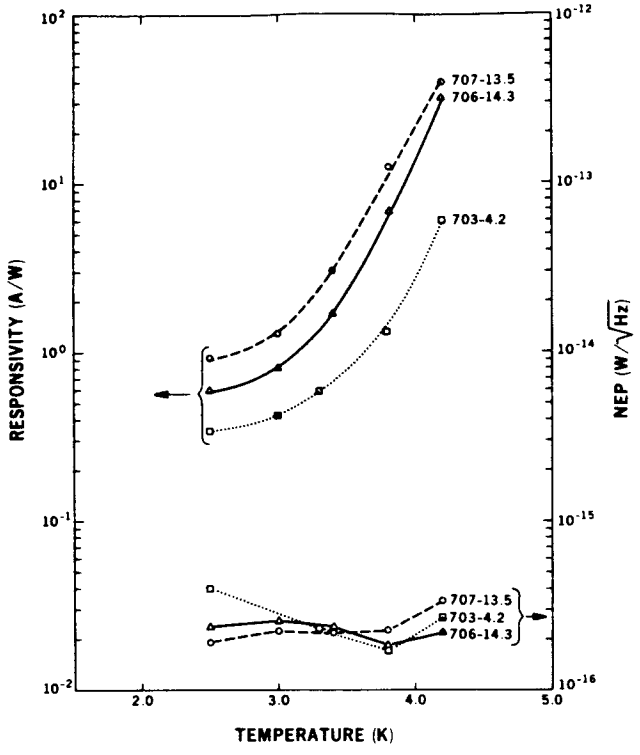

Figure 4
Responsivity and NEP versus temperature for three Ge:Be detectors
$NEP_{back.lim.} = 1.2 \times 10^{-16}$ W/√Hz

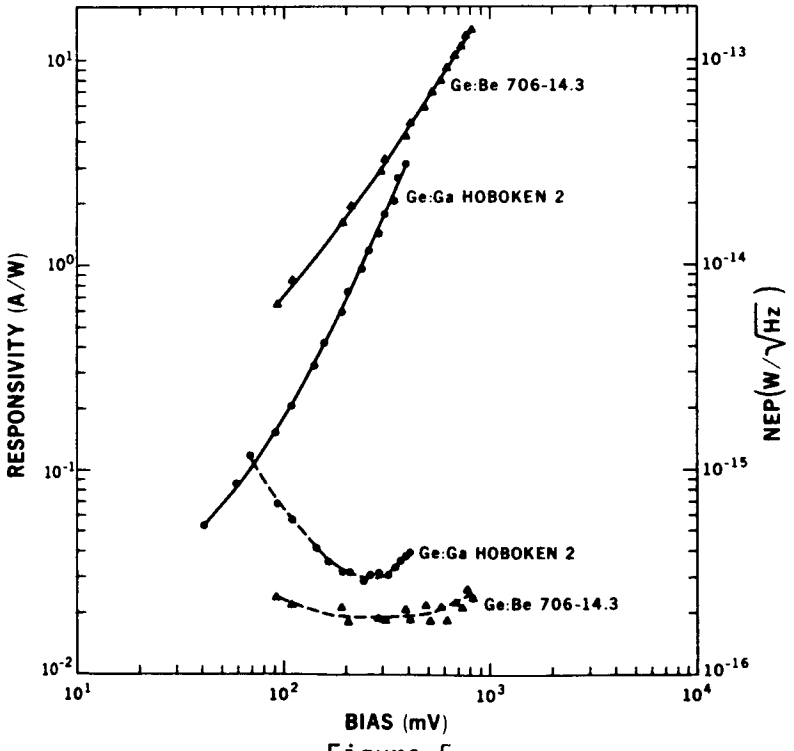

Figure 5
Responsivity and NEP as a function of bias for a Ge:Ga and Ge:Be detector under the same test conditions
T(Ge:Ga) = 3.0 K; T(Ge:Be) = 3.8 K; $NEP_{back.lim.} = 1.2 \times 10^{-16}$ W/√Hz

The improved performance of the LBL Ge:Be as compared to Ge:Ga has been confirmed in the use of these detectors in aircraft-based astronomy. These detectors have been flown on the Kuiper Observatory in a far-infrared grating spectrometer (J. Houck et.al., Cornell University (10)). They report an inprovement of a factor of 2-3 in NEP over the Ge:Ga that was previously used to cover the Ge:Be wavelength range.

Temperature Dependence of Responsivity

The data in Figure 4 indicate that the responsivity of Ge:Be can be strongly temperature dependent. The responsivity increases over an order of magnitude as the device temperature is raised from 2.5 to 4.2 K. A responsivity increase, under fixed bias for a given intercontact length L, must be due to either an increase in free carrier mobility or lifetime. This temperature dependence, however, is much stronger than would be predicted based on the temperature dependence of the lifetime as given by the cascade capture model (11,12) or the well characterized scattering mechanisms that determine mobility (13).

Such strong increases in detector responsivity with increasing temperature have been predicted for the case of multi-level semiconductors in which the shallow acceptors are closely compensated, i.e., $N_{A(shallow)} \simeq N_D$ (14,15). An increase in free carrier lifetime can occur when thermal ionization from the shallow levels becomes strong enough that these centers no longer act as effective recombination centers. The temperature at which this increase in lifetime will occur is given approximately by:

$$T_c = \frac{E_A}{k \ln(\frac{Nv}{gp})}$$

where E_A is the activation energy of the shallow level dopant, p is the free hole concentration, N_v is the valence band density of states, g is the degeneracy factor, and k is Boltzmann's constant.

The models predict however, that the maximum responsivity which can be obtained is strongly dependent on the exact compensation of the shallow residual impurities, and that variations of 5-10% in the quantity $[N_A-N_D]$ are sufficient to change the maximum responsivity by over an order of magnitude. For this reason. special attention must be given to ways to achieve very close compensation of residual levels if this enhanced responsivity is to be achieved consistently and reproducibly in a large number of devices.

One way of obtaining close compensation of shallow levels is to use a high purity crystal growth facility and, if necessary, to counterdope, generally with the n-type impurity. In Ge, residual impurities can be controlled to levels of $\sim 10^{10}$ cm^{-3} under optimum growth conditions (6), while high purity Si generally has [B] and [P] $\sim 10^{13}$ cm^{-3}. The high responsivity values shown for the Ge:Be detectors in Figure 5 were all attained in crystals in the as-grown condition, without intentional counter-doping.

A second approach, which has been used to achieve close compensation in Si, is neutron transmutation doping (16). NTD is used to provide uniform doping (Si→P) and can be done in a controlled manner since the concentration of P produced is directly proportional to the fluence of thermal neutrons to which the sample is exposed. This technique could also be used in Ge although the process would be less efficient since the transmutation of Ge leads to the production of both donors and acceptors with a fixed compensation ratio of $N_D/N_A \sim 0.4$ (17).

A third method, which is presently being evaluted as a means of obtaining closely compensated material, is to control the concentration of hydrogen-related impurity complexes such as A(Be-H) and A(Zn-H) (18,19). These shallow acceptors, which are present in the as-grown state of crystal grown under a H_2 atmosphere, can be removed with thermal annealing at temperatures of 500-700°C. The effect of this is seen in the Hall effect data of Figure 3 where different annealing treatments were used to obtain a variety of degrees of compensation of the shallow levels. With the proper choice of annealing treatment, very close compensation of the shallow levels can be achieved. Evaluation of photoconductors made from these various materials is in progress.

Transient Response of Ge:Be Photoconductors

In an idealized photoconductor model, neglecting all space charge and contact-related effects, the transient response of the device will be limited by the free carrier lifetime, which is generally on the order of 10^{-9} to 10^{-6} sec for Ge detectors at low temperatures. Other models, supported by extensive experimental data, also show that, for large photoconductive gain and high electric fields, detector response can be limited by the dielectric relaxation of space charge regions near the contact which are created by initial sweep-out conditions (20,21). In practice, however, some very long time constants, on the order of seconds, are observed to characterize some fraction of the total photoconductive response in many detectors. Usually this is a very small part of the total signal and the ac and dc responsivities do not vary greatly for frequenices less than the dielectric relaxation frequency.

In the Ge:Be detectors, however, as well as in the Ge:Zn detectors, we have observed time constants on the order of seconds, where the slow component of the signal is up to 10 times greater in magnitude than the initial fast component. This is illustrated in Figure 6 for a Ge:Be detector as a function of increasing temperature for a fixed bias. The data has been compiled schmatically in Figure 7 to show how the absolute and relative magnitude of the slow component increases with increasing device temperature.

Several experiments have clearly demonstrated that this slow component is not a dielectric-relaxation time controlled behavior. First, the dielectric relaxation time constant, $\rho\varepsilon\varepsilon_0$, can be calculated directly from the measured detector resistance and is found to be on the order of 1-10 msec. This is two to three orders of magnitude faster than the time constant of the observed behavior. Secondly, the time constant of the slow response is temperature-dependent, but is not affected by photon-induced changes in background free hole concentration, i.e., it is not dependent on material resistivity. Finally,

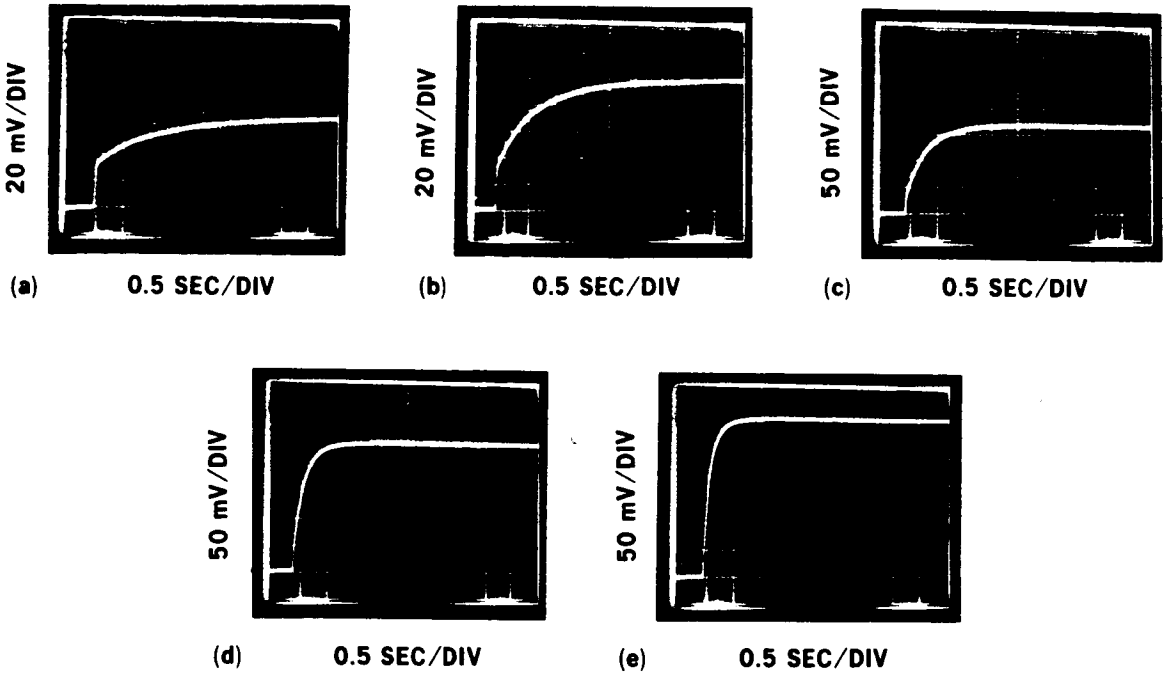

Figure 6
Photoconductive response as a function of time for a Ge:Be detector showing a slow time constant dominated response.
a) 2.5 K b) 2.6 K c) 2.7 K d) 2.8 K e) 2.9 K

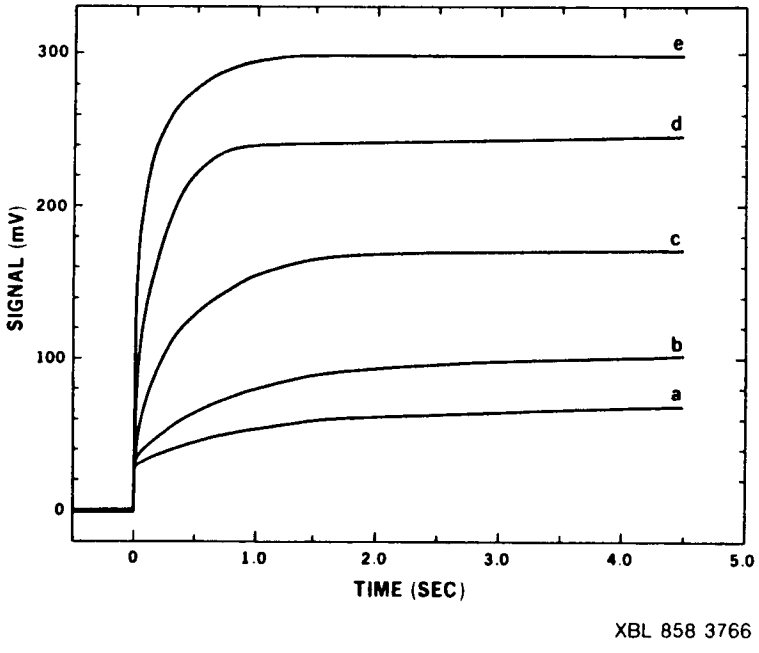

Figure 7
Data from Figure 6 compiled on a constant vertical axis
a) 2.5 K b) 2.6 K c) 2.7 K d) 2.8 K e) 2.9 K

the fast component of the signal does not saturate with increasing field as one would expect for dielectric relaxation.

From this evidence, we conclude that the slow transient response we observe is not explained by any of the present models for transient phenomena in photoconductors. We believe that the slow response may be associated with changes in the electric field profile inside the device due to slow changes in the space charge distribution in the near-contact region. In this region, free holes from the implanted contact diffuse into the bulk material. They are trapped by ionized acceptors and create a space charge region which determines the near-contact profile of the electric field. Steady state solutions for a theoretical model which includes the effects of contacts and space charge have recently been published (22). Progress has been made on the solution of the time-dependent response and the results from this model will be compared to the Ge:Be experimental results (23).

Material Selection for Multi-level Photoconductors

Because of the large role that residual shallow levels play in determining the performance of a multi-level photoconductor, the selection of optimized material for detectors such as Ge:Be or Si:Ga requires full characterization of the material with regard to both primary and residual dopants. In addition to the standard compromises (speed versus responsivity, high α versus hopping conduction, etc.) one must also determine, based on the temperature of device operation and the background flux levels expected during observation, whether enhanced responsivity due to close compensation is a desirable goal. An attempt has been made in Table 2 to consider the factors involved in material selection of multi-level materials.

One sees that the shallow levels will determine both the responsivity and the thermally generated current which will be present in the absence of a photon flux ("dark current"). Routine crystal growth, without counterdoping or NTD, will generally lead to the case $N_{A(shallow)}>N_D$ in both Si and Ge. This is usually undesirable with regard to both responsivity and dark current for the case of very low background astronomy. In compensated material, very high resistivity values can be obtained (see Fig. 3). A combination of materials characterization and dark current measurements on actual devices will be required to determine if observed dark currents at low temperature are material related or due to other effects such as surface leakage.

Finally, an example will illustrate the use of Table 2. Consider a Si:In photoconductor being developed for a low background ($p\sim10^8$ p/s) space application on a focal plane at T=3.0 K. It is generally true that float-zone Si (the technique used to produce Si:In) has a net shallow acceptor concentration due to the presence of residual boron. Boron is hard to remove from silicon because it has a segregation coefficient very close to one. Perhaps, because of the low background and small signals, one desires to have as high a responsivity as possible in order to overcome some fixed level of background noise, such as electronics related noise. Finally, suppose the resistivity in the as-grown case is sufficiently high at 3.0 K to eliminate measurable dark current noise.

TABLE 2

Material Selection:
Shallow Level Compensation

$N_D \gg N_{As}$	$N_D > N_{As}$	$N_{As} > N_D$	$N_{As} \gg N_D$
Highest ρ	High ρ	Lower ρ	Lowest ρ
Lowest dark current	Low dark current	Higher dark current	High dark current
$R \alpha \frac{1}{N_D}$	$R \alpha \frac{1}{N_D}$ for $T < T_c$		$R \alpha \frac{1}{N_D + p}$
	$R \alpha \exp(-E_B/kT)$ for $T > T_c$		
	where $T_c = \frac{E_A}{k \ln(\frac{Nv}{gp})}$		

To determine if one should counterdope (i.e., add donors) to attempt to achieve $N_A \sim N_D$, one should calculate the temperature at which the lifetime increase due to exact compensation will occur. In this case, for $p = \mathring{p}\tau = 10^3$ cm^{-3} and E=45 meV for B, T_c= 17 K. Thus, the focal plane temperature is so far below T_c that the responsivity will be given by

$$R \sim 1/N_D$$

and the addition of counterdopants would be detrimental rather than beneficial to achieving high responsivity. If, however, the resisitivity of the as-grown material was not high enough to eliminate dark current effects, then counterdoping would be required, with some sacrifice in responsivity. Analysis of similar cases in Ge might lead to other conclusions because the shallower levels in Ge means that enhanced responsivity can be achieved at lower temperature for a given flux.

Conclusions

The performance of Ge:Be in the 30–50 μm wavelength range has been reviewed and shown to be superior to the Ge:Ga detectors which have previously been used in this application. The use of Czochralski growth from a carbon susceptor under high vacuum has been effective in achieving reliable crystal growth and in avoiding the precipitation of Be as stable BeO.

Shallow residual impurities are present in all extrinsic photoconductors based on semi-deep and deep levels (Ge:Be, Ge:Hg, Si:Ga, Si:In) and affect both the resistivity and responsivity of the devices. Enhanced responsivity can be attained in these materials if the shallow levels are closely compensated and the device is operated at sufficiently high temperature. Choices of optimized material for detectors will depend on the resistivity and responsivity required for a particular astronomy application.

Acknowledgements

The assistance of W. L. Hansen, D. M. Watson, and Prof. C. Townes are gratefully acknowledged. T. A. Germer performed several of the Hall effect measurements. One of us (NMH) acknowledges the support of a National Science Foundation graduate fellowship.

This work was supported by NASA Contract No. W-14,606 under Interagency Agreement with the Director's Office of Energy Research, Office of Health and Environmental Research, U.S. Dept. of Energy under Contract No. DE-AC03-76SF00098. The encouragement and support of N. Boggess is greatly appreciated.

References

1. Shenker H, Swiggard E M and Moore W J, Trans. Met. Soc. AIME 239, 347 (1967).
2. Cross J W, Ho L T, Ramdas A K, Sauer R and Haller E E, Phys. Rev. B 28, No. 12, 6953 (1983).
3. Goncharov L A and Kervalishvili P D, Inorganic Materials 14, No. 6, 775 (1978).
4. Darken L S, IEEE Trans. Nucl. Sci. NS-26, No. 1, 324 (1979).
5. Haegel N M, "Performance and Materials Aspects of Ge:Be and Ge:Ga Photoconductors for Far Infrared Detection", M. S. Thesis, Univ. of Calif., Berkeley, 1983. LBL-16694.
6. Hansen W L and Haller E E, Proc. Materials Research Society 1982 Annual Meeting, Symposium F, Vol. 16 (New York: Elsevier Science) pp. 141-173, 1983.
7. Putley E H, The Hall Effect and Related Phenomena (London: Butterworths) 1960.
8. Haegel N M, Haller E E and Luke P N, Intl. J. Infrared and Millimeter Waves 4, No. 6, 945 (1983).
9. Watson D M, Ph.D. Thesis, University of California, Berkeley, 1982.
10. George Gull, private communication.
11. Lax M, Phys. Rev. 119, 1502 (1960).
12. Abakumov V N, Perel' V I and Yasslevich I N, Sov. Phys. Semicond. 12, 1 (1978).
13. Zawadski W, "Mechanisms of Electron Scattering in Semiconductors" in Handbook on Semiconductors, T.S. Moss, ed., Vol. 1, 714, 1982.
14. Alexander D H, Baron R and Stafsudd O M, IEEE Trans. Elec. Dev. ED-27, No. 1, 71 (1980).
15. Geim K, Pensl G and Shultz M, Appl. Phys. A 27, 71 (1982).
16. Thomas R N, Braggins T T, Hobgood H M and Takei W J, J. Appl. Phys. 49, 2811 (1978).
17. Fritzsche H and Cuevas M, Phys. Rev. 119, 1238 (1960).
18. McMurray Jr. R E, Haegel N M, Kahn J M and Haller E E, Solid State Commun. 53, 1137 (1985).
19. McMurray Jr. R E, Haegel N M, Kahn J M and Haller E E, to be published.
20. Milton A F and Blouke M M, Phys. Rev. B 3, 4312 (1971).
21. Williams R L, J. Appl. Phys. 40, 184 (1969).
22. Westervelt R M and Teitsworth S W, J. Appl. Phys. 57, 5457 (1985).
23. Haegel N M, Teitsworth S W and Westervelt R M, to be published.

Detectorsystems for ISO's Photometer ISOPHOT

J. Wolf, D. Lemke, M. Burgdorf, D. Lutz
Max-Planck-Institut für Astronomie
Heidelberg, West Germany

1. Introduction

One of the four focal plane instruments of the Infrared Space Observatory is ISOPHOT, a photopolarimeter for the wavelength region 3 - 200 μm, with D. Lemke as principal investigator. Each experiment occupies a quadrant of the focal plane (see fig.1). The telescope beam is directed into each experiment by means of a pyramid mirror and by tilting the satellite. The diameter of the unvignetted field of view is 3 arcmin or 7.85 mm in the focal plane (1 mm = 23 arcsec).
The temperatures provided are 3 K for cooling the detector systems and 8 K for the experiment structure.

2. The ISOPHOT experiment

The ISOPHOT team is a European consortium of nine groups from four countries (see fig.2). The PI-institute is the Max-Planck-Institut für Astronomie in Heidelberg, where most of the cold focal plane unit will be developed and all the detector developments are made or managed.

ISOPHOT consists of four photometric subsystems:

ISOPHOT - P, a classical mulitband-multiaperture photopolarimeter, 3 - 30 μm,

ISOPHOT - C, a photometric camera , 30 - 200 μm,

ISOPHOT - S, a spectrophotometer, 3 - 16 μm,

ISOPHOT - A, two (or three) linear mapping arrays, 3 - 18 (or 30) μm.

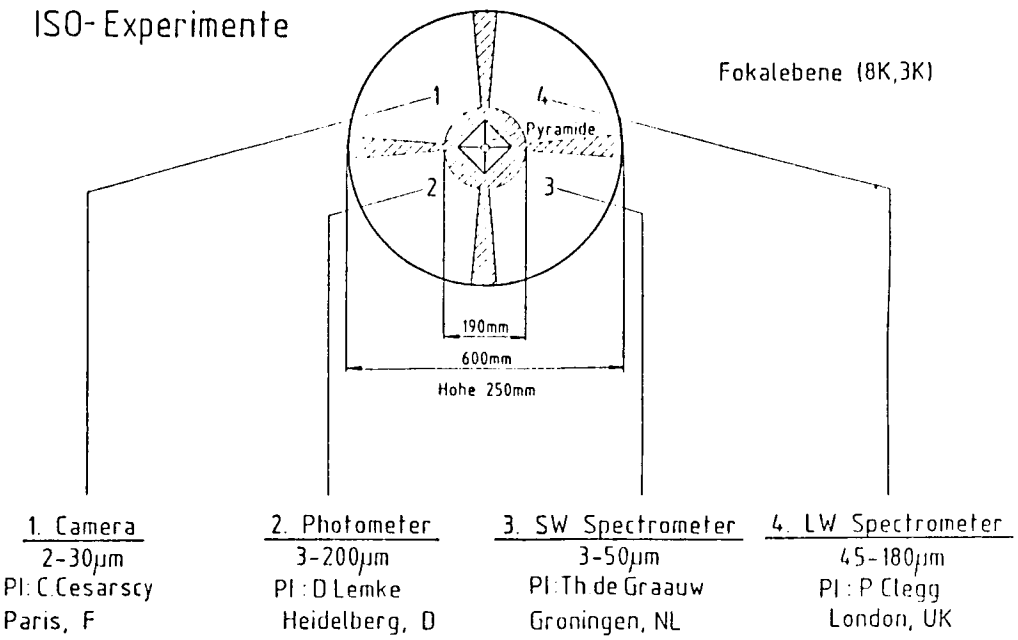

Figure 1
The four focal plane experiments for the Infrared Space Observatory ISO.

Principal Investigator:

D. Lemke, Max-Planck-Institut für Astronomie,
Königstuhl, D-6900 Heidelberg 1,
Tel. 49-6221-528259, Tx. 461789 MPIA D

Co-Investigators:

J. Riedinger J. Wolf	Max-Planck-Institut für Astronomie, Heidelberg, D
L. Drury E. Grun W. Kratschmer H. Volk	Max-Planck-Institut für Kernphysik, Heidelberg, D
R. Joseph M. Selby	Imperial College, London, UK
J. Abolins	Rutherford Appleton Laboratory, Chilton, UK
I. Rasmussen H. Schnopper	Danish Space Research Institute, Lungby, DK
B. Reipurth	Observatory Copenhagen, DK
P. Alvarez C. Sanchez Magro	Instituto Astrofisica Canarias, La Laguna, E
E. Kreysa	Max-Planck-Institut für Radioastronomie, Bonn, D
W. Martin	Freie Universität Berlin, D

Figure 2
The ISOPHOT consortium (ref./1/).

Table 1 ISOPHOT-P (Multiband-Multiaperture Photopolarimeter)

Wavelength range (μm)	3 ... 30
Total number of spectral bands	10
Central wavelength (μm)	4, 6.5, 10, 16, 25, others TBD
Spectral resolution	2.5, 2.5, 2.5, 2.5, 2.5, others TBD
Total number of apertures	15
Field of view (arc sec)	5, 8, 12, 20, 30, 40, 60, 80, 110, 150, 180, others TBD
Polarization measurements	3 grid polarizers with 0^0, 60^0, 120^0
Min. detectable flux[1] (mJy)	
Photometry	
4 μm[2]	0.18
25 μm[3]	5.0
Polarimetry	
4 μm[2]	0.44
25 μm[3]	12.4

1 Integration time 100 s; S/N = 10; broadband filter
2 NEP = $5 \cdot 10^{-18}$ W·Hz$^{-1/2}$
3 NEP = $3 \cdot 10^{-17}$ W·Hz$^{-1/2}$

Table 2 ISOPHOT-C (Far Infrared Camera)

	Array I	Array II	Array III
Wavelength range (μm)	30 ... 60	60 ... 120	120 ... 200
Pixels	4 x 4	3 x 3	2 x 2
Broad bands, Central wavelength (μm)	45	90	160
Broad bands, $\lambda/\Delta\lambda$	2.5	2.5	2.5
Narrow bands, Central wavelength (μm)	35 , 50	75 , 105	140 , 180
Narrow bands, $\lambda/\Delta\lambda$	4	4	4
Min. detectable flux[1] (mJy)			
Photometry	21	32	140
Polarimetry	52	80	350
Polarisation Measurements	3 grid polarizers with 0^0, 60^0, 120^0		

1 Integration time 100 s; S/N = 10; broadband filter

Table 3 ISOPHOT-S (Spectrophotometer)

	Channel I	Channel II
Type	Ebert-Fastie	Ebert-Fastie
Wavelength range (μm)	3.3 ... 6.6	8 ... 16
Spectral resolution	81	96
Field of view (arc sec) (slit size)	8	8
Elements	64	64
Efficiency	0.2	0.2
Min. detectable flux[1)] (mJy)	34 (5 μm)	250 (10 μm)

1 Integration time 100 s; S/N = 10

Table 4 ISOPHOT-A (Mapping Arrays)

Operation mode: 3 linear arrays measure simultaneously; scanning by telescope motion. Channel III is an option.

	Channel I	Channel II	Channel III
Detector material	Si:In	Si:Ga	Si:P
Central wavelength (μm)	4.2	11	22
Spectral resolution	1.5	1.4	1.8
Elements	32	16	8
Pixel size (μm^2)	200 x 200	400 x 400	800 x 800
FOV, pixel (arc sec^2)	4.6 x 4.6	9.2 x 9.2	18.4 x 18.4
FOV, array (arc min)	2.8	2.8	2.8
Gap between pixels[1)] (arc sec)	0.7	0.7	0.7
Min. detectable flux[2)] (mJy)	0.4	7	12

1 If staggered arrays are selected there is no gap.
2 Integration time 100 s; S/N = 10

More detail of the subsystems is given in tables 1 -4. The mechanical and optical layout is shown in fig.3.

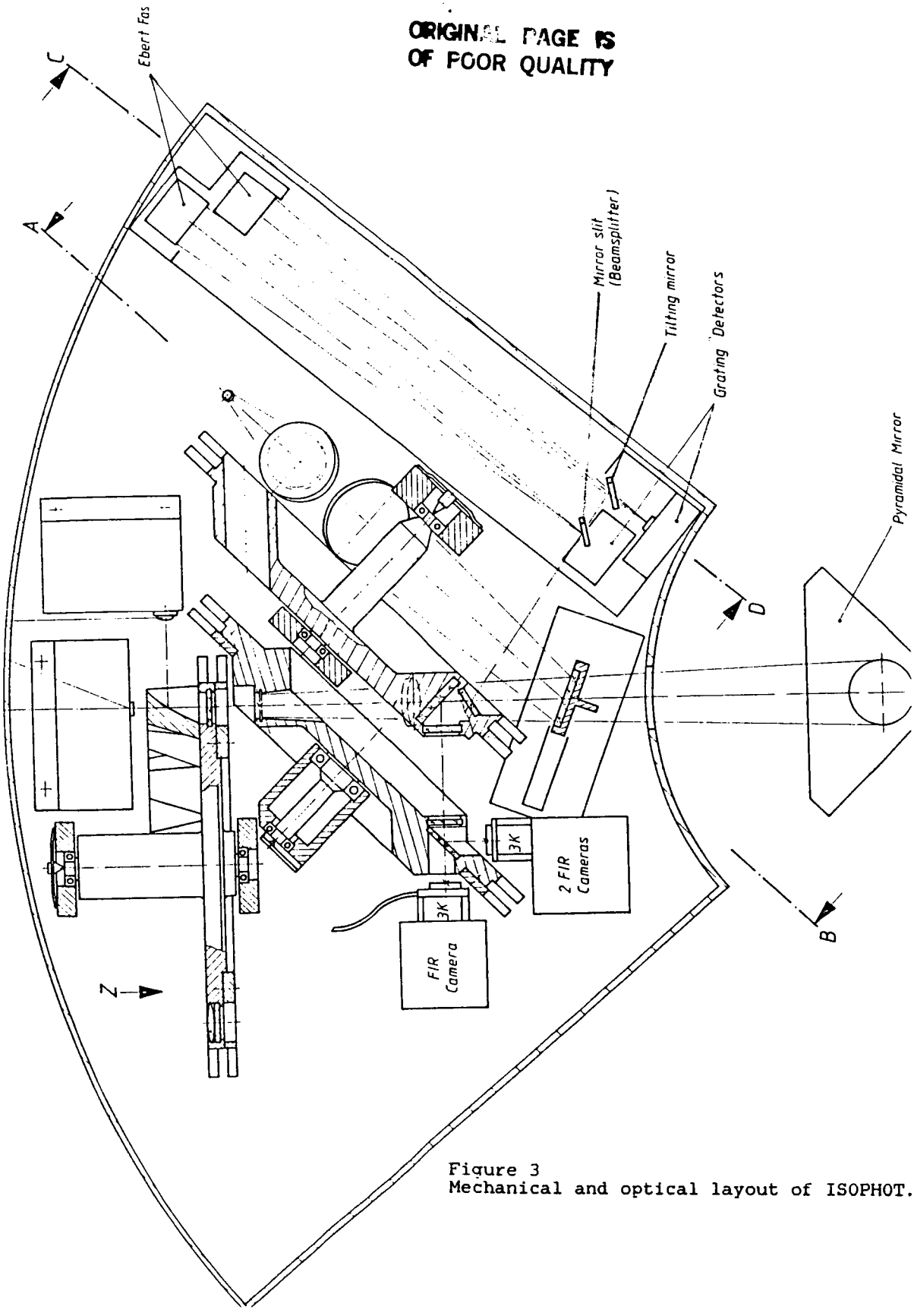

Figure 3
Mechanical and optical layout of ISOPHOT.

One out of the four subsystems is selected by a wheel, which carries various mirrors, field optics, apertures, spectral filters and polarizers. Polarization measurements are possible in all subsystems except - S because of its higher instrumental polarization.

The three identical wheels (fig.4) are driven by ratchets which were developed and fully tested in the GIRL project. They proofed to be very reliable under long term cryovacuum tests and vibration tests according to the shuttle conditions. The advantages of these ratchet drives are their simplicity and their low heat dissipation (2.5 mW per step in the laboratory modell of GIRL E2). The wheels are self positioning with high accuracy.

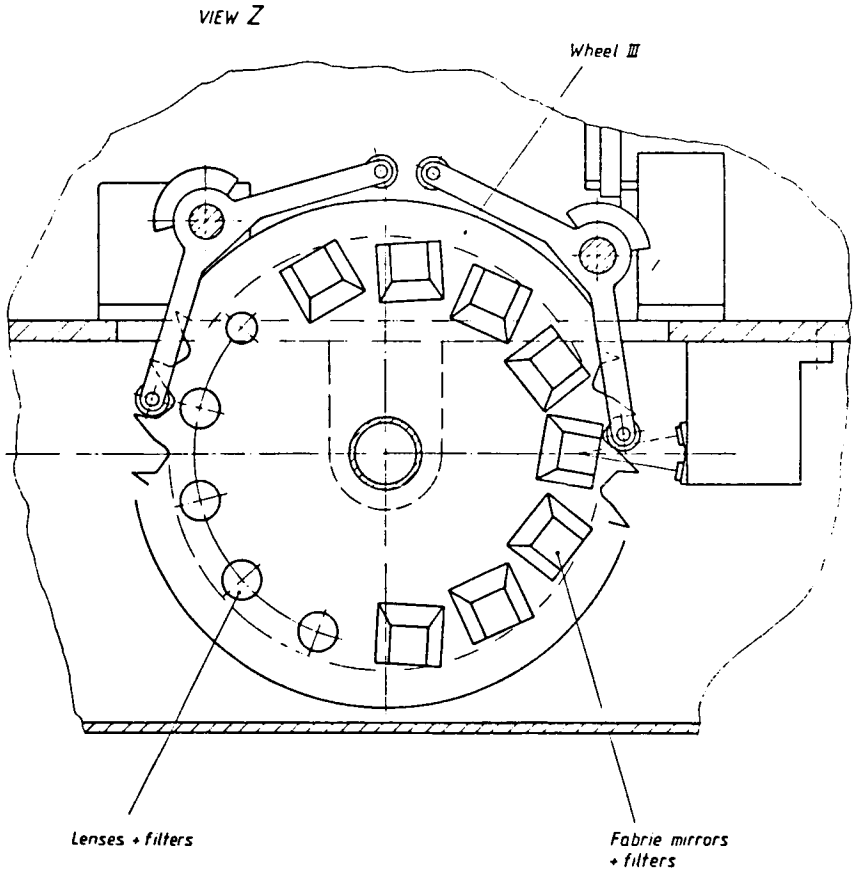

Figure 4
The rachet wheel III of ISOPHOT - P.

3. Detectors for ISOPHOT

Discrete detectors (Si:In, Si:Ga and Si:P) with the classical trans-impedance-amplifier will be used in ISOPHOT - P. Monolithic arrays (Si:In, Si:Ga and possibly Si:P) will be used in ISOPHOT - A and - S, and hybrid Ge:Be-, Ge:Ga- and stressed Ge:Ga-arrays will be used in ISOPHOT - C.

Table 5 shows some examples of detectors available in Heidelberg. We found excellent sensitivities with the Si:In and Si:Ga arrays, but cross talk effects up to 30 % to the next pixel were found at very low photonbackgrounds. New arrays with different geometry and layout to reduce this cross talk are currently manufactured.

Table 5
Detectors available at Max-Planck-Institut für Astronomie

TYP	SERIAL-NUMBER	MANUFACTURER	Q_B [PH S^{-1} CM^{-2}]	R_F [OHM]	NEP [W $HZ^{-1/2}$]	R [A W^{-1}]	λ_{MAX} [μM]
SI:IN	NC 5 ARRAY	AEG-TFK	$2.3\ 10^{7}$	$1.2\ 10^{10}$	$4.7\ 10^{-18}$ (?)	40	5
	IR-8 BP 1242 ARRAY	AEG-TFK	$5.0\ 10^{8}$	$1.1\ 10^{10}$	$5.0\ 10^{-17}$ (?)	8.2	
SI:GA	C 230 - 3	SBRC	$3.5\ 10^{7}$	$1.5\ 10^{10}$	$3.5\ 10^{-17}$	3.0	17
	C 230 - 4	SBRC	$2.0\ 10^{8}$	$7.6\ 10^{9}$	$1.6\ 10^{-16}$	2.3	
	C 230 - 11	SBRC	$2.5\ 10^{8}$	$7.6\ 10^{9}$	$1.0\ 10^{-16}$	3.1	
	DS 64	BATTELLE	$2.1\ 10^{7}$	$1.5\ 10^{10}$	$4.5\ 10^{-17}$	2.0	
	ARRAY	AEG-TFK	$2.5\ 10^{8}$	$1.2\ 10^{10}$	$9.0\ 10^{-18}$ (?)	36	
SI:AS	C 230 - 5	SBRC	$6.9\ 10^{8}$	$7.7\ 10^{9}$	$1.6\ 10^{-16}$	9.4	24
	C 230 - 10	SBRC	$4.4\ 10^{8}$	$7.6\ 10^{9}$	$1.2\ 10^{-16}$	2.5	
	C 230 - 12	SBRC	$6.9\ 10^{8}$	$3.1\ 10^{9}$	$9.5\ 10^{-17}$	8.7	
SI:SB	C 230 - 7	SBRC	$7.2\ 10^{8}$	$3.1\ 10^{9}$	$7.9\ 10^{-17}$	4.8	29
	C 230 - 9	SBRC	$5.8\ 10^{8}$	$7.6\ 10^{9}$	$1.2\ 10^{-16}$	3.9	
SI:P	1	BATTELLE	$2.8\ 10^{7}$	$2.0\ 10^{10}$	$3.0\ 10^{-16}$	2.5	25
	2	BATTELLE	$3.5\ 10^{7}$	$1.5\ 10^{10}$	$2.1\ 10^{-17}$	8.6	
GE:BE	K 9 C 11	BATTELLE	$2.0\ 10^{8}$	$1.2\ 10^{10}$	$7.0\ 10^{-17}$	2.0	45
GE:GA	IRL 101	IRL	$2.2\ 10^{8}$	$1.5\ 10^{9}$	$1.3\ 10^{-16}$	4.3	100
	IRL 102	IRL	$4.4\ 10^{8}$	$7.9\ 10^{9}$	$3.1\ 10^{-16}$	2.7	
	IRL 107	IRL	$2.2\ 10^{8}$	$1.5\ 10^{10}$	$6.0\ 10^{-17}$	6.7	
	DS 47	BATTELLE	$2.2\ 10^{8}$	$1.5\ 10^{10}$	$1.2\ 10^{-16}$	1.9	
	IRD 2071	UNIV. OF ARIZONA	$2.2\ 10^{8}$	$1.5\ 10^{9}$	$1.7\ 10^{-16}$	6.6	
GE:GA:CU		UNIV. OF CALIF. BERKELEY, LBL	$1.7\ 10^{8}$	$2.0\ 10^{10}$	$3.0\ 10^{-17}$	26.0	100
GE:GA STRESSED	G5E-2.1	BATTELLE	$1.5\ 10^{8}$	$2.5\ 10^{10}$	$6.0\ 10^{-17}$	2.0	$\lambda_C \sim 192$
	G5E-2.2	BATTELLE	$1.5\ 10^{8}$	$1.4\ 10^{10}$	$3.0\ 10^{-17}$	4.5	$\lambda_C \sim 184$
HGCDTE		AEG-TFK	$2.3\ 10^{8}$	-	$1.1\ 10^{-13}$	-	12

Q_B = PHOTON BACKGROUND; λ_{MAX} = PEAK RESPONSE; F = 10 HZ CHOPPERFREQUENCY; T = 2.0 ... 4.2 K
λ_C = CUT-OFF WAVELENGTH

In order to extend the wavelength coverage up to 200 μm, a region which was not explored by IRAS, we will use stressed Ge:Ga detectors. The sensitivity of such a detector which is stressed to a cut-off wavelength of 192 μm is shown in fig.5. Its reliability and reproducability have been shown in many cold-cycles.Four of these detectors will be arranged in a 2 x 2 hybrid array for ISOPHOT - C (see fig.6).

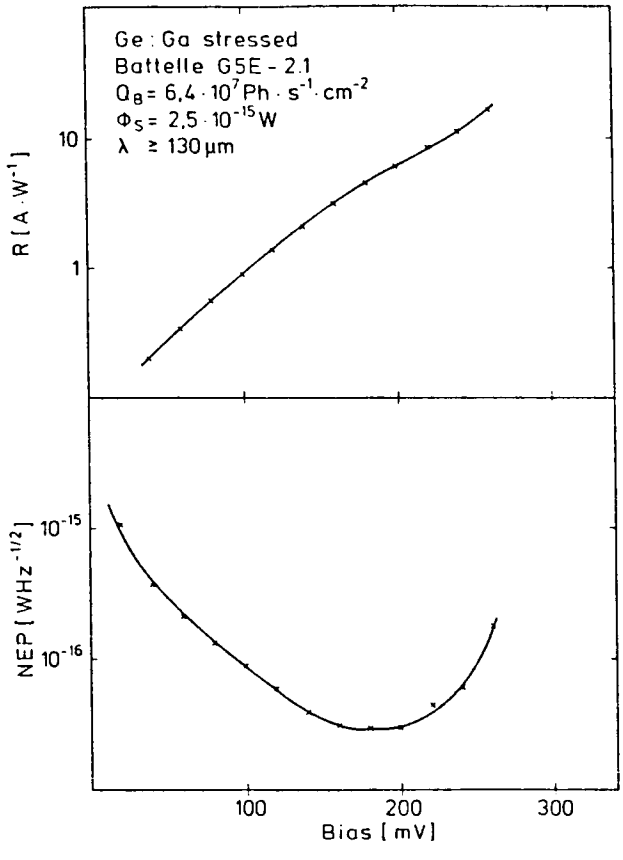

Figure 5
NEP and responsivity of a stressed Ge:Ga detector.

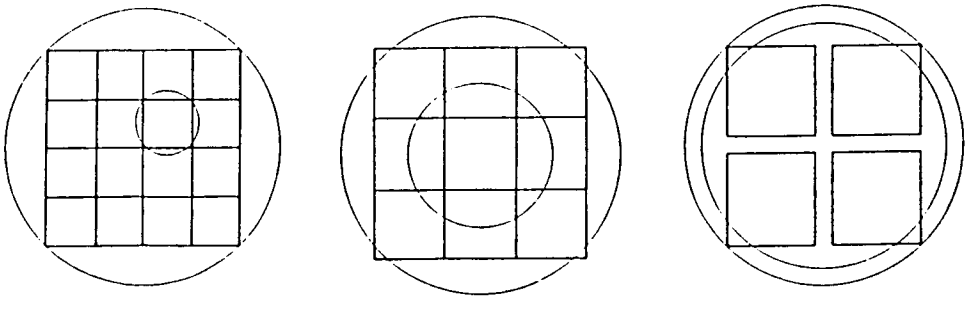

Figure 6
The four hybrid arrays of ISOPHOT - C. The outer circle shows the diameter of 3 arcmin field of view, the smaller circle defines the Airy disk at the cut-off wavelengths of the detectors.

Similarily Ge:Ga detectors will be arranged in a 3 x 3 element array and Ge:Be in a 4 x 4 matrix. The small number of pixels in these cameras is due to the large Airy disks at these long wavelengths and the relatively small unvignetted field of view.

The possible use of field optics in front of the ISOPHOT - C arrays, e.g. light pipes, is investigated currently. The mosaics in fig.6 would represent the light entrances then. The detectors could then be considerably smaller, beeing less sensitive to ionizing radiation.

Radiation effects have already been investigated. Responsivity increases up to 30 % after a 2 hour irradiation with γ - rays (0.03 mrad per sec.) were observed and could be cured by flashing the detector for a few minutes with near infrared radiation. For ISOPHOT it is anticipated to flash the detectors through a fibre optics. The light source can be arranged outside the cryostat then avoiding helium losses.

4. Read-out circuits

The restricted number of 60 cables available for ISOPHOT and the very low heat dissipation of 10 mW average, enforces the use of cold multiplexers for the array detectors.

Our basic concept is the use of charge coupled devices. We have successfully tested them at 4.2 K and investigated their properties. One example is shown in fig.7.

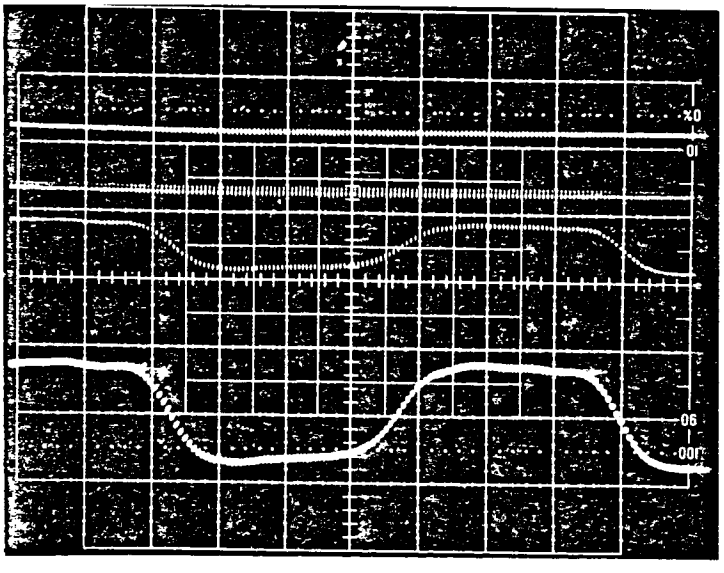

Figure 7
A Si:P detector was coupled to a CCD at 4.2 K. A 10 Hz chopped IR-signal of 3.3 10^{-12} W was applied at a bias voltage of 7.5 V. The photon background of the detector was 3.9 10^{10} Ph s^{-1} cm^{-2} and the CCD read-out frequency was 1 kHz. The lower trace shows the output signal with 0.5 V/div.

A discrete Si:P detector was coupled to a CCD. The NEP achieved is nearly two orders of magnitude higher than with the TIA, due to read-out noise of the CCD, which was found to be $\sim$ 3000 electrons. It should be mentioned, that the CCDs we used so far, were not optimized for low background astronomical applications. The high read-out noise at 4.2 K is considered to be due to a large number of traps at the Si/SiO_2 interface and is possibly generated at the input and output stages.

New custom made CCDs are currently under development. The density of the traps will be reduced by special manufacturing technologies and their total number will be reduced by smaller CCD channels. Noise sources at the input and output stages should be avoided by using diffused contacts with higher doping concentration instead of ion implanted contacts.

As an alternative concept a direct read-out system based on switched MOSFETs is beeing considered. Investigations on the behaviour of MOSFETs at LHe-temperature have been started and an industrial study for such an integrated transistor array is in preparation.

5. Status of the experiment

The ISOPHOT experiment was approved by ESA in June 85. All proposed subsystems were accepted and moreover our own option of using a third mapping array (Si:P which is not in our baseline proposal due to costs) in ISOPHOT - A was strongly recommended by the evaluation panels.

Several options concerning ISO itself are currently discussed between ESA and the ISOPHOT team. A major point is the inclusion of a chopping secondary in the ISO telescope.

The definition phase of ISOPHOT will last until the end of 1986. The hardware phase C/D will start in January 1987. In this phase the major activities will be turned to industry.

Except for minor contributions, funding for the experiment is approved and certain in all participating countries.

Acknowledgement

K. Haussecker and D. Johannsmann of the Max-Planck-Institut für Astronomie, Heidelberg, contributed with the development of electronics and far-infrared filters to the measurements of detectors and CCDs. We also like to thank the Battelle Institut, Frankfurt/M, and AEG-Tlefunken, Ulm, for the disposal of detectors and CCDs, as well as MBB/ZEISS for their technical feasibility study of ISOPHOT.

All detector developments are funded by the Deutsche For - schungs- und Versuchsanstalt für Luft- und Raumfahrttechnik (DFVLR), Porz, and the Bundesministerium für Forschung und Technologie (BMFT), Bonn.

References

/1/ Lemke,D., Riedinger,J., Wolf,J., Drury,L., Grün,E., Krätschmer,W., Völk,H., Joseph,R., Selby,M., Abolins,J., Rassmussen,I., Schnopper,H., Reipurth,B., Alvarez,P., Sanchez-Magro,C., Kreysa,E., Martin,W.: 1985, ISOPHOT Proposal to the European Space Agency for an Infrared Photopolarimeter on the Infrared Space Observatory ISO, available from Max-Planck-Institut für Astronomie, Heidelberg

STATUS OF NTD Ge BOLOMETER MATERIAL AND DEVICES

E. E. Haller, N. M. Haegel and I. S. Park
Lawrence Berkeley Laboratory and
University of California

Summary-Abstract

This status report is a direct follow up to the presentation given at the first IR Detector Technology Workshop which took place at NASA Ames Research Center on July 12 and 13, 1983 (1). The conclusions which we presented at that meeting are still fully valid. In the meantime we have learned more about the physics of hopping conduction at very low temperatures which will be important for bolometer design and operation at ever decreasing temperatures. Resistivity measurements have been extended down to 50 mK. At such low temperatures, precise knowledge of the neutron capture cross sections σ_n of the various Ge isotopes is critical if one is to make an accurate prediction of the dopant concentrations and compensation, and therefore resistivity, that will result from a given irradiation. We describe an empirical approach for obtaining the desired resistivity material and are in the process of conducting a set of experiments which will improve the knowledge of the effective σ_n values for a given location in a particular reactor. A wider range of NTD Ge samples is now available. Noise measurements on bolometers with ion implanted contacts show that no 1/f noise component appears down to 1 Hz and probably lower.

1. Introduction

High performance bolometers for far infrared, low background applications (2) typically utilize a semiconductor thermistor and are operated at very low temperatures ($T < 4.2$ K). At such temperatures, the electrical conductivity

of a doped and compensated semiconductor is dominated by the hopping mechanism: charge carriers tunnel from occupied to empty energy levels in the semiconductor bandgap. The hopping mechanism is thermally activated and depends exponentially on the hopping distance, which in turn depends strongly on the dopant concentrations and the compensation. The majority dopant provides the tunneling charge carriers whereas the minority dopant creates the empty majority sites due to compensation.

Incorporation of dopant impurities during growth of a semiconductor crystal from a melt typically leads to impurity concentration fluctuations which are called striations. At room temperatures these striations may lead to macroscopic fluctuations of the electrical conductivity of a few percent. In the hopping conduction regime these variations become much more important and local variations of several orders of magnitude in resistivity are not uncommon. The problem becomes worse as the temperature is lowered.

A much more uniform dopant distribution can be achieved with the neutron transmutation doping (NTD) process (3). This technique is based on the decay of a host crystal isotope into a dopant impurity after capture of a thermal neutron. Nuclear reactors are used as the source of thermal neutrons. The NTD process has been developed commercially for doping silicon with phosphorus donors for high voltage, high power devices. No acceptors are created in Si by NTD. This makes the process useless for doping Si for bolometer applications. Germanium, in contrast, contains isotopes which decay into acceptors as well as isotopes which decay into donors. Table 1 contains the information on the NTD reactions which are relevant for doping. The transformations of one Ge isotope into another stable Ge isotope are not listed. Because the natural isotopic abundance of a given element is fixed, the dopant concentration ratios and the compensation will be fixed as well.

2. Low Temperature Conductivity of NTD Ge

Since the last workshop, a number of new NTD Ge samples have been processed. Two groups have made electrical conductivity measurements down to ~ 250 mK and ~ 50 mK. Figure 1 displays the results obtained by E. Kreysa, MPI Bonn, using five of our NTD Ge samples. Figure 2 shows the results obtained by J. Krause, Lake Shore Cryotronics, Inc. The excellent fit of straight lines to the results displayed as an Arrhenius plot with modified temperature dependence $(1/T)^{\frac{1}{2}}$ supports the theoretical model of Shklovski and Efros (4) for low temperature hopping conduction. Their model leads to the following resistivity dependence:

$$\rho = c \exp(\Delta/T)^{\frac{1}{2}} \qquad \text{Eq. (1)}$$

The constants c and Δ in Eq. 1 can be theoretically estimated. The accuracy is, however, not sufficient for useful predictions of the resistivity in the temperature range of interest. Table II contains the experimentally determined preexponential factors c and the exponent constants Δ for the various samples. The measurements done by J. Krause on our NTD sample No. 12 do not permit the determination of c because the precise geometry of the Ge samples was not known. The deviations of the data at very low temperatures from the hopping conduction as described by Eq. 1 are currently attributed to resistive heating of the devices. Further measurements are required to verify this point. The resistivity dependence given by Eq. 1 is asymptotically approached at low temperatures and represents the ultimate low temperature dependence. All of our samples give results which are well described by Eq. 1 over several orders of magnitude which means that resisitivity values can be predicted accurately to much lower temperatures. This is useful for the design of bolometers to be operated at even lower temperatures.

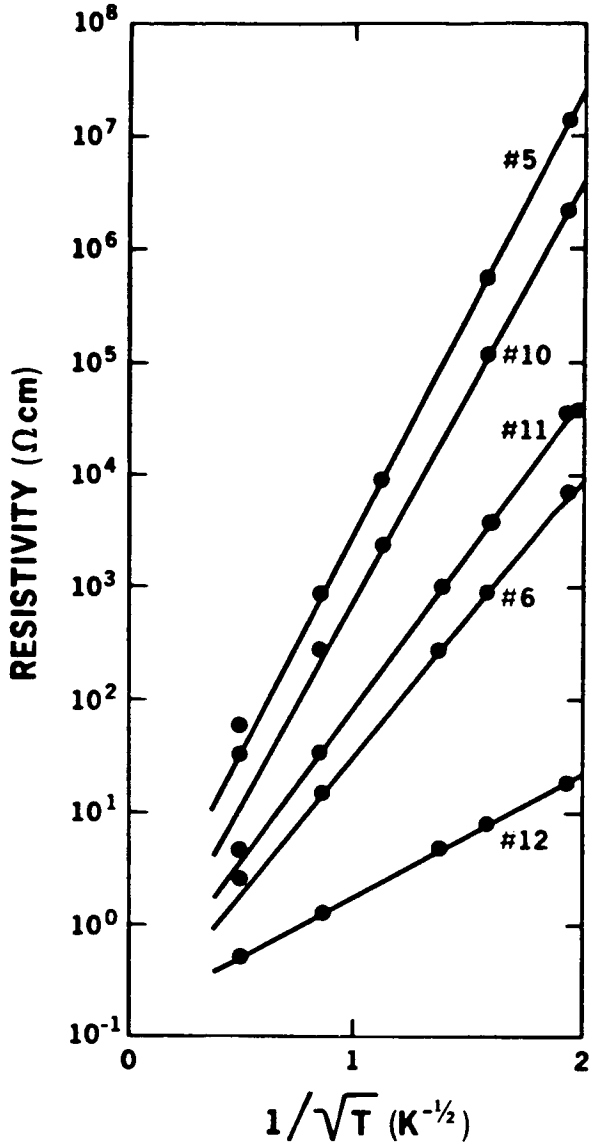

XBL 846-2621

Figure 1. Modified Arrhenius plot of the resistivity and the temperature of five neutron-transmutation-doped Ge samples. The excellent fit of straight lines to the experimental points supports the law described by Eq. 1.

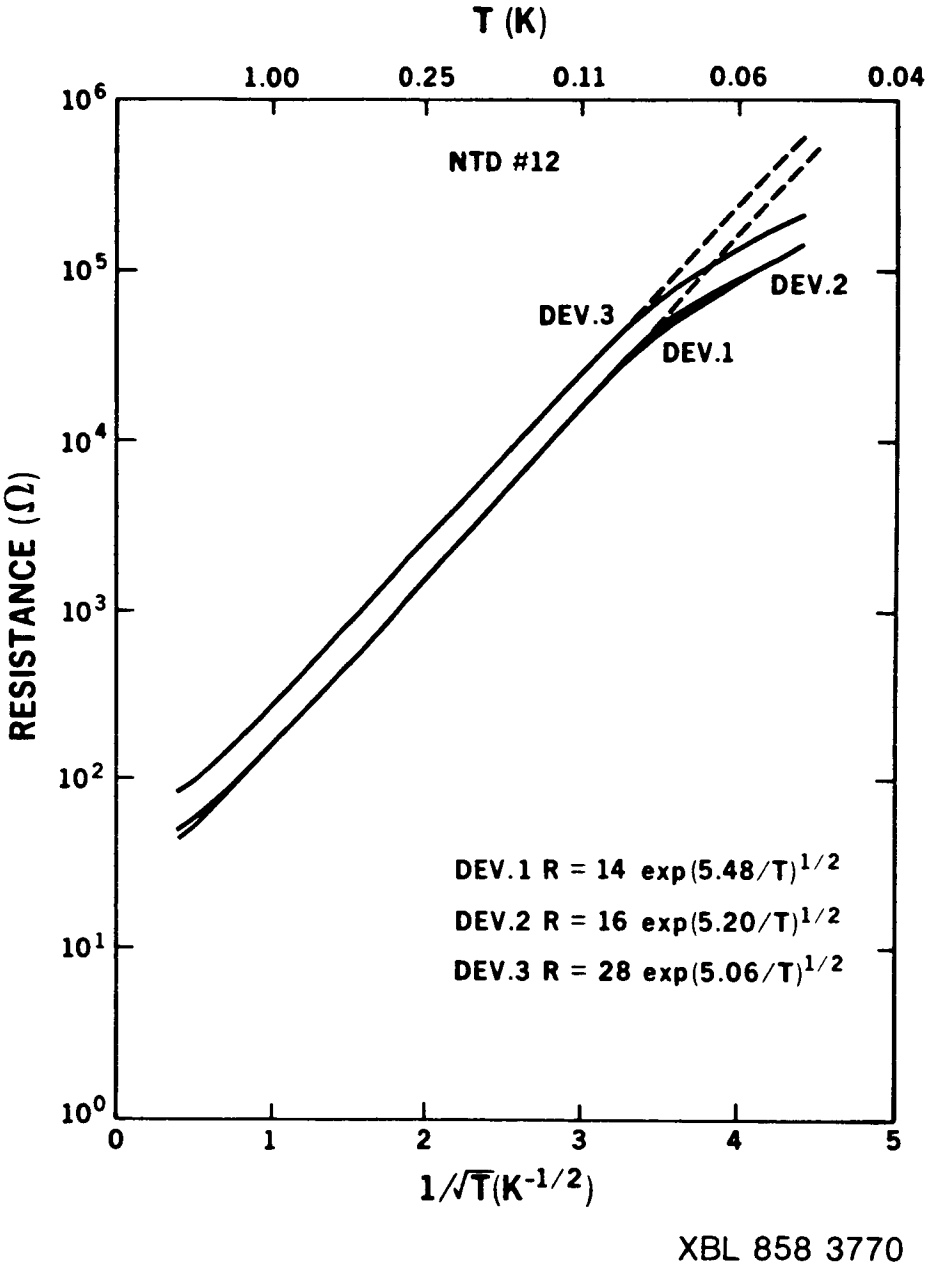

Figure 2. Modified Arrhenius plot of the resistance and the temperature of three resistors fabricated from NTD Ge sample No. 12. The deviation of the experimental data from the straight line is assumed to be due to self heating.

Figure 3 shows the range of resistivity and temperatures for which we currently have NTD Ge samples. We are interested in collaborating with groups who are interested in studying some of the samples, particularly at temperatures below 1 K.

3. Thermal Neutron Capture Cross Sections

The concentrations of the dopants obtained by the NTD process depend on isotopic abundance, neutron flux and the neutron capture cross sections. While the first two parameters are known to high precision, the value of the latter parameter shows large fluctuations from one reference to another. Table III summarizes cross sections σ for the relevant Ge isotopes from four reference sources. The difficulty in obtaining accurate values for σ lies in the fact that σ is an integral over the neutron energy dependent differential cross section $d\sigma/dE$. It appears difficult to obtain a perfectly "thermal" neutron energy spectrum with which a precise value of σ can be determined. Even if this could be achieved, it would be of little help to the experimenter who wants to dope a crystal at a given reactor which may not produce a perfectly thermal spectrum. From our experience with work done at the Missouri Research Reactor we find that NTD done always in the same location leads to reproducible results. A number of closely spaced neutron exposures will "box-in" the range of interest. One to two iterations have always been sufficient to create material with the required properties.

We are in the process of determining experimentally the neutron cross sections by measuring the net-carrier concentrations as a function of time after neutron exposure. The total exposure time for the NTD is negligibly short compared to the decay times of interest. Since the various dopants are produced with very different time constants, it is possible to observe the

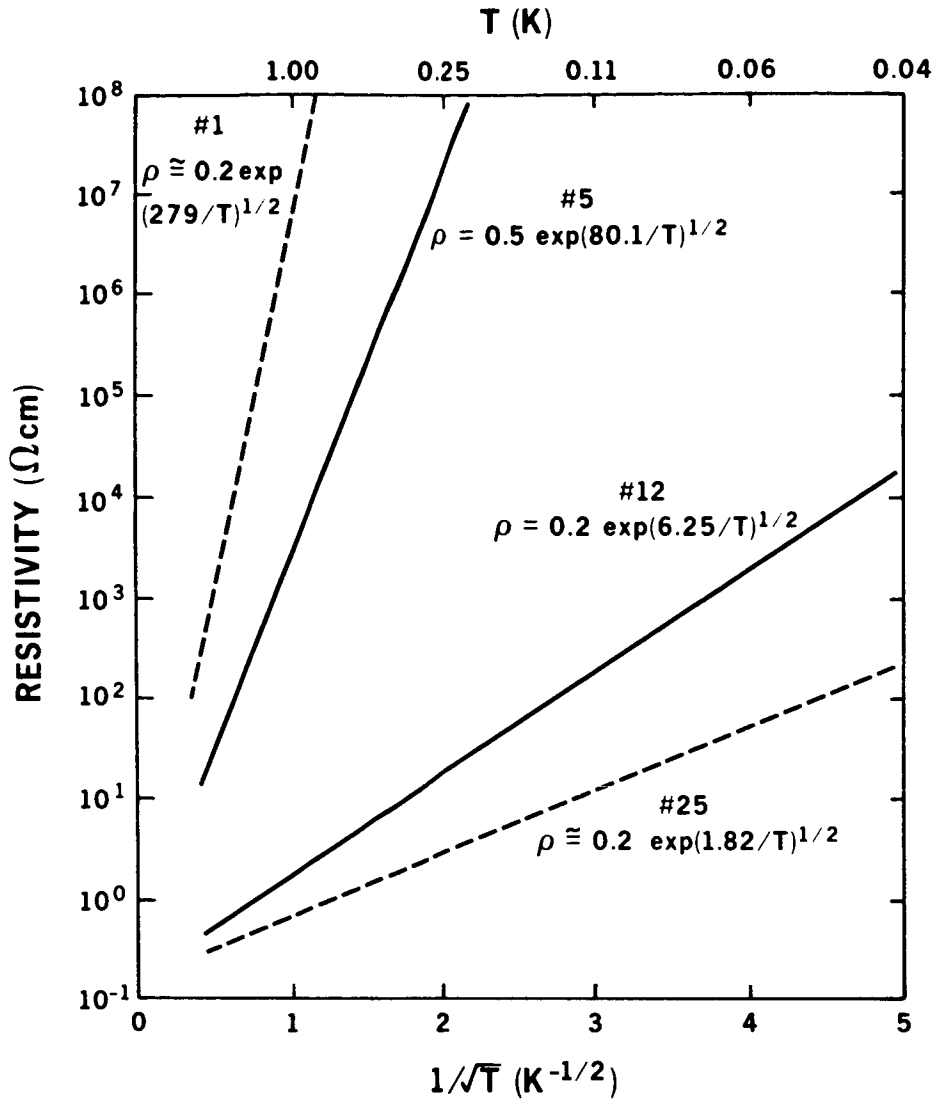

XBL 858 3769

Figure 3. NTD Ge in the range between #1 and #12 are currently available. More heavily doped samples (up to #25) are being processed.

generation of the arsenic donors ($T_{1/2}$ = 82.2 min) almost independently of the gallium acceptors ($T_{1/2}$ = 11.2 d) and the selenium double donors [$T_{1/2}$(dominant) = 38.8 hrs]. Figure 4 shows the dependences of the dopant concentrations as a function of time calculated for the cross sections reported in Ref. 1 of Table III. The net dopant concentration $N = N_{Ga} - N_{As} - 2N_{Se}$ is shown as well. The selenium concentration is counted twice because

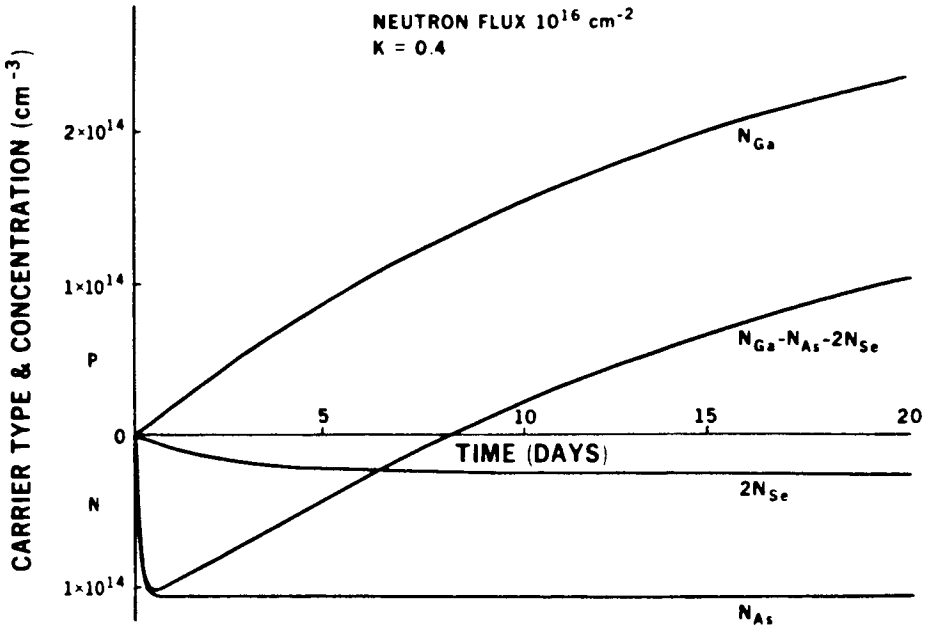

XBL 858 3768

Figure 4. The evolution of the Ga, As and Se concentrations as a function of time after a brief neutron irradiation cycle. The net-dopant concentration is shown as well. Cross sections given in Ref. 1 in Table III have been used.

each selenium double donor gives up two electrons to compensate two shallow gallium acceptors. The maximum of N on the n-type side occurs after 9.6 hrs and it reaches 96% of the ultimate arsenic concentration. After ~ 8.2 days, a type change occurs from n to p. After several half lives of ^{71}Ge creating ^{71}Ga, one reaches the ultimate net-acceptor concentration. Figure 5 shows how sensitive the net-dopant curve is to changes in cross sections. Depending on the set of cross sections, the time for the change of type changes from ~ 8.2 days (K = 0.40, Ref. 1, Table III) to ~ 6.3 days (K = 0.32, Ref. 2, Table III). The net-dopant concentration changes as well. The change of type occurs at a certain time, t_0, independent of the total neutron flux. This provides an additional restriction for a set of experimental curves. They all must cross on the x-axis at t_0. Thermal annealing of the residual fast

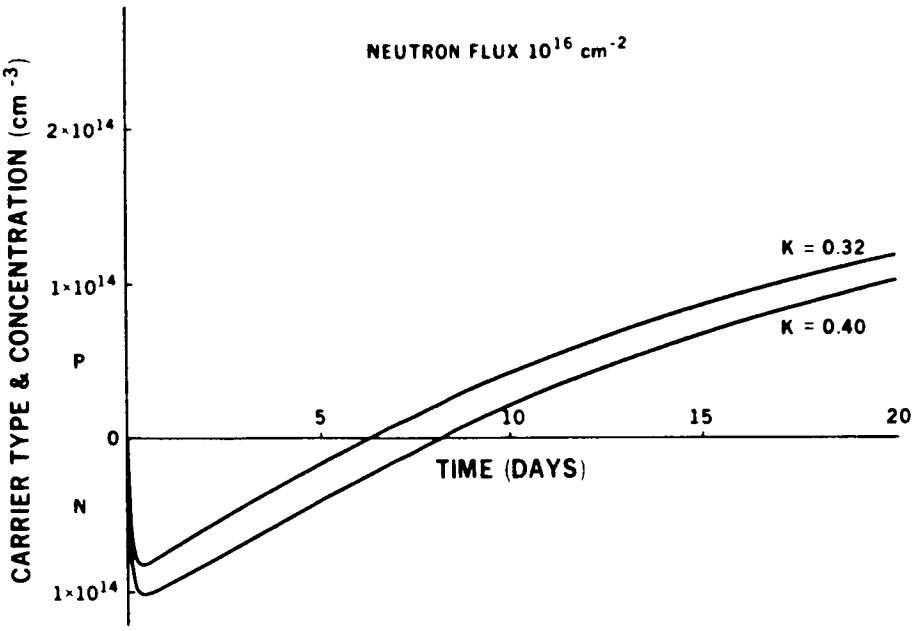

XBL 858 3767

Figure 5. The cross-over time from n- to p-type is very sensitive to the particular set of neutron cross sections. An experimental study of the net-carrier concentration as a function of time will determine whether the curve labelled with compensation K = 0.4 (Ref. 1 of Table III) or with K = 0.32 (Ref. 2 of Table III) or neither is appropriate for the reactor used in our case.

neutron radiation damage after irradiation can introduce rapidly diffusing impurities such as copper, a triple acceptor. When the Cu is in a substitutional position, the crossing point of the experimental curves will be offset to the p-type side if Cu contamination occurs. We are currently in the process of generating such curves to extract a much more accurate set of cross section values for a particular reactor.

4. Conclusions

Experimental and theoretical results show that NTD Ge can be used successfully as bolometer material down to 50 mK and most probably much lower. Predictions of resistivity at lower temperatures can be made with good accuracy because the law described by Eq. 1 is of asymptotic nature at low

temperatures. Despite the small dependence of the neutron capture cross sections of the various germanium isotopes on the neutron energy spectrum, one can achieve predictable doping by first "bracketing" the target neutron flux range and then using the same location in a given reactor for further doping cycles.

The question of heat capacity, C_v, of NTD Ge at very low temperatures has not been addressed. It seems probable that at very high doping levels and very low temperatures, deviations from the simple Debye law [$C_v \alpha(T/\theta)^3$] must be expected. In the case of NTD Ge the effect of the dopants is expected to be very small because the masses of the dopants fall inside the range of the masses of the stable Ge isotopes. No local vibrational modes or broad resonances will be created. We conclude from this that in NTD Ge the effect of dopants on the heat capacity must be much smaller than in a case where dopants of very different mass from the host crystal are introduced via diffusion or ion implantation. This latter case applies, for example, to silicon bolometer material. Careful measurements at very low temperatures will be required to explore this issue.

Acknowledgments

We are indebted to Jon Meese* and John Farmer at the Missouri Research Reactor facility for their great help in providing NTD Ge with excellent reliability. Ernst Kreysa of the Max-Planck-Institute in Bonn provided the measurements shown in Fig. 1 and John Krause of Lake Shore Cryotronics, Inc. made the measurements on three Ge resistors shown in Fig. 2. We are particularly grateful for these measurements as we are not in a position to evaluate samples down to such low temperatures in our laboratory.

* Current address: Standard Oil Co., AMOCO Research Center, Naperville, Ill.

This work was supported by NASA Contract No. W-14,606 under Interagency Agreement with the Director's Office of Energy Research, Office of Health and Environmental Research, U.S. Department of Energy under Contract No. DE-AC03-76SF00098.

References

1. "Infrared Detector Technology Workshop", Comment Edition compiled by C.R. McCreight, August (1983).

2. See for example: Haller E E, Infrared Physics 25, 257 (1985) and references therein.

3. For reviews of the NTD process, see: Proceedings of the 4th Conference on "Neutron Transmutation Doping of Semiconductor Materials", ed. R.D. Larrabee, Plenum Press, 1984; and earlier Proceedings.

4. See for example: Shklovski B I and Efros A L, Electronic Properties of Doped Semiconductors, Springer Series in Solid State Sciences, 45, 1984.

TABLE I.

$$^{70}_{32}Ge(n,\gamma)\ ^{71}_{32}Ge \xrightarrow[11.2\ d]{EC}\ ^{71}_{31}Ga$$

$$^{74}_{32}Ge(n,\gamma)\ ^{75}_{32}Ge \xrightarrow[82.2\ m]{\beta^-}\ ^{75}_{33}As$$

$$^{76}_{32}Ge(n,\gamma)\ ^{77}_{32}Ge \xrightarrow[11.3\ h]{\beta^-}\ ^{77}_{33}As \xrightarrow[38.8\ h]{\beta^-}\ ^{77}_{34}Se$$

TABLE II.

Sample* No.	Neutron Flux (cm^{-2})	Preexponential Factor c	Exponent Factor Δ
5	7.50×10^{17}	0.50	80.10
6	1.88×10^{18}	0.15	30.84
10	9.25×10^{17}	0.20	72.54
11	1.65×10^{18}	0.20	40.27
12	3.33×10^{18}	0.20	6.25
12**			
Dev. 1			5.48
Dev. 2			5.20
Dev. 3			5.06

*Data from E. Kreysa, MPI, Bonn.

**From the resistance measurements of J. Krause, Lake Shore Cryotronics,, Inc.

TABLE III. SUMMARY OF PUBLISHED CROSS SECTIONS (in barns)

$\sigma_n(^{70}Ge)$	$\sigma_n(^{74}Ge)$	$\sigma_n(^{76}Ge)$	$K = \frac{N_{As} + 2N_{Se}}{N_{Ga}}$	Ref.
3.46	0.62	0.36	0.40	1
3.25	0.52	0.16	0.32	2
3.20	0.50	0.20	0.33	3
3.68 ± 0.8	0.65 ± 0.2	0.20 ± 0.03	0.35	4

[1]H.C. Schweinler, J. Appl. Phys. 30, 1126 (1959).

[2]Table of Isotopes, 7th ed. (1978).

[3]Table of Isotopes, 6th ed. (1967).

[4]"Neutron Cross Sections", BNL-325, 2nd ed., No. 2 (1966).

Characterization of NTD Germanium and Ion-Implanted Si Bolometers at 0.3K and 0.1K

H. Moseley, R. Kelley,[1] and A. E. Szymkowiak
NASA/Goddard Space Flight Center

M. Juda, D. McCammon, and J. Zhang
Department of Physics
University of Wisconsin

E. E. Haller
Lawrence Berkeley Laboratory

Abstract

We have built and tested bolometer elements using NTD germanium and ion-implanted Si thermometer elements. The thermal links were made using aluminum wires and NbC_xN_y coated carbon fibers.

The temperature dependence of the detector resistance, lead thermal conductivity, and heat capacity were measured. The dependence of the detector resistance on applied electric field was also measured. This, combined with the current-voltage curve for the detector, allows us to calculate the detector responsivity.

We then deposited known amounts of energy into the detector by allowing X-rays from the decay of ^{55}Fe to be thermalized in the detector. In the best-measured case, the predicted pulse height/measured height was $1.04 \pm .05$.

The noise at frequencies above 25 Hz in the NTD Ge was near that predicted by thermodynamics. The noise below 25 Hz has a 1/f character and may be in the carbon fiber/bolometer junction. The implanted detectors show some 1/f noise which depends on the total thermometer volume. Comparison between noise measurements and theory will be presented.

[1]Also Department of Physics and Astronomy, University of Maryland.

Introduction

Thermal detectors operating at very low temperatures ($T \lesssim 0.3K$) can be made to operate as excellent infrared detectors. In principle it is possible to produce detectors whose sensitivity exceeds the limits set by statistical fluctuations in the photons emitted by the natural celestial backgrounds over moderate bandwidths. Alternatively, similar detectors can be used as microcalorimeters to measure the energies of individual X-ray photons. The predicted energy resolution of such a device, limited only by thermodynamic noise sources, is extremely good (Moseley, Mather & McCammon, 1984; hereafter MMM).

We have tested two thermal detectors at $T \lesssim 0.3K$. The purpose of the tests was to 1) determine whether the simple thermodynamic noise model of Mather (1982) accurately predicts the performance achievable in practical detectors, and 2) determine the thermal properties (heat capacity and thermal conductance) of candidate materials for low temperature detectors.

We will describe the fabrication procedure for the two detectors and the testing program. From the derived detector properties (resistance, heat capacity, and thermal conductance) we can predict the thermodynamic noise of the device. We compare the predicted noise to the measured noise. The discrepancies arise mostly from the non-ideal noise of the thermistor. Scaling laws for the excess resistor noise with volume and temperature are discussed.

The results of these measurements allow us to set limits on the performance of optimized detectors operating near 0.1K. We present anticipated performance for two types of detectors; one a "low tech" device, which can be constructed in any laboratory, and a more sophisticated device using a planar Si process.

Detector Construction

Two types of detectors were built for these tests. The first consisted of a thermistor of nuclear transmutation doped Ge (Palaio et al., 1983) with gold coated ion-implanted contacts. The thermistor is a parallelepiped about 0.8 mm between contacts, and about 0.2 x 0.2 mm in cross section (Fig. 1a). The thermal link to the cryogenic heat sink was provided by pieces of 7 μm diameter. NbC_xN_y-coated carbon fiber (Pike et al., 1976). Electrical and mechanical contact between the fiber and detector was provided by Epotek H-20 E conductive epoxy. The NTD germanium was chosen because of its excellent uniformity from device to device, and its low heat capacity at 0.3K. The carbon fibers combine negligible heat capacity with low thermal

conductance. The conductive epoxy provides adequate electrical contact to the detector, and the heat capacity has been measured at $T \lesssim 0.3K$ (Weyhe et al., 1983).

The second detector uses an ion-implanted Si thermistor (.5 mm x .5 mm x .5 μm) in a Si chip approximately 0.5 x 0.5 mm x .05mm (see Fig. 1b). The thermistor is a boron compensated phosphorus implant with ohmic contacts provided by arsenic implants into the thermistor. Electrical contact to the chip was made through aluminum contact pads covering the As ohmic contacts. The device was bonded with 0.001" aluminum wire (99% Al, 1% Si, all else $\lesssim 10^{-3}$ %) for electrical and thermal contact. The heat capacity of the device is dominated by the Al in the temperature range where substantial thermal activation of quasiparticles occurs. Thus, the detector is a low heat capacity, low thermal conductance device only below ~160 mK.

Test Apparatus

The two detectors were tested in two different cryostats. The Ge detector was primarily tested in a $^3He/^4He$ evaporation cryostat. The cryostat is operated with the ^4He bath cooled to $\simeq$1.4K by pumping to reduce the heat load on the ^3He stage. The ^3He cold surface could be operated down to 284 mK. The cryostat was provided with nichrome thin film load resistors (90 MΩ; nine 10 MΩ in series) made by MSI. JFETs for amplifying the signals were suspended on a thermally isolated structure of stainless steel wires. Since the FETs operate near 77K, the detectors were completely shielded from the thermal radiation emitted by the FETs by a box surrounding them. Electrical connection to the JFET gate was made by a 0.001" manganin wire. The gate leads were tensioned to ~15 gm to raise the resonant frequency to reduce the microphonic sensitivity. The entire cryostat was operated inside an electrically shielded enclosure to reduce extraneous pickup.

For testing at lower temperatures, we made use of a $^3He/^4He$ dilution refrigerator. The SHE refrigerator offers about 50 μW cooling power at 100 mK. The cryogenic electronics were modeled after the ^3He cryostat design with minor changes. The most notable is that the box containing the thermally isolated JFETs is rigidly mounted to the still in the refrigerator using a low thermal conductance fiberglass epoxy truss. Since the still can tolerate only ~10 mW power input, and the four JFETs can dissipate 30 mW, the JFET box was heat sunk to the 4.2K heat sink with a copper rod. This provides a low heat load to the still while holding the JFETs rigidly near the $^3He/^4He$ mixing chamber.

The refrigerator is operated in a manner which would allow its open loop temperature to be less than 50 mK. The

C-2

refrigerator is equipped with superconducting transition thermometers with fixed points at 98 mK, 162 mK, and 208 mK. We are able to servo the temperature at each of these fixed points using feedback control of the cold surface heater power.

Measurements

In an ideal bolometer in which the thermistor's resistance depends only on temperature and which has a single time constant, the responsivity can be derived from the detector bias current, I, resistance, R, dynamic impedance, Z, and effective time constant, τ_e (Mather, 1982). If the detector resistance has an electric field dependence, one requires the dynamic impedance at high frequency ($Z(\infty)$). In an "ideal" bolometer $Z(\infty)$ should be equal to R. In practice, however, $Z(\infty)$ can be substantially less than R (Mather, 1984). Measurements of all these parameters allow us to predict detector responsivity without any other knowledge of the details of the detector design.

Having determined the responsivity of the detector, we need only a measurement of the noise to determine the detector NEP. This measurement can be made with a spectrum analyzer at the output of the low noise preamplifier.

From the I-V characteristics of the detector, the resistance and thermal conductance can be determined. Having measured the thermal conductance, the heat capacity is then derivable from a measurement of the effective time constant. The measured I-V characteristics for the Ge and Si detectors are shown in Figure 2, and the derived parameters for these detectors are given in Table 1.

The measurements necessary to characterize our detectors are thus relatively straightforward to carry out. Special care was taken in the measurement of $Z(\omega)$ (Mather, 1984) to make proper allowance for the stray capacitance in the detector-load resistor network. This was accomplished by adopting an equivalent circuit model for the network and fitting the stray capacitances, using measurements made with the bolometer at zero bias, where it is a resistive device. We assume the capacitance values so derived are also correct when the detector is under bias. The shape of the $Z(\omega)$ curve indicates that this is a good assumption.

The R(T) measurements were made by measuring the device resistance at a series of calibrated temperature settings. Very low current is used to prevent self-heating or changes in resistance due to the applied field. The voltage coefficient of resistance R(V) has been measured on similar thermistors in two ways; first, the detector is maintained accurately at the bath temperature via good heat sinking, and the detector resistance is

measured as a function of applied field. In the second approach, a detector is suspended from the bath through a thermal conductance. A given amount of power is dissipated in the thermistor, and its resistance is noted. Then, the same power is dissipated in a resistor attached to the thermistor, which should result in the same detector temperature. The resistance of the thermistor is measured with a very small current. The difference between the thermistor resistance is due to the electric field dependence of the semiconductor thermometer.

X-Ray Responsivity Verification

X-rays provide a convenient and accurate means for absolute response calibration of thermal infrared detectors. The detectors were exposed to 5.9 KeV X-rays from a ^{55}Fe source. The expected pulse height from the deposition of this amount of energy into the bolometer can be calculated from the bolometer's load curve and $Z(\omega)$ data using an appropriate thermal and electrical model for the detector (Mather 1982, 1984; MMM 1984).

In the case of the Ge bolometer, a small dot of silver filled epoxy was painted on the detector. The X-ray is nearly completely thermalized when absorbed in the normal metal. Comparison of predicted to observed pulse heights show that the ratio of observed pulse height to predicted pulse height is 1.04 $\pm$ .05. This is strong confirmation of the electrothermal model for the bolometer. If the electric field dependence of the detector resistivity is ignored, the predicted pulse height is too high by nearly 30%.

The silicon detector is more difficult to analyze since it had no specific X-ray converter. We have observed that X-rays in our Si detectors deposit between ~70 and 95% of their energy as heat. The rest of the energy is stored as trapped holes and electrons.

The conclusion one draws from these results is that when a proper model is used for the detector, the predicted "electrical responsivity" is in excellent agreement with that determined by experiment. Thus, if one attaches an infrared absorber of known absorptivity to these bolometers, we can be quite certain of their performance characteristics.

Having verified the responsivity of the detector using the X-ray calibration and having obtained a power spectrum of the noise, we are ready to compare measured performance to theory.

Mather has developed a nonequilibrium theory predicting the thermodynamic limits to the sensitivity of ideal thermal detectors (Mather 1982). This theory, however, makes two

assumptions which may not be completely met by real detectors. The first is that the detector can be represented as a single time constant thermal system. This criterion does turn out to be nearly true for the devices discussed above. The second assumption is that the resistance is a function of temperature alone and this is not the case for these detectors. Mather (1984) has extended the theory to allow the calculation of the responsivity and effective time constant in this case. The only additional measured parameter required for this determination is the dynamic impedance at high frequencies $Z(\infty)$.

The noise of such a detector, however, depends on the detailed physical mechanism responsible for the electric field dependence on resistance, and cannot be derived from general thermodynamic arguments like the phonon noise and Johnson noise. Also, the calculated phonon noise power must be multiplied by the detector responsivity to predict the output voltage noise arising from this source. It is important that the proper value for the responsivity, allowing for the field dependence, be used in this calculation. Recognizing the uncertainty in predicting the noise due to electric field-assisted conduction, we will nonetheless use this procedure to obtain an estimate of the NEP.

Comparison between measured noise and calculated noise is shown in Fig. 3. Note the significant rise in noise below 20 Hz in the NTD Ge detector. E. Kriese (private communication) has produced detectors from the same material using soldered contacts which exhibit noise which is flat to below 2 Hz. We attribute the excess noise in our system to the superconductor/conductive epoxy joint used for electrical contact, and believe it is not inherent to the thermistor material. It is possible however that any thermistor operated in a regime where its resistance is significantly reduced by electric field dependance may show some excess noise. Further tests are required to test this possibility. The ion-implanted Si thermometers show significant 1/f noise which becomes more severe as the size of the thermistor is reduced. The mechanism responsible for this noise is not well understood, but we note that it occurs under bias conditions where the field assisted condition is important.

Expected Infrared Performance

The detectors we have tested can be fitted with infrared absorbers and provide optical NEP's $\lesssim 1\times10^{-16}$ W/$\sqrt{\text{Hz}}$. This is near the sensitivity required for a broad band far infrared photometer for SIRTF (P. Richards, this conference). Table 2 shows how the addition of the absorber would affect the performance of the two detectors tested. Note that the Si detector need only have an absorbing film added.

These detectors represent a first step towards the sensitivity regimes available at 0.1K. Improved fabrication techniques (monolithic structures) will allow us to make small, low-heat capacity devices which will have a performance substantially in excess of that available with current devices.

Acknowledgments

The authors wish to thank Dale Arbogast, Andre Burgess, Dave Dargo, Mike DiPirro, Richard McClanahan, Harry Meyer, Paul Murdock, and Carol Sappington for invaluable assistance in the preparation and testing of calorimeter detectors.

References

Mather, J. C., "Electrical Self-Calibration of Non-Ideal Bolometers", Appl. Optics, Vol. 23, p. 3181, 1984. Erratum: Vol. 24, p. 1407, 1985.

Mather, J. C., "Bolometer Noise: Nonequilibrium Theory", Appl. Optics, Vol. 21, pp. 1125-1129, 1982.

McCammon, D., Moseley, S. H., Mather, J. C., and Mushotzky, R. F., "Experimental Tests of a Single-Photon Calorimeter for X-Ray Spectroscopy", J. Appl. Phys., Vol. 56, pp. 1263-1266, 1984.

Moseley, S. H., Mather, J. C., and McCammon, D., "Thermal Detectors as X-Ray Spectrometers", J. Appl. Phys., Vol. 56, pp. 1257-1262, 1984.

Moseley, S. H., Kelley, R. L., Mather, J. C., Mushotzky, R. F., Szymkowiak, A. E., and McCammon, D., "Thermal Detectors as Single Photon X-Ray Spectrometers", IEEE Trans. Nucl. Sci., Vol. NS-32, pp. 134-138, 1985.

Palaio, N. P., Rodder, M., Haler, E. E. and Kreysa, E., "Nuclear-Transmutation-Doped Germanium Bolometers", Int. J. Infrared Millimeter Waves, Vol. 4, p. 933, 1983.

Pike, G. E., Pierson, H. O., Mullendore, A. W., and Schirber, J. E., "Superconducting Thin Film Niobium-Carbonitrides on Carbon Fibers", Applied Polymer Symposium No. 29, pp. 71-81, 1976.

Weyhe, S., Junge, B., Petzoldt, F., Bruns, S., and Gey, W., "Specific Heat of Delta Bond 152, EPO-TEK H20E, and Wood's Metal at Low Temperatures", Cryogenics, p. 166-167, March 1983.

Table 1

Summary of Physical Parameters

	Ge Detector	Si Detector
Dimensions	0.2x0.8x0.2 mm	0.5x0.5x0.08 mm
T_{Bath} T_{bol}	0.284K 0.328K	0.098K 0.113K
Heat Capacity	$1.1x10^{-12}$ J/K	$3.8x10^{-13}$ J/K
Conductance	$1.1x10^{-9}$ W/K	$1.3x10^{-10}$ W/K
Resistance	15.7 MΩ	9.4 MΩ

Table 2

Predicted Infrared Characteristics of NTD Ge Detector with a 1 mm Absorber

Measured heat capacity of detector as tested	1×10^{-12} J/K
Diamond substrate 1 mm diameter, 25 μm thick	3.3×10^{-14} J/K
Metallic absorbing film: 20 Å Cr	1.2×10^{-13} J/K
32 Å Au	5.4×10^{-14} J/K
Epoxy for connection (~ 0.0025 cm diam. sphere)	~ 5×10^{-13} J/K
Total heat capacity of IR absorber	7.1×10^{-13} J/K
Total heat capacity of IR detector	1.7×10^{-12} J/K

Predicted Detector Parameters:

NEP_{Elec} (20 hz)	8.4×10^{-17} W/√Hz
Absorption efficiency (freq. independent)	50%
$NEP_{Optical}$	1.7×10^{-16} W/√Hz
τ_e	1.8 msec.

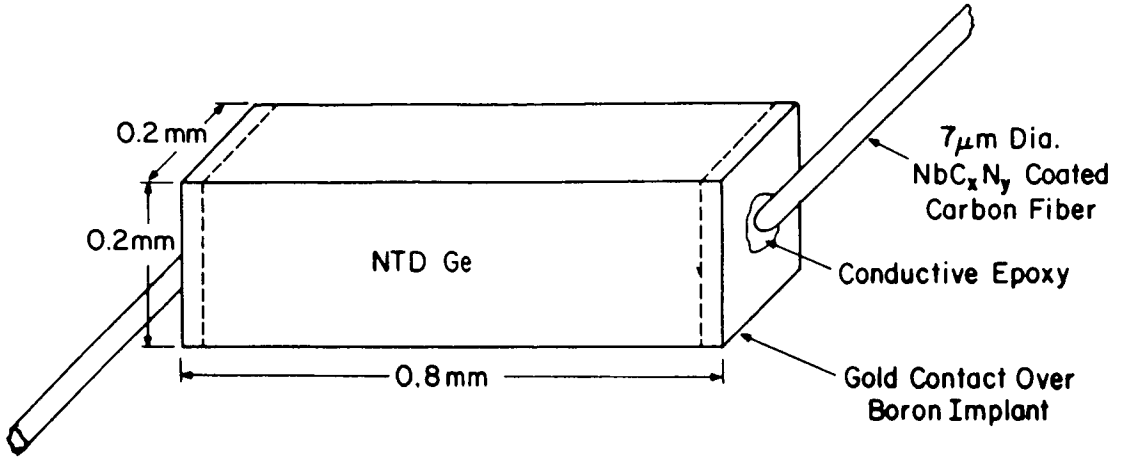

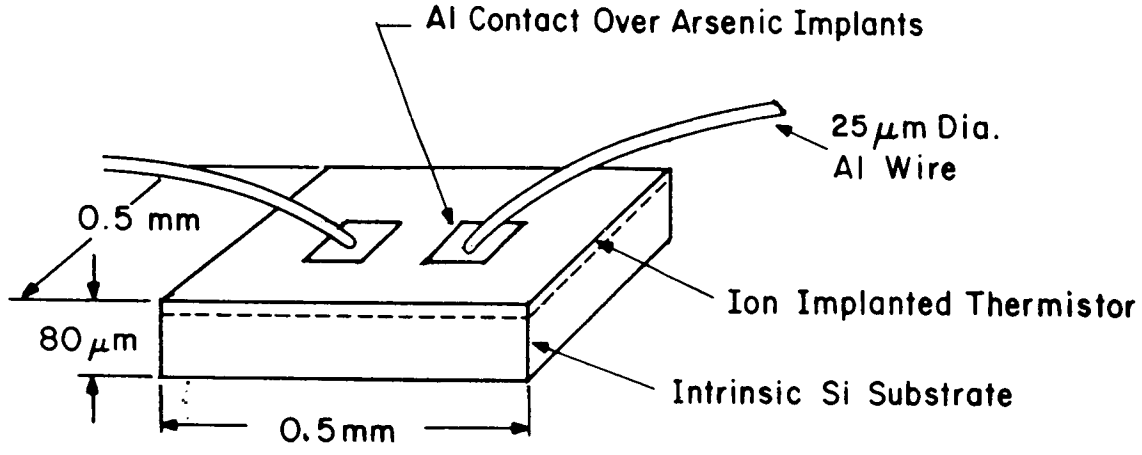

Figure 1: (a) Schematic of test NTD Ge detector with superconductor-coated carbon fibres attached to gold-covered boron contacts. The fibres are attached using conductive epoxy.
(b) Schematic of test Si detector with ion-implanted thermistor. The contacts are aluminum on arsenic. The device is suspended by the wedge-bonded Al wires, which serve as both electrical and thermal connections. The depth of the ion implant is about 0.5 μm.

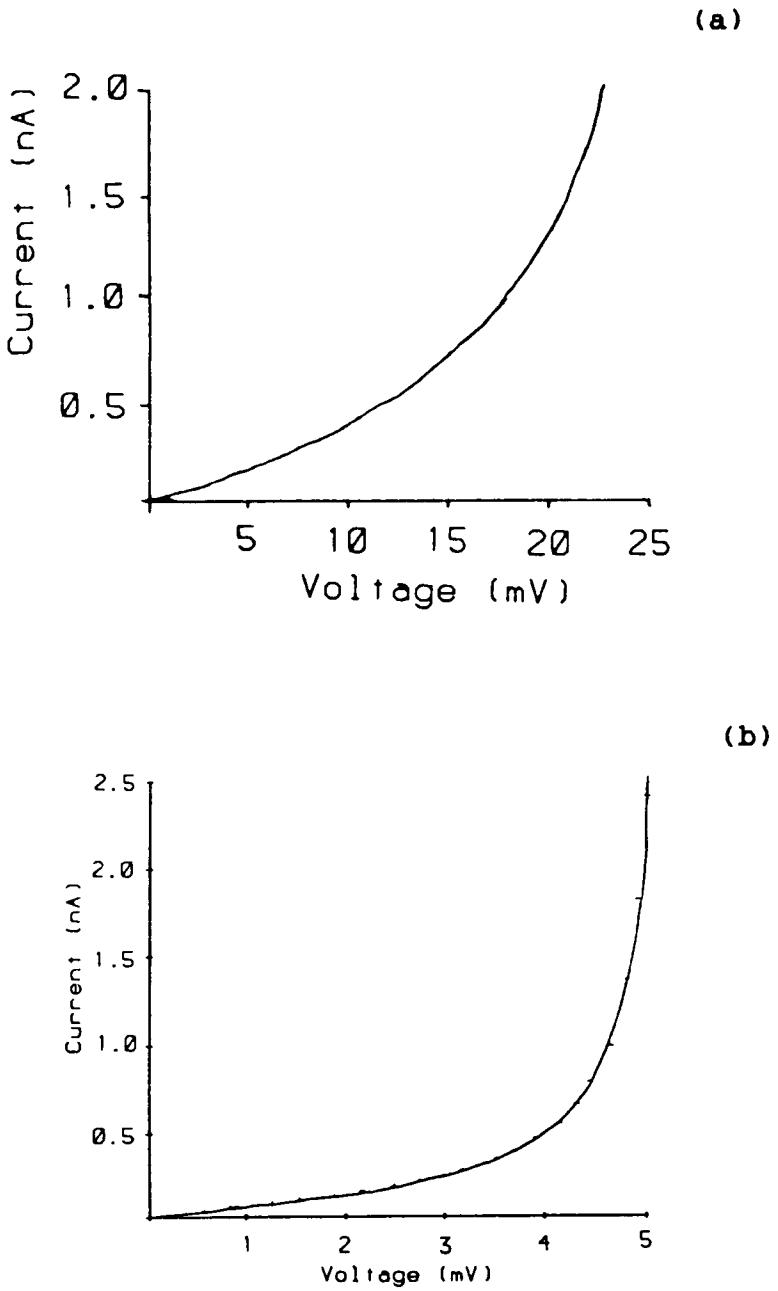

Figure 2: (a) Current-voltage characteristics of Ge detector operated at a temperature of 0.328K.
(b) Current-voltage characteristics of Si detector operated at a temperature of 0.113K.

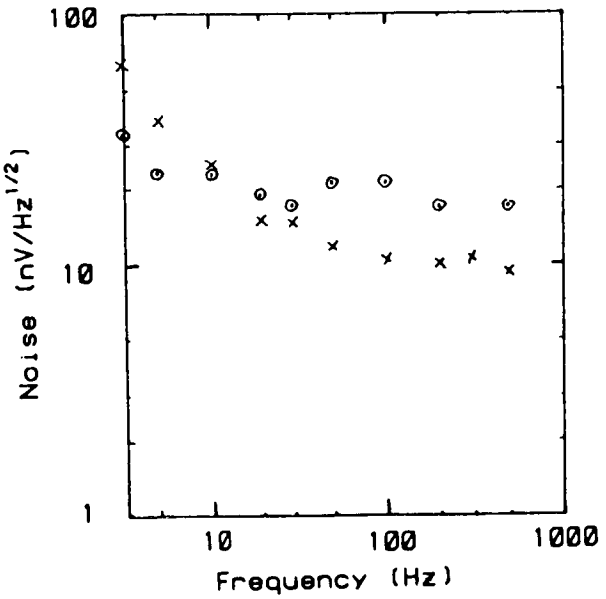

Figure 3: Measured noise spectrum of the Ge detector with zero bias (circles) and 0.110 volts bias (crosses). The coldplate temperature was 0.284K and the detector temperature under bias was 0.328K.

A PROGRESS REPORT ON BOLOMETERS OPERATING AT 0.1 K USING ADIABATIC DEMAGNETIZATION REFRIGERATION

T. Roellig, L. Lesyna, M. Werner, and P. Kittel (Ames Research Center)

SUMMARY

Bolometers are still the detectors of choice for low background infrared observations at wavelengths longer than 200 microns. In the low background limit, bolometers become more sensitive as their operating temperature decreases, due to fundamental thermodynamic laws. Cooled space telescopes such as SIRTF will provide a background low enough that bolometers will need to be operated at a temperature lower than that of pumped helium-3 (0.3K) if the observations are not to be detector noise limited. Out of the different techniques that may be utilized to reach temperatures significantly lower than 0.3 K, we have chosen to investigate the possibility of using the technique of adiabatic demagnetization of a paramagnetic salt as a method of cooling bolometers for space missions. This technique is gravity independent, compact, has no moving parts, and can have low power dissapation with careful design. With the appropriate choice for the salt, the technique is also easily capable of reaching temperatures below 50 mK. It should be noted that whatever technique is used to achieve a low bolometer operating temperature, it must be very stable with little thermal noise. Since bolometers are thermal devices, they will be very sensitive to sink temperature variations.

We have chosen to evaluate the adiabatic demagnetization technique by building a bolometer detector system operating at a wavelength of 1 millimeter for use at a ground based telescope. We have constructed a small refrigerator (approximately 18 inches high, 30 pounds weight) with optical and mechanical interfaces for mounting at the cassegrain focus of the 5m Hale telescope. (See Figure 1). With this system we can achieve temperatures below 50 mK. By only partially demagnetizing, the temperatures achieved are higher, but magnetic field is then available for balancing the heat flow into the salt, allowing stable temperatures to be maintained for many hours. The magnetic temperature stabilization system is controlled by a small personal computer system through an RS 232 interface as shown in Figure 2. With our system, a thermal stability of 18 μK is obtained at an equilibrium temperature of 0.14 K over a time period in excess of 4 hours. This corresponds to a bolometer responsivity variation of less than 1%. Ultimately, the system is expected to be able to maintain a temperature of 0.1 K for over 12 hours before recycling the refrigeration system is necessary. As presently configured, the system takes less than one hour to recycle.

The system we have constructed has been fit checked at the telescope and is expected to take its first data in November, 1985. The bolometers for this program have been developed independently using a larger laboratory adiabatic demagnetization refrigerator. After some initial disappointments with a variety of materials, including silicon on sapphire, we have found a crystal of Ge:Ga that has the correct resistivity for operation at 0.1 K. Based on our electrical tests of this material we expect to reach a background limited optical NEP of 9×10^{-16} w/$\sqrt{\text{Hz}}$ with our filter bandpass (8.5 cm^{-1} to 11 cm^{-1}) at the telescope.

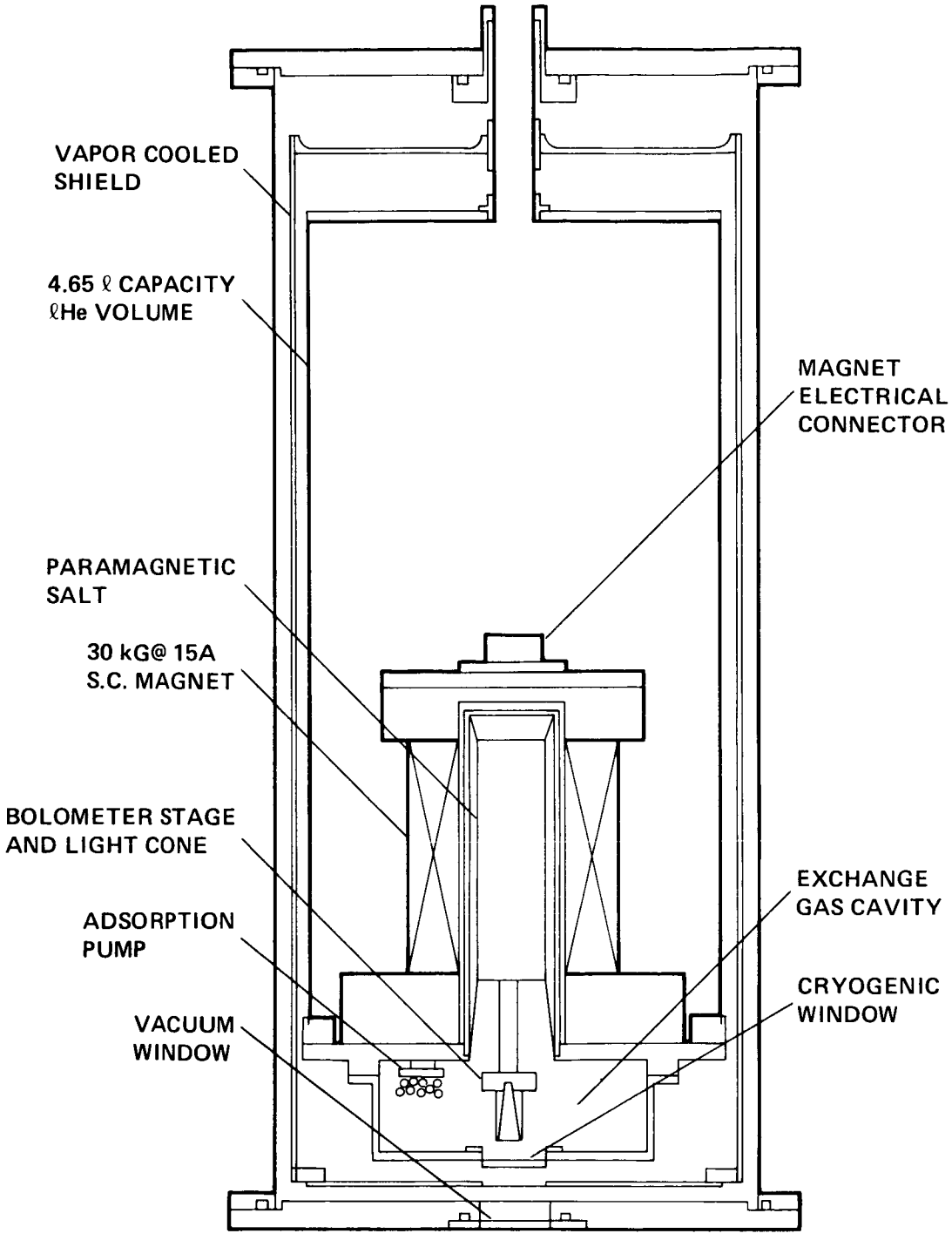

FIGURE 1. Diagram of adiabatic demagnetization test dewar.

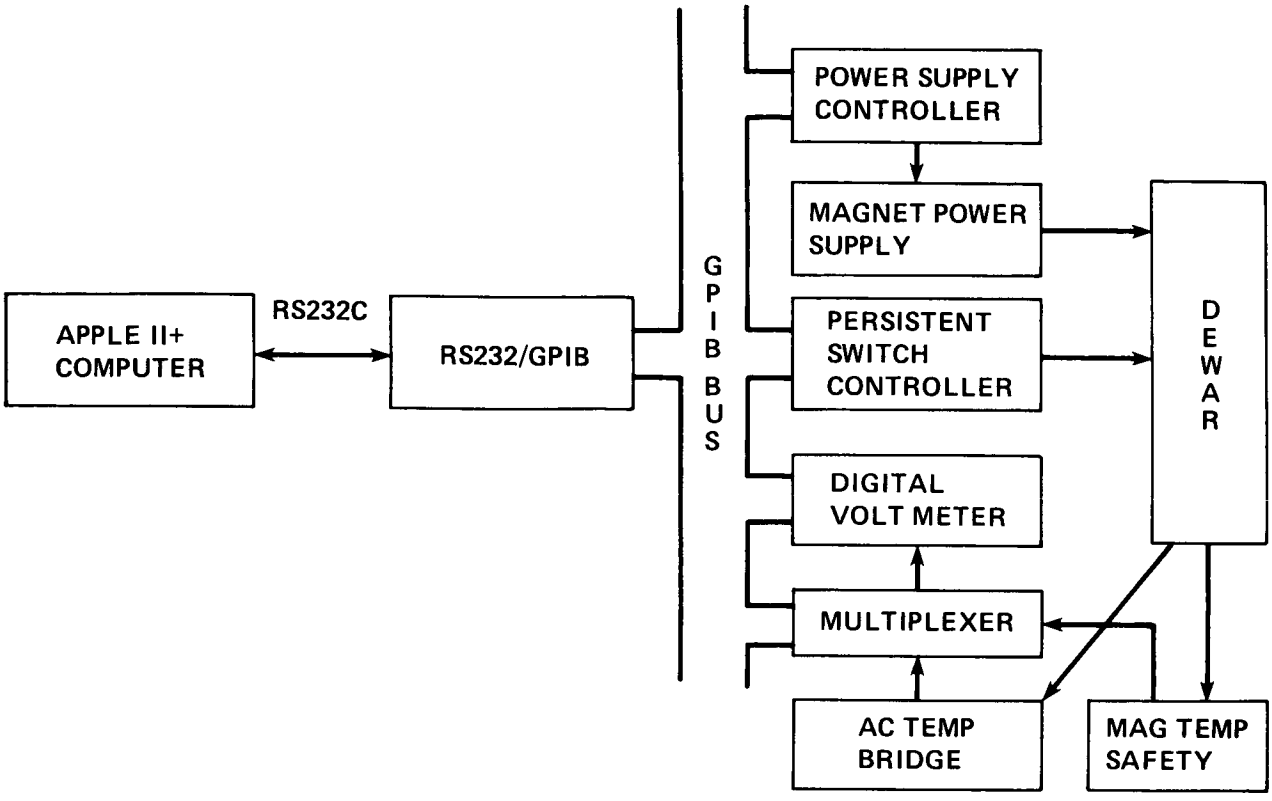

FIGURE 2. Schematic diagram of temperature regulation electronics interface.

N87-13714

LOW-BACKGROUND InSb ARRAY DEVELOPMENT

R. D. Thom and B. T. Yang

Santa Barbara Research Center, Goleta, CA 93106

ABSTRACT

Photovoltaic indium antimonide (PV InSb) detector array technology has matured over the past several years to enable a wide variety of applications to use this high-performance detector material to advantage. The operating conditions for most of the applications to date for back-side illuminated PV InSb arrays have encompassed focal plane temperatures ranging from 40K to approximately 95K, with the majority in the narrower range between 60 and 80K. Background flux (Q_B) conditions have ranged from 10^{10} ph/cm^2-sec to 10^{16} ph/cm^2-sec, most typically between 10^{12} and 10^{14} ph/cm^2-sec. Appropriately, the array parameters have been optimized for maximum performance over these temperature and background ranges. The key parameters which were "peaked" in this process were the resistance-area product (R_oA) of the detectors and their quantum efficiency. The Space Infrared Telescope Facility (SIRTF) Infrared Array Camera requirements, however, present very low temperature (7K) and background ($<10^6$ ph/cm^2-sec) operating conditions, plus the need for very high signal-to-noise ratios. Preliminary analysis indicates that back-side illuminated PV InSb arrays can be optimized for operation under these conditions, and some performance projections will be presented.

I. INTRODUCTION

Photovoltaic indium antimonide (PV InSb) detector array technology has matured over the past several years to enable a wide variety of applications to use this high-performance detector material to advantage. Linear arrays, linear arrays with time-delay-and-integration (TDI), two-dimensional arrays in 32 × 32 to 62 × 58 formats and even larger arrays in the classified arena have been fabricated in InSb. The majority of these arrays have been mated to silicon readout or multiplexer (MUX) chips using the hybrid indium bump interconnection technique, the most mature design approach for implementing solid-state readout of intrinsic detector arrays (Ref 1). The several advantages of InSb include: quantum spectral response from ~1 μm to its cutoff wavelength of 5.4 μm (77K); high quantum efficiency ($\gtrsim$60% without antireflection (AR)

coating and >85% with AR coating); availability of highly pure InSb material with excellent crystalline perfection; and a mature detector fabrication process at SBRC utilizing ion implantation to form the PV diodes and photochemically-deposited SiO_2 for device passivation.

The operating conditions for most of the applications to date for back-side illuminated PV InSb arrays have encompassed focal plane temperatures ranging from 40K to approximately 95K, with the majority in the narrower range between 60 and 80K. Background flux (Q_B) conditions have ranged from 10^{10} ph/cm^2-sec to 10^{16} ph/cm^2-sec, most typically between 10^{12} and 10^{14} ph/cm^2-sec. Appropriately, the array design parameters, material doping levels, junction profiles, substrate thickness, etc., have been optimized for maximum performance over these temperature and background ranges. The key parameters which were "peaked" in this process were the resistance-area product (R_oA) of the detectors and their quantum efficiency.

The Space Infrared Telescope Facility (SIRTF) Infrared Array Camera requirements, however, present very low temperature (7K) and background ($<10^6$ ph/cm^2-sec) operating conditions, plus the need for very high signal-to-noise ratios. Knowledge of the physics of back-side illuminated PV InSb detectors and preliminary analysis indicate that it should be possible to improve their performance under these extremely low T and Q_B levels by reoptimizing certain device parameters.

The key issues are:

- Reduction of dark current
- Reduction of detector capacitance to reduce the direct readout (DRO) noise
- Preservation of useful quantum efficiency in back-side illuminated InSb detector arrays at very low temperatures

These are discussed in turn in the following sections.

II. DARK CURRENT ANALYSIS

Reduction of dark current is the primary goal of this detector development program. It is appropriate to discuss the dark current in two different temperature regimes: (1) the 40K to 80K range, which we will call the "thermal regime"; and (2) the range less than 40K.

For temperatures between 40K and 80K, PV InSb leakage current is described reasonably well by the simple current-voltage equation (Ref 2):

$$I = I_s[\exp(qV/\beta kT) - 1], \tag{1}$$

where I is the current, V the applied voltage, I_s the saturation current, T the temperature, q and k the usual physical constants, and β a number between 1 and 2, depending on the origins of the leakage current in the device. It has been well-established (Ref 3) that PV InSb in this temperature regime is dominated by generation-recombination (G-R) current, for which to first order $\beta = 2$. Equation (1) may be differentiated to relate the saturation current to the dynamic resistance R_o of the detector at V = 0:

$$\left.\frac{dI}{dV}\right|_{V=0} = \frac{1}{R_o} = \frac{qI_s}{\beta kT}, \tag{2}$$

or its normalized figure-of-merit the R_oA product to the saturation current density J_s:

$$R_oA = \frac{\beta kT}{qJ_s}. \tag{3}$$

R_oA is the most commonly measured and intercompared parameter for PV detectors.

The R_oA product when controlled by G-R current depends on: the density of G-R centers contained within the volume of the diode's depletion region, which is characterized by an effective lifetime τ_o; the width of the depletion region W; the built-in voltage V_{BI}; and the intrinsic carrier concentration n_i. The latter two parameters may be found in any standard semiconductor device text (Ref 4). The R_oA product in terms of these parameters is

$$R_oA \simeq \frac{\tau_o V_{BI}}{qn_i W_o}. \tag{4}$$

Figure 1 expresses measured R_oA product versus temperature data for a number of SBRC PV InSb detector arrays in terms of their corresponding saturation current densities and dark currents. Equation (3) was used to calculate J_s, shown on the left-hand scale, from the measured R_oA's. The dark current

specific to a detector area of $(75\ \mu m)^2$ and a bias voltage V = -40 mV is shown on the right-hand scale, from

$$I_{pixel} = J_s A_{pixel}[\exp(qV/\beta kT) - 1]. \quad (5)$$

The data show that meeting the requirement of $I_{pixel} < 25$ fA at T = 50K and V = -40 mV is feasible; however, the statistical base at this relatively low temperature is scarce. The data point shown by the solid diamond (◆) at 56K is University of Rochester (Ref 5) data for an SBRC 32 × 32 array.

The broken curve in Figure 1 shows the theoretical dependence of the (G-R only) dark current calculated using Equation (4) with $N_A = 10^{18}/cm^3$, $N_D = 2 \times 10^{15}/cm^3$, and $\tau_o = 2 \times 10^{-8}$ sec. The measured currents are seen to follow the expected exponential decrease until temperatures reach the vicinity of 55K, where new leakage sources (as well as leakage associated with dewars and measurement apparatus) become nonnegligible. Extrapolating the curve to 50K suggests that for the existing InSb array with a nominal 75 μm × 75 μm size, an I_{pixel} of 25 fA or less should be attainable.

At temperatures below approximately 40K, thermally-generated currents diminish rapidly. In particular, at temperatures in the vicinity of 7K, all thermal leakage sources will effectively be zero, since they depend on the intrinsic carrier concentration n_i, with metallurgical junction G-R current, field-induced junction (if any) G-R current, generation out of surface states being directly proportional to n_i, and diffusion current proportional to n_i^2. One can quickly evaluate n_i at 7K from the applicable equation

$$n_i = (1.044 \times 10^{14})T^{3/2} \exp(-E_g/2kT), \quad (6)$$

where T is the temperature and E_g is the bandgap (0.234 eV at 7K) with the result

$$n_i(7K) = 1.19 \times 10^{-69}/cm^3, \quad (7)$$

which is 78 orders of magnitude smaller than its 77K value. Hence it can be safely assumed that thermal sources will be negligible.

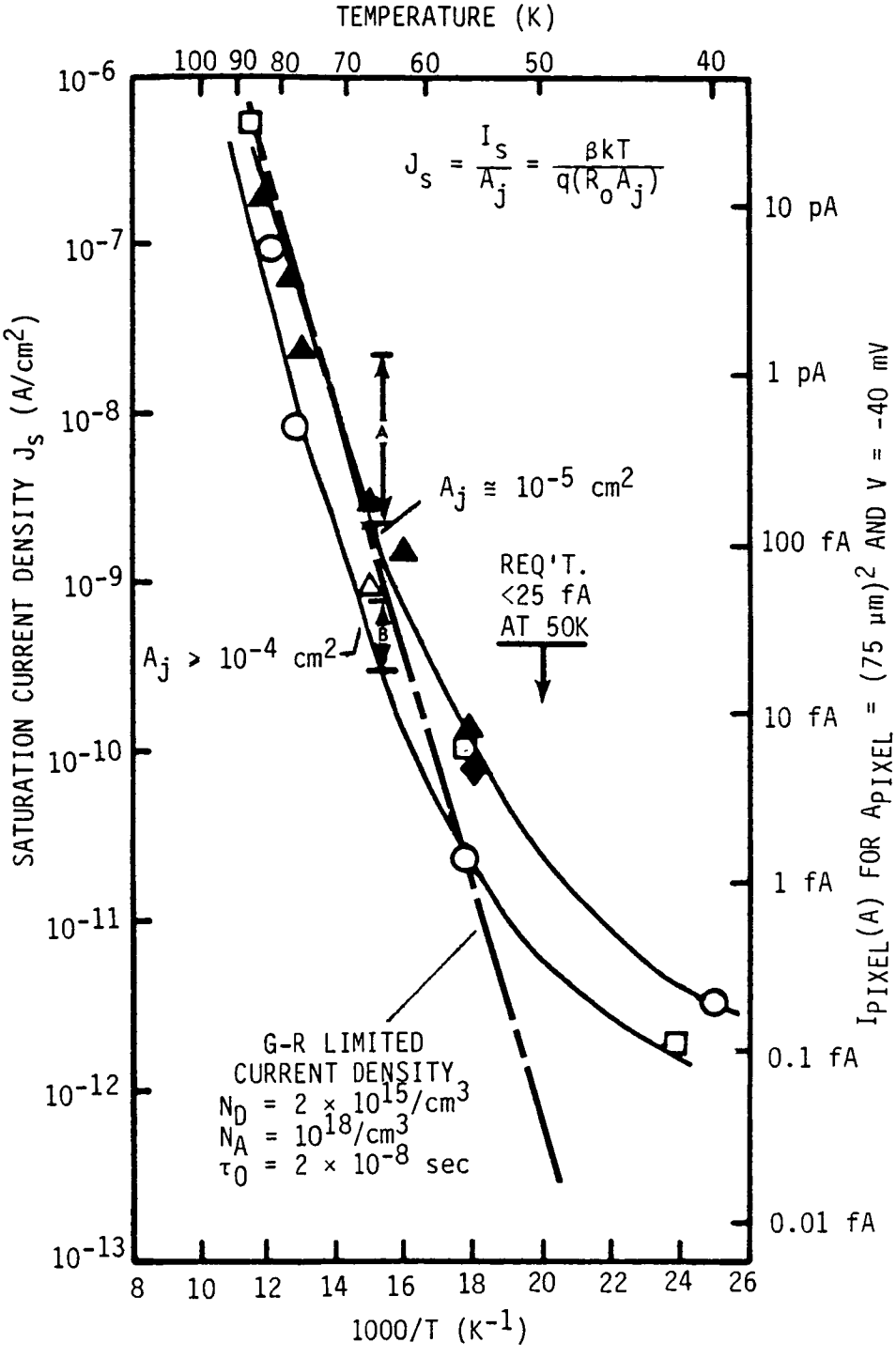

DATA POINTS ARE FOR A NUMBER OF SBRC PV InSb DETECTORS. RANGES LABELED A AND B ARE FOR RELATIVELY LARGE SAMPLE SIZES OF TWO CONFIGURATIONS BEING FABRICATED CONCURRENTLY.

Figure 1. Dark Current Density versus Temperature for PV InSb in the "Thermal Regime"

Therefore other sources - usually safely neglected in the 40-to-80K range - will dominate. These include:

- Band-to-band tunneling
- Trap-assisted tunneling
- Tunneling in the surface region
- Surface leakage, i.e., shunt paths as distinct from field-induced junction currents
- Leakage through the gate oxide

The physics of some of these mechanisms, or, more correctly, the input parameters necessary to calculate quantitative estimates of leakage due to them, are not generally known, so an experimental approach must be taken. Dark current measurements at 7K and low Q_B are therefore important in this development program.

The magnitudes of the first three mechanisms listed above are a very strong function of the electric field in the junction region, and the electric field in the region where the junction intersects the InSb surface, which is in general different than the field in the bulk junction. The magnitudes of these fields may be reduced by increasing the depletion region width and, as previously discussed, this is accomplished primarily through reduction of base doping.

Prediction of tunneling current magnitudes is difficult at best, due to various simplifications in modeling and lack of knowledge of the actual electric fields in a real PV detector. What will be illustrated here is an attempt to reduce band-to-band tunneling current through parameter optimization. The resultant magnitudes of dark current are not in themselves reliable due to the factors mentioned above; however, the change in tunneling current with doping is believed to be significant. Band-to-band tunneling, since it depends on electric field rather than temperature (except through the dependence of bandgap on temperature), is still active at liquid helium temperatures. The interband tunneling current density J_t, in amperes/m^2, is given by

$$J_t = \frac{q^3 m_r^{1/2} MEV}{4\pi\hbar^2 E_g^{1/2}} \exp\left[\frac{-\pi m_r^{1/2} E_g^{3/2}}{2\hbar qME}\right], \quad (8)$$

where V = applied voltage, in volts,

m_r = reduced mass = $m_c m_v/(m + m_v)$

= $0.0136\ m_o = 1.2349 \times 10^{-32}$ kg for InSb,

E_g = bandgap, in joules,

E = maximum electric field of a plane abrupt junction

= $2(V_{BI} - V)/W$, in volts/meter,

V_{BI} = built-in voltage, in volts,

W = depletion width, in meters,

M = field factor (see discussion below),

$\hbar$ = 1.0544×10^{-34} joule-sec, and

q = 1.602×10^{-19} coul.

The current at relatively large reverse biases was measured for ion-implanted planar InSb diodes (Ref 6) and was found to be fit well by Equation (8), where M was treated as a fitting parameter. M is the ratio of the average field in a real device to the field in an ideal plane (not planar) junction, and is ≥ 1. There are at least three reasons why M may exceed unity:

1. Surface effects around the perimeter of the diode. For example, an accumulated surface in the lightly doped n-type region would increase the field in the junction-surface intersection region, hence the local tunneling current.

2. Junction curvature, which occurs naturally in planar diodes, increases the field at the diode edges relative to that of a plane junction.

3. Material inhomogeneity, which can give rise to local high field regions in the junction region (microplasmas).

M was found to be 1.3 ± 0.2 for a wide variety of diodes.

For SIRTF purposes, these earlier data do not extend to the required very low current regime (limited by the instrumentation used in the measurements). However, we can utilize Equation (8) and a representative empirically-determined M-factor to determine the interband tunneling component for the lower detector voltages applicable to SIRTF. The results of such a calculation are shown in Table 1.

Table 1. Estimated Interband Tunneling Current for PV InSb at 7K for Various Values of Diode Applied Voltage, V

$\|V\|$ (V)	Existing Array		Improved Array	
	J_t (A/cm^2)	J_t (fA)	J_t (A/cm^2)	J_t (fA)
0.1	2.1×10^{-15}	1.2×10^{-4}	3.2×10^{-57}	1.8×10^{-46}
0.2	1.1×10^{-12}	0.06	1.9×10^{-49}	1.1×10^{-38}
0.5	2.7×10^{-8}	1.5×10^{3}	1.1×10^{-36}	6.2×10^{-26}
1.0	6.2×10^{-5}	3.5×10^{6}	6.3×10^{-27}	3.5×10^{-16}
E_g = 0.234 eV $N_{A_{1/2}}$ = 10^{18}/cm^3 m_r = 1.111267×10^{-16} kg$^{1/2}$			M = 1.462 T = 7K A_{pixel} = 5.63×10^{-5} cm^2	

The extremely strong dependence on voltage and the other parameters is evident from the table. While it cannot be concluded whether or not interband tunneling current will be a significant dark current source at 7K with the existing material (left-hand columns of Table 1), the predicted dark currents are close enough to the 0.01 fA requirement to cause concern. This is particularly so when one considers the possibility that the field in the surface region of the diode may be several times larger than that in the bulk junction (i.e., M >> 1), dependent on junction passivation conditions at T = 7K, which would increase the currents by orders of magnitude. Table 1 does demonstrate, however, the improved array (right-hand columns) is designed to reduce the tunneling current to negligible levels for the same diode conditions and assumptions.

III. DETECTOR CAPACITANCE

A key parameter affecting the performance of InSb in Band 1, in addition to the leakage current, is the detector capacitance. It is desirable to reduce the detector capacitance to reduce the direct readout (DRO) noise.

As pointed out in the previous section, the existing InSb product is designed to optimize the R_oA product; whatever capacitance results is accepted. The photodiode junction capacitance is inversely related to the depletion width, at zero volts given simply by:

$$C_j/A_j = \varepsilon_s/W_o, \tag{9}$$

so that detectors optimized for R_oA have a relatively large capacitance per unit area. It is estimated that with appropriate process control and proper selection of material properties, the junction capacitance can be reduced from 3.26×10^{-8} F/cm^2 to about 1.05×10^{-8} F/cm^2. In other words, for a 50 μm × 50 μm detector the junction capacitance will be about 0.26 pF. Assuming the gate overlap capacitance of 0.19 pF, the total detector capacitance will be about 0.45 pF, compared to 1.53 pF for the existing array.

In a future SIRTF-optimized mask redesign, anticipating that tunneling mechanisms will be potential sources of dark current, it will be important to minimize high-field regions, such as can occur at inside or outside corners of junctions, etc. Although small radii are normally incorporated at the corners of the detector junctions (and/or occur naturally in the photolithography and etching processes), it is believed that larger radii may be very beneficial for this application, or in the extreme, use of circular detectors. It has been experimentally verified that the breakdown voltage of InSb diodes - the voltage at which substantial tunneling current is observed in the I-V curve - is much higher for circular geometries compared to square.

IV. QUANTUM EFFICIENCY AT VERY LOW TEMPERATURES

A final issue that will be addressed in the Band 1 Detector Development Program is that of the quantum efficiency (as a function of wavelength) for back-side illuminated InSb detector arrays at very low temperatures (i.e., 7K). Limited (and conflicting) data on some material parameters measured at low temperatures suggest that the minority carrier diffusion length - which controls the spectral responsivity of the array - may be shorter than it is in the 40-to-80K temperature range. This is not believed critical, since an alternate array configuration is possible that would eliminate any concern over loss of quantum efficiency at low T, if it were found to exist. However, it is essential to make radiometric measurements at T ≅ 7K to obtain the necessary data base.

The responsivity (Ref 7) of the back-side illuminated InSb diode structure is primarily determined by the diffusion length L_p of the minority carriers in the n-type substrate:

$$L_p = (D_p \tau_p)^{1/2}$$
$$= \left(\frac{\mu_p kT \tau_p}{q} \right)^{1/2} \qquad (10)$$

where D_p is the diffusion coefficient, τ_p the minority carrier lifetime, and μ_p the mobility of the holes in the n-type substrate. The thickness d of the InSb substrate is reduced by lapping and etching in the standard baseline process to somewhat less than the diffusion length, $d < L_p$, for high internal quantum efficiency.

The issue for SIRTF is that the temperature will be a factor of 10 lower than at 77K; hence, a loss of $\sqrt{10}$ or 3 due to T alone in Equation (10). The mobility and lifetime are also functions of temperature, in general. The lifetime is approximately 500 ns (measured on starting material) and, as it is Schockley-Reed limited in the 77-to-7K range, it does not change appreciably as a function of temperature. Some limited data on hole mobility (Refs 8,9) show μ_p decreasing below 20K. The resulting diffusion lengths L_p are tabulated in Table 2.

Table 2. Estimated Minority Carrier Diffison Length for InSb

T (K)	μ_p (cm^2/V-sec)	L_p (μm)
77	8,000 - 10,000 (Ref 8)	~55
50	15,000 - 20,000 (Ref 8)	~60
7	3,000 - 4,000 (Ref 8)	~10
4	10,000 (Ref 9)	~13
τ_p = 500 ns		

For 77K-to-50K operation, thinning of the InSb to its standard thickness of d = 10 to 12 μm satisfies the condition for high internal quantum efficiency. For $T \lesssim 10K$, however, if the limited data are correct, it may be necessary to thin the base further or suffer some loss of short wavelength

response. It should be noted that there are further uncertainties in the above predictions in that the quoted mobilities are Hall mobilities (i.e., calculated from Hall coefficients and sample conductivities) and do not necessarily apply to the diffusion problem.

Note that with this mechanism, the responsivity loss will be greater at shorter wavelengths, which are absorbed within a shallower depth at the back surface and therefore require the photogenerated holes to diffuse a greater distance to the junction. Also it should be understood that this mechanism is a result of basic material properties and the back-side illuminated configuration, and will be independent of individual vendor fabrication processes. (Improper back surface etching/passivation procedures will, however, exacerbate the situation.) Note, as well, that a loss in diffusion length at low temperatures in front-side illuminated devices will have the opposite effect; i.e., the responsivity will be degraded at long wavelengths, since those photons are absorbed deeper in the base, and therefore must diffuse back to the junction.

V. SUMMARY

1. A dark current of 25 fA at 50K should be attainable for the existing array.

2. Band-to-band tunneling current is the dominant leakage current at 7K, since the thermal current dwindles to zero.

3. Optimized array performance is sensitive to high electrical field and junction passivation.

4. An optimized array will reduce junction capacitance, subsequently reducing readout noise.

5. Quantum efficiency depends on the minority carrier diffusion length.

REFERENCES

1. R.M. Hoendervoogt et al., "Hybrid InSb Focal Plane Array Fabrication," Technical Digest of the 1978 International Electron Devices Meeting, Washington, DC, Dec. 4-6, 1978, pp 510-512.

2. D. Long, "Optical and Infrared Detectors," R.J. Keyes, editor, Topics in Applied Physics, Vol. 19, Berlin, Springer-Verlag, 1980.

3. R.D. Thom et al., "A Fully Monolithic InSb Infrared CCD Array," IEEE Trans. on Electron Devices, ED-27, Jan. 1980, pp 160-170.

4. S.M. Sze, Physics of Semiconductor Devices, New York, Wiley-Interscience, 1969.

5. W.J. Forrest et al., University of Rochester Infrared CCD 32 × 32 InSb Detectors, University of Rochester Dept. of Physics and Astronomy (no date).

6. R.D. Thom, W.H. Konkel, and R.M. Hoendervoogt, "Planar P-N Junctions in InSb by Be Ion Implantation," Proceedings of IEEE Device Research Conference, Ithaca, NY, Cornell University, June 27-29, 1977.

7. R.K. Willardson and A.C. Beer (eds), Semiconductors and Semimetals Volume 18: Mercury Cadmium Telluride, New York, Academic Press, 1981, p 231.

8. C. Hilsum and A.C. Rose-Innes, Semiconducting III-V Compounds, New York, Pergamon Press, 1961.

9. L. Chin Ch'ao and D.N. Nasledov, Soviet Physics-Solid State, 1, No. 4, 1959, pp 514-514.

InSb Arrays: Astronomy with a 32x32 CCD/ Development of a 58x62 DRO

W. J. Forrest and J. L. Pipher
Department of Physics and Astronomy
University of Rochester
Rochester, N.Y. 14627

Text of report presented at the Infrared Detector Technology Workshop held at NASA Ames Research Center August 13-14, 1985.

I. Introduction

This report summarizes experience gained at the University of Rochester in operating infrared detector arrays for high sensitivity astronomical applications. It is intended as an update to earlier reports (Forrest and Pipher 1983, Forrest et al 1985) as well as a window into our future plans in this area.

The first section describes progress made in operating the 32x32 InSb array with bump-bonded Silicon CCD readout. Full details of this system are revealed in Forrest and Pipher 1983 and Forrest et al 1985. The middle section describes some astronomical work done with the 32x32 camera. The last section describes our plans for the future, including improvements for the 32x32 Camera system as well as implementing a new generation of 58x62 InSb arrays using switched-MOSFET direct read out multiplexing system in place of the older CCD technology.

II. 32x32 InSb/CCD Hybrid Update

A. Sensitivity of Camera System

Of particular interest to Astronomers is the sensitivity actually achieved with detector arrays in a working camera system used for Astronomical observations. The intrinsically low backgrounds experienced in ground-based observing at wavelengths less than 3 microns make this an appropriate test-bed for achieving the SIRTF-class performance discussed elsewhere at this conference. The CCD technology limits the performance of our 32x32 InSb array, but it is reassuring nontheless to be able to report quite good performance levels for this device.

1. Low Backgrounds

In the course of our observational program, a series of 6 exposures of the central 14" region of our Galaxy was acquired at the IRTF 3m telescope in August of 1984. The exposures were made in the J band (1.23 micron wavelength) using a 190 sec on-chip integration time. The data was processed as described in Forrest et al (1985) to a final calibrated image. This image is shown in fig. 6. The noise level was determined by investigating the RMS

fluctuations in a 6x6 window moved around the 63x63 final image. In regions away from bright source structure, the RMS noise level corresponded to a J magnitude of +21.5 magnitude. This required 0.8 hours of total observing time of which 0.3 hours were spent integrating on source and the rest on beam-switching and background measurement. Some of this RMS noise could represent residual source structure, so this procedure really under-estimates our sensitivity. Extrapolating to a standard 1 hour of observing, we achieved a 1 sigma noise level of +21.6 magnitudes/pixel in the J band. Using our calibrated counts for zero magnitude for this run gives a 1 sigma noise level of +20.9 magnitudes/pixel in the K (2.2 micron) band.

This sensitivity exceeds that estimated in Forrest et al (1985) by 30%. It should be mentioned that these sensitivity estimates do not correct for the fact that our detectors occupy only 80% of the pixel area, so the detectors are actually more sensitive than estimated here. Nontheless, this sensitivity level is better by about 1 magnitude (factor of 2.5) than the best published claims of sensitivity of single-detector InSb systems developed for astronomy. It also exceeds by 2.2 magnitudes (a factor of 8) the published sensitivity achieved by the University of Arizona group (Philips-Walker, Rieke and Montgomery 1985) in the J band using a single Ge photodiode and a Low (1984) type optimized JFET integrating preamplifier. This demonstrates the good performance that can be achieved using off-the-shelf fully multiplexed infrared arrays.

2. High Backgrounds

At the high backgrounds experienced in ground-based observing longward of 3 microns, each of the working (about 920) detectors in our array is "background limited" in the sense that the noise in electrons is proportional to the square root of the background flux incident on each detector. As described in Forrest et al (1985) we achieve a noise level about 1.5 times the shot-noise limit in the lab when running near full buckets. At the telescope a similar noise level is observed when observing under good conditions. It is interesting that we can achieve this level of performance without "chopping" in the traditional sense. Rather, we "nod" the entire telescope and alternate between source measurements and background measurements on blank sky typically 100" away. Typically we spend 20 sec on the background followed by 40 sec on source, followed by 20 sec on bacground etc. This corresponds to a nodding frequency of 1/60 Hz rather than the more usual 5-10 Hz chopping frequencies typically employed in the thermal infrared. We find that background limited performance requires a well-designed low background telescope, such as the KPNO 1.3m and IRTF 3m, and a sky completely free of clouds. In addition, when subtracting the background flux from the source frames in our data reduction process, we can employ an arbitrary linear combination of unit weight of the background frames before and after a given source frame. It is often necessary to adjust this linear combination in order to achieve a uniform background subtraction

and low noise.

B. Re-imaging optics.

The optics we employ are shown in Fig. 1. The relay lens images the telescope secondary on the cold Lyot stop, which is placed at the filters, while re-imaging the celestial objects onto the infrared array. There are several advantages to this system. The single lens is outside the dewar, allowing easy focus and alignment adjustments. The initial image of celestial objects occurs in free space, preventing dust, scratches, etc. from degrading the image. By substituting a different focal length lens, the dewar can be matched to telescopes of differing f/#'s, without any internal adjustments; we have succesfully employed lenses for f/14, f/30 and f/35 telescopes. The quality of imaging with the f/35 lens is demonstrated in fig. 2. Finally a zoom lens feature can be had by moving only one element; unfortunately the element is the detector array itself. By moving the array closer to the Lyot stop, and refocussing the telescope, we would zoom out and look at a larger region of sky. The zoom feature hasn't been tried yet. The disadvantages of our current setup are: the lens is chromatic and transmits only 70%, reflecting the rest. The former results in a plate scale varying with wavelength, which makes comparisons of images at differing wavelengths more complex. This could be solved by employing an achromatic doublet. The latter reduces our signal and increases the background longward of 3 microns. We plan to investigate the possibilities of anti-reflection coating the KRS 5 lenses. This should result in much better sensitivities in the thermal infrared through reduced backgrounds.

C. Dark Current

Because of the extremely low backgrounds possible with a cooled space telescope, such as SIRTF, we desire similar low dark current levels in any detector materiel to be used in such an experiment. Typical levels of 1-10 e^-/sec are desired. A concern with InSb detectors are the dark currents attainable. We have therefore extended our dark current vs. temperature measurements below the 60K point reported by Forrest et al (1985). Temperatures down to 53K are now possible with our current dewar using pumped N_2. Temperatures down to 45K have been attained using LHe. Below 45K, the operation of the CCD readout becomes unreliable and it stops working at 41K. The results are shown in fig. 3. It is gratifying to see that the dark current, with 30 mV of back-bias, continues to decrease about a factor of 2 every 2K down to the lowest temperatures we can operate at. A dark current of .16 fA or 1000 e^-/sec has been achieved in the 45-50K region. We therefore have begun construction of an observing dewar which will be able to operate in the optimum 46-47K range using pumped N_2. The new dewar will also employ 1-2% circular variable filter wheels covering the 1.3-4.5 micron region, as well as our standard photometric filters. This will widen the scope of our scientific investigations as well as allowing us to reach very low background levels, around 30

photons/sec/detector, from ground-based telescopes. Since the new InSb detector arrays, in 58x62 format, currently being constructed by SBRC are similar to our current 32x32 array, we anticipate much lower dark currents will be achievable by operating the arrays at the lower temperatures attainable with the switched-MOSFET DRO.

III. Astronomy

We present some results of our current astronomical research, showing the power of fully multiplexed infrared detector arrays.

A. The Galactic Center

Of considerable interest in understanding the dynamics and energetics of the galactic center region is: does any infrared source lie at the position of the Sgr A* non-thermal point radio source? In collaboration with W.A. Stein, we have attempted to answer this question using our 32x32 array camera mounted on the IRTF 3m in an August 1984 observing run. This configuration gives approximately 0.45" pixels for fine positional resolution, while still allowing us to simultaneously observe several objects to derive accurate offsets. Images of the central 14" (0.7 pc) of the galactic center at J, H, K, L', and M' (1.23 through 4.7 microns) have been obtained. To obtain accurate astrometric positions, we calibrated our plate scale at each wavelength by observing 4 star pairs with well known separation and position angle. We supplemented this with star streaks, exposures of a bright star with the telescope drive off, to determine the E-W direction accurately. Then we measured the offset between the prominent infrared source IRS 7 and the visible star A, which has a well known absolute position. This could be done without moving the telescope by placing Star A in the NE corner of the array and IRS 7 in the SW corner. Having thus determined the position of IRS 7, the position of Sgr A* on our various images followed immediately.

The K image is shown in fig. 4, a cross marks the position of Sgr A*. It can be seen that no discrete 2 micron source coincides with it. A plot of the equal surface brightness contours from this image are shown in fig. 5, with some of the infrared sources marked. Images at the other wavelengths are shown in fig. 6; again no source appears at the Sgr A* position.

The only discrete object which could possibly coincide with Sgr A* lies to the North about 0.7" in our images. Because of its proximity, we have studied this object, which we call IRS 16 NW, in more detail. We find that it lies at the same position as CCD 2, an object seen in various 1 micron images of this region. We have derived the infrared brightness of this object by comparing it to the brightness of IRS 7. This was necessary because of the extremely crowded field, with diffuse emmission and discrete sources everywhere. The brightness ratios to IRS 7 were derived by shifting and subtracting the IRS 7 image until the IRS 16 NW source disappeared. In fig. 7 are given the results.

It can be seen that when de-reddened, the colors of IRS 16 NW are nearly neutral, which implies a hot object. If we take the de-reddened K brightness of 7.3 mag and a temperature of 30,000K, which is suggested by the excitation level of the central regions, the luminosity of this object would be about 10^6 solar luminosities. This is comparable to the observed luminosity (about $2x10^6$ solar) of the central 30" region, but falls short of the higher total luminosity ($2x10^7$ solar) inferred by current models. Thus it appears that IRS 16 NW is not the whole story here. Further, it seems that the "central engine", if it exists, should be 10 times brighter than IRS 16 NW; no such object is immediately evident in our images. This work is being prepared for publication (Forrest, Pipher and Stein, 1985).

B. Improved images of IRTF 3m

In a July 1985 observing run on the IRTF 3m, the telescope images were much improved over those seen in August 1984. Fig. 8 shows a comparison between stellar images. Figure 9 shows the improved quality of Galactic Center images which resulted from this. We note that the best images were obtained with the telescope tracking in the manual, rather than computer, mode. Also, some image degradation was experienced with the telescope tilted far from the Zenith. Interestingly, we experienced some of the best "seeing" conditions, when a major fraction of the light could fall on one 0.45" pixel, at the same time as other telescopes on this mountain were reporting poor visual seeing.

C. Active Protostars

We have found fascinating structure in star-formation regions in our galaxy. As examples, we show 2.2 micron images of regions around AFGL 2591 (=U of A 27) and S 140 IRS 1 in figs. 10 and 11. These are 10^4-10^5 solar luminosity protostars. Each shows high-velocity, bipolar outflow in CO and high linear polarization at 2.2 microns. In our images, well-defined circular (S 140) and oval (UofA 27) loops are seen, with the bright primary source at one edge of the loop. Significantly, the orientation of the loops is along the direction of bipolar flow. We suggest that the loops may be due to shocked H_2 emission where the high velocity flow is colliding with dense molecular cloud material. The three dimensional structure may actually be that of a bubble blown into the molecular cloud by the protostellar wind.

IV. Future Plans

A. New InSb and Si:In Arrays.

Our plans for improving the 32x32 InSb array system have been mentioned above. We now have on order a new 58x62 InSb array from SBRC, which is expected to give much improved performance. A comparison of the two arrays is given in fig. 12. In addition, as part of SIRTF detector development program, a second 58x62 InSb array is on order from SBRC, with lower doping level to reduce the

dark current and read noise. The InSb arrays will be compared to Si:In photoconductive arrays to determine the best detector arrays for the 2-5 micron region for the Infrared Array Camera and the 4-8 micron region for the Infrared Spectrometer on SIRTF.

Besides the larger format, the new 58x62 arrays employ a switched-MOSFET direct read out multiplexer which should give better performance and more flexibility than the CCD readout on our 32x32 array. The array will be x-y addressible on a pixel by pixel basis and capable of non-destructive readout. It should operate well in the 4-60K temperature range, allowing us to reach much lower dark currents. Finally, the rms read noise is expected to be less than 400 e^-, with a goal of less than 100 e^- in the second-generation, lower doped device. Because of the similarity of material and array construction, we expect the good imaging properties of our current 32x32 array to be maintained in the new InSb arrays.

The Si:In arrays are expected to deliver very low dark current and read noise, but sensitive, calibratible performance and good image quality under SIRTF conditions must be demonstrated.

B. Testing in the Lab and at the Telescope for SIRTF-class Performance

As summarized in fig. 13, the backgrounds expected on SIRTF are extremely low, leading to extremely good sensitivity if good enough detectors can be developed. Also summarized in fig. 13 are calculations which show that these low background conditions can be simulated in the lab and at the telescope using our current dewar design, with a window to the outside where objects to be imaged are placed. Thus, in the lab, in the J and H bands, extremely low background levels can be achieved in a darkened but still 300K room. To get these low levels, filters with $<10^{-8}$ of thermal leak must be developed. We plan to measure the leak and add blocker glass, such as OW-1 which transmits 10^{-3} per mm, to achieve this level.

At the telescope, fairly low backgrounds are encountered in the J band, while the H band suffers from large OH airglow and the K band from thermal emmision. However, by careful choice of wavelength using our 2% spectral resolution filter wheel, we can achieve very low backgrounds, around 30 photons/sec/detector, at 2.05 and 1.35 microns. Thus we will be able to operate the arrays and test various clocking algorithims and observing techniques under conditions very similar to those expected on SIRTF. We feel this experience will be very important to ensure that the maximum performance from the SIRTF experiments is achieved. Because of the extremely large thermal backgrounds, this kind of testing is not possible at longer infrared wavelengths, as summarized in figure 13.

References

Forrest, W.J. and Pipher, J.L. 1983, in Proc. Infrared Detector Technology Workshop, C. McCreight, ed. (NASA Ames Research Center).

Forrest, W.J., Moneti, A., Woodward, C.E., Pipher, J.L. and Hoffman, A. 1985, P.A.S.P. 97, 183.

Forrest, W.J., Pipher, J.L. and Stein, W.A. 1985 (preprint)

Low, F.J. 1984, Applied Optics 23, 1308.

Philips-Walker, C., Rieke, G.H. and Montgomery, E.F. 1985 Bull. A.A.S. 17, 571.

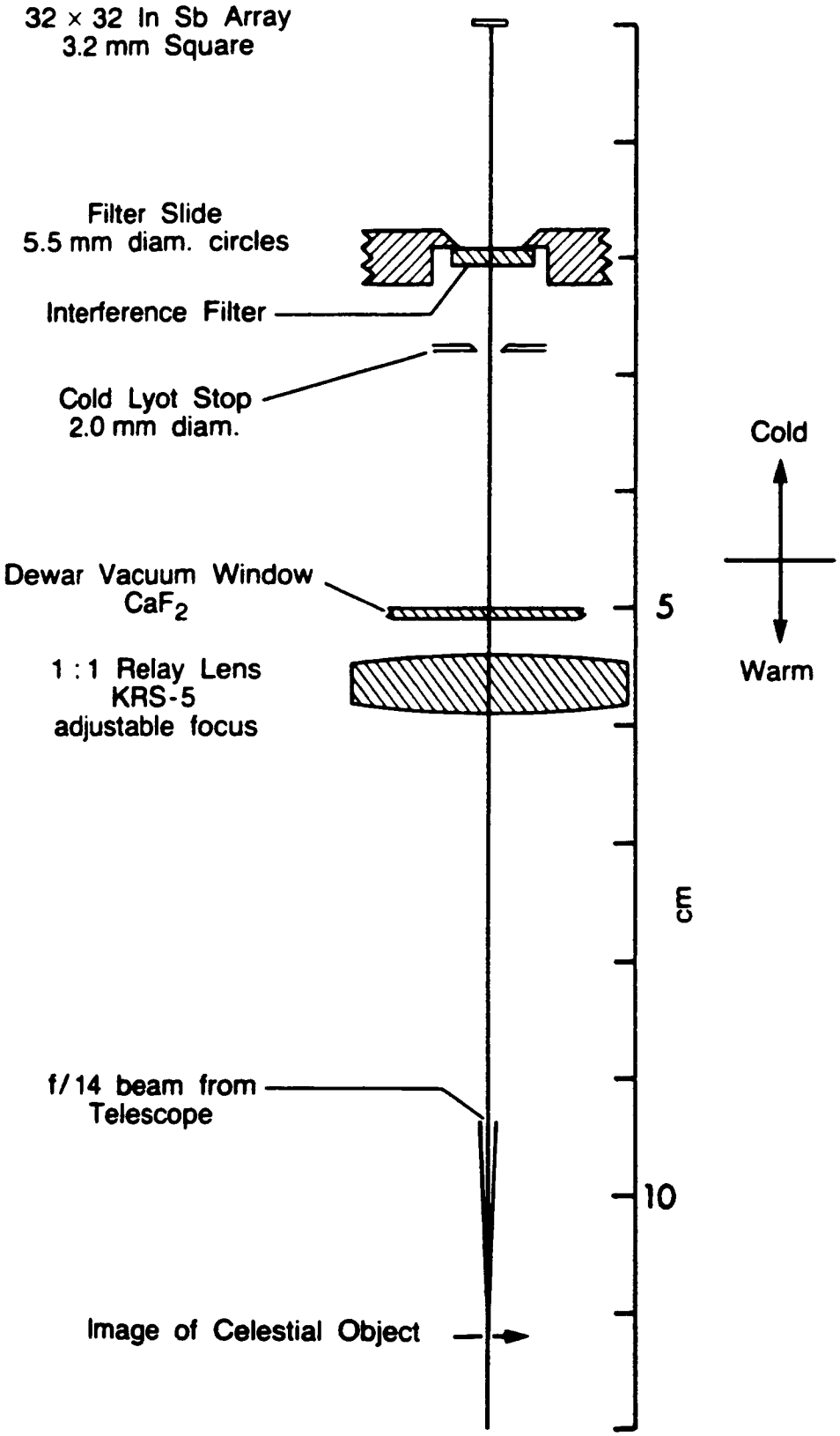

1. Re-imaging optics for the InSb array camera. Shown is the 1:1 mode for operation at f/14 telescopes.

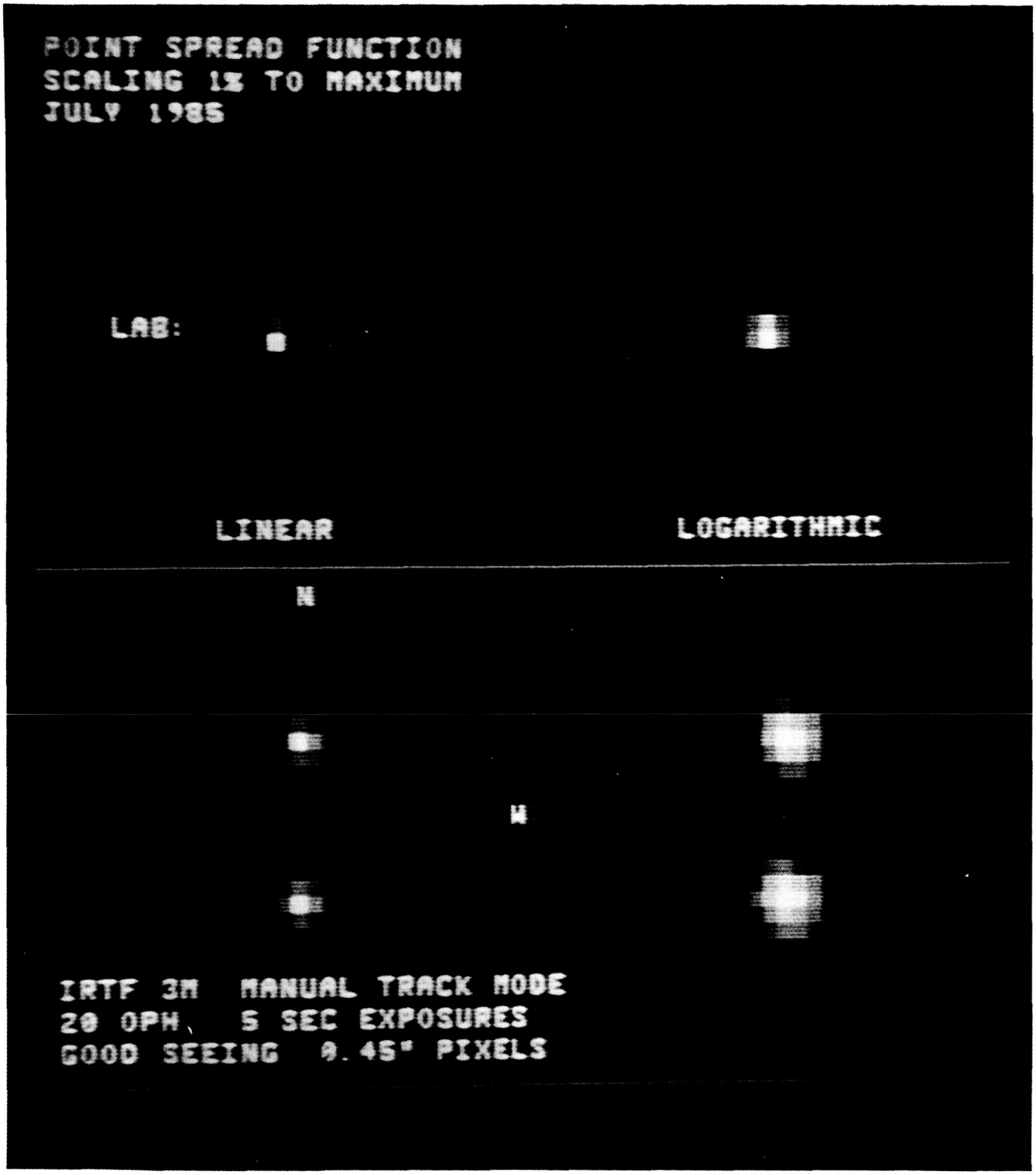

2. 32x32 InSb array image quality attained with re-imaging optics in the 2.5:1 mode for operation at f/35 telescopes. Data obtained during a July 1985 observing run at the IRTF 3m. The image of a laboratory point source is displayed in the upper 2 panels, the logarithmic display accentuates the low level signals. Two images of the star 20 Oph are shown in the lower two panels, illustrating the influence of telescope optics and atmospheric distortion on the image quality. These are the sharpest stellar images we have obtained to date. The pixel size was 0.43" square and the wavelength 2.2 microns (K).

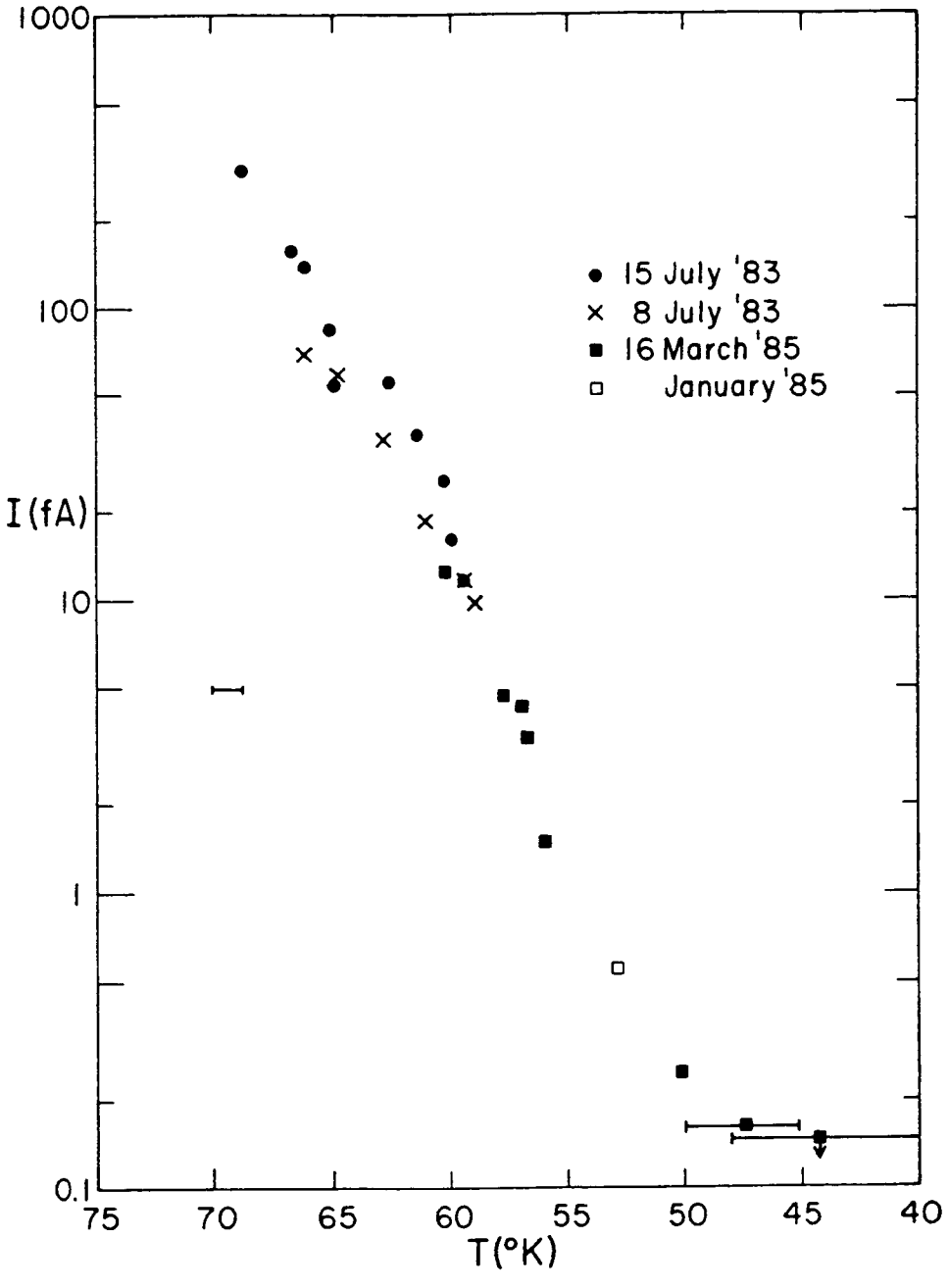

3. Dark current vs. temperature for typical InSb detectors on the 32x32 CCD array. A back-bias of 30 mV was applied to insure good charge injection efficiency. Horizontal error bars represent the range in temperature during a dark current measurement.

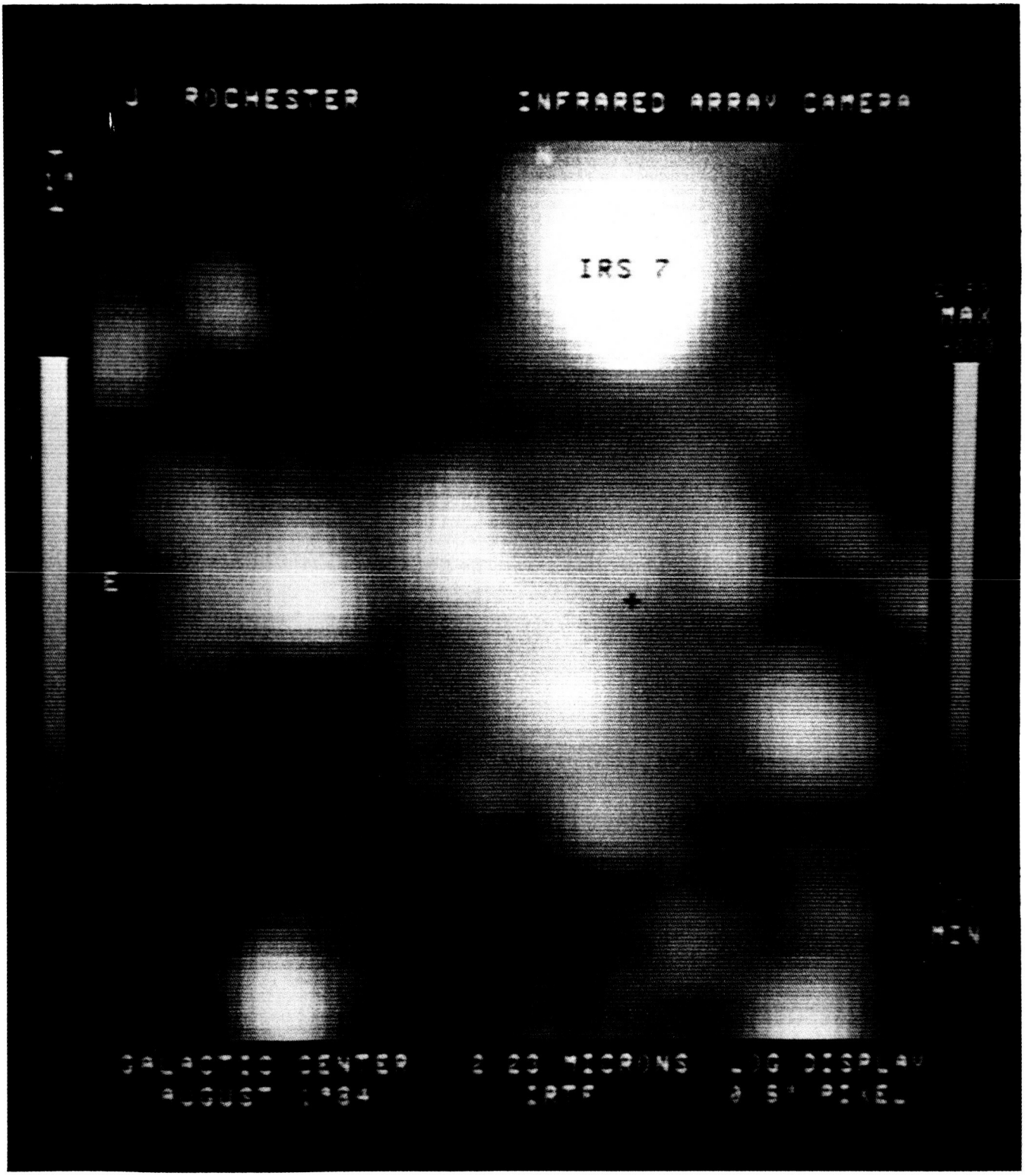

4. The 2.2 micron (K band) image of the galactic center. The region portrayed extends 15.1" N-S and 13.8" E-W. The scaling is logarithmic to display the wide dynamic range of this image. A "+" marks the calculated position of the Sgr A* source.

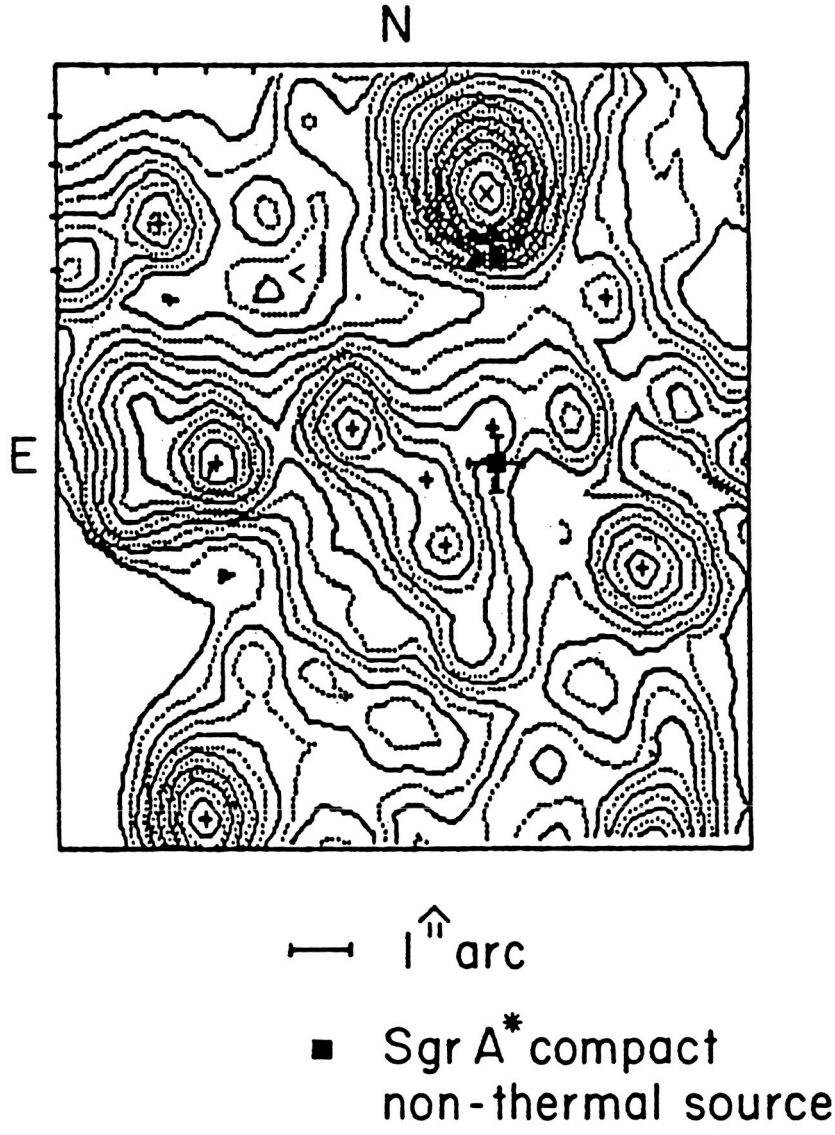

5. A plot of the equal surface brightness contours from the 2.2 micron image of figure 4. Contours are shown every factor of 1.20 (0.2 magnitudes) in surface brightness with every other contour dotted. The display has been rectified to portray the true appearance on the sky with tic marks 1" apart shown in the upper left corner. An "X" marks IRS 7 and +'s mark various 2 micron sources. The filled box represents the calculated position of the Sgr A* compact radio source; the $\pm$0.5" error bars are our estimate of the positional uncertainty.

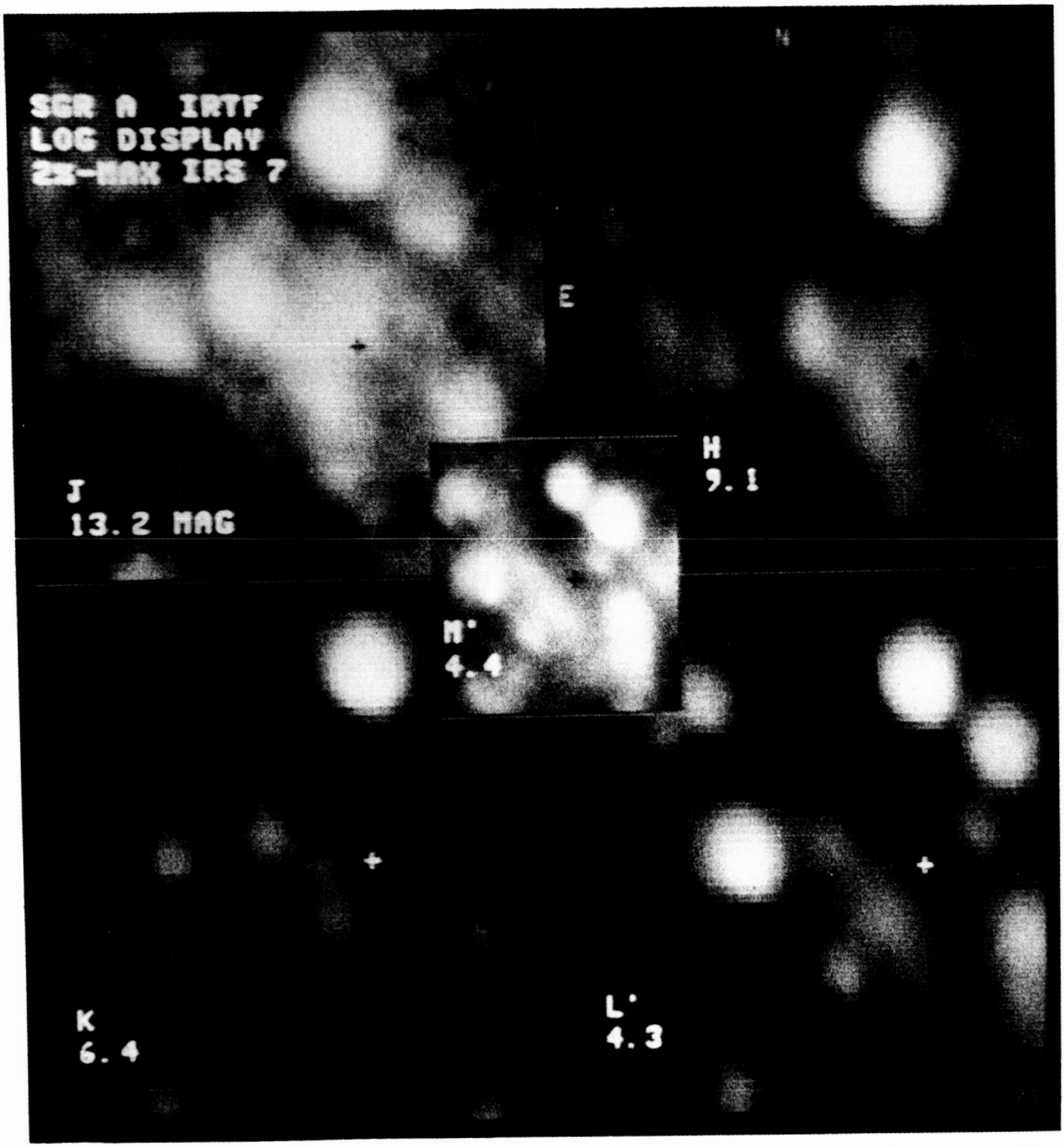

6. 1.23 (J), 2.23 (K), 3.75 (L') and 4.67 (M') micron images of the central regions of the galactic center. The displayed levels are scaled logarithmically from 2% to the peak IRS 7 brightness; the magnitude of IRS 7 is given for reference in each image. A "+" marks the calculated position of Sgr A*. The presence of IRS 3 in the J image may be due to a thermal leak in our J filter.

Table 2

Brightness of the IRS 16 NW Point-Like Object

λ(μm)	Brightness ratio IRS 7/IRS 16 NW	[λ] IRS 16 NW	De-reddened† [λ] IRS 16 NW
1.23	4 ± 1	+ 14.7 mag	7.0
1.65	16 ± 4	+ 12.1	7.4
2.23	28 ± 5	+ 10.0	7.3
3.75	65 ± 15	+ 8.8	7.5
4.67	> 25	> 7.9 ± 0.3	> 7.1

† assuming the extinction law of Becklin et al. (1978)

7. The derived brightness of the IRS 16 NW point-like object from Forrest, Pipher and Stein (1985).

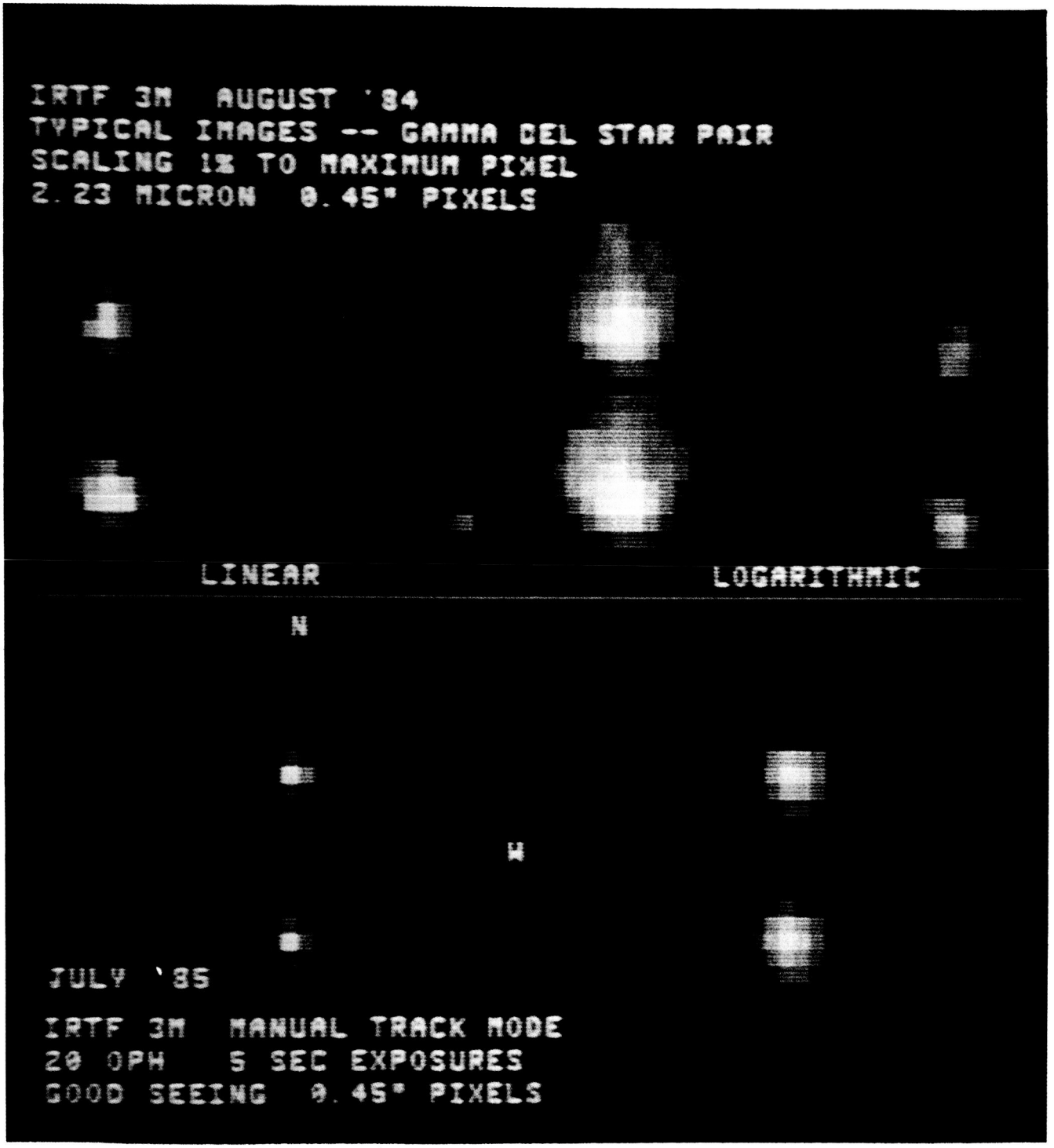

8. Comparison of stellar images from August 1984 and July 1985 IRTF 3m telescope runs. The display scaling is the same as in figure 2. The dramatic improvement in the July 1985 images is due primarily to improved alignment of the IRTF mirrors. Bob Howell of the IRTF staff did much of the alignment work.

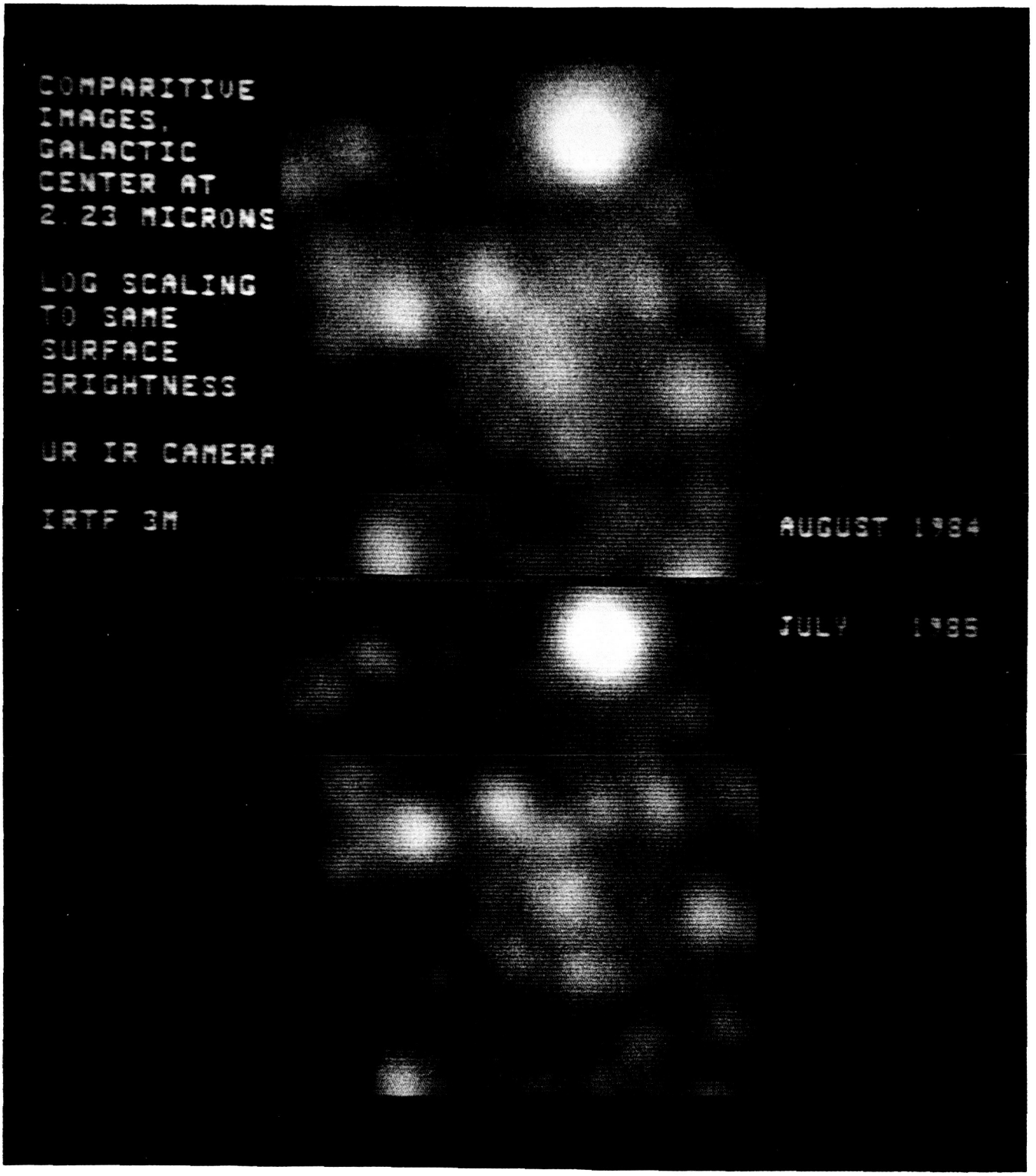

9. Comparison of images of the galactic center in the K band (2.23 microns) from the August 1984 and July 1985 IRTF 3m runs. The improved telescope optics has revealed much new structure in the July 1985 image. Diffuse structure in previous images is resolved into a large number of point-like objects inhabiting this region.

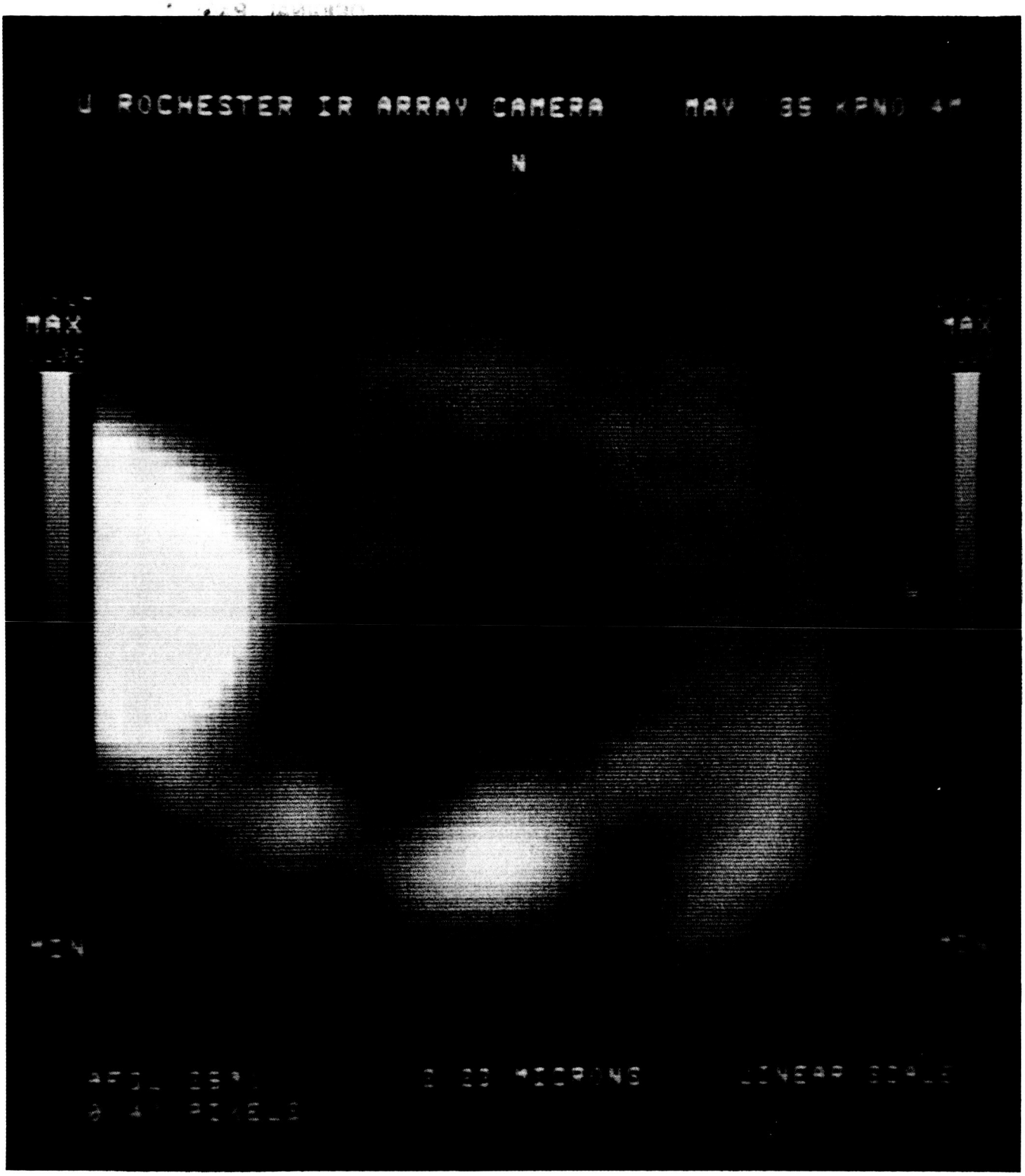

10. The 2.2 micron (K) image of the region around AFGL 2591, also known as U of A 27, from a May 1985 KPNO 4m run. The "protostar" is the bright source at the Eastern edge of the image. The axis of high velocity, bipolar outflow is approximately West by Southwest and the 2 micron polarization E-vector is perpendicular to this flow.

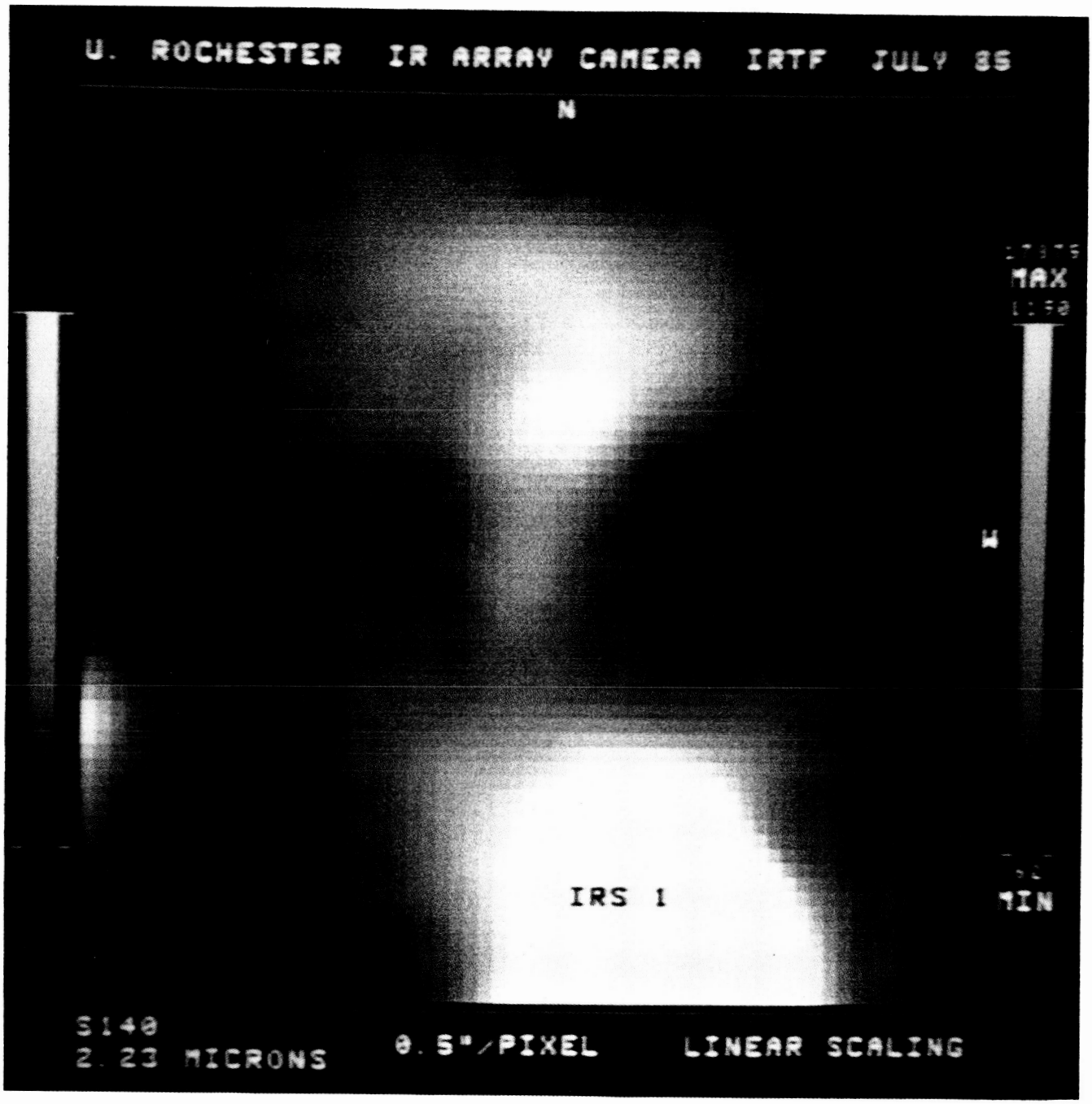

11. The 2.2 micron (K) image of the region around IRS 1 in the Sharpless 140 complex from a July 1985 IRTF 3m run. The young, luminous star is the bright object at the southern edge of the image. The axis of high velocity, bipolar outflow is North-South and the 2 micron polarization E-vector is perpendicular to this flow.

Comparison of SBRC InSb Arrays

	Old	New
Pixels	32x32	58x62
Readout	CCD, sequential	X-Y adressible, non-destructive, switched FET.
Operating Temp.	41-60 K	4-60 K
Pixel Spacing	101 μm	76 μm
Area Filled	80%	90%
Dark Current	1000 e^-/sec @ 45K & 30 mv	TBD
Detector Resistance	$2x10^{14}$ Ω	TBD
Read Noise	<1400 e^- rms	<400 e^-, TBD
Bucket Size	10^7 e^-	10^6 e^-
Quantum Efficiency	0.6-0.65	0.6-0.8, TBD
Sensitive Wavelengths	1.2-5 μm	TBD
Imaging Quality	excellent	TBD
Working Detectors	85-90%	TBD
Pixel-pixel Non-uniformity	<10%, resistance and responsivity	TBD

12. Comparison of the present 32x32 InSb array with CCD readout to the new 58x62 InSb array with switched MOSFET direct readout. Both arrays manufactured by Santa Barbara Research Center.

TABLE 1: TYPICAL BACKGROUNDS IN SPACE

SIRTF Effective Area 4.9×10^3 cm^2, Pixel diameter = $2.4\lambda/D$

Wavelength (μm)	Δλ (μm)	Background (photons/sec)	current (fA)	Theta (arc sec)
2.1	0.6	6.8	1.1×10^{-3}	1.2
3.54	1.1	12.8	2.0×10^{-3}	2.0
4.6	1.4	85.2	1.4×10^{-2}	2.6
12.6	3.8	1.4×10^4	9.9	7.0
26.9	8.1	1.1×10^6	180	15

TABLE 2: ACHIEVABLE BACKGROUNDS IN LABORATORY AND AT TELESCOPE

Laboratory, f/14, 75μm pixels, 300K, Emissivity = 1

Wavelength (μm)	Δλ (μm)	Background (photons/sec)	current (fA)	Source
1.25	0.23	0.03	4.8×10^{-6}	\
1.65	0.32	130	0.02	\ all,
2.23	0.41	10^5	15	> thermal
3.3	0.2	10^7	1.6×10^3	/ emission
12.6	0.1	10^9	1.8×10^5	/

Telescope, f/14, 75 μm pixels

1.25	0.23	300+	0.05+	OH emission
1.65	0.32	3000+	0.5+	OH emission
2.23	0.41	3000*	0.5*	Primarily thermal emission
2.05	0.036	42+	7.0×10^{-3}+	thermal emission
1.35	0.024	3+	4.8×10^{-4}+	Zodiacal scat.
		<30+	<4.8×10^{-3}+	OH emission

+estimated

*measured

13. Photon background levels anticipated for SIRTF compared to backgrounds achieveable in the laboratory and at a ground based telescope. The SIRTF backgrounds are due to the Zodiacal light. At the telescope and in the lab, similar very low backgrounds can be achieved in the 1 to 2 micron region by careful selection of wavelength and spectral bandpass.

DEVELOPMENT OF INSB AND SI:GA ARRAYS FOR ISO CAMERA

F. SIBILLE

Observatoire de Lyon
69230 St. Genis Laval
France

I Introduction

The Infrared Space Observatory (ISO) satellite will contain a 60 cm telescope. The temperature of the mirrors is below 12 K, and the temperature of the 4 instruments at the focal plane is below 8 K.

A 4 faces pyramid mirror feeds each experiment with a 3 arc minute part of the telescope field of view. In principle, only one instrument operates at a time, but parallel operation of 2 instruments on 2 different points is also considered. Each instrument takes a 90° quadrant of the Focal Plane Assembly container : a 60 cm diameter cylinder, 30 cm high, located just below the support of the primary mirror.

The 4 experiments, which will be built with national Space Agency funding, have been selected in June 1985 by ESA :

- Long wavelength spectrometer	ISO-LWS	P.I.	: P. Clegg
- Short wavelength spectrometer	ISO-SWS	"	: T. de Graauw
- Photometer	ISOPHOT	"	: D. Lemke
- Camera	ISOCAM	"	: C. Cesarsky

II ISOCAM

Figure (1) shows the principle of the camera, in its current most complicated version. Cost and technical constraints could introduce some simplifications. The architecture is organized in 2 wavelength channels using 32 x 32 arrays :

- Short wavelength channel (SW) : 3 to 5 microns with an InSb CID
- Long wavelength channel (LW) : 5 to 17 microns with an Si:Ga DRO

The 2 channels have an identical optical layout, with an off-axis field mirror in the focal plane of the telescope, imaging the pupil on a filter, and a lens imaging the focal plane on the array.

Only one channel operates at a time, 2 field mirrors are mounted on a wheel, feeding alternatively the LW or the SW channel.

There are 2 wheels in each channel, the first one holds 15 discrete band-pass filters and a CVF, the second one holds a set of 3 lenses providing field of view per pixel between 3 and 12 arc second.

At the entrance of the camera, a wheel introduce in the beam a set of polarizers, or a mirror feeding in the beam the light from an internal calibration source for flat fielding of the arrays.

III Array for the 3 to 5 microns channel

The SW channel will use a 32 x 32 InSb CID, its characteristics are summarized in Table (1). This array is already developed in France by Société Anonyme des Telecommunications (SAT), samples have been delivered to the Département de Recherche Spatiale of the Observatoire de Paris at Meudon, who is responsible for its integration in ISOCAM.

The ongoing development work at Meudon aims at improving :
- the readout noise, with a reasonable design goal of 500 electrons with one preamplifier per raw.
- the dark current, using optimized bias voltage parameters.
- the heat dissipation, which must be below 10 mW.

IV Array for the 5 to 17 microns channel

For wavelength beyond 5 microns, and for the level of performance requested on ISO, there was no array readily available in Europe. The Laboratoire Infrarouge (LIR) of the Laboratoire d'Electronique et de technologie de l'Informatique (LETI) in Grenoble was ready and equipped for undertaking the development of an array for this purpose, and has signed with CNES a contract for a feasibility study.

The baseline of the study is a 32 x 32 array of Si:Ga photoconductors, hybridized by metal bump technique with a MOSFET DRO array.

The Si:Ga material already produced is satisfactory, providing a peak responsivity of 3 $A.W^{-1}$ between 4 and 10 K.

With the design goal of a 200 electrons readout noise, the first try on the DRO circuit was a success above 30 K, but failed below this temperature. An improved circuit is in a production phase, with results expected for the end of 1985.

For this array, because of the rather large volume of the detectors, radiation environment on the nominal 12 hour orbit of ISO will probably limit the integration time to about 1 second.

TABLE 1 : CHARACTERISTICS OF ARRAYS

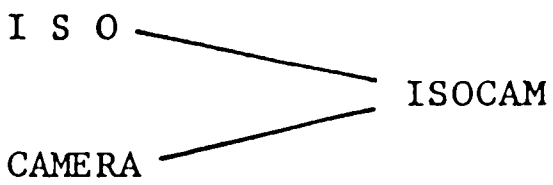

2 CHANNELS :

2 TO 5 μm CHANNEL :

- 32 X 32 InSb CID (SAT)
- 100 X 100 μm^2 Pixels
- Filling factor = 80 %
- Q.E. = 50 % at 4K
- N_e = 1200 elect. (limit : 500)
- Integration up to 100 second

5 TO 17 μm CHANNEL :

- 32 X 32 Si:Ga (LETI-LIR)
- 2 10^{16} Ga cm^{-3}
- R_{peak} = 3 $A.W^{-1}$
- Direct readout MOSFET array
- Metal bump hybrid circuit

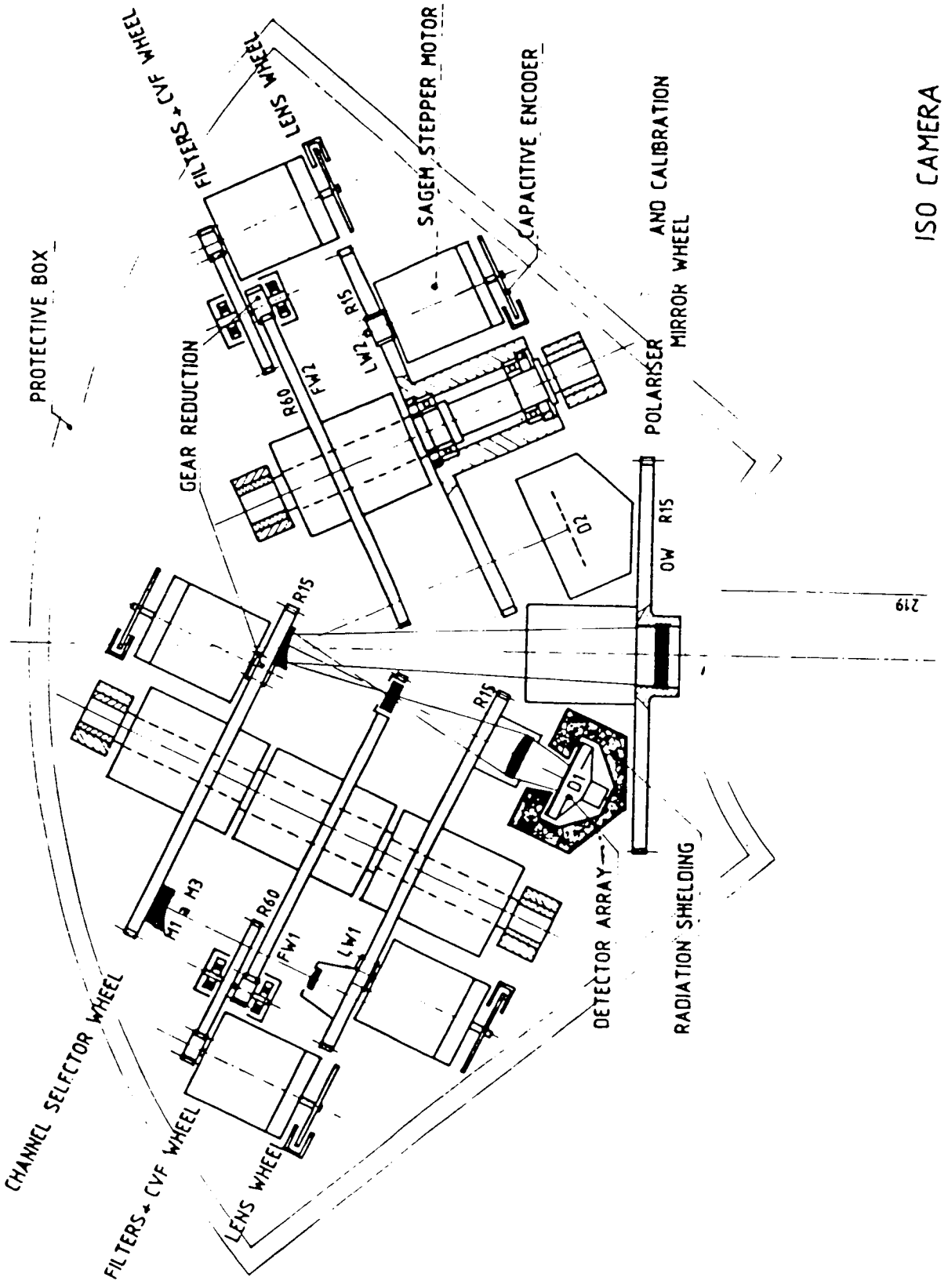

FIGURE 1 : LAYOUT OF ISOCAM (PROVISIONAL)

SIRTF - THE SPACE INFRARED TELESCOPE FACILITY

by

Michael W. Werner, Project Scientist
NASA/Ames Research Center
Moffett Field, CA 94035

SIRTF - THE SPACE INFRARED TELESCOPE FACILITY

1. Introduction and Background

The potential benefits of the advanced infrared detectors discussed elsewhere in the volume can be realized only if they are operated under conditions of very low infrared background. These conditions are provided by a cryogenic telescope in space, for which the infrared background brightness is approximately ten million times lower than the background characteristic of an ambient temperature telescope within (or outside of) the atmosphere. SIRTF - The Space Infrared Telescope Facility - will be a long-lived, cryogenically-cooled observatory for space infrared astronomy. By exploiting the low background of the space environment and utilizing advanced infrared detectors operating at the background limit in this environment, SIRTF will provide gains in sensitivity of one to ten thousand over our current capabilities. SIRTF will provide both tremendous capabilities for the study of known astrophysical problems and great potential for the discovery of new phenomena in the Universe. The scientific and technical rationale for SIRTF, and its capabilites in comparison to those of other infrared telescopes such as IRAS, are discussed in greater detail in References 1 and 2.

SIRTF has been under study by the NASA/Ames Research Center, members of the scientific community, and the aerospace industry for more than a decade, and it has consistently been awarded the highest priority by scientific peer review groups. The SIRTF Science Working Group and the instruments for definition study were selected by NASA in the summer of 1984. Current plans call for initiation of the industrial Phase B studies for the facility in 1987 or 1988, leading to launch in 1994. SIRTF will be an observatory for the entire scientific community, and the bulk of the observing time over SIRTF's lifetime will be used by General Investigators. It will be an essential member of a family of space observatories operating across the electromagnetic spectrum and providing a multi-spectral approach to astrophysical exploration.

2. The Observatory and the Mission

The current design for SIRTF telescope is shown in Figure 1, and the basic performance parameters of the system are given in Table 1 and compared with those of the successful IRAS mission. The SIRTF concept shows direct heritage from IRAS, particularly in the area of cryogenics. The SIRTF cryogen system, using liquid helium as the coolant, maintains the optics and the baffles at temperatures of 10K and below. This will allow SIRTF to achieve natural-background limited performance at wavelengths out to 200um and very high sensitivity out to the long wavelength limit of 700um. The basic optical form is Cassegrainian, with space chopping provided by the secondary mirror. The infrared radiation

is reflected to one of several focal plane instruments arranged circumferentially about the optical axis, while the optical image passes through to a visual star tracker. Mirrors made of fused silica or, possibly, an advanced beryllium fabrication process will permit achievement of diffraction-limited performance at SIRTF's shortest operating wavelength of 2um. The sub-arcsecond pointing stability and accuracy required to exploit this image quality will be achieved by spacecraft body pointing updated by signals from the star tracker within the instrument chamber.

Several options, including use of Multi-Mission Spacecraft (MMS) modules or the use of a co-orbiting platform to be developed as part of NASA's Space Station program, are under consideration for the SIRTF spacecraft. In either case, SIRTF would be carried into space by the Space Shuttle and boosted by the Orbiting Maneuvering Vehicle (OMV) to the final orbital altitude of 900km. The Science Working Group, working together with the SIRTF Study Office at the Ames Research Center, has selected a 28 degree inclination orbit for SIRTF in preference to the polar, sun-synchronous orbit by IRAS. The lifetime for the initial cryogen load will be at least 2 years. Means of resupplying the cryogen in space to permit achievement of an ultimate lifetime of 5 to 10 years are under active study.

3. Focal Plane Instrumentation

Three instruments are under definition study for SIRTF. Their characteristics are outlined in Table 2. Together these instruments cover wavelengths from 2 to 700um and provide the capabilities-photometry, polarimetry, high time resolution, low-to-moderate resolution spectroscopy, and both high spatial resolution and wide-field imaging - required for the study of a wide range of astrophysical problems. Optimizing dectectors to take full advantage of the unique environment provided by SIRTF and other cryogenically-cooled space telescopes presents major technological challenges. Consequently, intensive investigation of detector and cold electronics technology issues will be the main focus of the instrument definition activity over the next year. Contributions elsewhere in this volume provide detailed discussion of the current status of detector development for SIRTF.

4. Current and Future Activities

Over the past year, the Science Working Group and the SIRTF Project have completed an extensive review of the long-life SIRTF mission, which included the choice of the orbit and refinement of the scientific goals and the related mission performance requirements (3). Definition studies for the SIRTF observatory and mission will be continued during the coming year. Particular emphasis will be given to the SIRTF spacecraft; to maintenance and refurbishment issues, including cryogen transfer in space; and to developing baseline plans for mission and science

operations. Work on the telescope system will concentrate on high technology areas such as cryogenics, optics and pointing. Laboratory development and test of protoflight hardware will be supplemented by analytical studies using the extensive system modeling capability now in place at the Ames Research Center. The work on both the instruments and the facility is pointed at advancing the definition of the SIRTF mission in a careful but efficient manner in preparation for the facility Phase B studies, leading to the initiation of the final design and development SIRTF at the end of the decade.

5. Conclusions

These few pages provide only a quick overview of the tremendous amount of work which has been carried out to bring the SIRTF mission to its present state of readiness. Further information is available in the references listed below or from the author of this paper. SIRTF will be a facility for the entire scientific community, and comments and reactions from interested scientists are always welcomed.

6. References

1. "SIRTF - The Next Step," by F. C. Gillett and M. W. Werner, NASA TM #86663, 1984. Reprinted in NASA Conference Publication 2353, "Airborne Astronomy Symposium", eds. H. A. Thronson and E. F. Erickson, 1984.

2. "Infrared Astronomy After IRAS," by G. H. Rieke et al. (accepted by) Science (in press; to appear in 1986).

3. "SIRTF - The Space Infrared Telescope Facility," by M. W. Werner et al. SPIE Paper 589032, presented at November 1985 SPIE conference on "Instrumentation for Optical Remote Sensing from Space," Cannes, France.

TABLE 1. BASELINE SPECIFICATIONS FOR SIRTF
WITH IRAS PERFORMANCE FOR COMPARISON

PARAMETER	SIRTF	IRAS
PRIMARY MIRROR DIAMETER	0.85 M	0.60 M
EFFECTIVE COLLLECTING AREA	0.58 M	0.22 M
WAVELENGTH COVERAGE	1.8 TO 700 MICRONS	8 TO 120 MICRONS
DIFFRACTION-LIMITED PERFORMANCE	2 MICRONS	15 MICRONS
IMAGE DIAMETER	0.6 ARC SEC	6 ARC SEC
POINTING STABILITY	0.15 ARC SEC RMS	2 ARC SEC RMS
FIELD OF VIEW	7 ARC MIN	60 ARC MIN
MODULATION	SECONDARY MIRROR ARTICULATION	TELESCOPE SCANNING
CRYOGEN	SUPERFLUID HELIUM	SUPERFLUID HELIUM
CRYOGEN TEMPERATURE	1.8 K	1.8 K
OPTICS TEMPERATURE	<5 K	<5 K
MODE	OBSERVATORY	SURVEY
LIFETIME	>5 YEARS	10 MONTHS
BROADBAND SENSITIVITY*		
10 MICRONS	0.006 MJY	70 MJY
100 MICRONS	0.1 MJY	300 MJY
ANGULAR RESOLUTION AT 60 MICRONS	18 ARC SEC (DIFFRACTION-LIMITED)	90 ARC SEC (DETECTOR-WIDTH-LIMITED)
SPECTRAL RESOLVING POWER	>1000	20
NUMBER OF DECTECTORS	10,000	60

*SIRTF SENSITIVITY: 1 IN 15 MINUTES
IRAS SENSITIVITY: 1 /SURVEY SCAN

TABLE 2. SIRTF INSTRUMENT COMPLMENT

Instrument	Principal Investigator	Characteristics
Infrared Array Camera (IRAC)	G. Fazio, SAO	Wide-field and diffraction limited imaging, 1.8-30um, using arrays with up to 128 x 128 pixels. Polarimetric capability.
Infrared Spectrometer (IRS)	J. Houck, Cornell	Grating and prism spectometers, 2.5-200um, using detector arrays. Resolving power from 50 to >1000.
Multiband Imaging Photometer (MIPS) for SIRTF	G. Rieke, Arizona	Background-limited imaging and photometry, 3-200um, with pixels sized for optimum sampling of the Airy disk. Broadband photometry 200-700um. Polarimetric capability.

SIRTF TELESCOPE ASSEMBLY

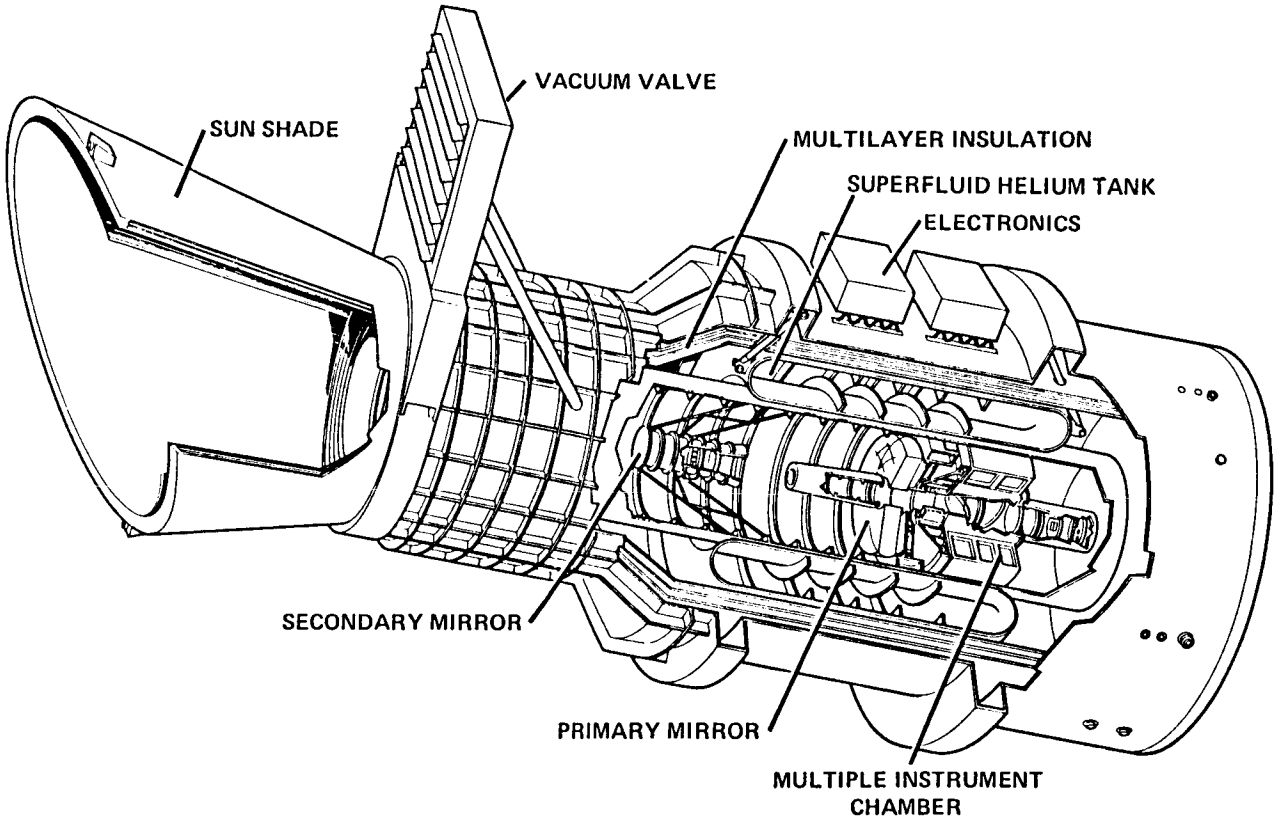

FIGURE 1 - A CUTAWAY VIEW OF THE LONG-LIFE SIRTF TELESCOPE CONCEPT.

N87-13718

The Status of the ISO Project

M.F. Kessler, Space Science Department of ESA, Noordwijk, Netherlands

1. Introduction

The Infrared Space Observatory (ISO), an approved and funded project of the European Space Agency (ESA), will be an astronomical satellite observatory operating at wavelengths from 3μm to 200μm. ISO will provide an environment enabling astronomers to derive maximum benefit from improvements in infrared detector technology.

The original proposal for ISO was submitted to ESA in 1979. After several studies and assessments, a very intensive Phase A study was undertaken in 1982. As is normal within ESA, this was in competition with other studies, and in March 1983, ISO was selected to be the next new start in the ESA Scientific Programme. The present period is being used to select and start development of the scientific focal plane instruments and to prepare the ground for a swift and effective start to the industrial Phase B in 1986 leading to a launch in late 1992.

This paper summarizes briefly the ISO Project and its status. Section 2 deals with the overall goals of mission while the Phase A design is outlined in section 3. The scientific instruments are described in section 4 and current activities in section 5.

2. Overall Mission

The scientific goals of ISO are to make spectroscopic, imaging, photometric and polarimetric measurements of selected celestial sources at a sensitivity approaching the limits set by natural astrophysical backgrounds. More detailed discussion of the astronomical goals of ISO is contained in references 1 and 2. The operations of ISO will be conducted in as near to real time as is possible by a team of scientists and engineers located at the ground segment. The majority of the observing time will be available to the general astronomical community via the submission and selection of proposals; however, some time will be reserved for the groups building the instruments and for the observatory team.

3. Summary of the Phase A Design

The 1800kg ISO satellite is dominated by its Payload Module, essentially a cryostat which contains the telescope and the scientific instruments. The former is a Ritchey-Chretien design with a 60cm diameter primary mirror and an overall focal ratio of 15. It provides a 20 arcmin unvignetted field of view which is distributed to the four focal plane experiments by a pyramid mirror. Temperatures of 2-3K for the germanium detectors, 7K for the other detectors and instruments, and around 10K for the primary mirror are maintained for a period of at least 18 months by a dual openloop hybrid cryogenic system containing 750l of superfluid helium and 750l of liquid hydrogen. Figure 1 depicts the Payload Module in an exploded form together with a view of the Service Module. The latter provides the 3-axis stabilisation and other basic spacecraft services e.g. telemetry, power etc. ISO will be launched by Ariane into a synchronous, 12-hour elliptical orbit.Further details of the Phase A design can be found in reference 2.

4. Focal Plane Instrumentation

A "Call for Experiment and Mission Scientist Proposals" was issued to the European and U.S. scientific communities in July 1984. This led to the approval, in June 1985, of four instruments to be flown. These will be built using national funding by consortia of institutes.

Two instruments provide the satellite's photometric, imaging and polarimetric capabilities. The ISO camera (ISOCAM) consists of two 32x32 element detector arrays operating in the wavelength ranges 3-5μm and 6-17μm. Each channel contains selectable filters (including circular variable filters), changeable fields of view and can give polarisation information. The ISO photometer (ISOPHOT) contains four subsystems: firstly, a multi-band, multi-aperture photopolarimeter for wavelengths of 3-30μm; secondly a longer wavelength (30-200μm) photopolarimeter with imaging capability; thirdly, linear detector arrays for imaging between 2-28μm; and fourthly, a grating spectrometer with a resolution of around 100 for the band 3-16μm.

Infrared Space Observatory

esa

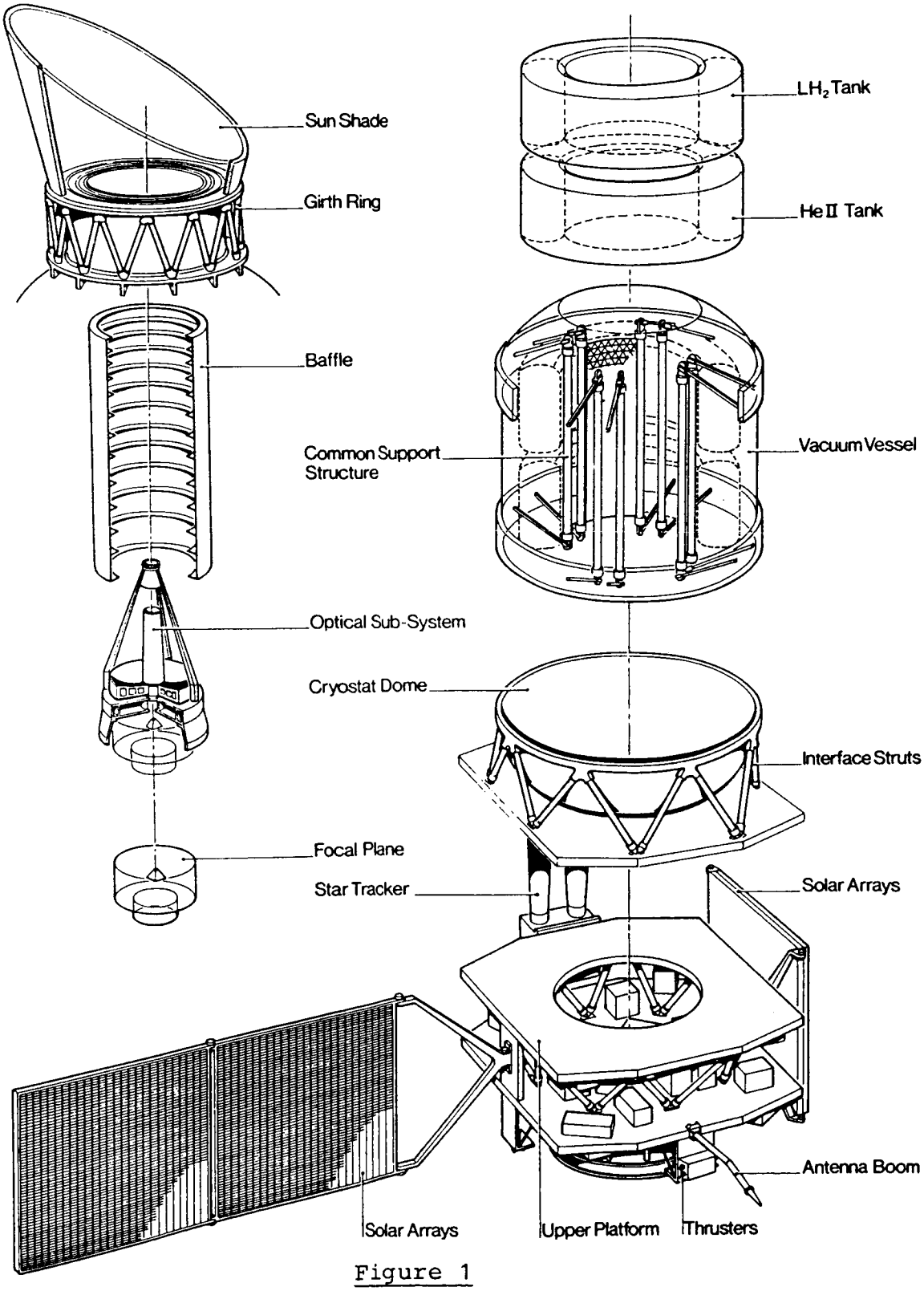

Figure 1

The ISO payload contains two dedicated spectroscopic instruments, the short wavelength spectrometer (SWS, 4-50μm) and the long wavelength spectrometer (LWS, 45-180μm). Both instruments use combinations of grating and Fabry-Pérot (F-P) Interferometers to achieve resolving powers of around 10^4. The F-P's can be removed from the optical train to obtain a lower resolution, which is approximately 200 for the LWS and 1000 for the SWS.

5. Current Activities

The ISO Science Team (Table 1) has been established. It consists of five Mission Scientists, the four instrument Principal Investigators (PI's), the Payload Manager and the Project Scientist.

The role of the Mission Scientists is both to provide scientific input to the project across a broad astrophysical front and also, to represent the interests of the general astronomical community. They were selected competitively following submission of proposals.

Table 1: ISO Science Team

C. CESARSKY, Saclay, F	PI, ISOCAM
P. CLEGG, Queen Mary College London GB	PI, LWS
Th. ENCRENAZ, Obs. de Paris, F	Mission Scientist
W. FRANK, ESA/ESTEC, Noordwijk, NL	Payload Manager
Th. de GRAAUW, Groningen, NL	PI, SWS
H. HABING, Leiden Obs, NL	Mission Scientist
M. HARWIT, Cornell Univ, USA	Mission Scientist
M. KESSLER, ESA/ESTEC, Noordwijk, NL	Project Scientist, Chairman
D. LEMKE, MPIA, Heidelberg, D	PI, ISOPHOT
A. MOORWOOD, ESO, Garching, D	Mission Scientist
J-L PUGET, ENS, Paris, F	Mission Scientist

Design and development activities are continuing in all of the instrument consortia in order to meet the delivery dates of autumn 1987 for a mass/thermal model and end 1988 for the experiment qualification model.

Within ESA, the ISO project team is being built up at ESTEC in Holland under the leadership of the Project Manager, Derek Eaton, and will be virtually complete by the end of 1986. This team is currently discussing with various companies, including Aerospatiale of France who will be the prime contractor, details of the industrial development of ISO. There are also a very large number of studies underway, which are aimed at examining, proving, and improving various technologies and components needed by ISO.

Another area in which the ISO team and industry are actively working is in assessing the implications of the fact that while the Phase A study assumed use of an Ariane II launcher, it is now clear that by 1992 this will have been phased out and replaced by the more powerful Ariane IV. The latter vehicle is easily adequate for the above mission, however it also permits consideration of certain options that were firmly excluded during the previous studies. These options include modifications to the cryogenic system and to the operational orbit. A detailed technical, scientific and financial evaluation of these possibilities is underway.

6. Conclusion

ISO is a fully-approved fully-funded project with a selected complement of focal plane instruments under development. Much preparatory work for an industrial Phase B start in 1986 is already in progress and more will be undertaken. Thus, the astronomical community can look forward to the availability in 1992 of a highly sensitive and versatile Infrared Space Observatory.

7. References

1. Proceedings of the ISO Science Workshop, Alpbach. Eds C.J. Cesarsky and Th. de Graauw. (Copies available from Th. de Graauw, Groningen Space Research Laboratory, Postbus 800, 9700 AV Groningen, The Netherlands)
2. Infrared Space Observatory. ESA Report on the Phase A Study. November 1982. project (page)t SCI(82)6. (Copies available from Martin F. Kessler, Space Science Department ESA, European Space Research and Technology Centre, Postbus 299, 2200 AG Noordwijk, The Netherlands)

SHORTWAVE PHOTOVOLTAIC HgCdTe DETECTOR ARRAYS FOR SPACE ASTRONOMY*

A. Sood, N. Hartle, J. Marciniec, and P. Zimmermann

Honeywell Electro-Optics Division, Lexington, MA 02173

OUTLINE

Program objectives

Theoretical considerations

Detector array configuration

Summary/conclusions

*This work has been supported by NASA contract NASW 3688. Technical Monitor: Dr. Nancy Boggess.

Program Objectives

Fabricate short wavelength photovoltaic HgCdTe detector arrays in a mosaic configuration.

Test and analyze the current-limiting mechanisms in PV-HgCdTe detector for operation between 300-77°K.

Deliver HgCdTe arrays to the University of Hawaii (Dr. Don Hall) for low temperature and low background characterization.

Theoretical Considerations

Total current $I_t = I_{diff} + I_{g.r.} + I_{tunneling}$

$$I_{diff} = \frac{kT\mu_e n_i^2 A}{L_e N_A}(e^{qV/kT} - 1)F_{3D}$$

$$I_{g.r.} = \frac{n_i W_o P kT}{V_{bi}}(e^{qV/kT} - 1)s_o f(b)$$

$$R_o = (\partial I/\partial V)^{-1}]_{V=0}$$

Temperature Dependence of R_o of a SW HgCdTe Photodiode Calculated for Various Surface Recombination Velocities

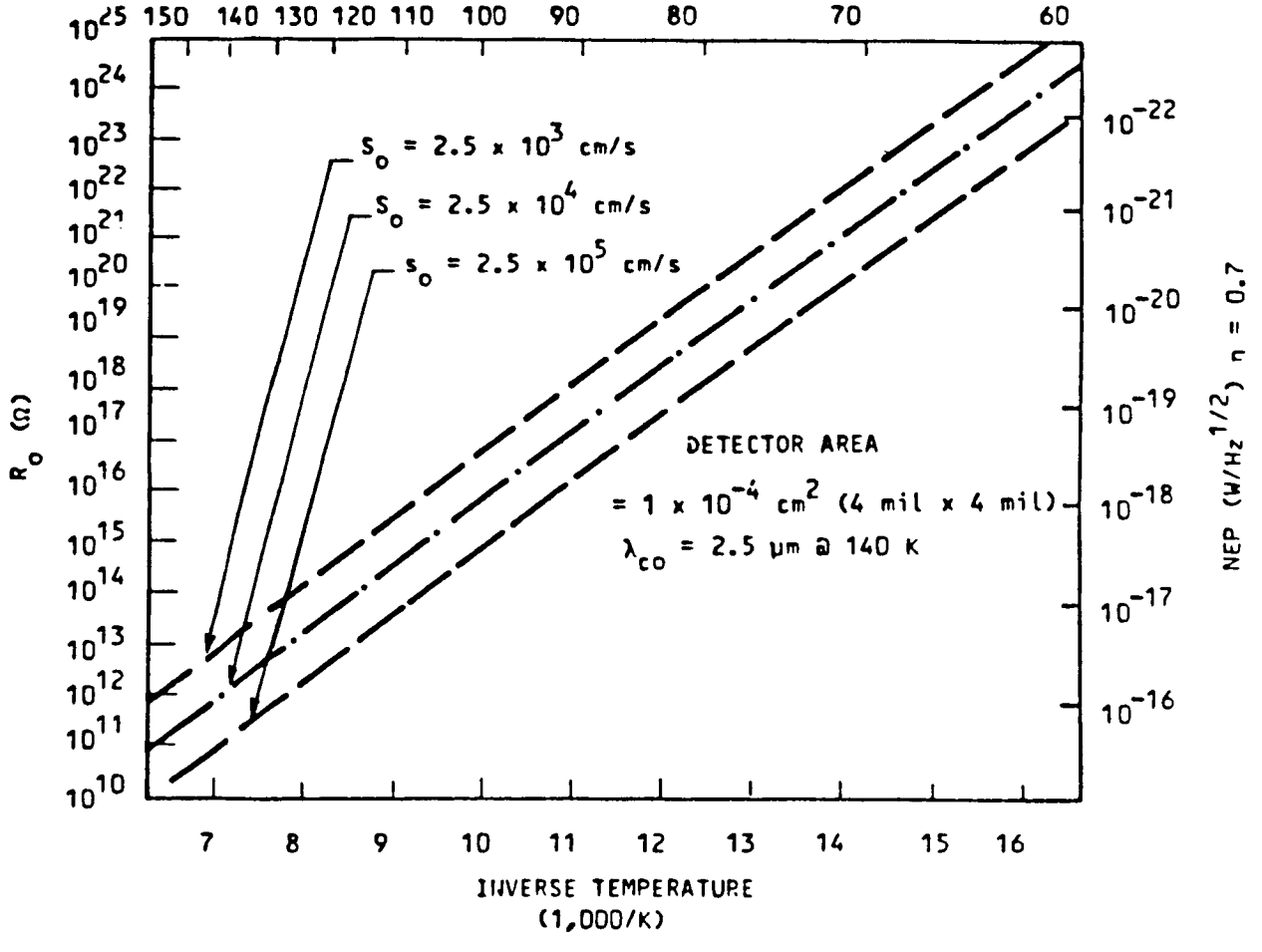

Calculated R_o vs Cutoff Wavelength at 120°K for Various Surface Recombination Velocities

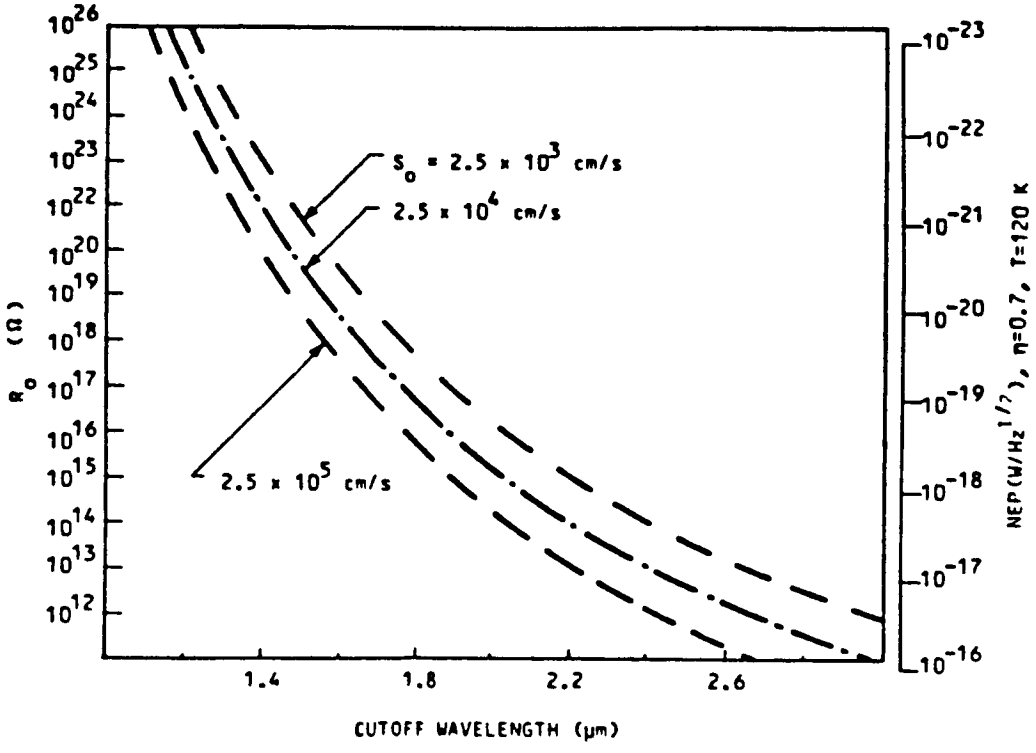

Simplified Detector Fabrication Outline

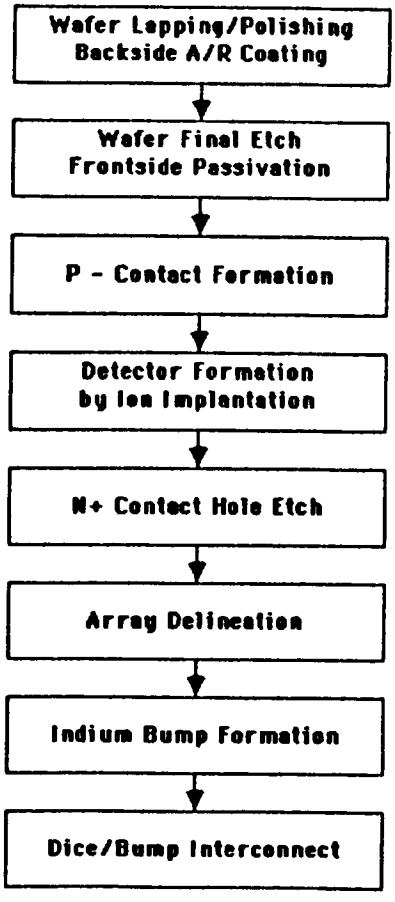

Detector Array

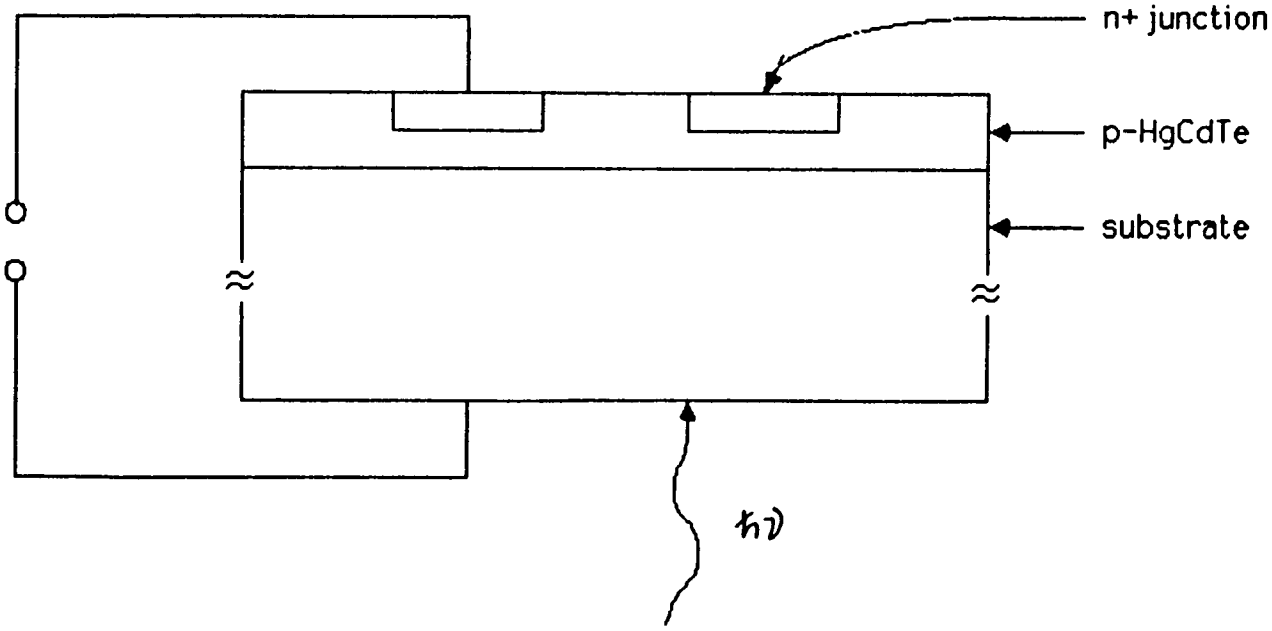

Mosaic Array Average R_0A Temperature Dependence Shows G-R Limited Performance

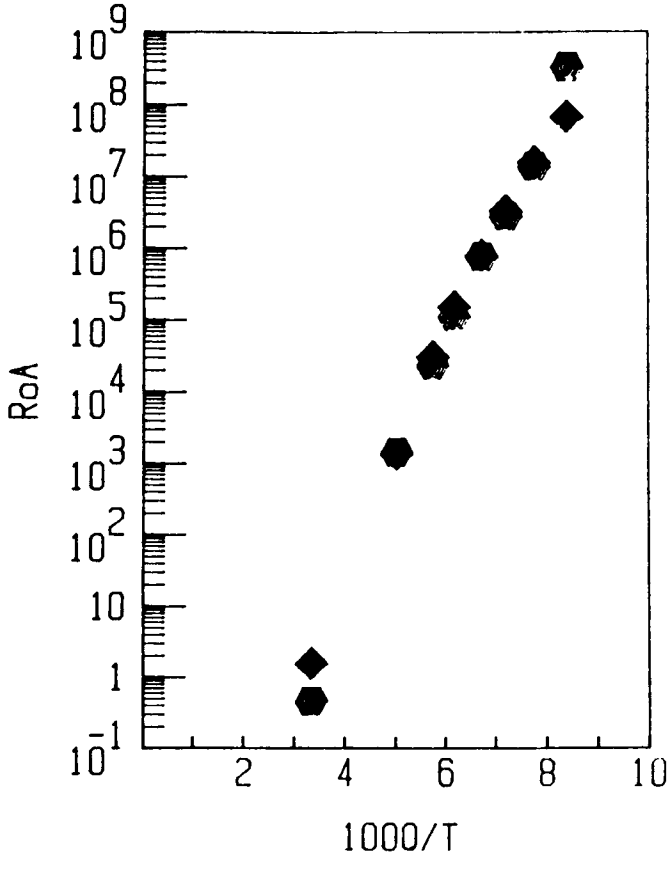

Temperature Dependent R_o Data Shows Device Performance Limited by Surface GR Currents at Moderate Temperatures

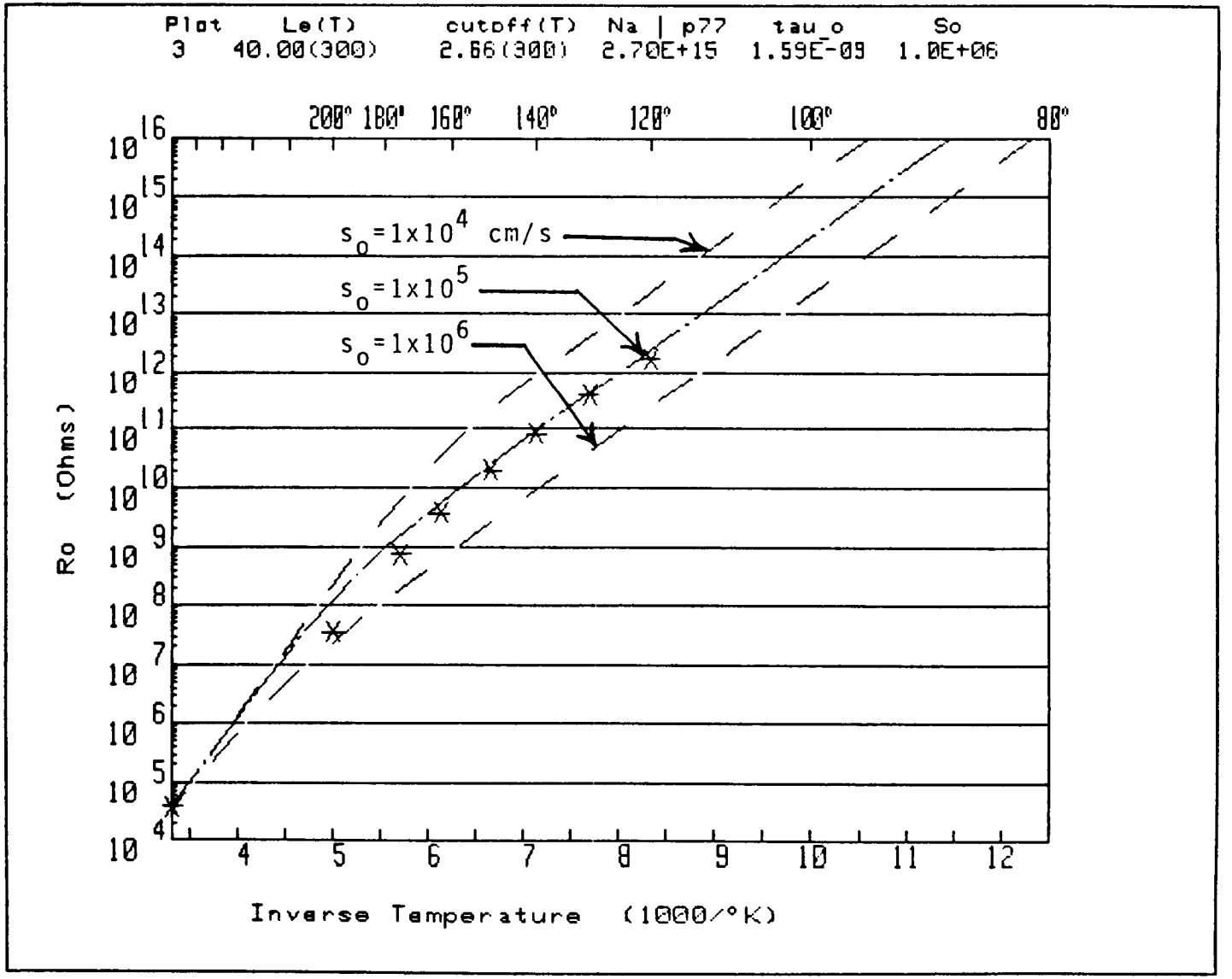

HgCdTe Diodes Provide Uniform Quantum Efficiency With Sharp Cut-offs

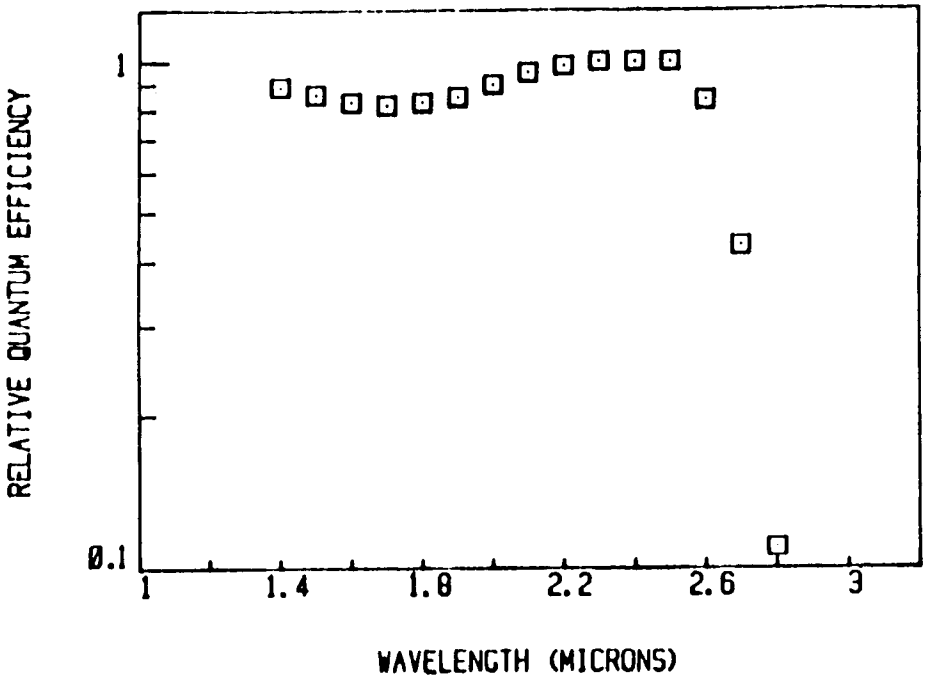

Device Linearity Over 5 Orders of Magnitude

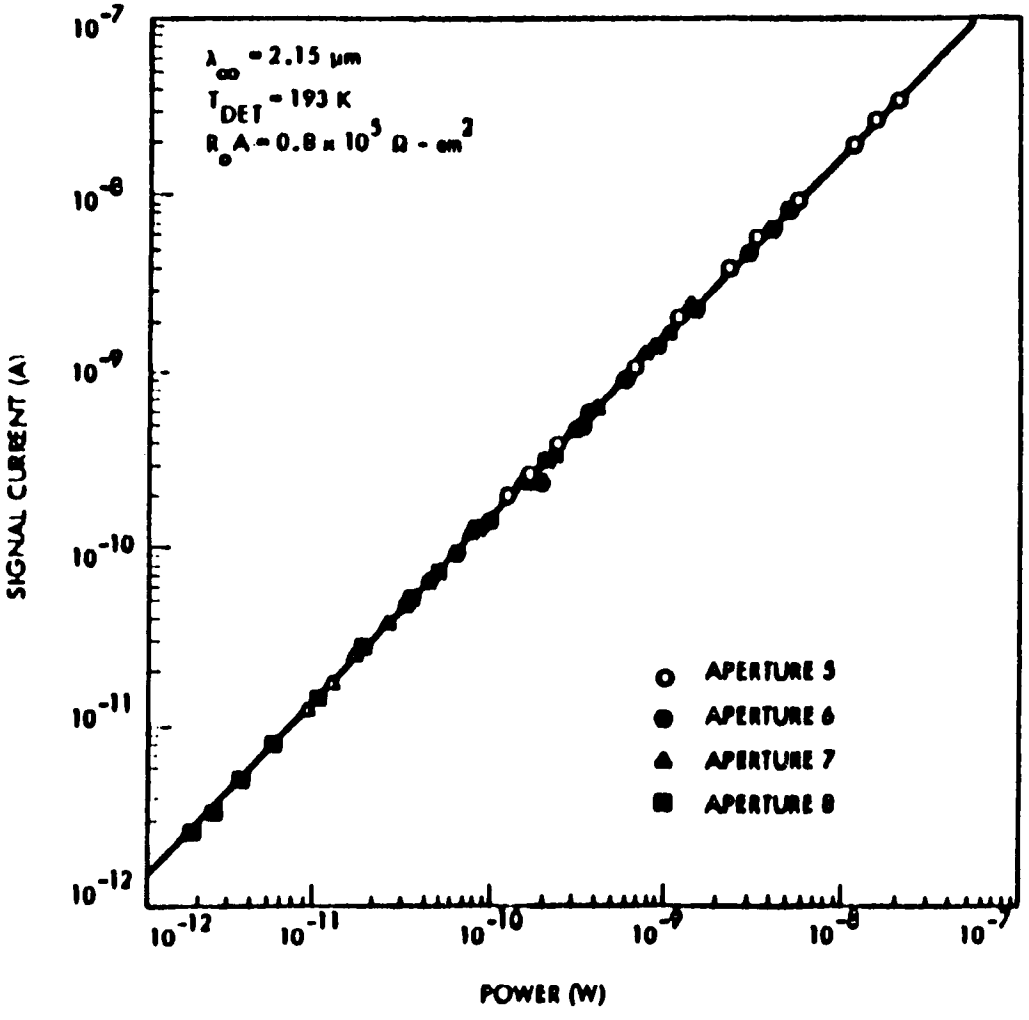

No 1/f Noise at Zero Bias

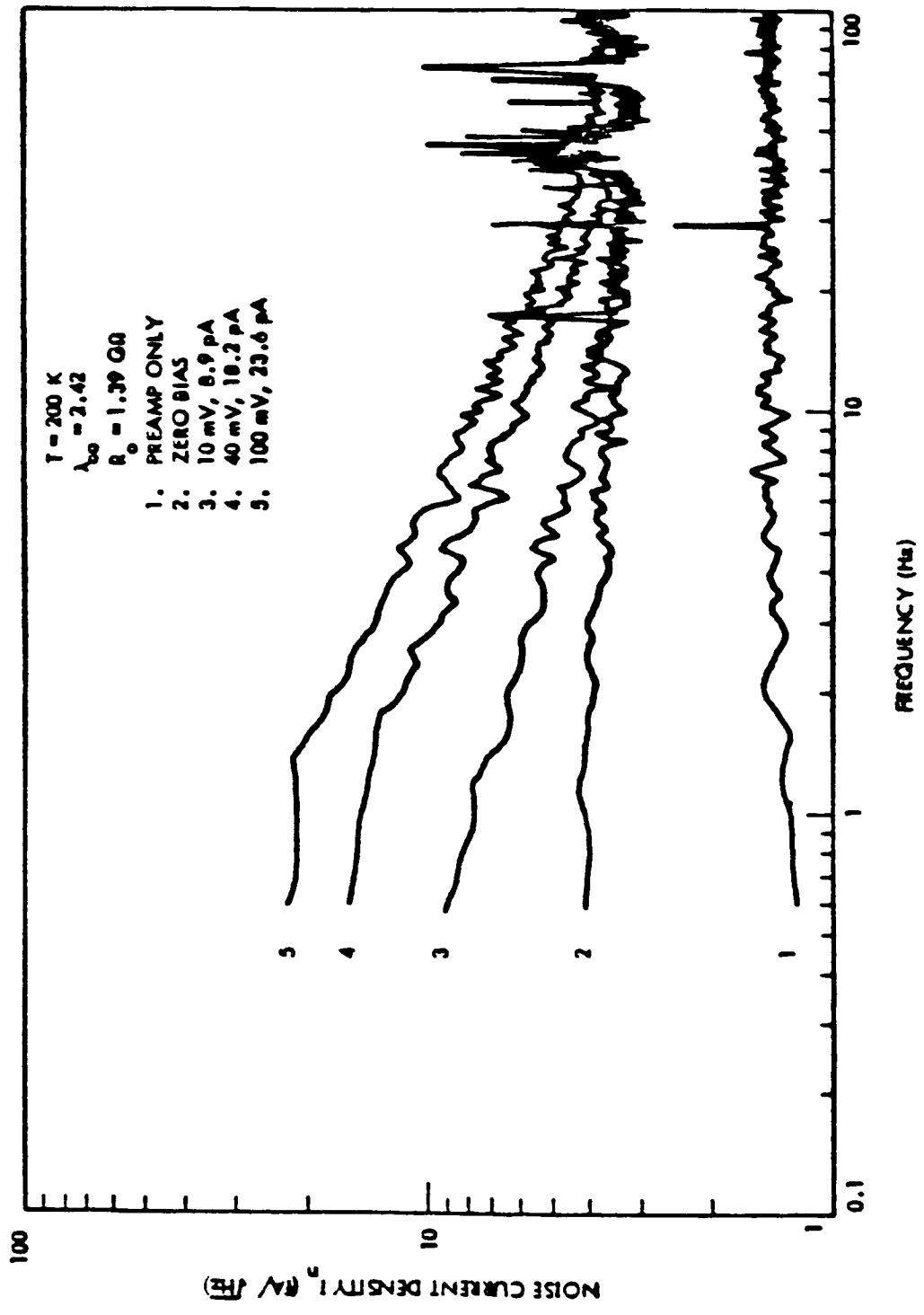

R_oA Histogram Shows Excellent Device Performance Uniformity on Short Wave HgCdTe

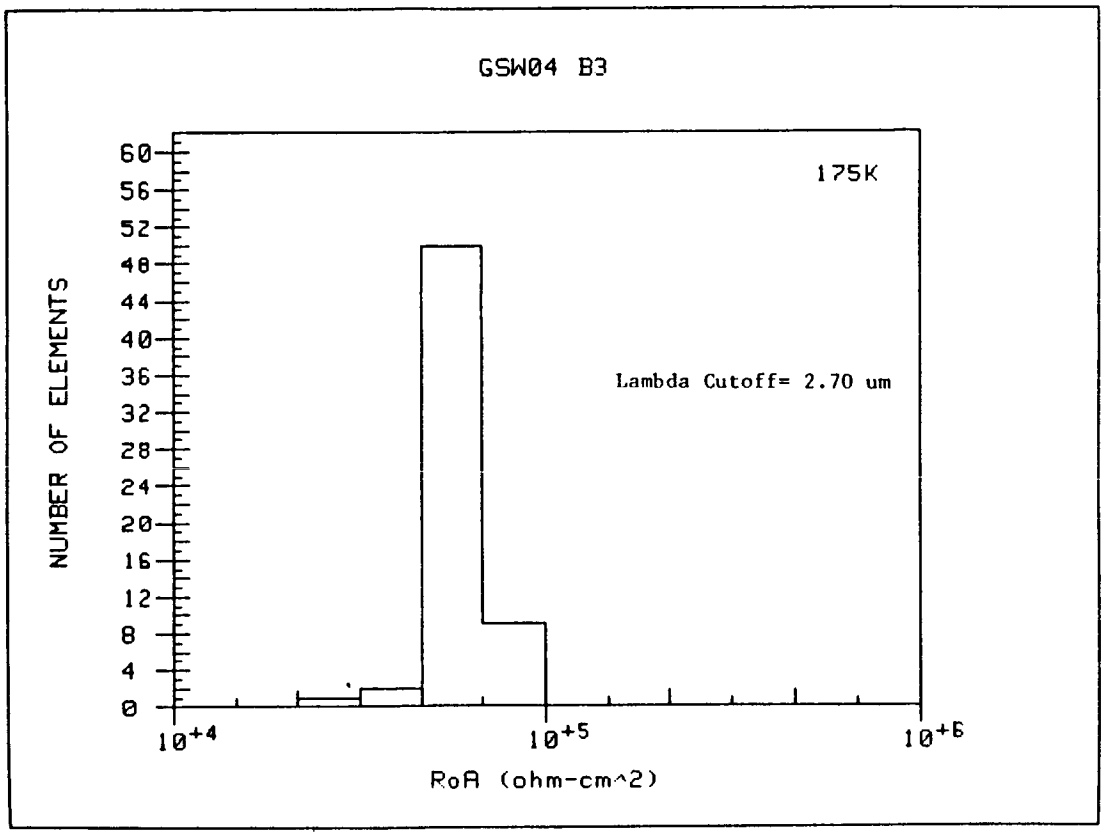

High Uniform Quantum Efficiencies Are Obtained on Short Wave HgCdTe Photodiodes

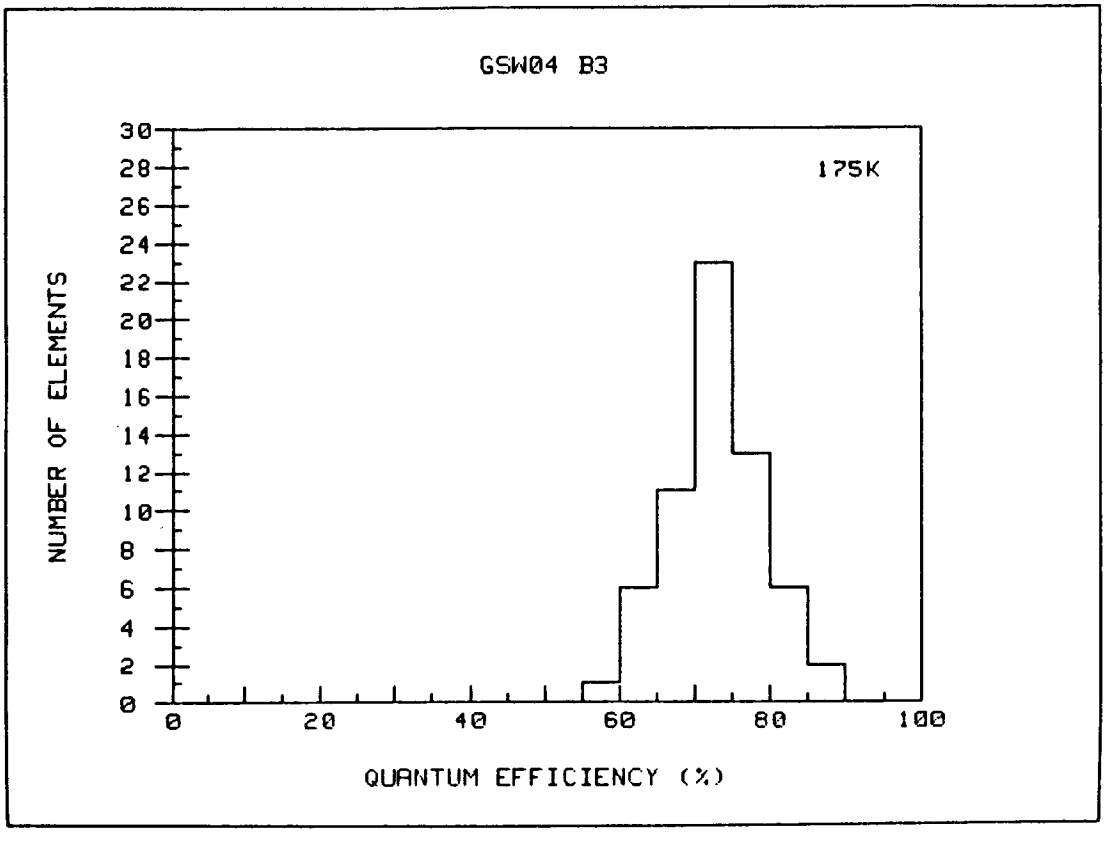

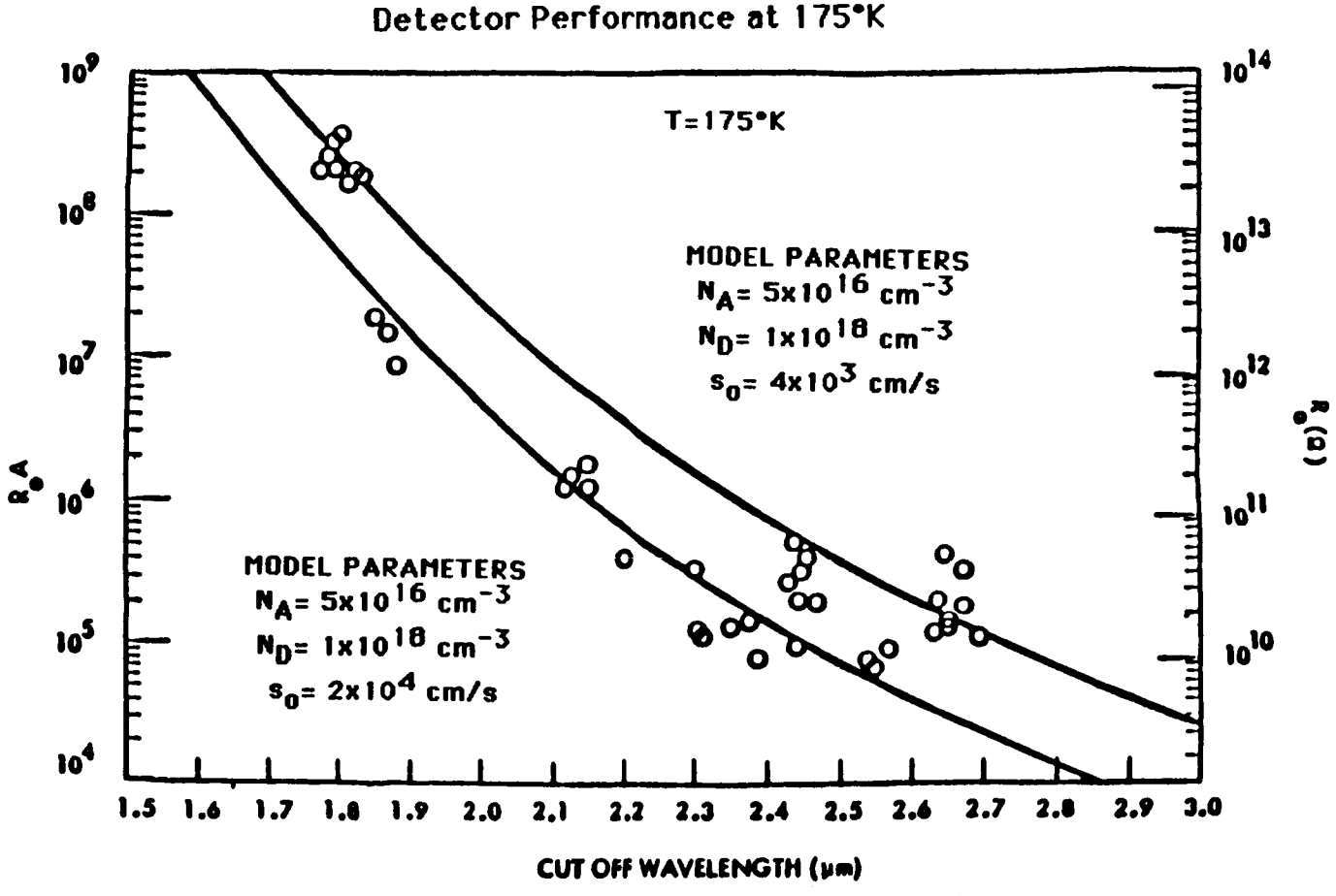
Detector Performance at 175°K
T=175°K
MODEL PARAMETERS
$N_A = 5x10^{16}$ cm^{-3}
$N_D = 1x10^{18}$ cm^{-3}
$s_0 = 4x10^3$ cm/s
MODEL PARAMETERS
$N_A = 5x10^{16}$ cm^{-3}
$N_D = 1x10^{18}$ cm^{-3}
$s_0 = 2x10^4$ cm/s
α_{λ_c}
$R_{\lambda_c}(\Omega)$
CUT OFF WAVELENGTH (μm)

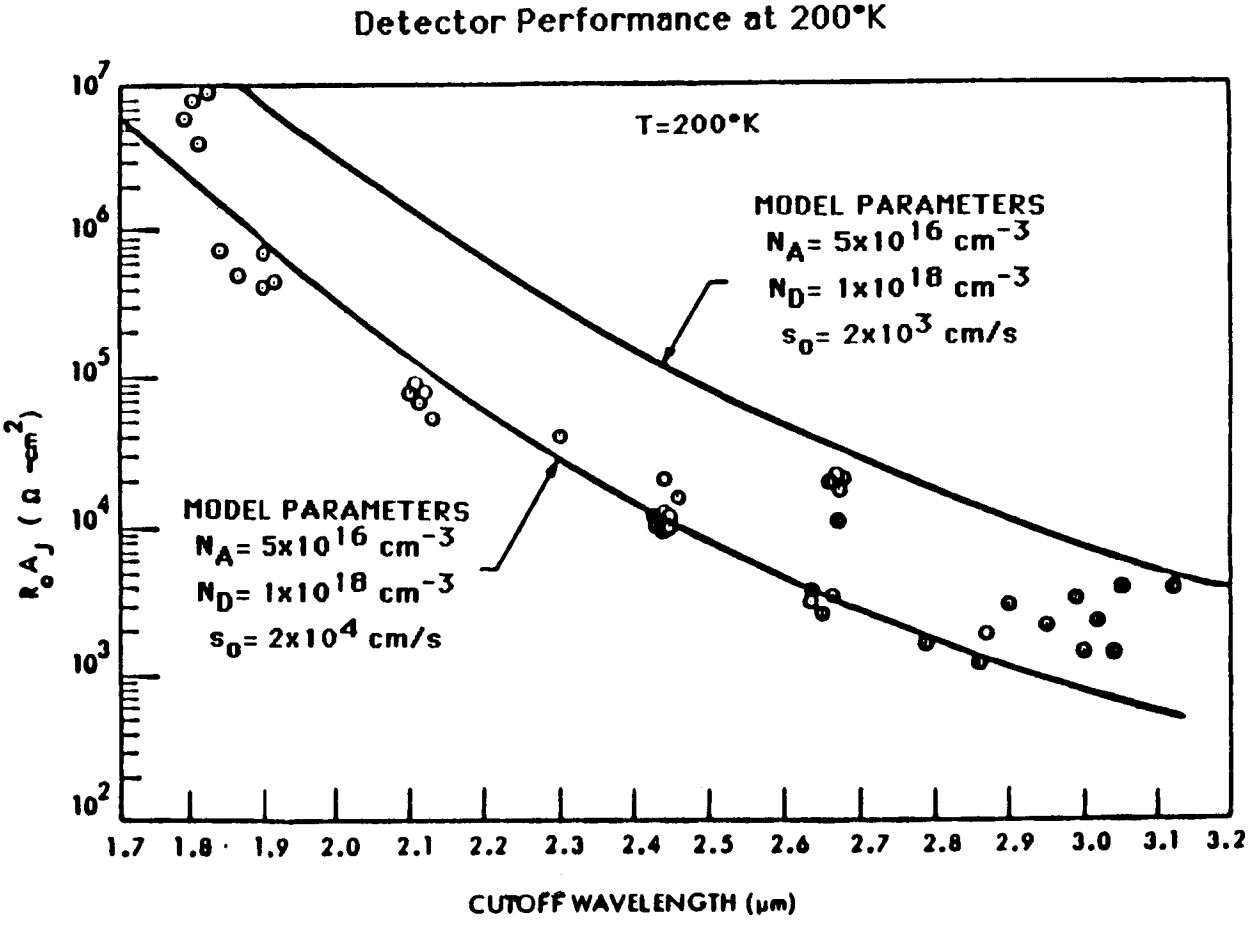
Detector Performance at 200°K
T=200°K
MODEL PARAMETERS
N_A= 5x10^{16} cm^{-3}
N_D= 1x10^{18} cm^{-3}
s_0= 2x10^3 cm/s
MODEL PARAMETERS
N_A= 5x10^{16} cm^{-3}
N_D= 1x10^{18} cm^{-3}
s_0= 2x10^4 cm/s
R_0A_J (Ω-cm^2)
10^7
10^6
10^5
10^4
10^3
10^2
1.7 1.8 1.9 2.0 2.1 2.2 2.3 2.4 2.5 2.6 2.7 2.8 2.9 3.0 3.1 3.2
CUTOFF WAVELENGTH (μm)

Conclusions

(1) Photovoltaic HgCdTe array technology offers a viable detector for space astronomy applications.

(2) Mosaic HgCdTe arrays show excellent performance uniformity and high quantum efficiencies at moderate temperatures (200-120°K). Measurements are underway at University of Hawaii to evaluate these arrays at low temperatures.

(3) Detector performance at moderate temperatures is limited by generation-recombination currents and at lower temperatures tunneling currents are expected to dominate the device performance.

(4) Further performance improvements will require modified device designs which incorporate techniques for reducing tunneling currents via multilayer structures.

Characterization of 2.5 μm HgCdTe Detectors for Low-Background Applications

D. L. DePoy and D. N. B. Hall

University of Hawaii, Institute for Astronomy
2680 Woodlawn Drive, Honolulu, HI 96822

I. INTRODUCTION

Short wavelength (1-3 μm) infrared detector systems currently in use at ground-based telescopes are inadequate for background-limited performance from space. Additionally, the usually single-channel devices seriously compromise the efficiency of any scientific program where the objectives include observations of a large area of the sky with high angular resolution. Therefore, sensitive array detectors and associated low-noise multiplexers are necessary for use in space-based infrared astronomical systems.

We have undertaken a program of testing aimed at the evaluation of systems that have the potential to provide the level of performance required for use in space-based instruments and to appraise their usefulness to astronomy overall. Here we report the results of the first phase of the program to characterize selected pixels of a HgCdTe photovoltaic array detector; no multiplexer devices were tested in this phase of the program. The array was obtained through a collaborative effort with Honeywell's Electro-Optics Division (see Sood in these proceedings), and our tests were specifically aimed at extending Honeywell's device characterization at higher temperatures into the 77-120 K regime of operating temperatures.

The array was composed of 2.6-μm-cutoff wavelength HgCdTe photodiodes in an 8x64 pixel format. Each element had an active area of 100x100 μm (10^{-4} cm^2). Within a single row, 32 alternate elements were bump bonded to a fan out board to which the readout electronics were connected. Each pixel was tested individually as though it were a discrete detector, and therefore the results should be representative of the entire array.

II. TEST PROGRAM GOALS

The primary goal of the current investigation was to determine the typical current versus bias voltage ("diode curve" or "I-V curve") characteristics of the array

diodes as a function of temperature. The two important device parameters to be determined from this data are (1) the zero bias impedance, which should be $>10^{15}$ Ω, and (2) the dark current, which should be $<<10^{17}$ amps. From these two parameters the limiting sensitivity of the detectors in the absence of other noise sources can be predicted.

The Honeywell measurements are at temperatures above 120 K. We have concentrated on extending the characterization to lower temperatures, between 77 and 120 K. In this way our measurements around 120 K could be compared to verify consistency while the lower temperature data is used to investigate the transition of the detectors from theoretical diode behavior to other limitations (e.g., tunneling, surface leakage).

III. TEST SETUP AND PROCEDURES

The devices were tested using a MOSFET front-end amplifier, shown in Figure 1, to integrate the diode current onto a capacitor in parallel with the detector. Standard resistive feedback transimpedance amplifiers are inadequate to measure the currents through the high impedances anticipated.

A Siliconix p-channel enhancement-mode MFE 823 MOSFET was used as the input stage because of its extremely low leakage currents at the temperatures at which the tests were conducted (80-120 K). Measurements made with no detector installed gave a system leakage current of 45 ± 50 e^-/s. We found that 2N6484 JFETs (from National Semiconductor and Intersil) have much higher leakage at these temperatures, on the order of 500 e^-/s. The gain from the MOSFET was 0.78 over the operating voltage range. A three op-amp instrumentation amplifier (CMRR trimmed to 125 dB) followed with a gain of 1.2, giving a system gain to the output voltage of 0.94.

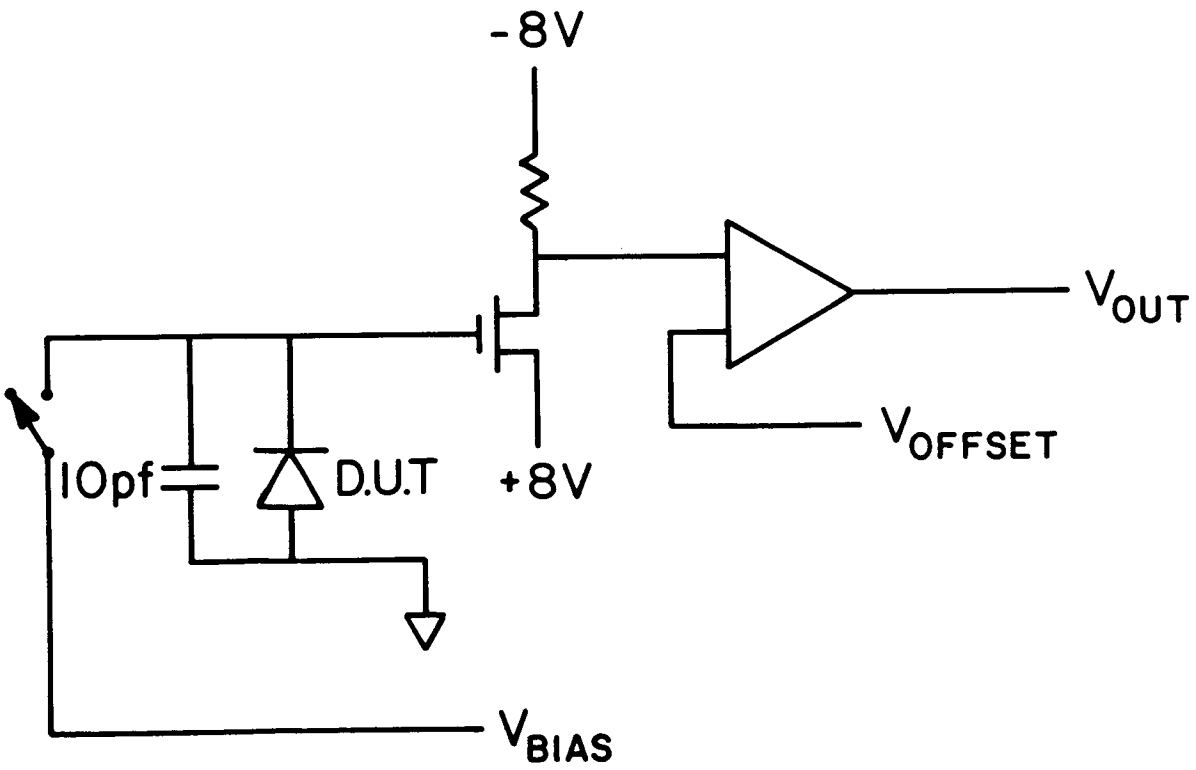

Figure 1: Circuit schematic of the preamp used in the HgCdTe characterization tests.

There were several reasons to use a 10 pf capacitor in parallel with the detector to measure the induced currents rather than integrate on the detector capacitance or on the gate capacitance of the MOSFET. Since 10 pf was substantially larger than the capacitance of any detector, MOSFET gate, or contact point, there was no need to redetermine the integrating capacitance for each measurement to find the absolute calibration of output voltage to current. Also, the capacitance of the diodes, and perhaps the MOSFET gates, changes with bias voltage applied, so relying on them to integrate the current adds another level of uncertainty in finding the absolute current. Additionally, the Ag-Mica capacitors used were carefully measured over the operating temperatures for stability and linearity, and hence could be relied on to give valid results.

The general procedure for measuring the diode current as a function of bias voltage was to (1) set the temperature with a feedback controlled 225 mW heater (temperature control stable to approximately 1 K at 80 K and approximately 2 K at 120 K), (2) apply the appropriate bias voltage through a mechanical switch, (3) open the switch and monitor the output voltage's change with time. Then the current can be found from

$$I = C\ (dV/dt)/g, \qquad (1)$$

where I is the current being integrated on the capacitor, C is the capacitance of the parallel capacitor (= 10^{-11} f), V is the output voltage, g is the gain, and t is the time that has elapsed.

IV. RESULTS

A. Impedance Measurements

The first tests were made by putting 10 mV of reverse bias across the HgCdTe diodes and integrating until the output was 0 volts. By recording the time elapsed, the average current over this bias range could be found with equation 1. If we assume that the diodes have approximately ohmic behavior around zero bias and that the diode current will be 0 amps at a bias voltage of 0 volts, then these measurements can be converted to effective device impedances via

$$R = (\partial I/\partial V)^{-1}\big|_{V\,=\,0}$$

where ∂I is the change in the current (= the current measured since we assume that I = 0 at V = 0) and ∂V is the change in the output voltage (= 10 mV). As will be seen below, the assumption that the diodes behave ohmically is correct, while the assumption that I = 0 at V = 0 is very poor; this consequently leads to a systematic underestimation of the diode impedances by roughly a factor of 5 at all temperatures since the I-V curve passes through zero bias at a substantial negative current, thus making the slope of the diode curve flatter than if it went through the origin. Therefore, a correction factor of 5 will be assumed and applied to all the data presented here.

The tests were done at 80, 90, 100, 110, and 120 K on 11 detectors. Figure 2 shows the average impedances determined versus temperature and corrected by factor 5 along with the higher temperature Honeywell data (see Sood in these proceedings). The two data sets join well at the common temperature point of 120 K. The transition from theoretical diode behavior occurs at approximately 100 K at an impedance of about 5 x 10^{14} Ω.

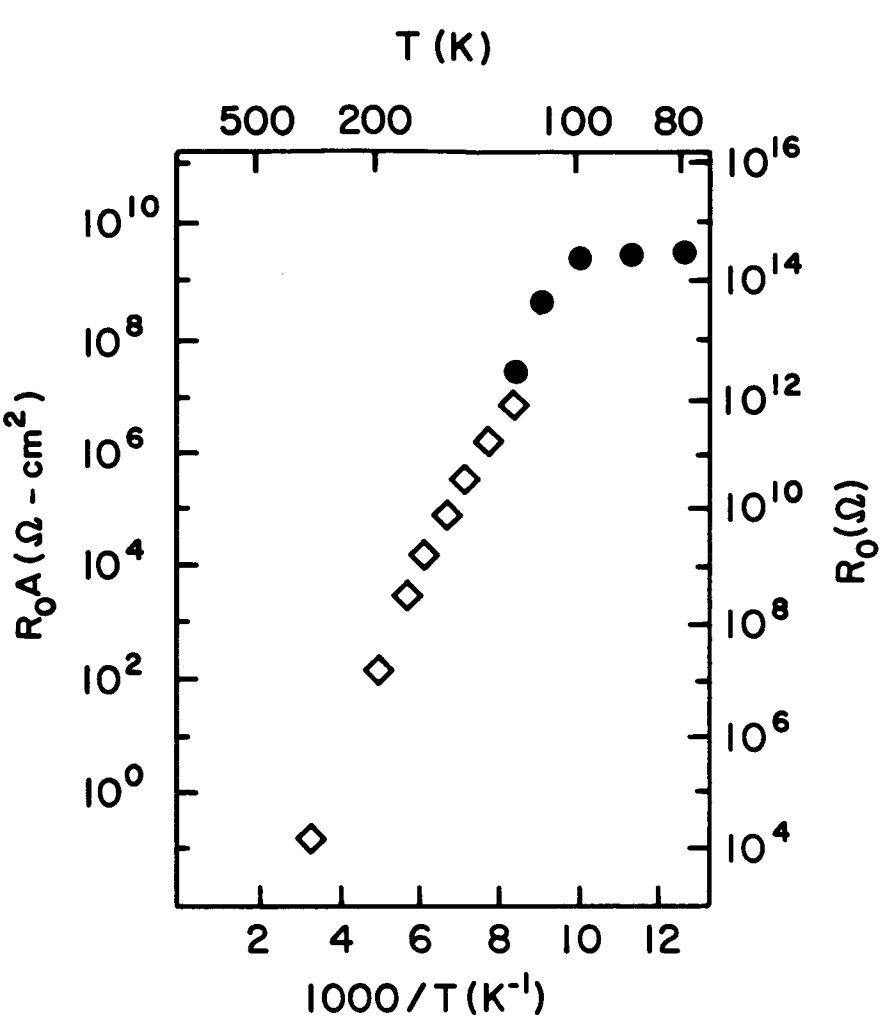

Figure 2: Average impedances measured in the Honeywell HgCdTe photodiodes plotted against inverse temperature. Data from 300 to 120 K is from Sood (in these proceedings).

The uniformity of the array is very good, with ten of the elements tested within ±10% of the mean impedance value at 80 K. Figure 3 shows a histogram of the impedance values found versus number in a 2.5 x 10^{13} Ω bin. Similar results were obtained at the higher temperatures.

B. Diode Curves

Diode curves were measured at 80, 100, and 120 K for a randomly selected detector element to test the assumptions made above. The procedure was to apply a large reverse bias across the diodes (100 mV at 80 and 100 K; 200 mV at 120 K) and to monitor the output voltage as the capacitor discharged through the diode. Measuring the time required for the output voltage to change by 10 mV at 80 and 100 K or by 25 mV at 120 K gives a measure of the current at that voltage as described in Section III.

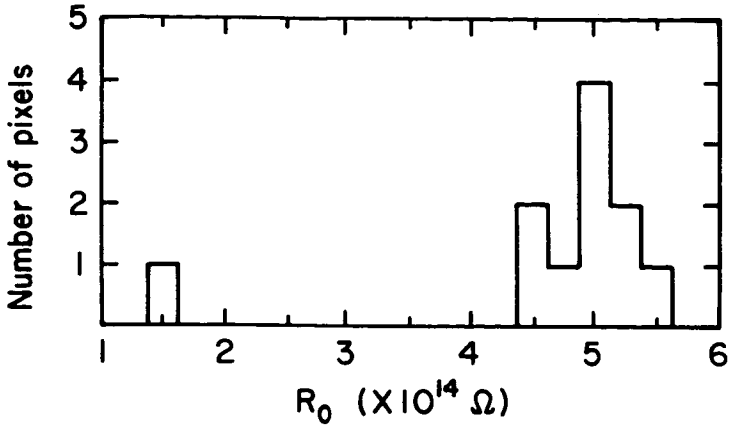

Figure 3: Histogram of HgCdTe photodiode impedances that shows good uniformity in 11 representative array elements.

The measured diode curves are given in Figures 4, 5, and 6 for 80, 100, and 120 K, respectively. A least-squares linear fit to the data gives the slope and offset for each measurement. The slope of the fits is the impedance of the diode over the operating range: 5.5 x 10^{14} Ω at 80 K, 5.6 x 10^{14} Ω at 100 K, and 4.0 x 10^{12} Ω at 120 K.

The impedance of the diode measured from the slope of the diode curve is approximately 5 times larger than the estimates from Section IVA due to the obvious zero point offset in the curves. The behavior of the diode is quite ohmic, however. A chi-square fit to a third-order polynomial varies from the least-squares fit to a straight line by less than 5%, indicating that the slope, and hence the impedance, is constant throughout the measurement range.

To ensure that the offset was not peculiar to the particular diode tested, another diode was selected and measured in the same manner. The diode curve found is shown in Figure 7. Again the detector shows the same zero point offset, within the experimental uncertainties, as present in the previous detector.

V. DISCUSSION

The preliminary conclusions at this point in the test program are as follows:

1. At T > 100 K the SWIR HgCdTe pixels exhibit the increase in impedance with decreasing temperature predicted if the current is due to bulk material conductivity, i.e., the impedance increases approximately an order of magnitude for each 10 K drop in temperature.

2. Over the range 80 K < T < 100 K the pixels exhibit ohmic current-voltage characteristics with a constant impedance of about 5 x 10^{14} Ω.

3. The I-V curve does not pass through the origin.

The transition from the theoretical diode behavior occurs at a temperature of about 100 K, i.e., where the impedance ceases to increase with decreasing temper-

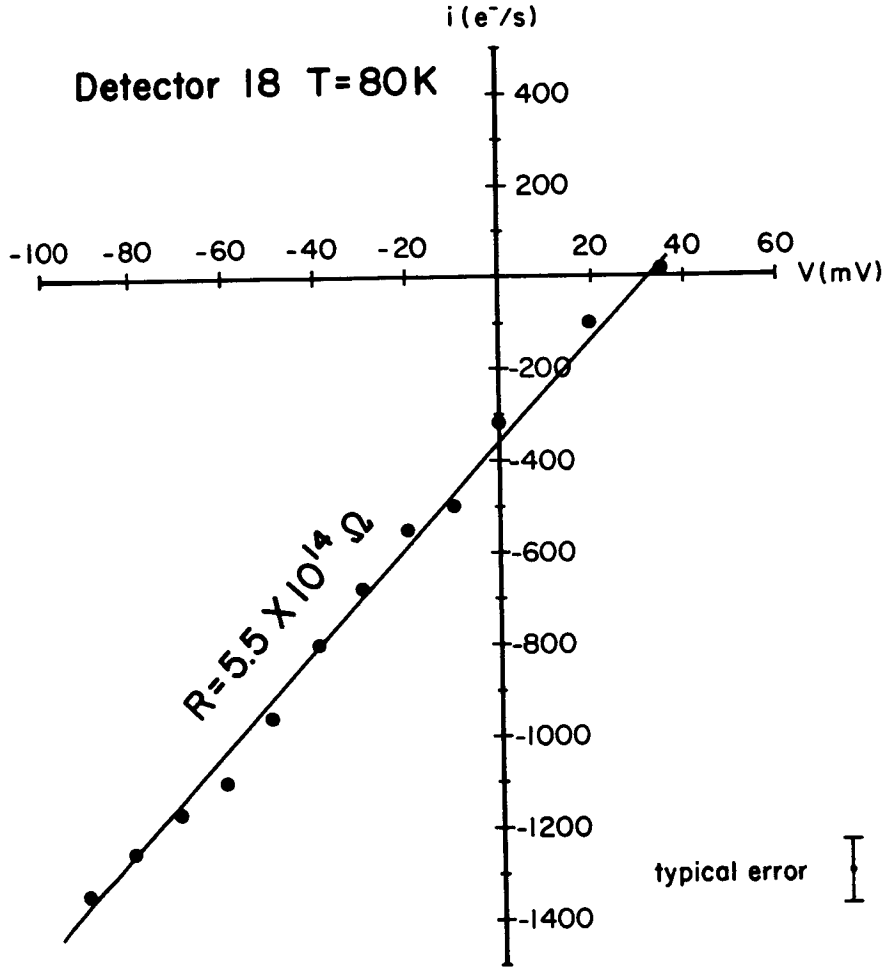

Figure 4: The current versus voltage curve measured at 80 K for detector #18.

ature. The cause of the transition is unknown. It may be due to tunneling or surface path leakage effects and be an inherent property of the devices. The ohmic characteristics of the data, however, do not rule out the possibility that the transition is created by leakage paths in the device packaging.

The reasons for the offset in the I-V curve from the origin are not completely understood. One plausible hypothesis (1) is that it is due to a current generator intrinsic to the devices. In this case the I = 0 point simply represents the balancing of two currents. An alternate hypothesis (2) would attribute it to a voltage offset in the system, such as an uncompensated electronic component offset, diode action in an Indium bump bond, or thermoelectric effects. The offset is not caused by photons impinging on the detector, since the detector was enclosed in a completely light-tight housing and saw only the radiation shield that was at the test temperature of 80-120 K.

The temperature dependence of the offset offers insight into its nature. As can be seen in Figures 4, 5, and 6, there is only a slight change in the voltage at zero current. The variation is not significant and could be entirely due to the experimental uncertainties. If, for example, the offset is from a voltage source in the elec-

tronics (hypothesis 2), then the lack of a strong temperature dependence is entirely consistent. If, however, the offset is due to a current generator inherent to the device (hypothesis 1), then the current generator must mimic the behavior of the diode current so as to produce no change from 80 to 100 K, and then a two orders of magnitude rise from 100 to 120 K. Fewer assumptions can therefore explain the simple voltage offset than are necessary to invoke in the current generator case. However, there is no decisive evidence either way. The noise as a function of bias voltage could perhaps discriminate between the two hypotheses, since the noise minimum would be offset from "zero current" if two currents are involved.

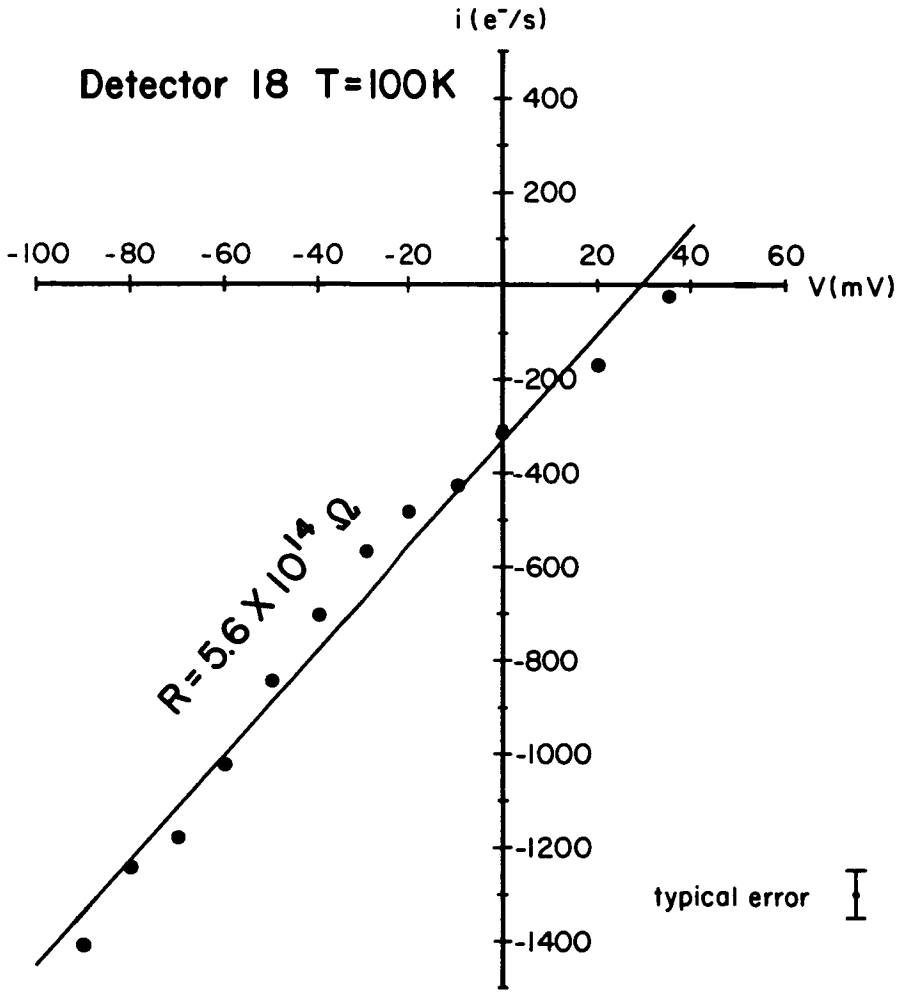

Figure 5: The current versus voltage curve measured at 100 K for detector #18.

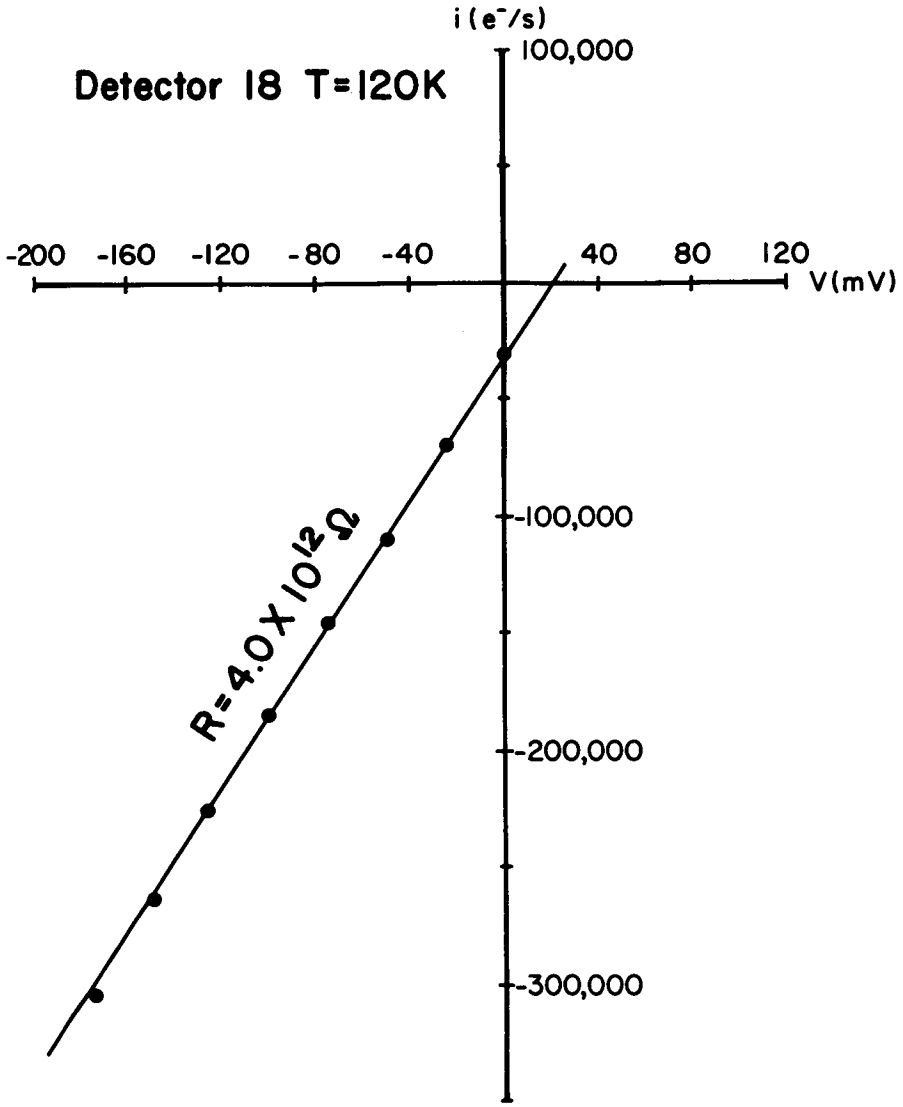

Figure 6: The current versus voltage curve measured at 120 K for detector #18.

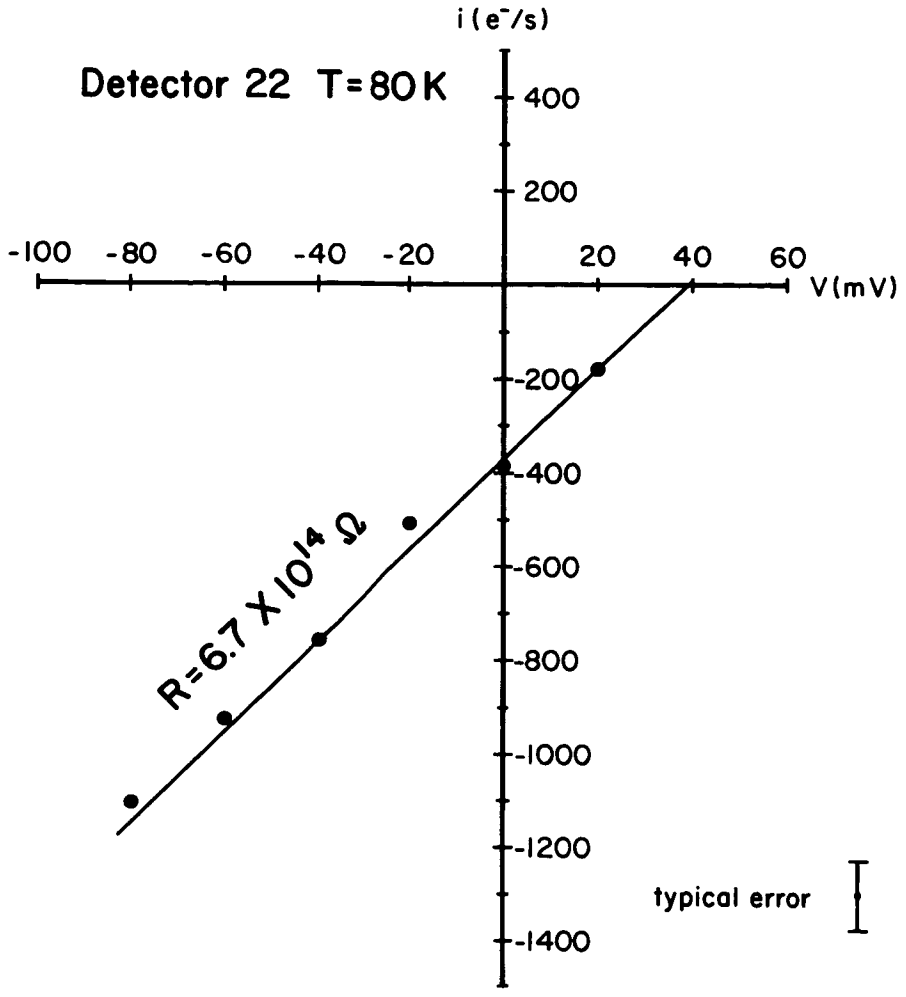

Figure 7: The current versus voltage curve measured at 80 K for detector #22.

Evaluation of Rockwell HgCdTe Arrays for Astronomical Use

M. J. Lebofsky, E. F. Montgomery, and W. F. Kailey
Steward Observatory, University of Arizona, Tucson AZ 85721

I. Introduction

A program of detector evaluation geared toward selection of a suitable near-infrared detector for use either on groundbased telescopes or Space Telescope has yielded interesting results on a 32x32 HgCdTe array manufactured by Rockwell International (Thousand Oaks). The original goal for groundbased use was selection of a detector to be used in conjunction with the Steward Observatory Transit Telescope survey, and the array described below will not only satisfy the needs of this project, but also will replace the liquid-helium cooled InSb aperture photometers which have been extensively used at the Observatory.

Second generation Space Telescope instruments may well include infrared systems with particular emphasis on near-infrared wavelengths. Virtually all high-sensitivity groundbased work has used InSb detectors, but HgCdTe may be an important alternative, especially for the Space Telescope environment where detector operating temperatures lower than 60 K may be difficult to maintain over the five-year lifetime projected for second generation ST instruments.

II. General Description of the Rockwell HgCdTe Array

Figure 1 presents a sketch of the array which consists of back-illuminated HgCdTe material grown by liquid phase epitaxy on a transparent CdTe substrate. Planar processing produces photovoltaic detectors. The detector surface is indium-bonded to a four-phase surface channel CCD used as a readout device. In prinicple, the detector surface could be indium-bonded to other readouts such as the MOSFET direct-out developed by Hughes although none of these alternative readouts were available for testing. HgCdTe detectors have also been grown on sapphire substrates; this combination yields higher quantum efficiencies because of the more favorable index of refraction of sapphire relative to CdTe (Rode, private communication, Herald and Harper presentation at this conference).

Table 1: Physical Properties of the Rockwell HgCdTe 32x32 Array

Detector Material	$Hg_{0.6}CdTe$
Cutoff Wavelength	2.52 μm
Readout	4-phase CCD
Pixel Size	68 μm x 68 μm
Pixel Spacing	75 μm x 75 μm
Detector Type	Photovoltaic

As shown in Figure 1, the CCD uses a direct injection gate to move the generated charge into the CCD storage wells. The CCD has large wells but suffers from high read-noise which can be overcome in high-background operation by integrating long enough for the background noise to be larger than the read noise. On ST using diffraction-limited pixels at 2μm, the integration time required for background-limited operation with this readout would be prohibitively long.

The detector material exhibited superior qualities such as low dark current and good quantum efficiency as demonstrated later in this paper. The cutoff wavelength of 2.5μm is well-suited to use on the ground and ST where large thermal backgrounds dominate at longer wavelengths. In fact, this cutoff actually simplifies the design of systems to be operated at 1-2.5μm because extensive cold baffling as is required with detectors like InSb (cutoff wavelength of 5μm) is unnecessary. This material is also very convenient from the standpoint of performing well with cooling to only 80 K as opposed to the 4 K required for optimum performance of InSb at these wavelengths (Rieke et al. 1981).

III. Method of Operation

The CCD was operated with the full four-phase clocking to ensure the maximum possible well-depth. The array has been operated in the staring mode.The clocking circuitry was built from discrete components allowing relatively easy adjustment of the clock pulse shapes. Some departures from standard CCD readout practice were made in the following areas. Because of the small number of pixels involved, we decided to have the double-correlated sampling of the voltage from the CCD output amplifier done not by an analog device but rather by two separate digitizations with the A/D converter. This method has the benefit that any pick-up of clocking pulses on the output line can be eliminated from the final signal by choosing the sampling points appropriately. Figure 2 presents the readout electronics and data acquisition computer in block form.

The signals were digitized using a 12-bit A/D converter with either a gain of 1 or a gain of 4.7 before the A/D converter. This arrangement was satisfactory for the laboratory test described in Section IV. but was inadequate for simultaneously digitizing the full dynamic range of the CCD and the read-noise. This resulted in the observational data reported later in this paper being limited by the digitizer noise rather than background or read-noise.

The digitized signals were fed into a microcomputer which did the double-correlated sampling and provided various data recording facilities. The computer was able to handle up to 10 frames/second so it imposed no further limitations beyond those imposed by the accuracy of the A/D converter.

All tests were performed with the array cooled with liquid nitrogen to a nominal temperature of 80 K although the actual temperature of the array was probably nearer to 90 K for most of the laboratory tests. The array mounted on a ceramic chip carrier which was in turn mounted on a copper substrate which was bolted to the copper work surface of the dewar. A thin nylon washer was inserted between the substrate and work surface to prevent thermal shock from cooling the array too rapidly. Unfortunately, the arrangement of the array on its carrier prevented mounting of thermal sensors close to the array.

External warm filters were used with cooled relay optics inside the dewar. None of the readout electronics were operated at cyrogenic temperatures.

III. Laboratory Tests

We used two different arrays during our evaluation, a "bad" array which has only 40% of its pixels active and a "good" array which has more than 95% of its pixels active. Both arrays were subjected to a battery of laboratory tests and both were used on telescopes. The only difference between the two arrays was the number of active pixels with the good pixels in both arrays having identical properties. The bad array has been cycled from room temperature to 80 K and back more than 30 times with no change in its properties.

Table 2: Measured Properties of the Rockwell HgCdTe 32x32 Array

Quantum efficiency @ 1.6μm	70%
Read noise	1100 electrons
Dark current @ 80 K	800 electrons/sec
Well depth	5×10^6
Linearity 0.4%-80% full well depth	99.57%
Uniformity	87% of all pixels within 5% of average sensitivity

A.Quantum Efficiency

The quantum efficiency was measured using a blackbody operated at 1270 K with a standard H (1.6μm, 0.4μm bandpass) filter mounted outside the dewar. The quantum efficiency at other wavelengths can be read from the graph in Rode (1983). If a sapphire detector substrate had been used rather than CdTe, the quantum efficiency would be near 90%.

B. Read Noise

The read noise was determined from a series of frames taken under identical conditions. The counts in a sample of pixels distributed uniformly across the array were compared with the variance in the counts being attributed to read noise. The measured value in Table 2 is typical for the surface channel CCDs used with infrared detectors. The read noise as a function of signal strength was also examined and found to vary as the square root of the signal read out with no evidence for excess read noise at high (80% of full-well depth) signal levels. This lack of excess noise is crucial to successful application of these devices in moderate to high background conditions.

C. Dark Current

The dark current was measured using a cold shutter to blank the detector

with an 80 K surface. This was the only parameter found to be significantly different from values supplied by Rockwell and was found to be substantially smaller. The discrepancy is due to Rockwell's use of a 300 K blocker rather than a cold blocker. The array was left to accumulate charge in the dark for periods ranging from 100 to 2000 seconds to derive the value quoted in Table 2. This value is to be compared with a dark current of 60000 electrons/second for InSb with 90μmx90μm pixels bonded to a CCD and measured at 60 K (Forrest et al. 1985). The dark current for InSb roughly doubles for each degree above 60 K (Forrest et al.) making it nearly useless for operation at temperatures in the 60-80K region.

The dark current as a function of temperature for HgCdTe was crudely measured by pumping on the liquid nitrogen reservoir to lower the temperature. The lack of a temperature sensor on the detector substrate prevented a quantitative measurement, but this test showed a drop from 880 electrons/sec measured a short while after the dewar was filled with cryogen to a value of 600 electrons/sec after several hours of pumping. Because the dark current is potentially the limiting factor in use of HgCdTe materials, further tests with material not bonded to a CCD are planned to determine how far this material should be cooled for optimum performance in low background conditions. For operation at 60 K and above, it clearly appears to be the best detector material available for use in the 2μm region.

D. Well Depth and Linearity

Figure 3 plots the signal readout as a function of exposure time to a 300 K surface. The device is linear over a range of 0.4% to 80% of full well capacity which occurs at 5×10^6 electrons. Data not plotted on the figure indicate that the array is not linear at very small signals, but operationally this is not a problem because either the dark current or background will provide enough counts to insure operation in the linear region. Injection of "fat zero" is unnecessary.

E. Uniformity

Only the good array was checked for uniformity. The array was exposed to a black ambient temperature surface while looking through a K (2.2μm,bandpass 0.5μm) filter,and the counts recorded in each pixel were compared. This procedure was done on each of the telescope runs where this array was used, and the histograms in Figure 4 show that the array has 87% of its pixels within 5% of the average sensitivity and 95% within 7.5% of the average. This pattern repeated on both runs with the relative sensitivites of the pixels essentially constant in time. Note that the black surface used in these measurements was actually the back side of a guider mirror which may not be perfectly uniform so that these statistics indicate the minimum level of uniformity.

V. Operation on Groundbased Telescopes

The maturity of the Rockwell HgCdTe array can be judged from the ease with which it has been used in the observatory environment. The array was used successfully on its first telescope run in April, 1985, and has performed flawlessly in subsequent runs. Figures 5-8 display some of its ability to produce photometrically accurate results on a variety of

astronomical objects. Note that these images were obtained using the same observing technique as used at optical wavelengths; the array is exposed to the sky for a period long enough to fill the wells to the 50% level, and then frames of a uniformly illuminated surface are taken for use in removing the pixel to pixel sensitivity variations. No sky chopping is used although some sky frames were taken, particularly when extended objects which fill the field of view were being studied. Exposure times of up to 8 minutes at 2.2μm with 0".4 pixels were possible with much longer exposures at the lower background, shorter wavelengths. Use of cooled filters has allowed longer exposures with integrations as long as 15 minutes at 1.6um with 0".5 pixels on a 2.25-meter telescope have been taken.

Table 3: Performance at a Telescope

Long integrations possible:	5 minutes at 2.2μm ($\Delta\lambda$=0.5μm, 0".25 pixels) gives 40% full wells
	50 minutes at low-background yields 50% full wells from dark current
Sensitivity:*	K=+20.7, one-sigma in one hour for 0".25 pixels on 2.25-meter telescope assuming 12 5 minute integrations
Noise:	Not degraded at high signal levels with read noise=1380 electrons at 25% full-well

* Warm filters and 12-bit A/D converter limited performance in these tests.

The sensitivity on the sky was limited by the A/D inadequacy mentioned earlier where the least significant bit corresponded to 4000 electrons. Another limitation was imposed by the use of warm filters. In spite of these limitations, the one-sigma sensitivity in one hour for one 0".25x0".25 pixel at K(2.2μm) was +20.7 using 12 5 minute integrations on the Steward Observatory 2.25-meter telescope, comparable to the +18.7 for a liquid helium-cooled InSb detector using cooled filters and an 8" aperture. When the filter and A/D improvements are implemented, the HgCdTe array will outperform the InSb detector including the factor for the difference in background between the 0".25 pixel size of the array and the 8" pixel for the InSb.

VI. Summary

The 32x32 HgCdTe array manufactured by Rockwell International has proven to be a highly competitive detector type for use at wavelengths shorter than 2.5um. The goal of a K=+16 sky survey using this array attached to the Steward Observatory Transit Telescope is clearly within reach. The detector material exhibits high quantum efficiency and low dark currents indicating that its usefulness may extended beyond its use with a CCD readout on groundbased telescopes.

Acknowledgements

We would like to thank George Rieke for useful advice, Craig McCreight for additional funding which made acquistion of the arrays possible, and Jon Rode of Rockwell for his advice and cooperation in making this project possible.

References

Forrest, W. J., Moneti, A., Woodward, C. E., Pipher, J. L., and Hoffman, A. 1985, PASP, 97,183.

Rieke, G. H., Montgomery, E. F., Lebofsky, M. J., and Eisenhardt, P. R. 1981, Applied Optics, 20, 814.

Rode, J. P. 1983, SPIE, 443, "Infrared Detectors", 120.

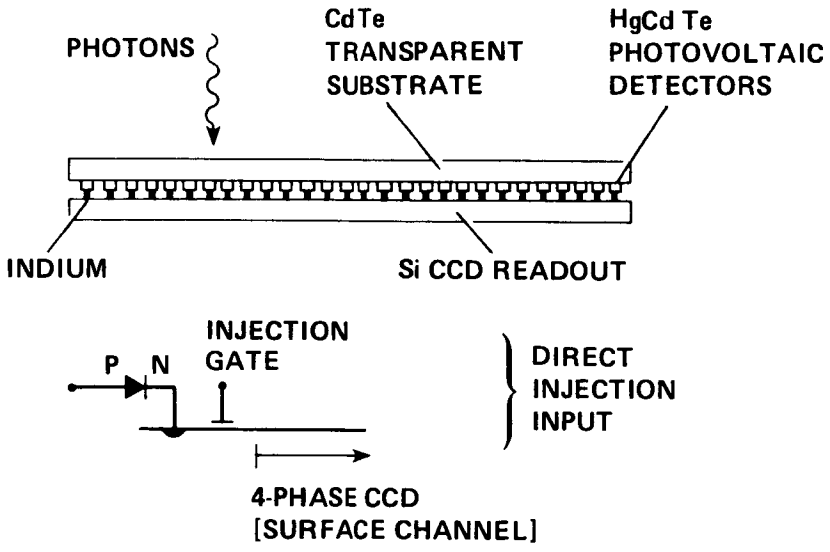

Figure 1: Cross-sectional sketch of the Rockwell 32x32 HgCdTe array mated to a CCD multiplexer. Shown below is the schematic of the injection gate.

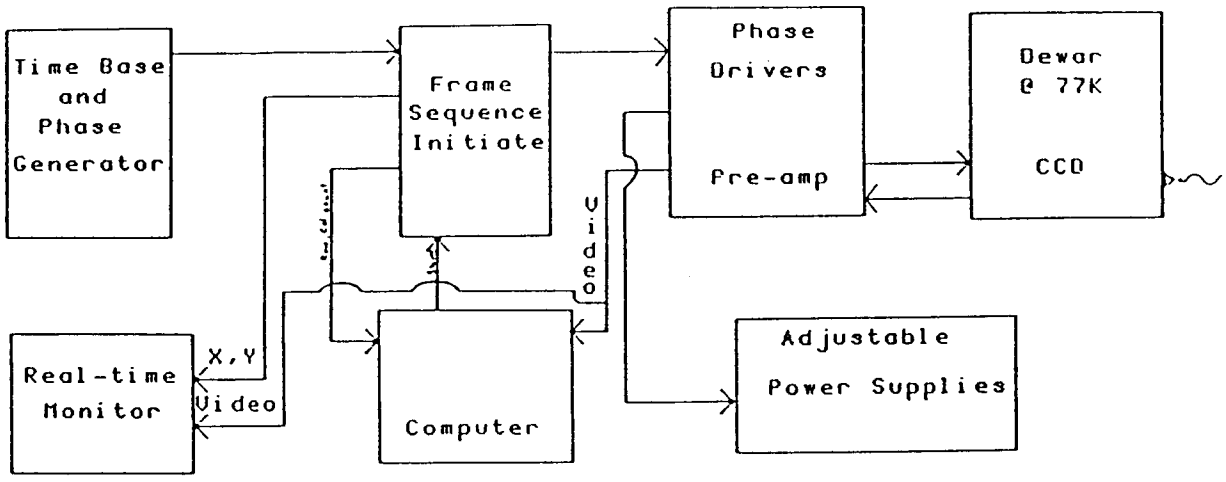

Figure 2: Block diagram of the CCD clocking electronics and the data acquisition system.

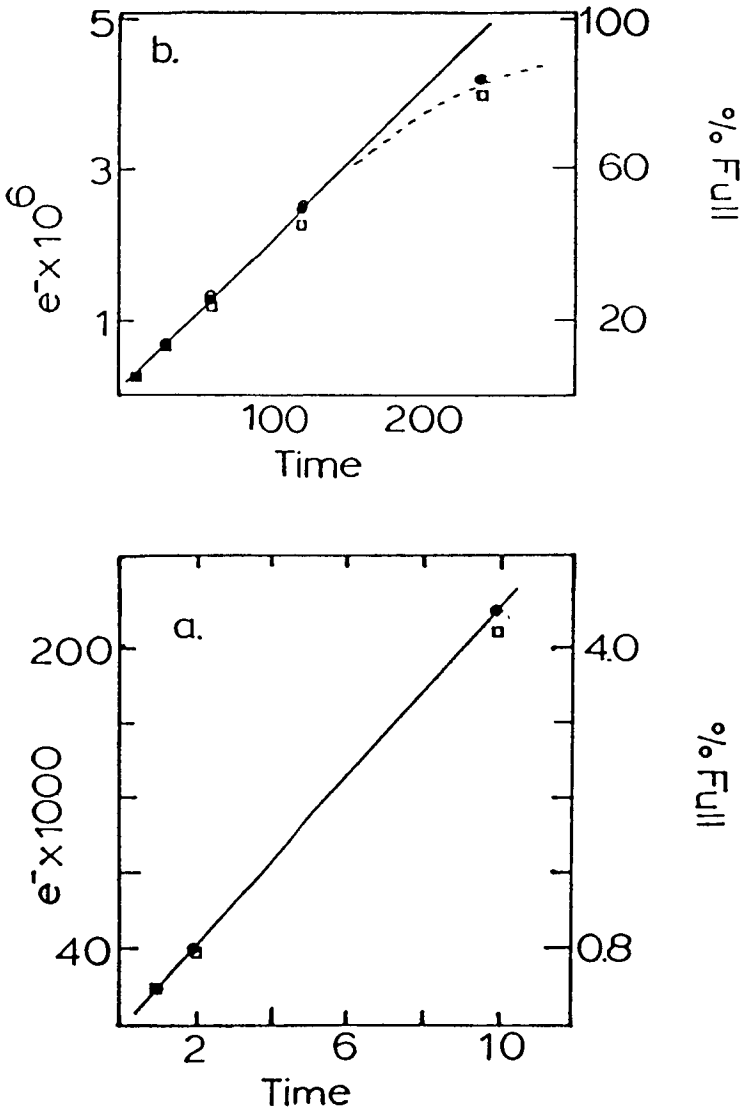

Figure 3: Linearity of the three pixels in the array. Small-signal linearity is shown in a.) where the number of electrons collected versus time while viewing a 300 K surface is shown. Linearity at high signal levels is shown in the same manner in b.).

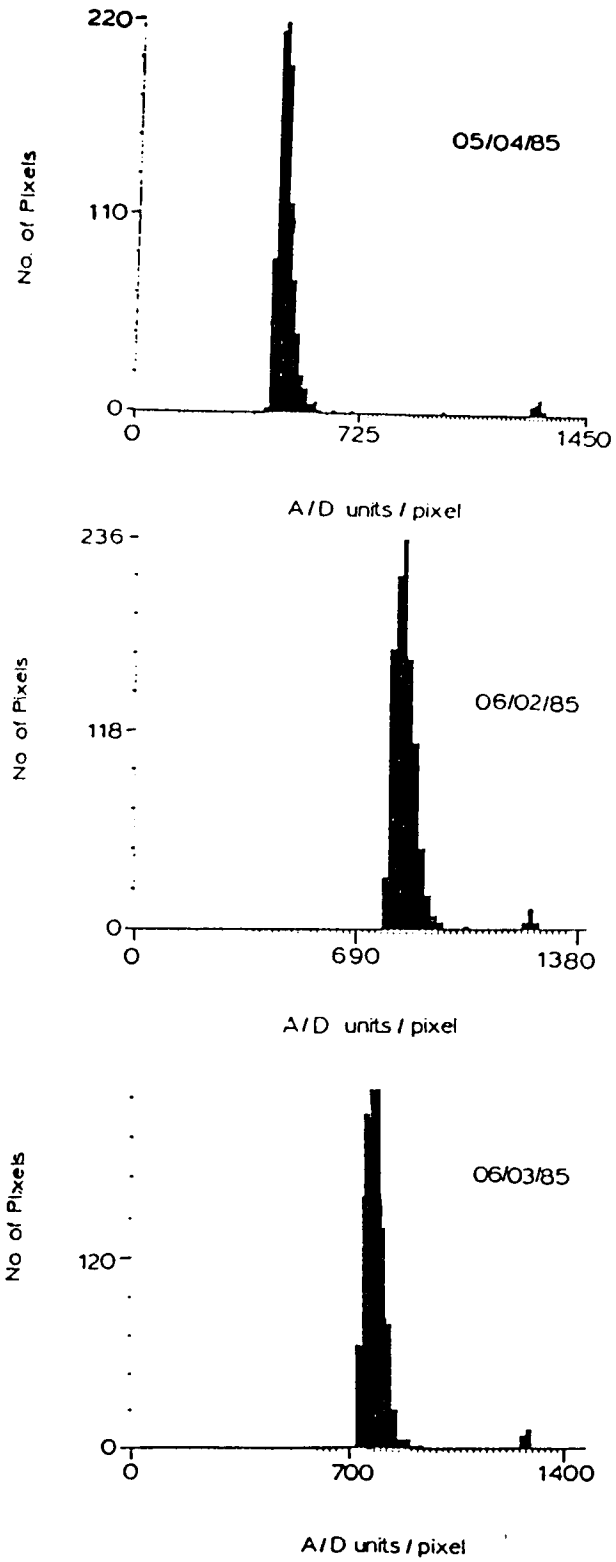

Figure 4: The uniformity of response over all pixels in the array is demonstrated by these histograms showing the raw signal while viewing an ambient temperature surface on three different telescope runs.

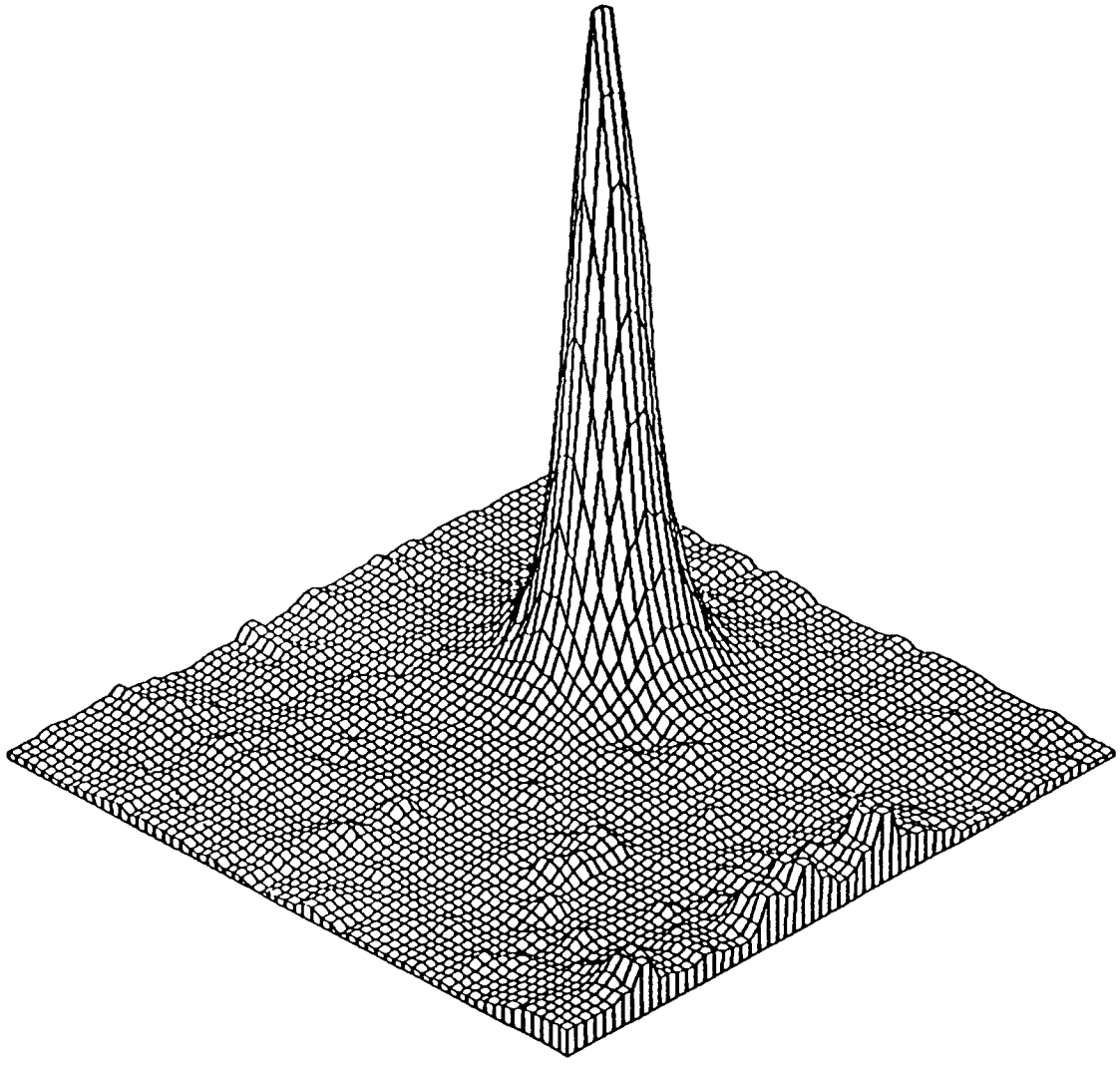

Figure 5: Three-dimensional representation of a 150-second exposure of Mrk 231 rebinned to 64x64. Data taken using a K-filter on the Steward Observatory 2.25-meter telescope with 0".25 pixels.

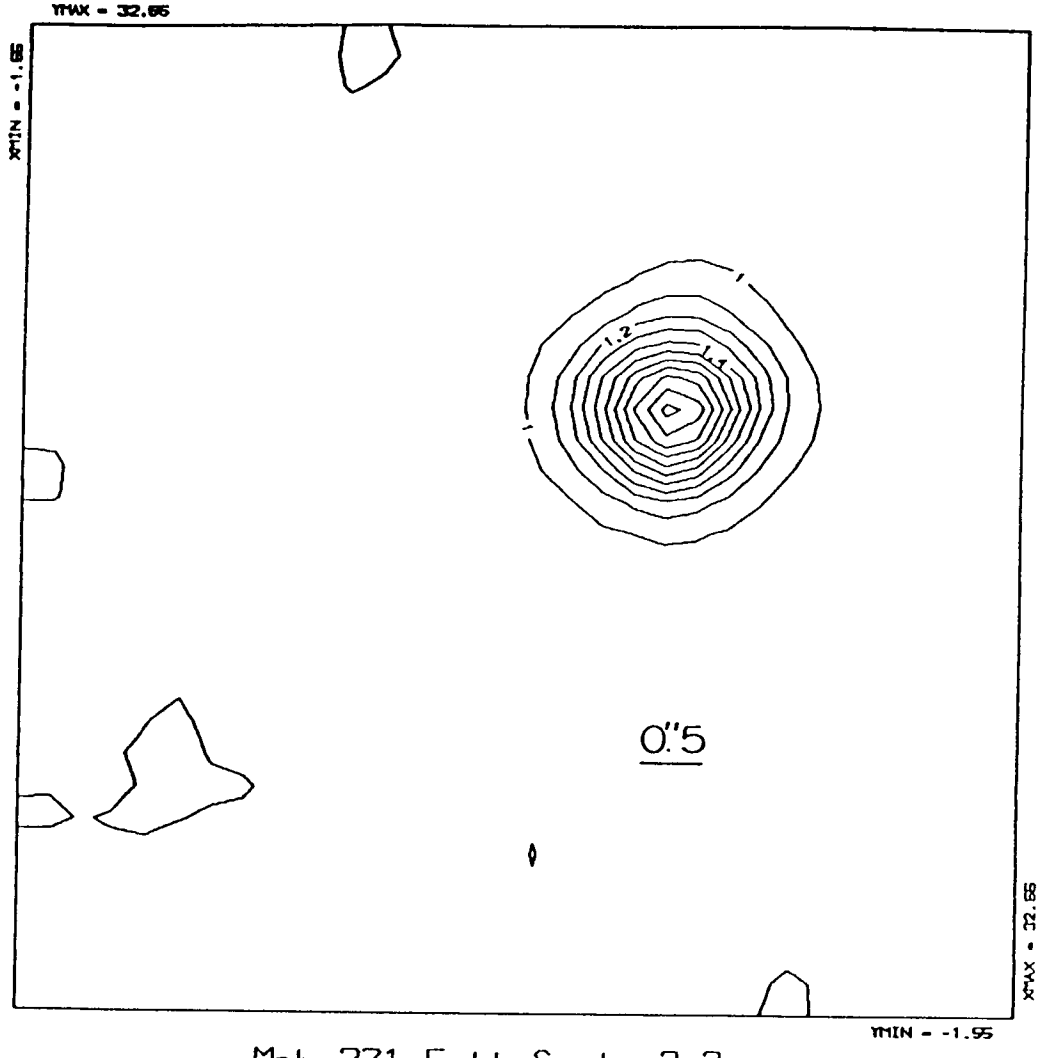

Figure 6: Contour plot of the same data as shown in Figure 5.

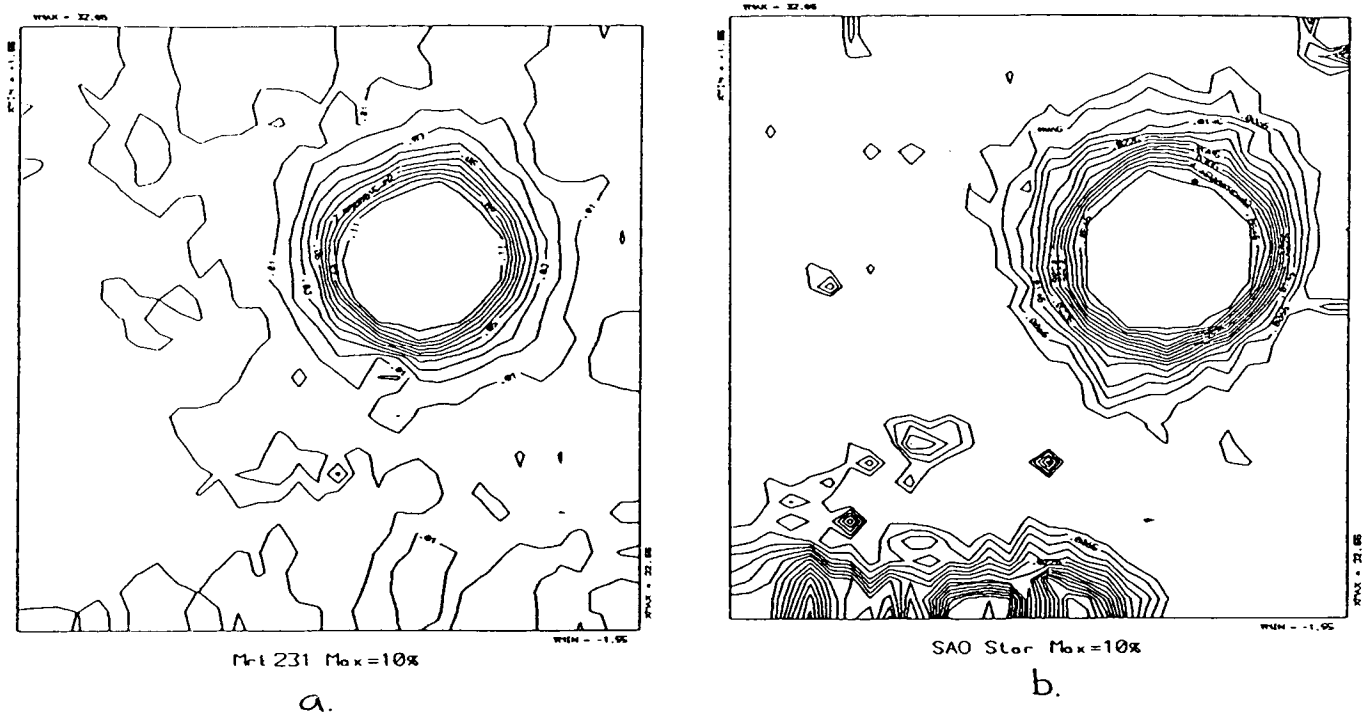

Figure 7: A. Contour plot of the data shown in Figure 6 but with the highest contour set at 10% of the peak value.
B. A star displayed in the same manner as Mrk 231 with the highest contour equal to 10% of the peak value.

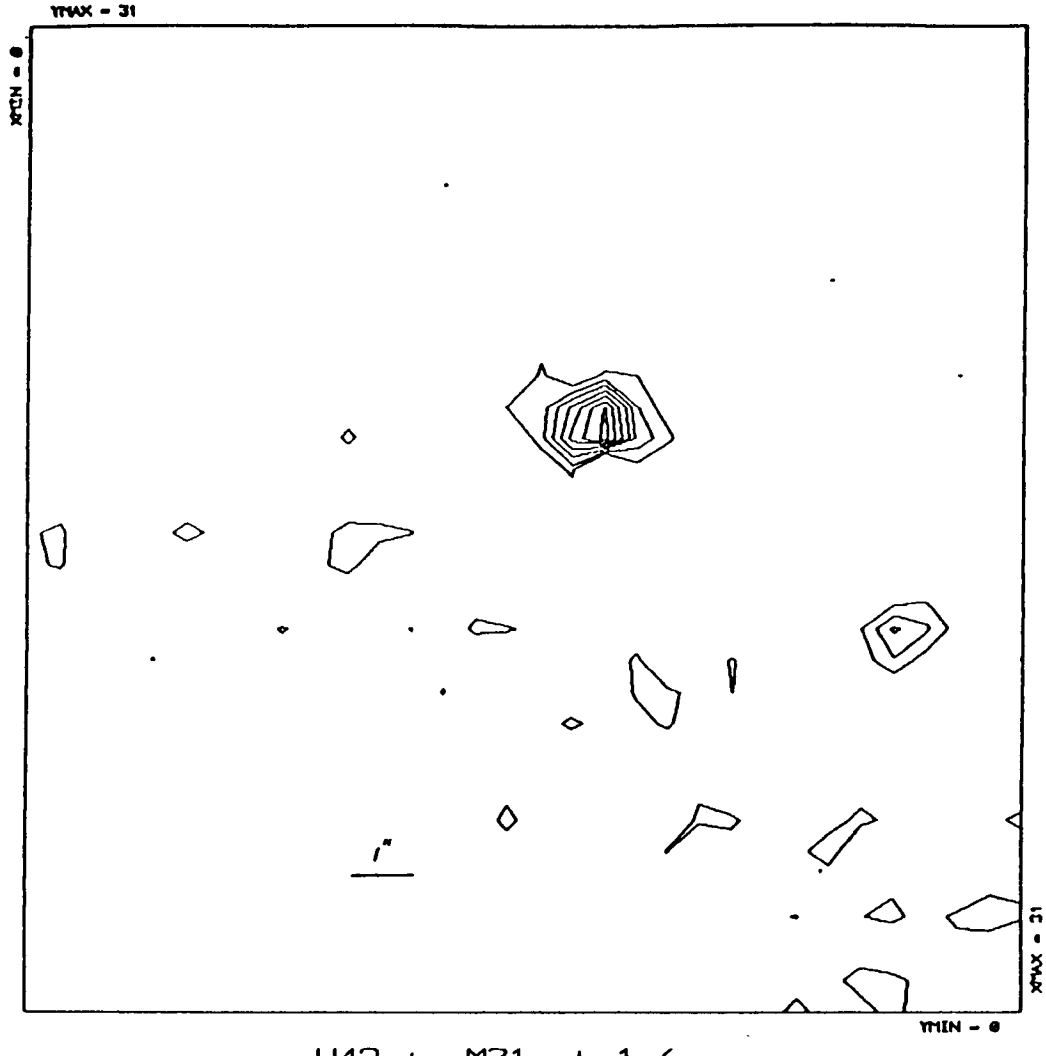

Figure 8: Contour plot of the Cepheid variable H42 in the galaxy M31 which has an H magnitude of approximately 16. This plot is the sum of two 15 minute exposures on the Steward Observatory 2.25-meter telescope with 0".5 pixels. An H-filter was used.

PRELIMINARY MEASUREMENTS OF VERY LOW DARK CURRENTS IN MLA/SWIR HgCdTe/DRO ARRAYS[1]

B. T. Yang
Santa Barbara Research Center
A subsidiary of Hughes Aircraft Company
Goleta, CA 93117

ABSTRACT

In IR astronomy observations, one of the key detector performance parameters is the dark current which, together with the optics, establishes the fundamental limit of a space-based instrument.

This technical note summarizes a SBRC-funded effort to measure dark current performance of the MLA/SWIR[2] PV HgCdTe array (2.5 μm cutoff) at temperatures from 65K to 120K. The preliminary results indicate that dark current decreased systematically to 100K, then the value became measurement-limited at about 3.0 E-18 A/pixel, or 19 electrons/sec/pixel.

I. INTRODUCTION

The MLA/SWIR PV HgCdTe hybrid array developed at Santa Barbara Research Center was designed for push-broom type of imaging. The critical device parameters are summarized in Table I. Note that the array was designed to operate at earth-looking background and at a much higher temperature. The photon flux range is from 3×10^{11} to 10^{14} photons/cm^2/sec with a nominal value of 4.7×10^{13} ph/cm^2/sec. The nominal operating temperature is 175K.

The MLA/SWIR array was selected for the dark current testing due to the following reasons:

1. the pixel size is similar to the pixel size for the Hubble Space Telescope (HST) mission.
2. the cut-off wavelength of 2.54 μm corresponds to the HST's requirement.

---

[1]Presented at the IR Technology Workshop, Aug. 13-14, 1985 at NASA/Ames

[2]The MLA/SWIR array program was funded under NASA contract No. 5-27-583.

3. the hybrid is in existence and the performance is well documented (see references 1, 2, and 3).

The MLA/SWIR hybrid is a 256-element array indium bumped onto a fanout board, which is electrically connected to a silicon feedback-enhanced direct injection (FEDI), direct readout multiplexer. In this study, we systematically cooled the hybrid to investigate the effects on the dark current values.

Table 1. MLA/SWIR ARRAY CRITICAL DEVICE PARAMETERS

Pixel Junction Size	18 μm × 18 μm
Optical Area	23 μm × 23 μm
Pixel Capacitance	< 0.39 pF
Average Sense Capacitance	0.15 pF
Nominal Detector Bias	20 mV (Reverse)
Pixel Size-Number product	5.9 mm
Cut-off Wavelength	2.54 μm
Average Quantum Efficiency	0.65
Average R_oA (at 145K)	5×10^6 Ω cm^2
Array Configuration	256 × 1

II. ANALYSIS

The schematic of a unit cell of the MLA/SWIR hybrid is shown in Figure 1. Under normal operation, photon induced current generated by the detectors is integrated in a CCD well under the ϕ_{INT} gate when ϕ_{INT} is held high. When ϕ_{INT} is pulsed low, this charge is transferred to the CCD well under the V_{STO}/V_{TR} gate. This charge is then transfered to the output sense capacitor when the combination of the appropriate address clocks and ϕ_{TR} are pulsed high. The signal is then read out through the output source follower. The normal frame rate (output from 256 pixels) is 1.6 ms.

The dark currents of interest are on the order of 10^{-16} to 10^{-18} amps. This requires slowing the frame rate to one frame every 100 to 3000 seconds, and subsequently requires modification of the device clocking/operation. The first technique attempted was to integrate charge on the output sense capacitor by stopping the reset clock operation at 65K. The experiment failed because of two reasons:

1. the sense capacitor leakage overwhelmed the dark current to be integrated.

2. the input circuit barely functioned due to freeze-out.

The second attempt was to integrate charge in the second CCD well (under the V_{STO}/V_{TR} gate). This was accomplished by holding ϕ_{TR} low. This prevents the charge from being transferred to the output sense capacitor until completion of the desired integration time. The third method tried involved integrating charge in the first CCD well (under the ϕ_{INT} gate). This involved keeping ϕ_{INT} high for the desired integration time. Both methods were used in this study and both methods proved to be successful.

The optimum operating conditions were determined by letting in the 300K blackbody flux at a given temperature. The dewar was then opened to cap off the hybrid. Then the array was recooled to make certain that the hybrid reached a steady-state temperature.

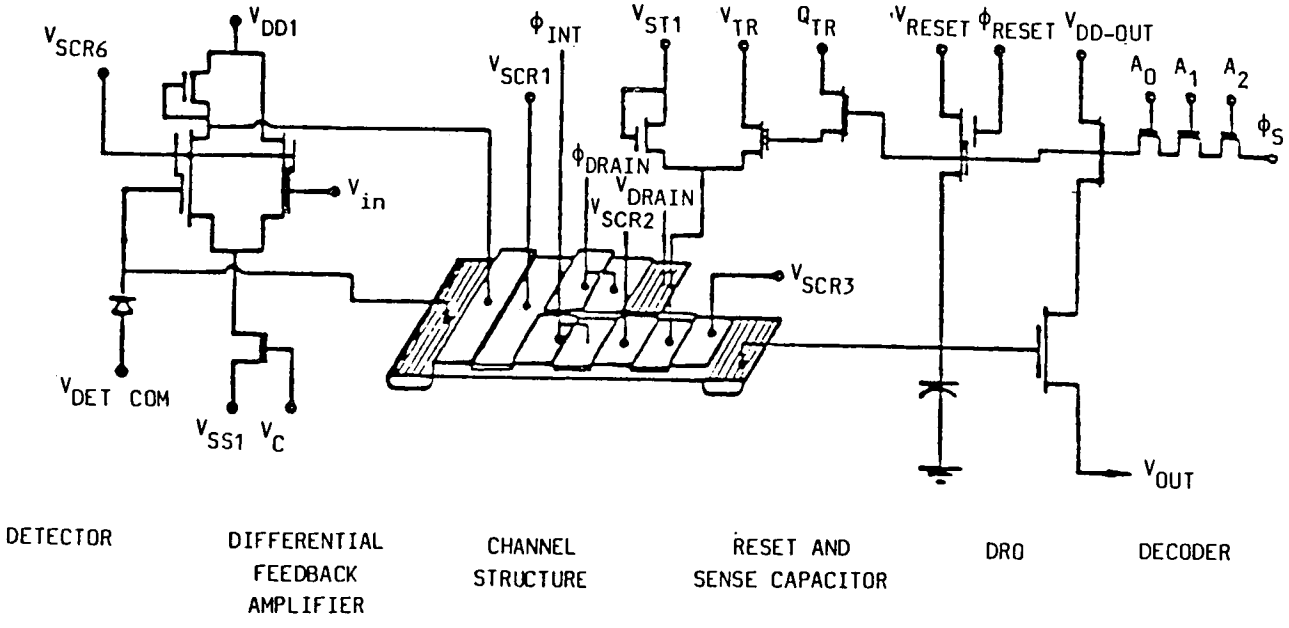

Figure 1. Unit Cell Schematic of Detector/ Preamplifier/Multiplexer Structure

The dark current value I was computed with the following formulas:

$$I = \frac{VC}{TA_v}, \tag{1}$$

where C is the average sensing capacitance (0.15 pF), A_v is the readout source follower voltage gain (0.9), T is the integration time and V is the output voltage in volts. Since the limiting resolution of the system is about 10 mV, the approximate integration time needed can be readily computed:

$$T(\text{sec}) = \frac{10 \times 10^{-3} \times 0.15 \times 10^{-12}}{I(0.9)} = \frac{1.67 \times 10^{-15}}{I(A)}. \tag{2}$$

Therefore, if the expected value is 100 electrons/sec/pixel (or 1.6×10^{-17}A), then the integration time needed is about 100 seconds.

III. MEASUREMENTS

The first measurement was carried out at 65K using the first CCD well and the second CCD well for a 75-minute period. It was found that the average values of 3×10^{-18}A and 6×10^{-19}A were below the limiting resolution. Subsequently, the temperature was raised to 80K and no apparent gains in dark current were observed beyond those at 65K.

At 100K, the dark current was integrated in the first CCD well for 75 minutes; the measured average value of 3.02×10^{-18}A was just below the measuring resolution. The skyline plot of dark current versus detector element is shown in Figure 2. Note that only half of the array was functioning due to a setup difficulty which was remedied later. The skyline plot seemed reasonably uniform except for about 10 "hot pixels".

Figure 3 presents the skyline plot for 110K temperature. The signal was, again, integrated in the first well for five minutes. The data showed wide scatter with the standard deviation (sigma) greater than the mean value. At 120K, the charge integration took place in the second well. Two measurements were made and the results are shown in Figure 4 (T = 50 sec) and Figure 5 (T = 2 min). The respective average dark currents are 6.8×10^{-16}A and 4×10^{-16}A, also with sigmas on the same orders as the average values.

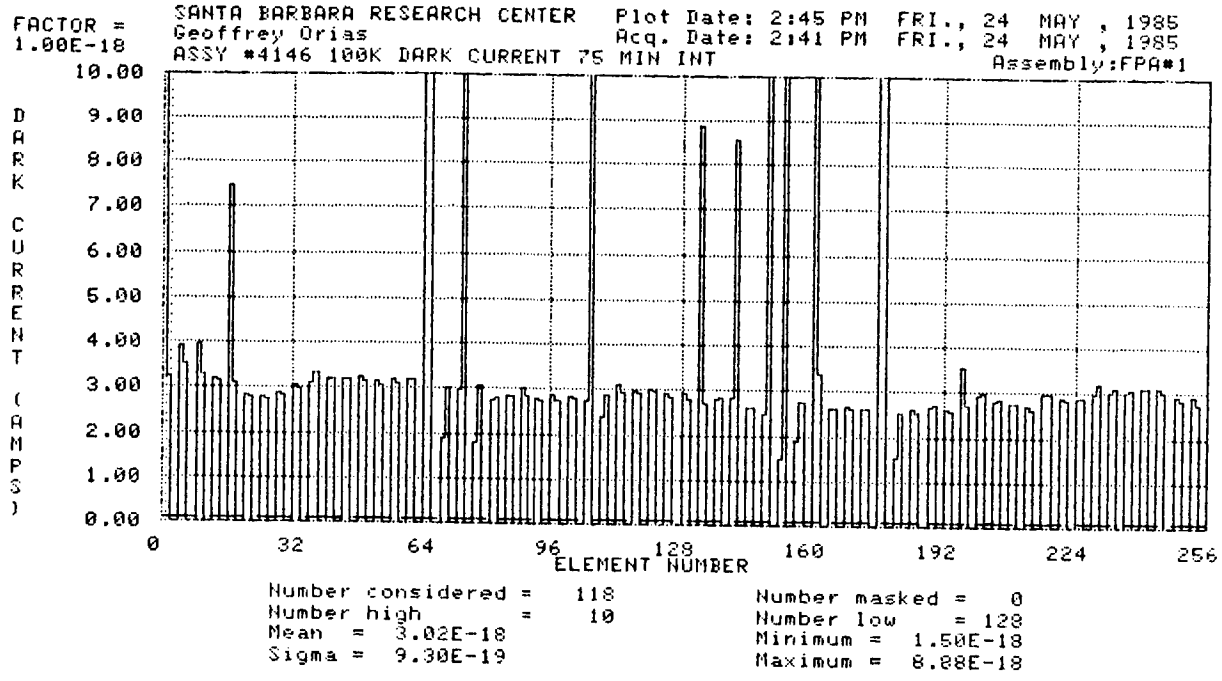

Figure 2. Skyline Plot of Dark Current Versus Detector Number at 100K (T = 75 min)

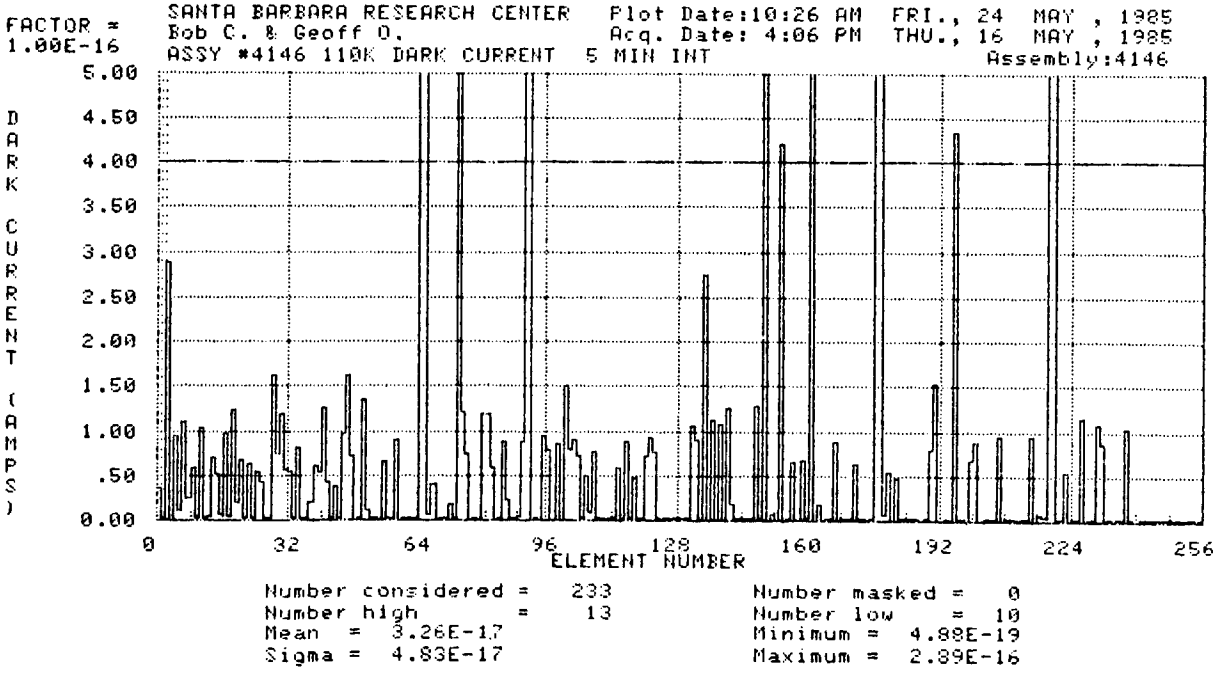

Figure 3. Dark Current Skyline Plot at 110K (T = 5 min)

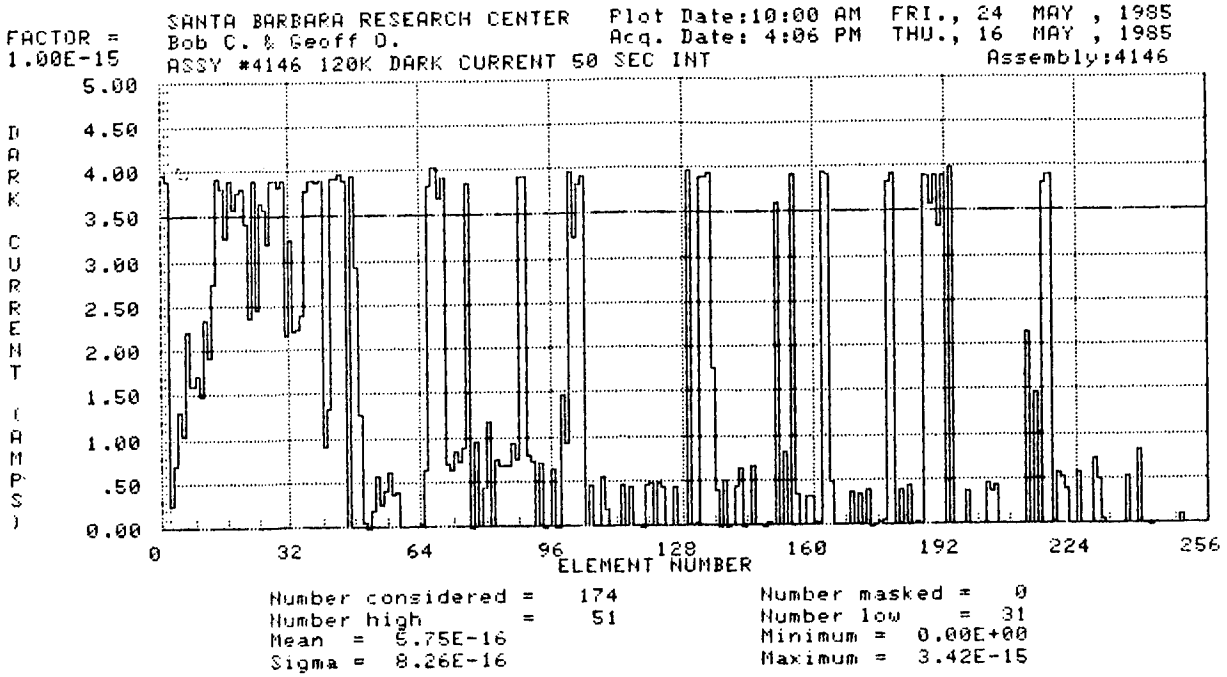

Figure 4. Dark Current Skyline Plot at 120K (T = 50 sec)

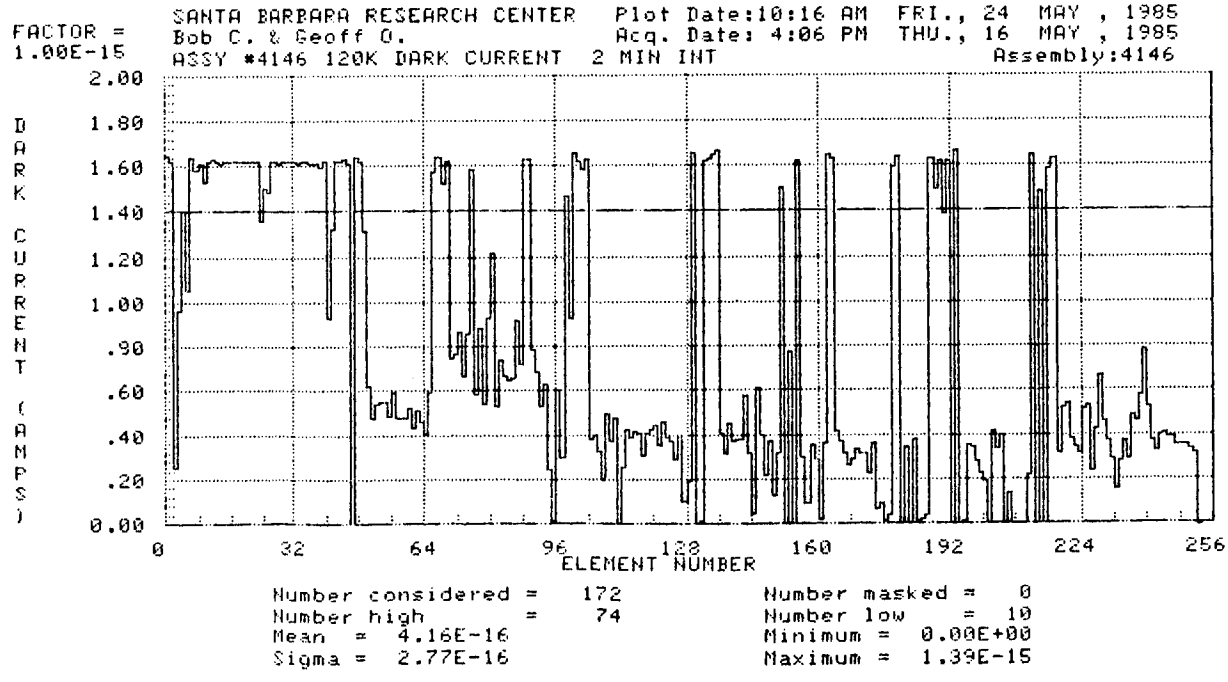

Figure 5. Dark Current Skyline Plot at 120K (T = 2 min)

IV. DISCUSSIONS

Table 2 summarizes the data from this study. This preliminary data set shows that a systematic decrease of dark current with reducing temperature is evident. The uniformity in terms of sigma-over-mean is somewhat greater than desired. It demonstrates that the SBRC 2.54 μm HgCdTe hybrid is able to achieve a per-pixel dark current value of less than 100 electrons. It is also believed that more measurements are needed to check the repeatability of these measurements. The last column in Table 2 lists the dark, normalized currents with the optical area of 5.2×10^{-6} cm^2. The data were plotted in Figure 6 for comparison with the existing HgCdTe diodes.

Table 2. Dark Current Data Summary

Temp K	% of Pixels Considered	Average Current		Sigma/mean	Dark Current/Area
		Amps	Elec/sec/pixel		A/cm^2
120	68	5.7 E-16	3,562	1.46	1.1×10^{-10}
110	91	3.3 E-17	206	1.46	6.3×10^{-12}
100	92	3.0 E-18	19	0.3	5.7×10^{-13}
65	100	3.0 E-18	19	N/A	5.7×10^{-13}

Since the theoretical dark current density follows the diode equation:

$$\frac{I}{A_o} = J_s[e^{\frac{qV}{\beta kT}} - 1] \ A/cm^2$$

where A_o = the optical area of diode (5.2×10^{-6} cm^2)

q = the electron charge (1.6×10^{-19} Coulombs)

β = 2 for G-R limited diode

V = diode bias voltage in volts

k = Boltzmann's constant = 8.62×10^{-5} eV/K

J_s = the saturation current defined as $\frac{\beta kT}{q(R_o A_o)}$ in A/cm^2

R_o = the diode impedance.

The J_s data for the existing larger diodes (between 10^{-3} cm^2 to 10^{-5} cm^2) are calculated from the measured R_oA_o values. It is obvious that the smaller diodes exhibit greater J_s. The current measurements show a steeper slope than the prediction. It also shows a somewhat less value than the larger diodes.

From the application point of view, it can be concluded that if a focal plane performance is dark current limited (for low background application) the MLA/SWIR hybrid (or any 2.54 μm hybrid) should be able to meet the 100 e/sec/pixel requirement at 100K. It is also felt further investigations are needed in the area of dark current behavior for astronomical observation.

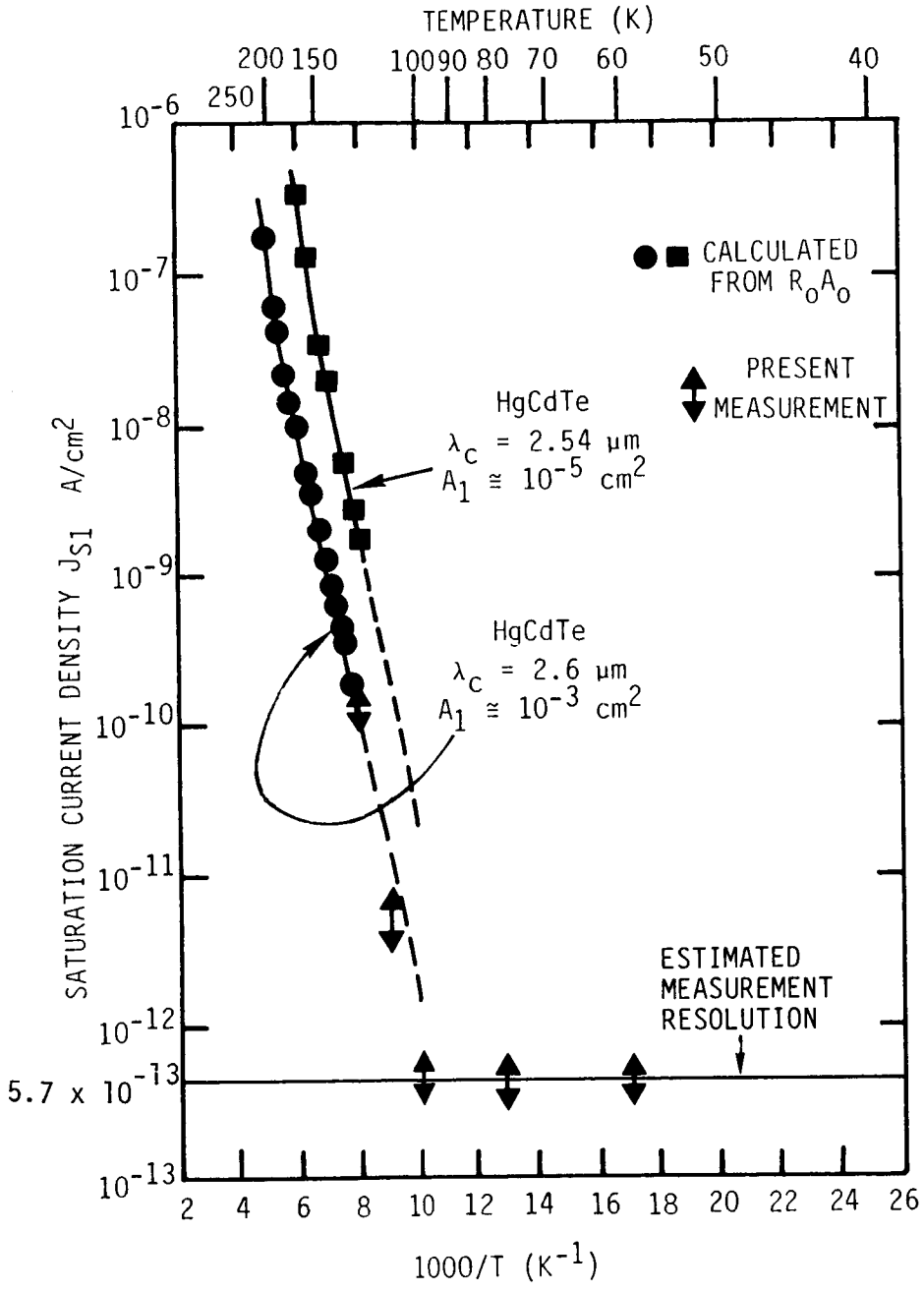

Figure 6. Normalized Dark Current Versus Temperature

ACKNOWLEDGEMENT

The author wishes to thank Rich Thom for his assistance in the entire study. Also, measurements performed by R. Cannata and G. Orias are appreciated.

REFERENCES

1. F.G. Brown, R.F. Cannata, and G. Orias, "High-Performance PV HgCdTe SWIR Arrays," Proceedings of the IRIS Specialty Group on Infrared Detectors, Boulder, CO, August 6-8, 1985, Paper No. B-6, (unclassified).

2. F.G. Brown, S.E. Botts, K. Kosai, A.M. Mika, "MLA Instruments and SWIR Focal-Plane Technology" Proceedings, SPIE National Symposium and Workshop on Optical Platforms, October 24, 1984, Paper No. 493-42.

3. P. King, S. Botts, G. Orias, B. Yang, "Characterization of an Advanced Focal Plane for MLA Application," Proceedings, SPIE International Symposium, San Diego, CA, August 20-23, 1984.

Tests of HgCdTe-on-Sapphire Focal Plane Arrays

Mark Hereld and D.A. Harper

University of Chicago

1. Introduction

In recent months we have received several sample HgCdTe diode arrays from the Rockwell International Science Center for the purpose of testing them for use in low background astronomical applications. These include several diode arrays for use in laboratory tests of material properties and one partially functioning 64x64 element imaging array These devices are similar to focal plane arrays designed for use in an airborne imaging spectrometer.[1] Their development has been sponsored by the Jet Propulsion Laboratory, California Institute of Technology.

With the sample HgCdTe diodes we have begun to characterize R_0A as a function of temperature and cutoff wavelength. Measurements to date show R_0A greater than $10^{11}\ \Omega\text{-cm}^2$ for material samples with cutoff wavelengths of 2.5 μm and 3.5 μm , in this range, measured currents do not deviate from those expected in the generation-recombination limit.

The imaging array is a HgCdTe-on-sapphire detector array mated to a silicon CCD readout substrate. Although the active area of the array is limited to a contiguous 20% along one of its sides, the CCD readout substrate is fully functional. We have built a camera dewar and associated telescope-mounting hardware, assembled clocking and readout electronics, and begun preliminary tests of the camera in the lab and on the 24" telescope at Yerkes Observatory.

In this paper we will describe the general architecture of the imaging array, some merits of HgCdTe-on-sapphire as a detector material, and the current status of our lab tests and SWIR camera.

2. Architecture

This kind of detector array is known as a "backside illuminated planar hybrid focal plane array"[2,3,4] The hybrid FPA (for short) is made up of two parts, the detector array and the signal processor, mated via an array of deposited indium columns labelled as "flexible metallic interconnect" in FIG 1. In addition to providing a space-efficient electrical connection, the array of metallic columns also provides a flexible mechanical joint that is tolerant of the relative strain between detector array and signal processor introduced by cycling the FPA between room temperature and its cryogenic operating temperature.

Different schemes for fabricating the array of detectors have been developed and discussed in detail elsewhere.[5,6,7] The highest yield has been attained by liquid-phase epitaxy on sapphire substrates, a process called PACE (Producible Alternative to CdTe for Epitaxy). The sapphire is durable, inert, transparent (to 5.5 μm), inexpensive, and available in large, regularly shaped blanks. A thin CdTe buffer layer is first epitaxially grown on the sapphire. The alloyed HgCdTe is then grown on the CdTe. The n-on-p junction is created by positive ion implantation. Because of its superior crystallographic properties, more uniform epitaxial arrays can be grown on sapphire than on CdTe.

The multiplexer used in the array we have incorporated into our SWIR camera is a parallel-to-serial CCD. Sixty-four shift registers in parallel, one for each column of the array, feed a single high speed shift register which presents the charge contents of each row, pixel by pixel, to an output circuit. This is very similar to the familiar optical CCD architecture except that the photo-electrons aren't produced in the silicon.

3. Performance

HgCdTe, as an alloy of HgTe and CdTe, has a bandgap which can be tuned from below 0.1 eV to above 10 eV by varying the molar ratio of HgTe to CdTe. The corresponding cutoff wavelength varies from about 1 μm to

above 10 μm. The relative quantum efficiency as a function of wavelength has been plotted in FIG 2 for a typical diode in a 2.5 μm cutoff array. The HgCdTe epitaxy-on-sapphire process yields peak quantum efficiencies in the range of 60 to 90% over 95% of the pixel elements of a given array with a standard deviation of only about 5%.[1,2,3] A histogram of the quantum efficiency for the elements of a 32x32 element device is shown in FIG 3 (taken from references 2 and 3).

HgCdTe with a cutoff wavelength in the SWIR (1 - 3 μm) has a very high resitance and correspondingly low dark current. We have extended measurements made at Rockwell[2] of the temperature dependence of R_0A to values approaching 10^{12} Ω-cm^2, three orders of magnitude higher than previous determinations. These values lie on the extrapolated generation-recombination current limit. The results are shown in FIG 4. These results are of particular importance for low background applications. They imply potentially long integration times before dark current saturates the detector well. Furthermore, because these (and possibly higher) values of R_0A are attained at modest temperatures, long-lived, passive, cryogenic coolers can be designed for "warm telescopes" such as the Hubble Space Telescope without recourse to liquid helium.

For low background applications readout noise is often the limiting factor in signal to noise ratio. Hybrid FPAs of the kind that we are currently testing have an RMS readout noise of about 1500 e^- This is not unexpected since they were developed for high signal and background applications in which a full-well signal of 10^7 e^- results in a signal to noise of 10^4. However, it should be possible to reduce noise to much lower levels by optimizing well size and readout circuitry for low background conditions.

4. SWIR Camera Status

Our current electronics system was assembled using parts from three different optical CCD systems. We are fabricating a more portable system with software-controlled clocking circuitry and improved real-time

display capability. FIG 5 shows the hybrid FPA mounted inside the dewar.

Although our tests of the FPA have only just begun, we have managed to try the camera out on the 24" telescope at Yerkes Observatory. In the configuration shown in FIG 6, the dewar is mounted to the telescope with a single refocusing lens and a K-band filter (1.9 - 2.5 μm) in the optical path. FIG 7 shows a picture of Saturn taken with the SWIR camera and presented in grey scale with no processing of the data.

5. Acknowledgements

We gratefully acknowledge the assistance of Jon Rode, John Blackwell, and Dave Seib at Rockwell, Harvey Moseley at Goddard Space Flight Center, Don Long at the Plasma Physics Lab at Princeton, and Sean Casey, Jim Fowler, Bob Pernic, Bob Spotz, and Don York at Chicago.

6. References

1. "HgCdTe infrared focal plane arrays for imaging spectrometer applications", J.P. Rode, M.L. Brownell and M. Herring, *International Technical Conference*, SPIE Vol. 398, Geneva, Switzerland, April 1983.

2. "HgCdTe hybrid focal plane", J.P. Rode, *Infrared Phys.* Vol. 24, No. 5, pp. 443-453, 1984.

3. "Infrared focal plane arrays using HgCdTe epitaxially grown on sapphire", J.P. Rode, J.D. Blackwell, N.H. Sheng, K. Vural, E.R. Gertner and W.E. Tennant, *Proceedings of the DARPA Strategic Space Symposium*, 1983.

4. "Short wavelength infrared hybrid focal plane arrays", K. Vural, J.D. Blackwell, E.C. Marin, D.D. Edwall and J.P. Rode, *Technical Issues in Infrared Detectors and Arrays*, SPIE Vol. 409, Arlington, Virginia, April 1983.

5. "Liquid phase growth of HgCdTe epitaxial layers", C.C. Wang, S.H. Shin, M. Chu, M. Lanir and A.H.B. Vanderwyck, *J. Electro. Chem. Soc.*, **127**, pp. 175-179, 1980.

6. "Liquid phase epitaxial growth of large area $Hg_{1-x}Cd_xTe$ epitaxial layers", D.D. Edwall, E.R. Gertner and W.E. Tennant, *J. Appl. Phys.*, **55** (6), pp. 1453-1460, 1984.

7. "Material characteristics of HgCdTe/CdTe/sapphire", E.R. Gertner, D.D. Edwall, L.O. Bubulac, L.E. Wood, J. Bajaj, S.H. Shin and W.E. Tennant, *Proceedings of IRIS Detector Specialty Group on infrared detectors*, Boulder, Colorado, August 1983.

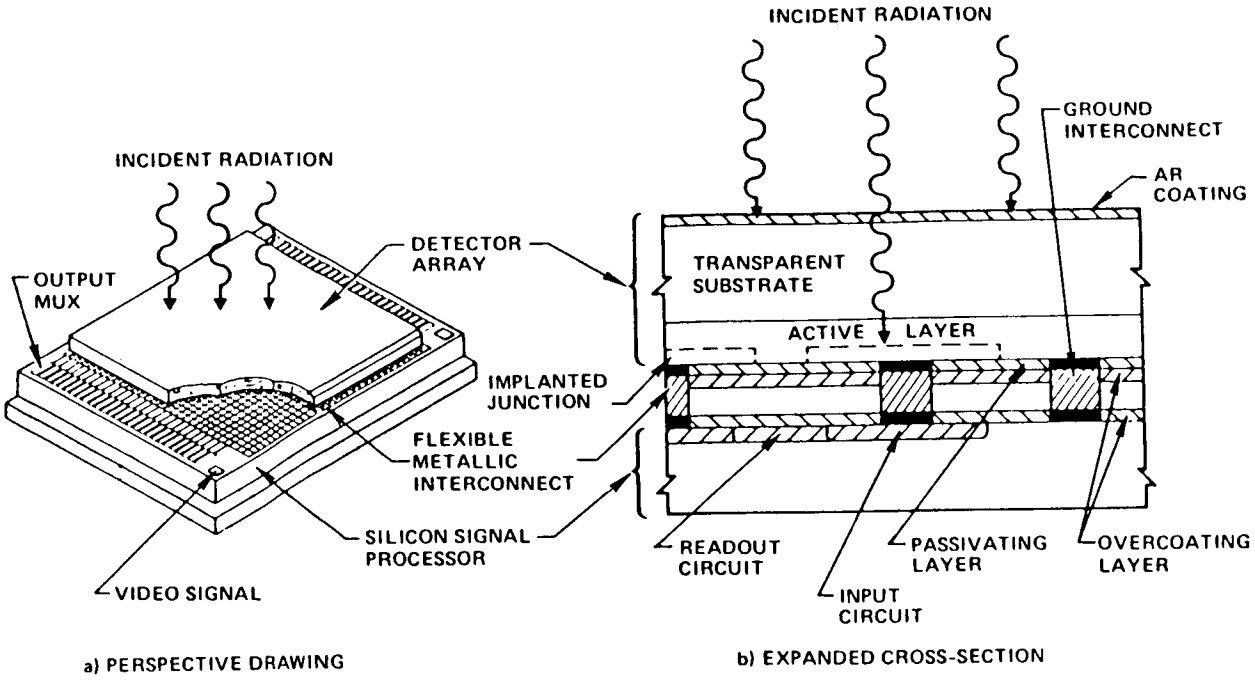

FIG 1. A schematic of the hybrid focal plane array.

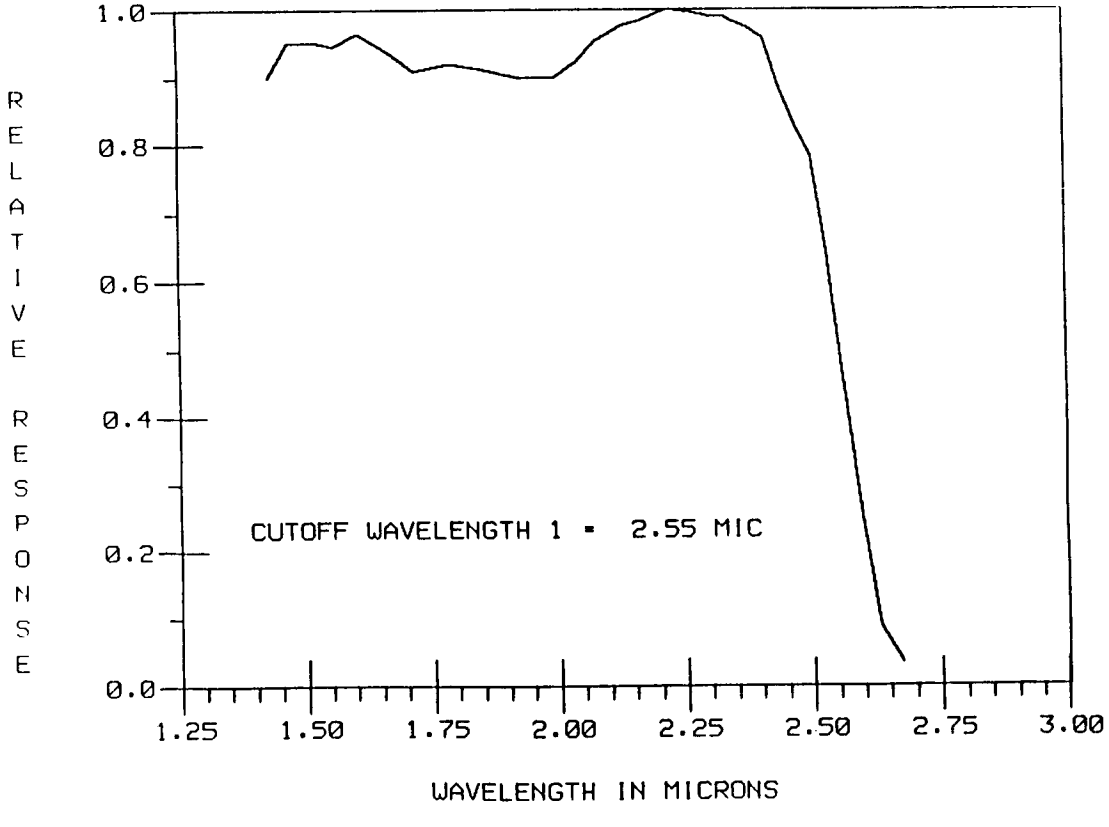

FIG 2. Relative quantum efficiency for a diode with a cutoff wavelength of 2.5 μm.

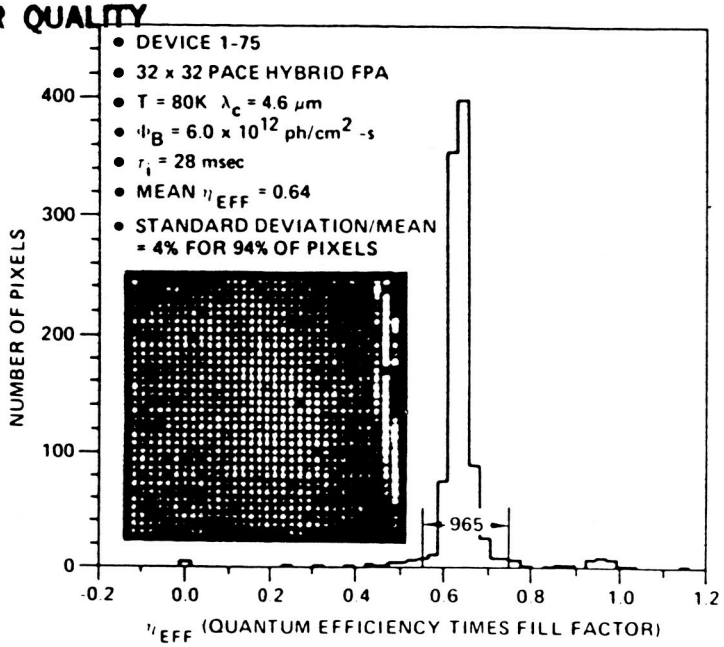

FIG 3. Histogram of the effective quantum efficiency of diodes in a 32x32 HgCdTe on sapphire FPA.

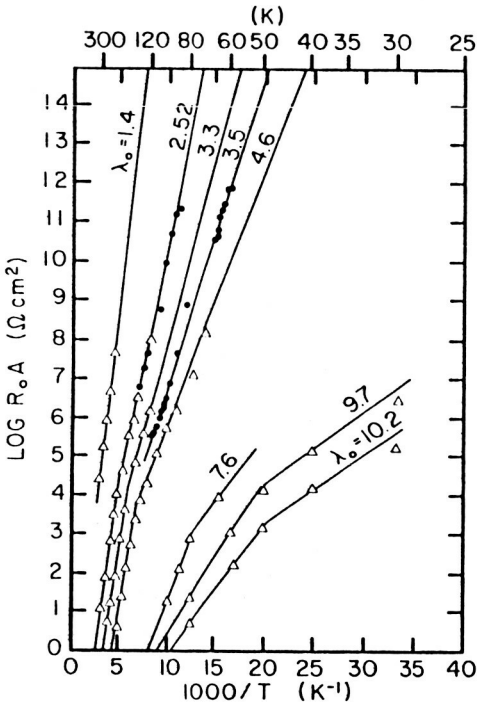

FIG 4. R_0A as a function of 1/T for several HgCdTe material samples with different cutoff wavelengths. The open triangles represent measurements made at Rockwell.[2] The measurments indicated by the closed circles were made at the University of Chicago and Goddard Space Flight Center.

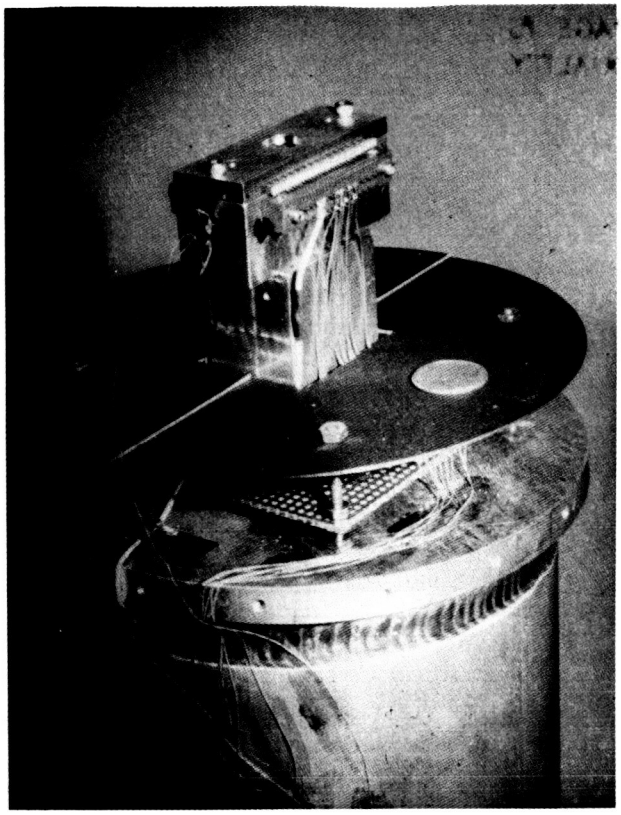

FIG 5. The hybrid FPA mounted in the dewar. The dewar cover and cold shield have been removed to expose the mounting hardware and electrical connections. The array is mounted on a cold finger attatched to the cold surface of the nitrogen reservoir.

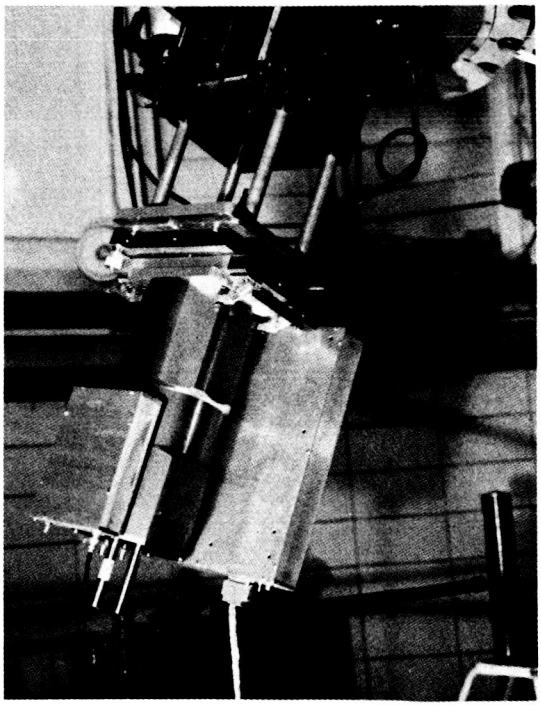

FIG 6. The SWIR camera mounted to the 24" telescope at Yerkes.

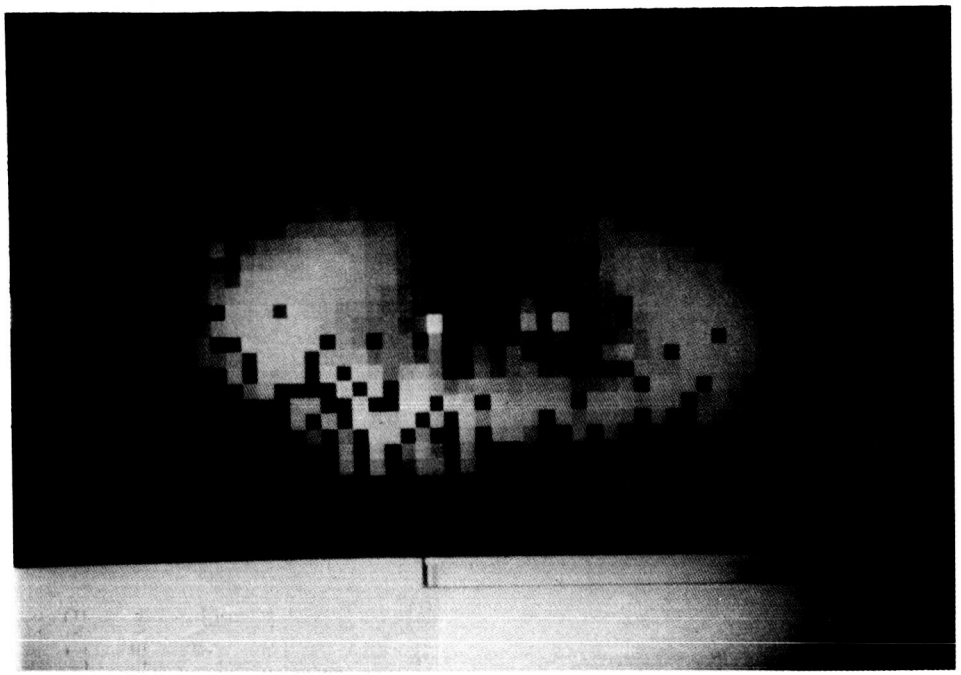

FIG 7. Saturn at 2.2 μm. In this unprocessed image of Saturn in the K-band the rings are evident. The disc is absent due to absorption in the gaseous atmosphere.

Si:As BIB DETECTOR ARRAYS*

R. Bharat, M. D. Petroff, J. J. Speer, and M. G. Stapelbroek

Rockwell International Science Center, Anaheim, CA

Highlights of the results obtained on arsenic-doped silicon blocked impurity band (BIB) detectors and arrays since the invention of the BIB concept a few years ago at Rockwell International are being presented here to the infrared astronomy community. After a brief introduction and a description of the BIB concept, data will be given first on single detector performance. Then different arrays that have been fabricated will be described and test data will be presented.

OUTLINE

Introduction

Detector theory

Detector performance

Array data

Summary

*Presented at the Infrared Detector Technology Workshop, NASA Ames Research Center, August 13-14, 1985. Part of the work was supported by a contract from NASA Ames (Monitor: Craig McCreight).

BIB DETECTORS

BIB DETECTORS WERE INVENTED AT ROCKWELL INTERNATIONAL AS A MEANS OF OBTAINING IMPROVED RADIATION HARDNESS IN INFRARED DETECTORS CAPABLE OF OPERATING AT LONG WAVELENGTHS. OTHER ADVANTAGES THAT HAVE ALSO ACCRUED ARE OF CONSIDERABLE IMPORTANCE TO PRACTICAL SYSTEM APPLICATIONS.

THE THINNESS OF THE ACTIVE REGION MAKES IT POSSIBLE TO DESIGN ARRAYS OF DETECTORS WITH VERY CLOSE SPACING WITHOUT INCREASING OPTICAL AND ELECTRICAL CROSSTALK. SINCE THE THIN ACTIVE LAYERS ARE OBTAINED BY EPITAXIAL DEPOSITION, UNIFORMITY OF DETECTOR CHARACTERISTICS IS SUPERIOR TO THAT OBTAINED WITH BULK PHOTOCONDUCTIVE DETECTORS WHICH ARE TYPICALLY FABRICATED FROM FLOAT-ZONED CRYSTALS. IN ADDITION, DUE TO THE DIFFERENCE IN THE PHYSICS OF OPERATION OF THE DEVICE, BIB DETECTORS DO NOT EXHIBIT THE VARIOUS ANOMALIES TYPICAL OF PHOTOCONDUCTIVE DETECTORS, AND THEY ARE NOT AS LIMITED IN THEIR FREQUENCY RESPONSE.

BIB DETECTORS

- INVENTED AT ROCKWELL TO PROVIDE INHERENTLY LESS NUCLEAR RADIATION SENSITIVITY WITHOUT COMPROMISING IR DETECTION PERFORMANCE

- DEMONSTRATED TO HAVE ADDITIONAL SIGNIFICANT ADVANTAGES

  - REDUCED CROSSTALK BETWEEN CLOSELY-SPACED DETECTORS IN ARRAY

  - FREE OF THE IRREGULAR BEHAVIOR TYPICAL OF PHOTOCONDUCTIVE DETECTORS

  - INCREASED FREQUENCY RANGE FOR CONSTANT RESPONSIVITY

  - SUPERIOR UNIFORMITY OF RESPONSE OVER AREA OF DETECTOR, AND, DETECTOR TO DETECTOR

IMPURITY BAND CONDUCTION

THIS FIGURE SHOWS THE ENERGY BAND DIAGRAM OF AN n-TYPE SEMICONDUCTOR (SUCH AS Si:As) MATERIAL UNDER AN APPLIED BIAS VOLTAGE*. SINCE THE DOPING DENSITY IS MADE HIGH IN ORDER TO MAINTAIN A HIGH QUANTUM EFFICIENCY EVEN WITH A THIN IR-ACTIVE LAYER, THE IMPURITY LEVEL EXHIBITS BAND-LIKE BEHAVIOR. IONIZED DONOR (D^+) CHARGES IN THE IMPURITY BAND CAN BE TRANSPORTED BY HOPPING IN THE PRESENCE OF AN ELECTRIC FIELD, RESULTING IN IMPURITY BAND CONDUCTION.

AN INCIDENT PHOTON OF SUFFICIENT ENERGY CREATES AN ELECTRON -D^+ PAIR AND BOTH CHARGES ARE COLLECTED RESULTING IN A PHOTOCONDUCTIVE GAIN OF 1. SINCE D^+ CHARGES ARE REMOVED FROM THE MATERIAL BY THE FIELD, ELECTRON RECOMBINATION LIFETIME IS VERY LONG. THE HIGH FREQUENCY RESPONSE IS LIMITED ONLY BY THE HOPPING MOBILITY OF THE D^+ CHARGES. DUE TO THE SPREADING OF THE IMPURITY LEVEL WITH HIGH DOPING, THE CUTOFF FOR IR RESPONSE EXTENDS TO LONGER WAVELENGTHS ; HOWEVER, IN ORDER TO KEEP DARK CURRENT DUE TO THERMAL IONIZATION LOW, THE TEMPERATURE OF OPERATION HAS TO BE SLIGHTLY REDUCED.

---

* ANALOGOUS DIAGRAMS CAN BE GENERATED FOR p-TYPE SEMICONDUCTORS

IMPURITY BAND CONDUCTION

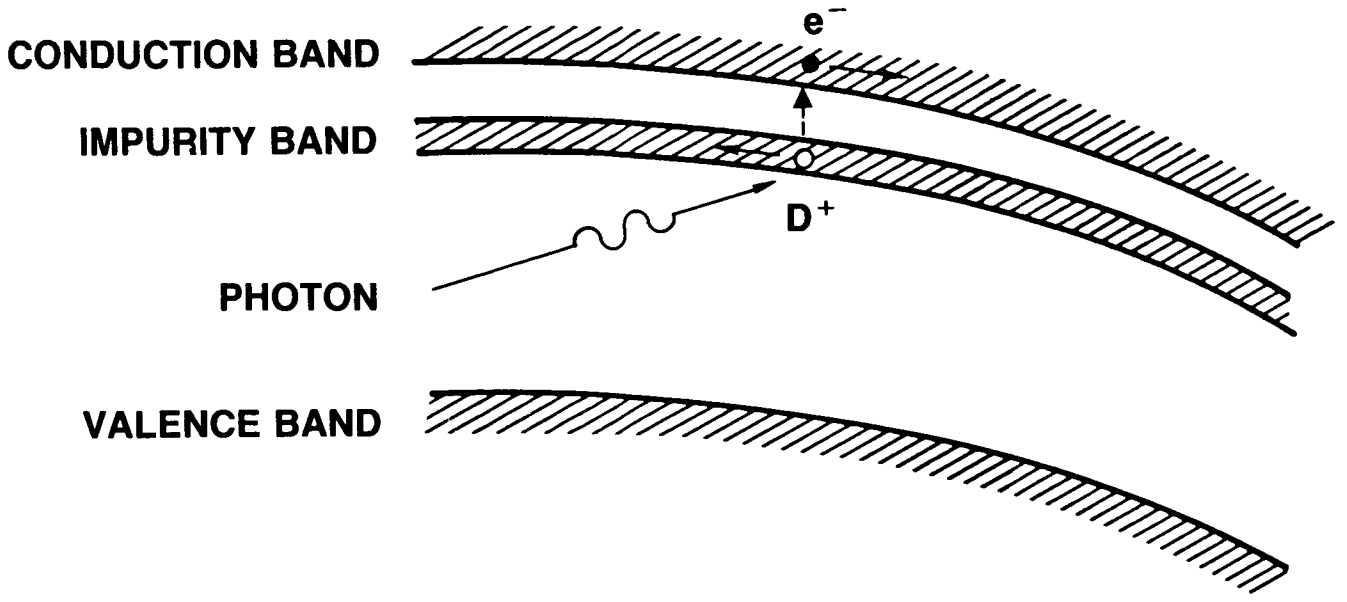

- PHOTON GENERATES ELECTRON (e^-) AND IONIZED DONOR (D^+)
- CURRENT DUE TO FLOW OF e^- IN CONDUCTION BAND AND D^+ IN IMPURITY BAND

BIB DETECTOR CONFIGURATION

ONE POSSIBLE CONFIGURATION FOR EXPLOITING IMPURITY BAND CONDUCTION FOR A PRACTICAL IR DETECTOR IS SHOWN HERE, USING AN n-TYPE SILICON IR-ACTIVE LAYER. *

THE HEAVILY-DOPED IR-ACTIVE LAYER AND THE UNDOPED BLOCKING LAYER ARE EPITAXIALLY DEPOSITED.

A BIAS VOLTAGE IS APPLIED BETWEEN THE (FRONT) TRANSPARENT CONTACT AND THE HEAVILY DOPED n-TYPE SUBSTRATE. THE BLOCKING LAYER PREVENTS D^+ INJECTION FROM THE FRONT CONTACT INTO THE IR-ACTIVE LAYER, SINCE IT IS UNDOPED AND CANNOT SUPPORT IMPURITY BAND CONDUCTION. HOWEVER, SINCE ELECTRONS ARE TRANSPORTED IN THE CONDUCTION BAND, THEY MOVE THROUGH THE BLOCKING LAYER AND ARE COLLECTED IN THE FRONT CONTACT.

---

* ANALOGOUS CONFIGURATIONS CAN BE USED WITH p-TYPE SEMICONDUCTORS

BIB DETECTOR CONFIGURATION

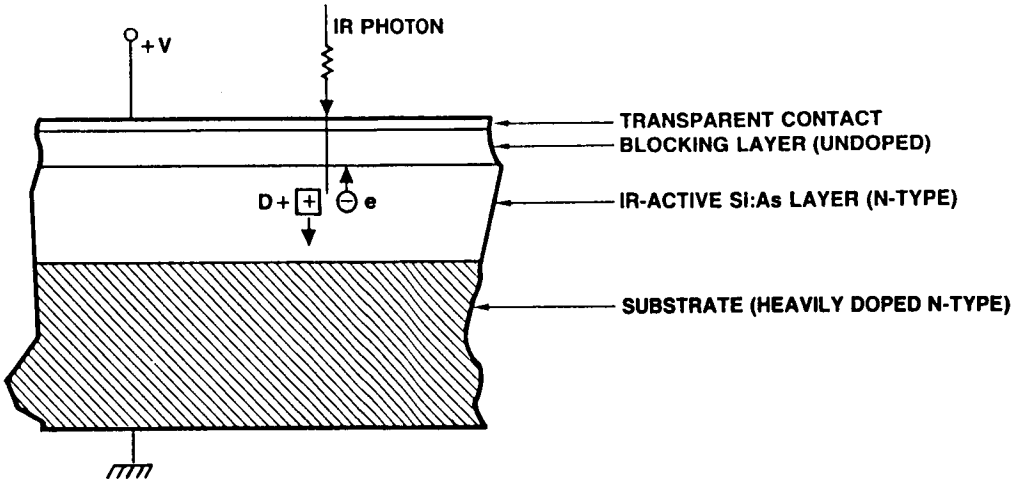

ELECTRON (e) TRANSPORT IS IN CONDUCTION BAND

IONIZED DONOR (D+) TRANSPORT IS IN IMPURITY BAND

SPECTRAL RESPONSE

THE RELATIVE SPECTRAL RESPONSE PEAKS AROUND 23 MICRONS. THE CUTOFF WAVELENGTH IS SOMEWHAT EXTENDED TO LONGER WAVELENGTHS THAN IS EXPECTED FOR Si:As OF LOW DOPING DENSITY.

INCREASING THE BIAS VOLTAGE INCREASES THE DEPLETION REGION AND HENCE THE COLLECTION VOLUME IN THE ARSENIC DOPED SILICON LAYERS; THE RESPONSIVITY THEN INCREASES AT ALL WAVELENGTHS.

THE SPECTRAL RESPONSE DATA WERE GENERATED BY THE NAVAL OCEAN SYSTEMS CENTER ON A BIB DETECTOR PROVIDED BY ROCKWELL.

SPECTRAL RESPONSE OF BIB DETECTOR AT VARIOUS BIAS VOLTAGES

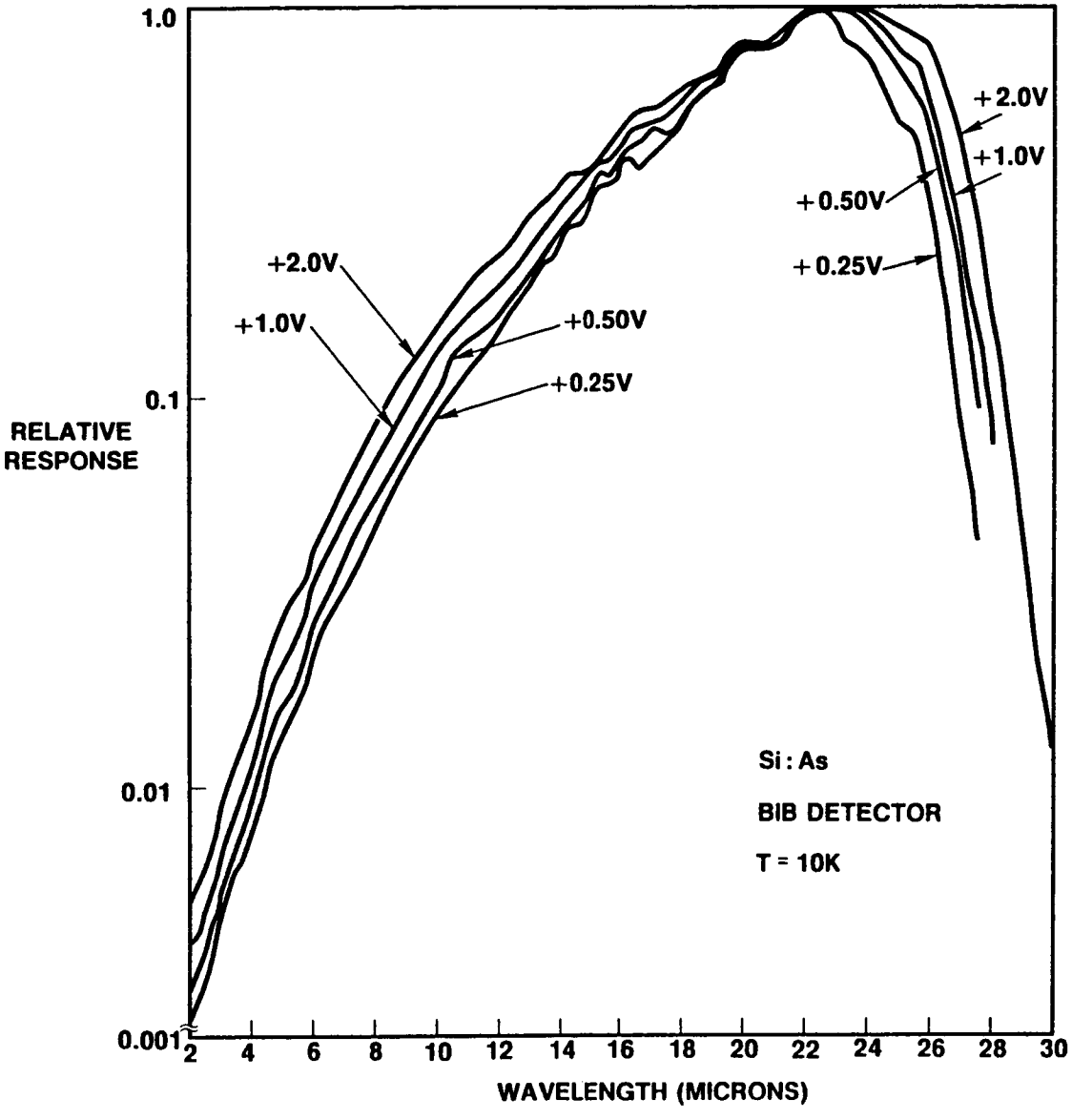

RESPONSIVITY

ABSOLUTE RESPONSIVITY OF AN ARSENIC-DOPED SILICON BIB DETECTOR WITH A 22 MICRON THICK IR-ACTIVE LAYER IS SHOWN HERE AS A FUNCTION OF DETECTOR BIAS. IT CAN BE SEEN THAT THE RESPONSIVITY IS EXCELLENT. THESE VALUES ARE REPRESENTATIVE OF ALL DETECTORS IN ARRAYS TO BE DISCUSSED LATER.

RESPONSIVITY OF BIB DETECTOR

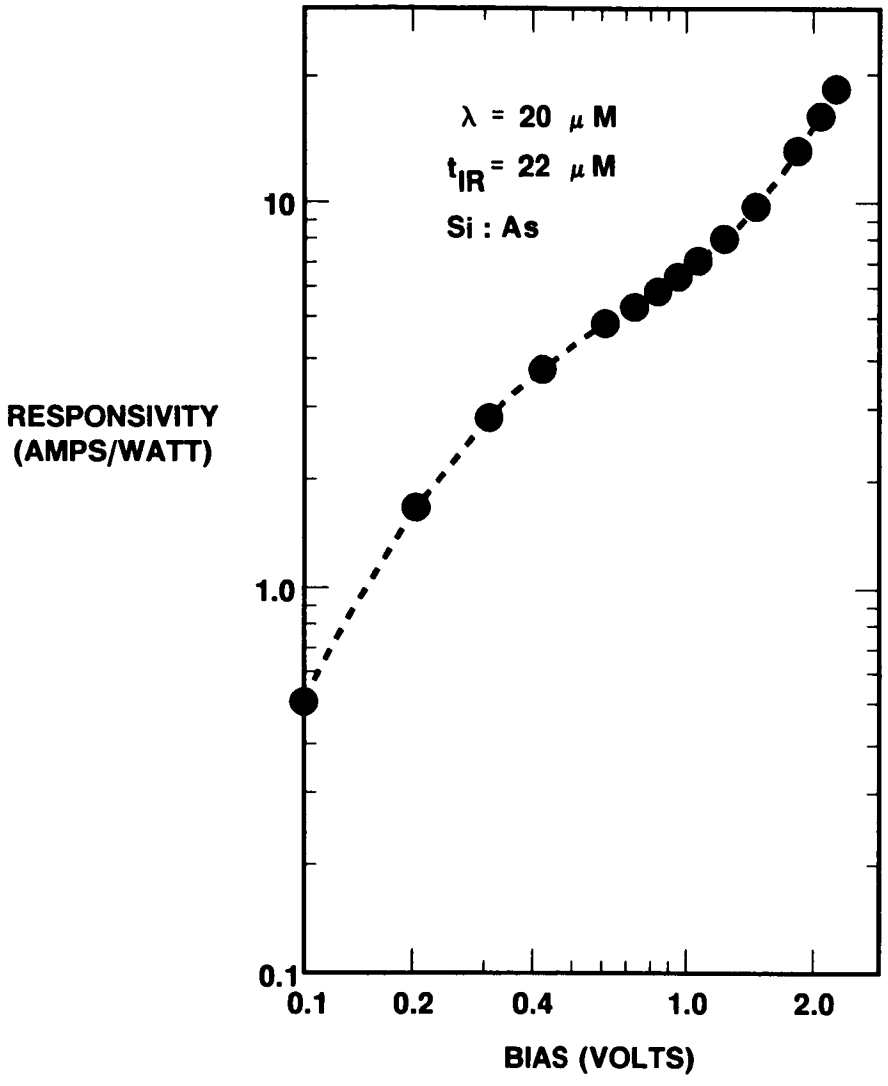

DARK CURRENT

MEASURED VALUES OF DARK CURRENT DENSITY (ELECTRONS/ CM^2-SEC) AT SEVERAL TEMPERATURES ARE SHOWN HERE FOR A Si:As BIB DETECTOR AT A BIAS OF 1.5V. THE DARK CURRENT FOR A $(100\ MICRONS)^2$ DETECTOR OPERATING AT 7K CAN BE PROJECTED TO BE LESS THAN 2 ELECTRONS/SECOND.

DARK CURRENT Si:As BIB DETECTOR

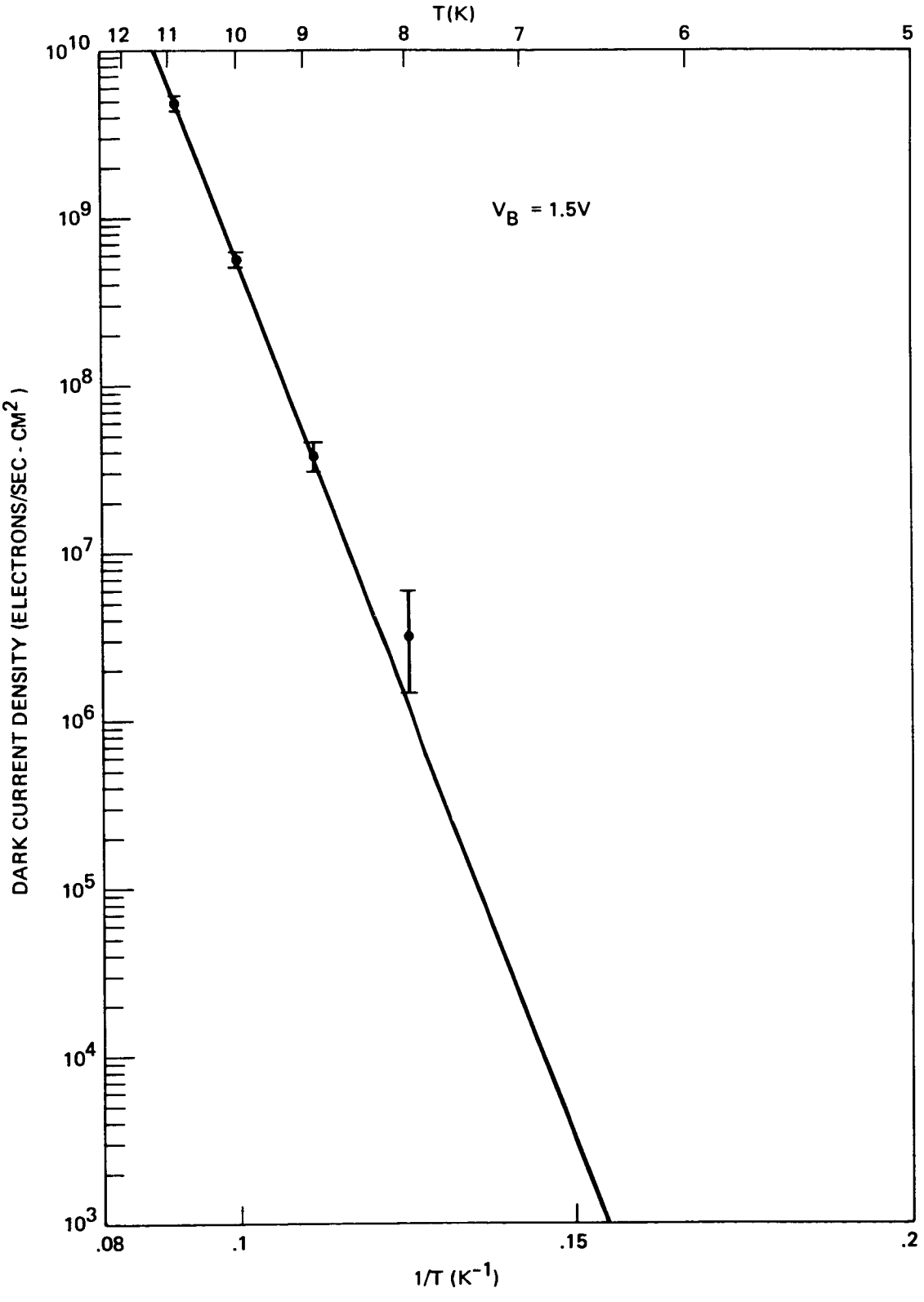

THE NOISE EQUIVALENT POWER (NEP) OF A Si:As BIB DETECTOR WAS CALCULATED FROM MEASURED VALUES OF DARK CURRENT DENSITY USING A SHOT NOISE MODEL AND ASSUMING A PHOTOCONDUCTIVE GAIN OF UNITY. THE MEASUREMENTS WERE MADE BETWEEN 6 AND 16K FOR THE DETECTOR OPERATING TEMPERATURE AT A BIAS OF 1.5V. IT CAN BE SEEN THAT BIB DETECTORS ARE CAPABLE OF BEING BACKGROUND LIMITED AT PHOTON ARRIVAL RATES N_B CLOSE TO 10^3 PER SECOND (ASSUMING PHOTON WAVELENGTH OF 20 MICRONS AND A QUANTUM EFFICIENCY OF 50% ON A DETECTOR WITH NO ANTI-REFLECTION COATING). IN ORDER TO OBTAIN THE NEP OF 10^{-18} W/$\sqrt{\text{Hz}}$, IMPROVED AMPLIFIERS ARE NEEDED FOR READING OUT THE SIGNAL FROM THE DETECTOR.

NEP OF BIB DETECTOR

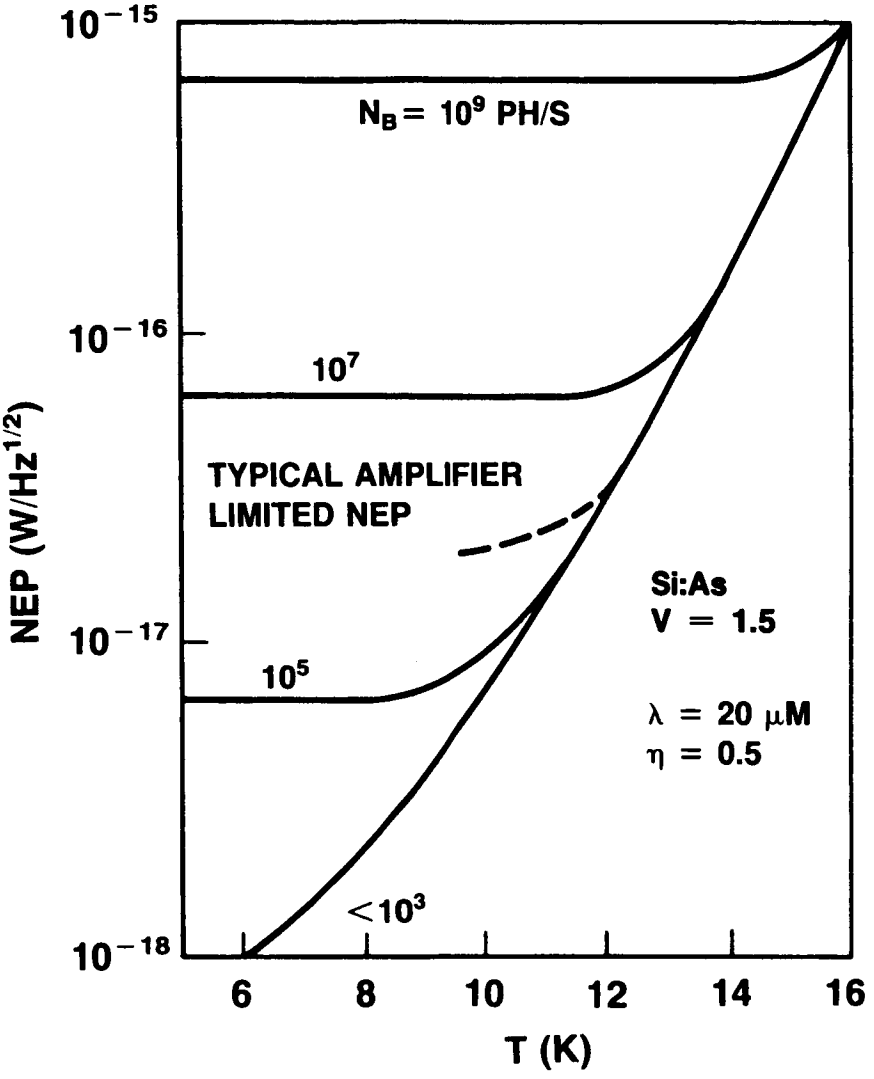

FREQUENCY RESPONSE

THE SUPERIORITY OF THE FREQUENCY RESPONSE OF BIB DETECTORS IS CLEARLY DEMONSTRATED IN THIS COMPARISON WITH EXTRINSIC SILICON PHOTOCONDUCTIVE (ESPC) DETECTORS AT VARIOUS PHOTON ARRIVAL RATES.

THE ESPC DETECTOR EXHIBITS THE FAMILIAR ROLL-OFF IN RESPONSIVITY (CORRESPONDING TO A DROP IN PHOTOCONDUCTIVE GAIN), WITH THE FREQUENCY OF ROLL-OFF DETERMINED BY THE PHOTON FLUX.

THE BIB DETECTOR, HOWEVER, HAS A FLAT FREQUENCY RESPONSE, INDEPENDENT OF PHOTON FLUX. THE SLIGHT SCATTER WAS DUE TO THE MEASUREMENT SET UP, WHICH HAS SINCE BEEN IMPROVED. RECENT MEASUREMENTS HAVE ALSO BEEN EXTENDED BEYOND 2 KHz AND SHOW THAT BIB DETECTOR RESPONSE STAYS FLAT OVER THAT RANGE.

FREQUENCY RESPONSE OF BIB AND ESPC DETECTORS

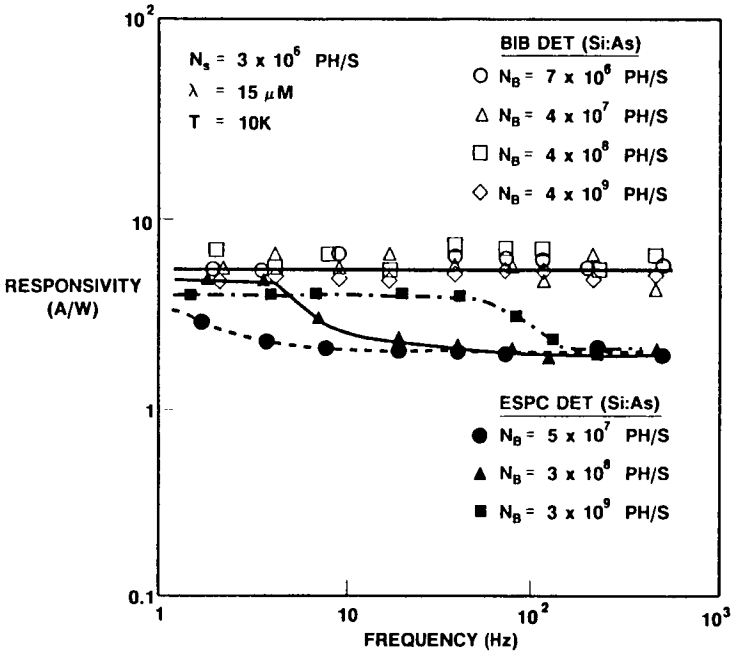

- BIB DETECTOR RESPONSE IS INDEPENDENT OF BACKGROUND AND FREQUENCY
- ESPC DETECTOR RESPONSE SHOWS TYPICAL BACKGROUND- AND FREQUENCY-DEPENDENT GAIN SATURATION EFFECT

AT LOW IR FLUX LEVELS, ESPC DETECTORS HAVE BEEN KNOWN TO EXHIBIT A VARIETY OF ANOMALIES IN ADDITION TO THE LONG TIME CONSTANT FOR RESPONSE BUILD UP. BIB DETECTORS, HOWEVER, DO NOT EXHIBIT ANY OF THESE PROBLEMS AT THEIR NORMAL OPERATING TEMPERATURES, I.E. ABOVE 6K. CALIBRATION OF DETECTOR RESPONSE CAN, THEREFORE, BE UNIQUE AND CAN BE RELIED UPON WHEN BIB DETECTORS ARE USED IN SYSTEMS.

COMPARISON OF STEP RESPONSE FOR ESPC AND BIB DETECTORS

- EQUIVALENT RESPONSIVITY AND DETECTIVITY FOR BOTH DETECTORS
- ESPC DETECTOR RESPONSE EXHIBITS ANOMALIES
- BIB DETECTOR RESPONSE FOLLOWS IR EXCITATION UNDER LOW BACKGROUND CONDITION

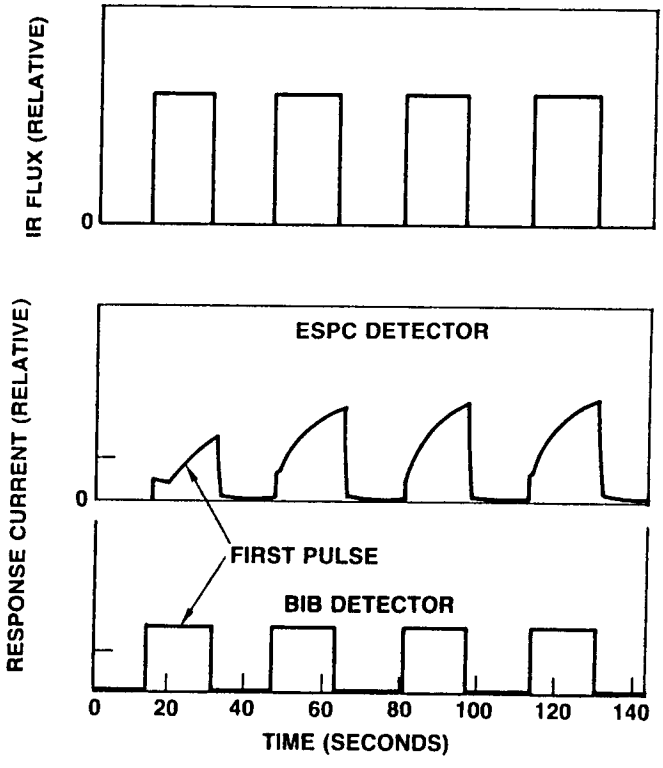

CROSSTALK

THIS FIGURE REPRESENTS SCHEMATICALLY THE INHERENT ADVANTAGE BIB DETECTORS HAVE OVER EXTRINSIC SILICON PHOTO-CONDUCTIVE (ESPC) DETECTORS FOR CLOSELY SPACED ARRAYS. WHILE THE ESPC DETECTOR IN AN ARRAY MAY COLLECT CHARGE CARRIERS FROM UNDER SEVERAL DETECTORS, GIVING HIGH CROSSTALK, THE SUPERIOR ASPECT RATIO OF THE ACTIVE REGION OF THE BIB DETECTOR RESULTS IN VERY MUCH LOWER CROSSTALK.

CROSSTALK IN ESPC AND BIB DETECTOR ARRAYS

ESPC DETECTOR ARRAY GEOMETRY

BIB DETECTOR ARRAY GEOMETRY

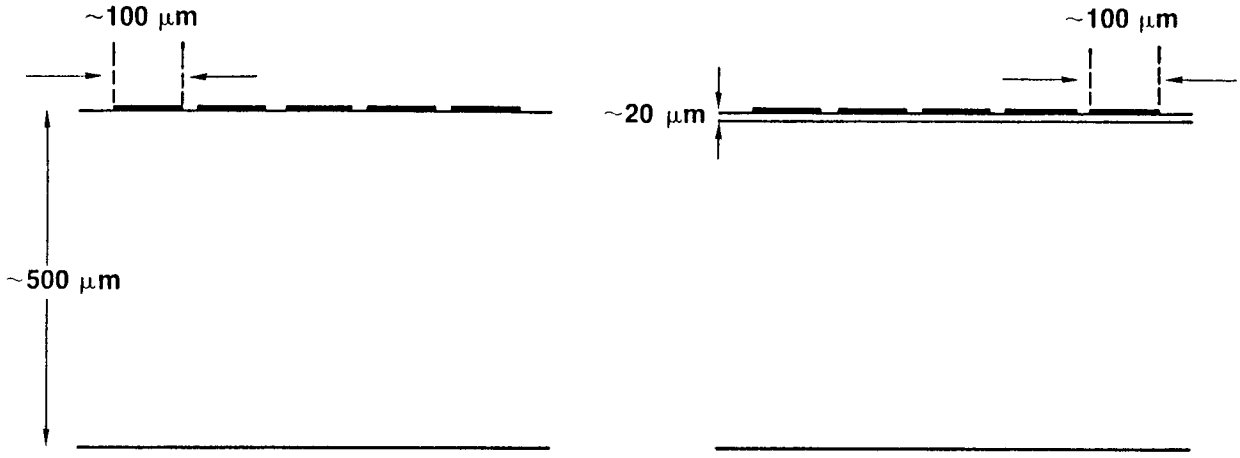

BIB DETECTOR HAS SUPERIOR ASPECT RATIO AND, HENCE, REDUCED CROSSTALK IN ARRAY STRUCTURE

BIB DETECTOR TEST DEVICES

AT THE LOWER RIGHT PART OF THE FIGURE IS A 10x1 ARRAY OF BIB DETECTORS, EACH OF WHICH IS BROUGHT OUT TO A SEPARATE BONDING PAD. AREA OF EACH DETECTOR IS 100 MICRONS x 250 MICRONS; SPACING IS 25 MICRONS.

THIS ARRAY WAS CHARACTERIZED UNDER CONTRACT TO NASA-AMES.

ORIGINAL PAGE IS
OF POOR QUALITY

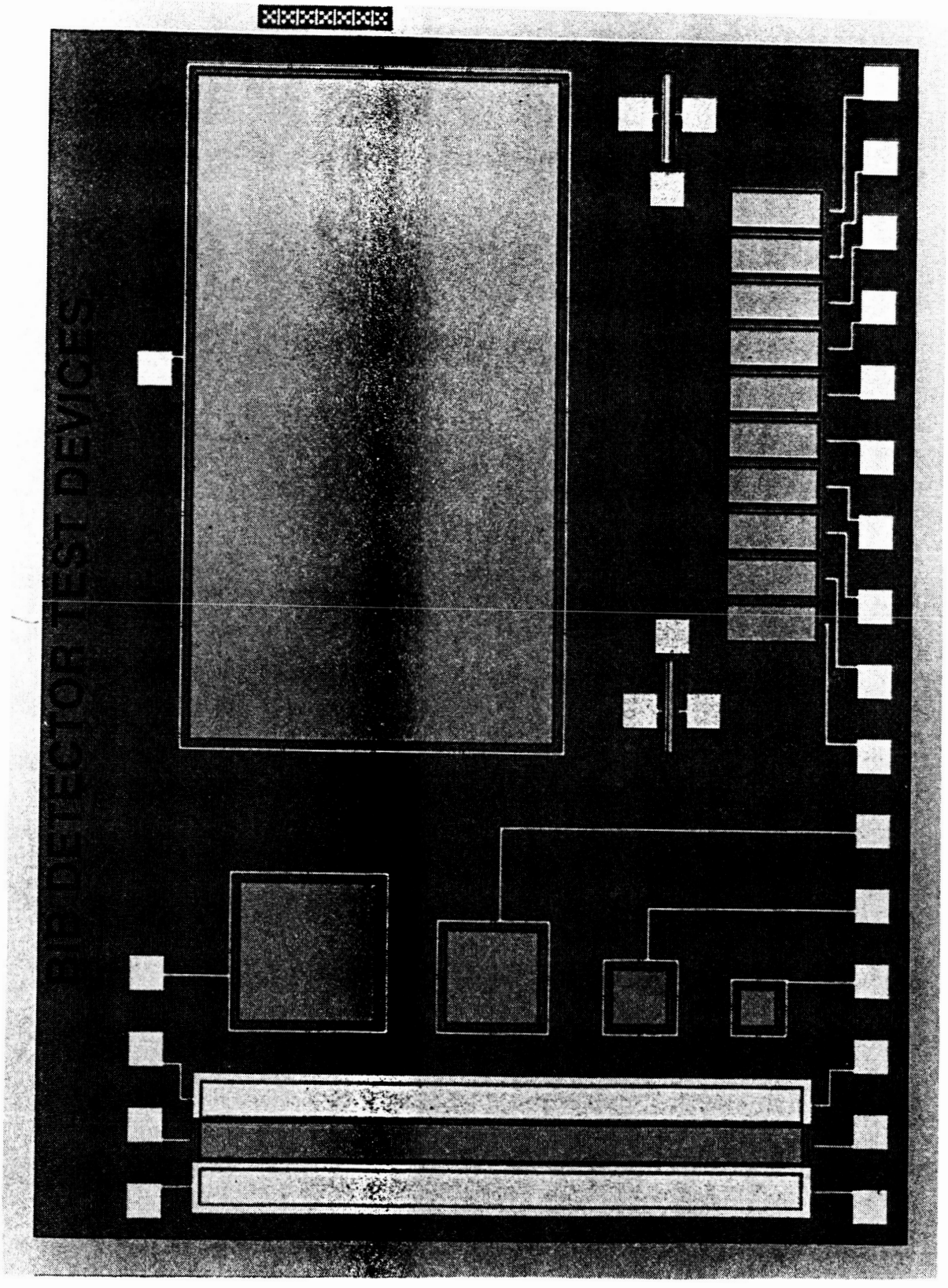

AC TEST CONFIGURATION

EACH DETECTOR WAS BIASED THROUGH A LOAD RESISTOR AND ITS OUTPUT WAS MEASURED USING A JFET IN A SOURCE FOLLOWER CONFIGURATION. THE JFET WAS ONE HALF OF A JFET PAIR WHICH WAS FURNISHED TO ROCKWELL BY NASA-AMES.

AC TEST CONFIGURATION

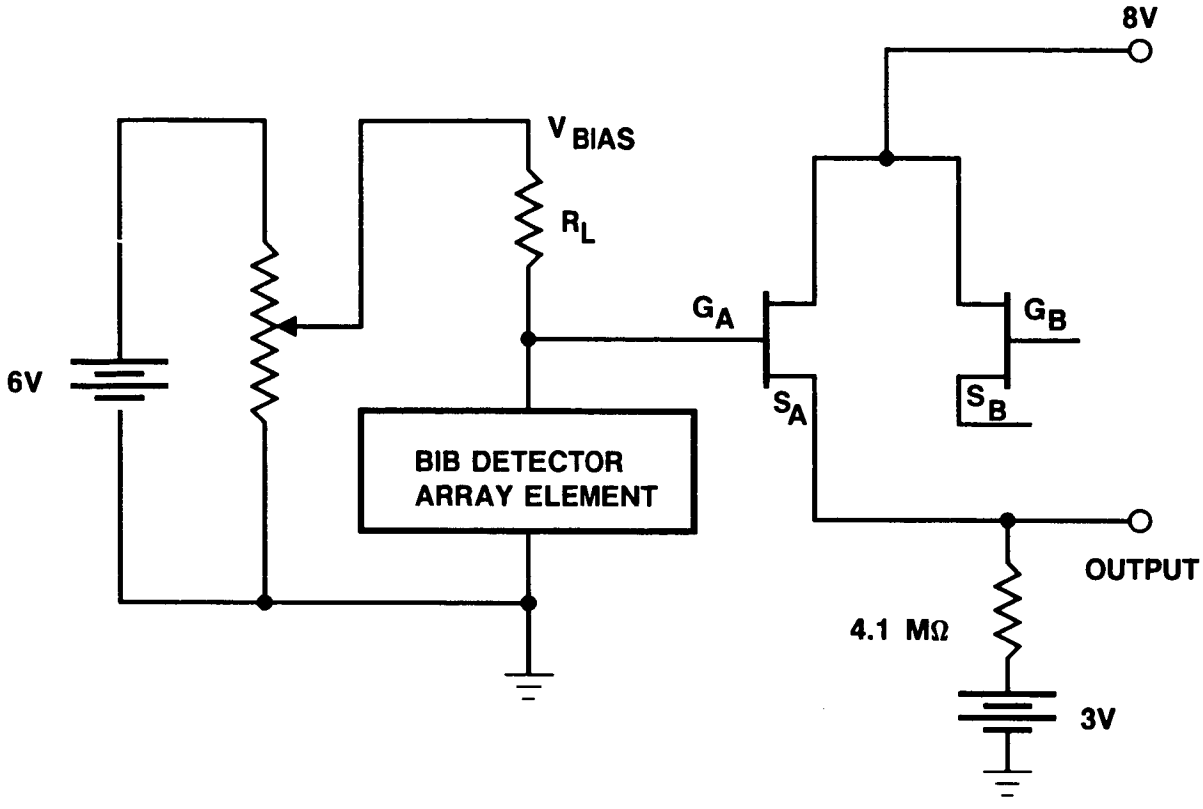

HEAT SINK AND ARRAY ASSEMBLY

THE DETECTOR ARRAY WAS MOUNTED ON A CARRIER WHICH WAS ATTACHED TO A HEAT SINK WHOSE TEMPERATURE WAS CONTROLLABLE BETWEEN 4.2 AND 16K. THE JFETs WERE THERMALLY ISOLATED FROM THE HEAT SINK SINCE THEY OPERATED AT A MUCH HIGHER TEMPERATURE.

ONE ASSEMBLY AS SHOWN WAS DELIVERED TO NASA-AMES AFTER CHARACTERIZATION.

HEAT SINK AND ARRAY ASSEMBLY

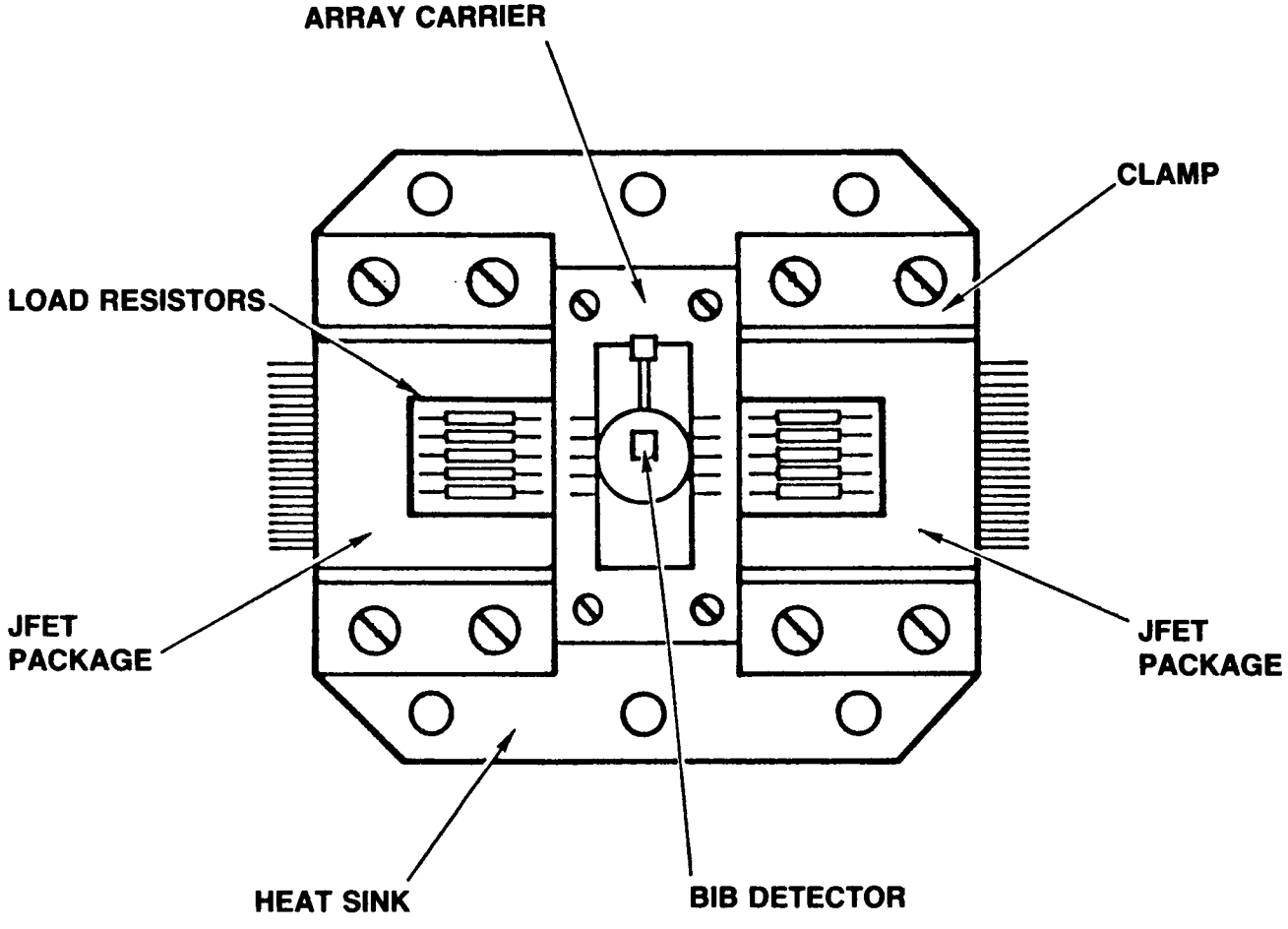

RESPONSE UNIFORMITY

RESPONSIVITIES OF TWENTY DETECTORS (TWO 10x1 ARRAYS) WERE MEASURED AS FUNCTIONS OF BIAS VOLTAGE. SINCE THE CURVES FOR THE DETECTORS ARE VERY SIMILAR, THEY ARE INDISTINGUISHABLE IN THE FIGURE. THE PEAK-TO-PEAK VARIATION AT ANY BIAS IN THE MEASUREMENT RANGE WAS LESS THAN $\pm$ 5%. THE MEASUREMENTS WERE MADE WITH AN INPUT FLUX OF 1.25×10^{10} PHOTONS/SECOND FROM A PULSED 3.2 MICRON WAVELENGTH LIGHT-EMITTING DIODE. THIS HIGH DEGREE OF UNIFORMITY IS DUE PRIMARILY TO THE FORMATION OF THE IR-ACTIVE REGION BY EPITAXIAL TECHNIQUES.

COMBINING THIS DATA WITH THE RELATIVE SPECTRAL RESPONSE DATA SHOWN EARLIER, THE RESPONSIVITY OF THESE DETECTORS TO 24 MICRON PHOTONS CAN BE CALCULATED TO BE 13 AMPS/WATT AT A BIAS OF 1.75V.

UNIFORMITY OF DC RESPONSE OF BIB DETECTORS

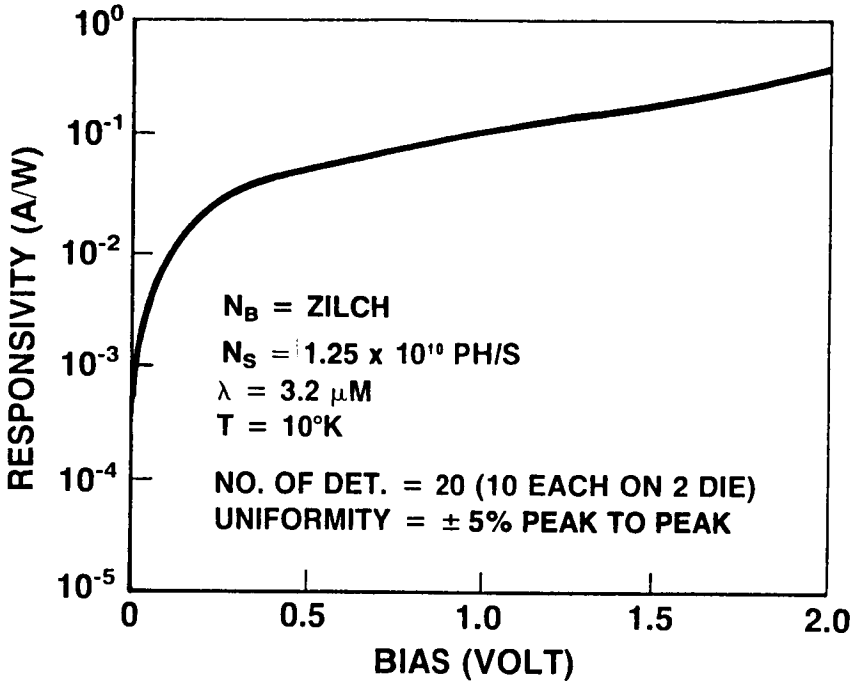

- OUTSTANDING UNIFORMITY DUE TO FABRICATION METHOD USED IN BIB DETECTORS — ACTIVE REGION IS IN EPITAXIALLY GROWN SILICON

  (BULK SILICON USED FOR ESPC DETECTORS HAS STRIATIONS WHICH CAUSE RESPONSE NON-UNIFORMITIES)

6x6 BIB DETECTOR ARRAY

THIS PHOTOGRAPH SHOWS A 36-ELEMENT ARRAY OF (150 MICRONS)^2 DETECTORS, WITH 50-MICRON SPACING. EACH DETECTOR IS BROUGHT OUT TO A SEPARATE BONDING PAD. MEASUREMENTS WERE MADE ON EACH DETECTOR BY CONNECTING AN EXTERNAL AMPLIFIER TO THE PADS.

6 x 6 BIB DETECTOR ARRAY

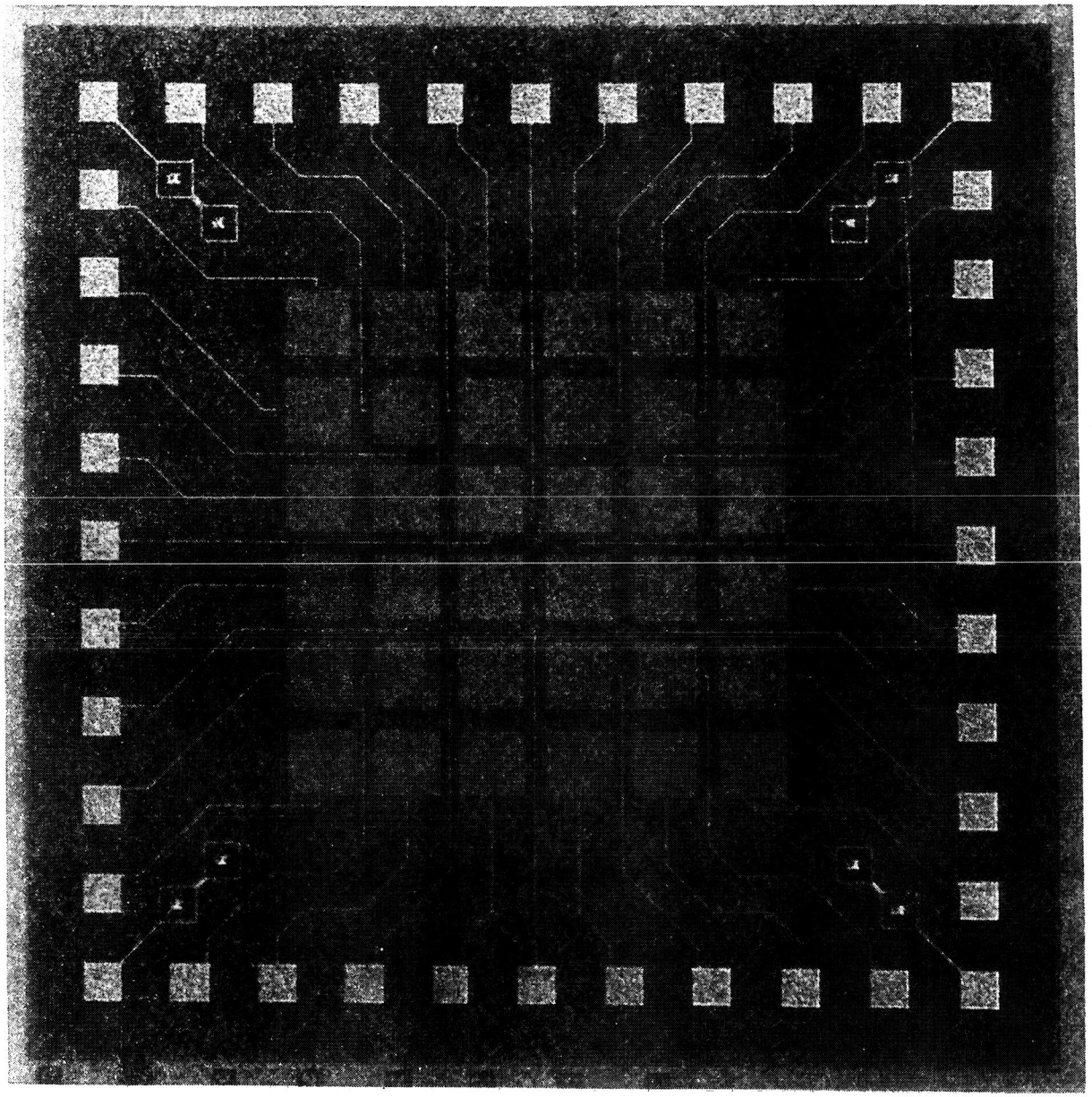

RESPONSIVITY OF 36 ELEMENT BIB DETECTOR ARRAY

THE NUMBER SHOWN WITHIN EACH DETECTOR IN THIS SCHEMATIC OF THE ARRAY IS THE RESPONSIVITY OF THAT DETECTOR IN AMPS/WATT TO 3.2 MICRON RADIATION FROM A LIGHT-EMITTING DIODE. THE MEASUREMENTS WERE MADE WITH A SIGNAL FLUX OF 4.5×10^{8} PHOTONS/SEC. AND ZILCH BACKGROUND FLUX. THE RESPONSIVITIES IN THE ARRAY ARE VERY UNIFORM, WITH THE STANDARD DEVIATION BEING LESS THAN 1.7% OF THE MEAN.

THE DARK CURRENTS WERE ALSO VERY LOW. THE UPPER LIMIT OF 0.1 pA PER DETECTOR WAS SET BY THE LIMITATIONS OF THE MEASUREMENT SYSTEM.

RESPONSIVITY OF 36 ELEMENT BIB DETECTOR ARRAY

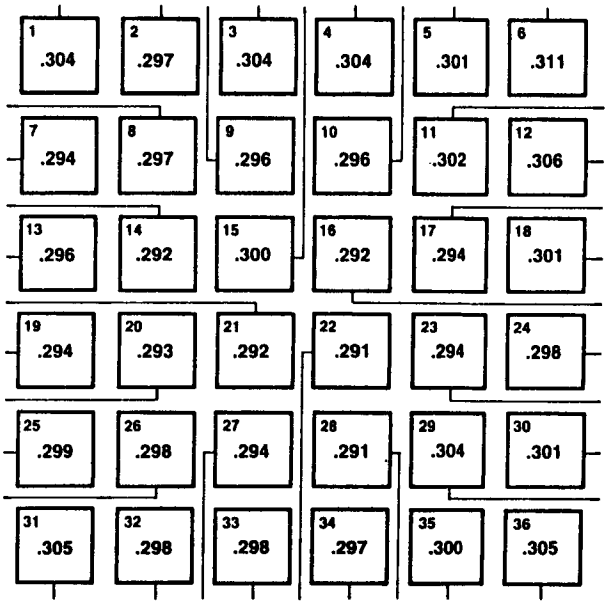

SI: As, 0.015 × 0.015 CM^2 ON 0.02 CM CENTERS

TEMPERATURE	10 K
BIAS	1.5 V
FREQUENCY	100 Hz
DARK CURRENT (EACH DETECTOR)	$<10^{-13}$ A

RESPONSIVITY SHOWN IN A/W
AT λ = 3.2 μm
MEAN = 0.298 A/W
σ = 0.005 A/W

EQUIVALENT RESPONSIVITY AT
λ = 20 μm
MEAN = 9.3 A/W
σ = 0.15 A/W

10x50 BIBIB DETECTOR ARRAY

THIS PHOTOGRAPH SHOWS AN ARRAY OF (125 MICRONS)^2 DETECTORS WITH 25 MICRON SPACING. THE 500 DETECTORS IN THE BACK ILLUMINATED BLOCK IMPURITY BAND (BIBIB) ARRAY HAVE TO BE READ OUT BY A MULTIPLEXER THAT IS BONDED TO THE FRONT OF THE DETECTOR ARRAY BY A METAL BUMP AT EACH DETECTOR LOCATION.

10 x 50 BIBIB DETECTOR ARRAY

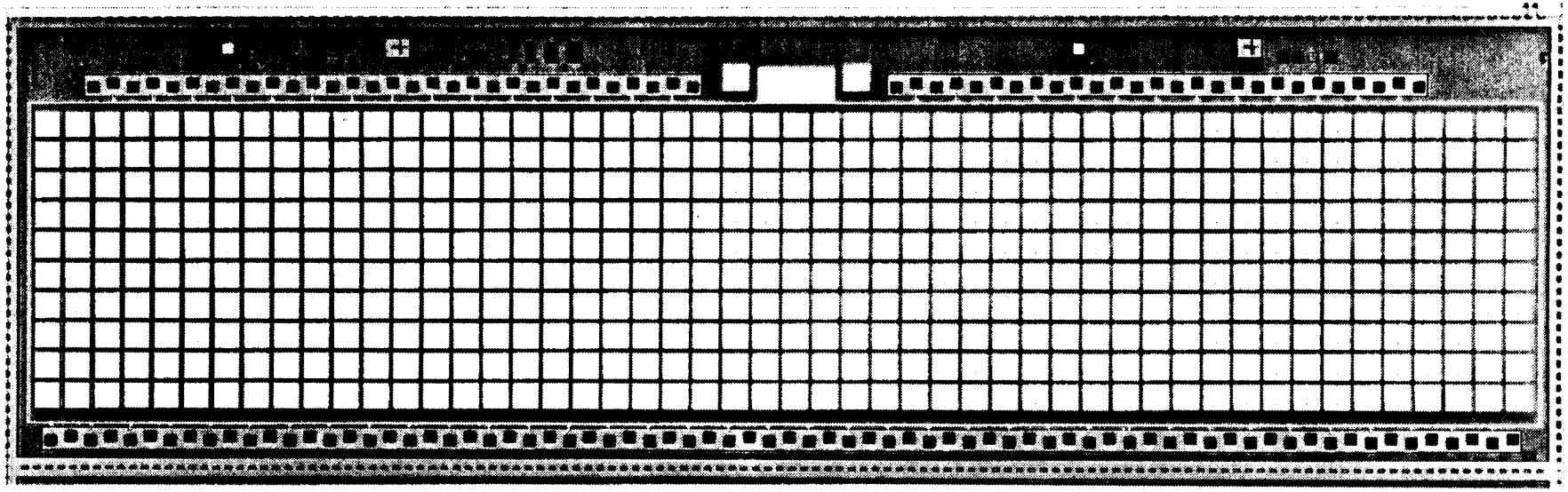

MULTIPLEXED BIBIB DETECTOR ARRAY

ONE POSSIBLE CONFIGURATION FOR A BIBIB FOCAL PLANE ARRAY IS SHOWN IN THIS SCHEMATIC CROSS SECTION (NOT TO SCALE). SINCE THE ILLUMINATION IS THROUGH THE SUBSTRATE, THE SILICON SUBSTRATE HAS TO BE TRANSPARENT AND HENCE UNDOPED. THE BACK CONTACT HAS TO BE PROVIDED BY A THIN BURIED LAYER WHICH HAS TO MEET CONFLICTING REQUIREMENTS OF TRANSPARENCY TO IR AND GOOD ELECTRICAL CONDUCTIVITY AT THE LOW OPERATING TEMPERATURES.

THE MULTIPLEXER ACQUIRES DETECTOR SIGNALS IN PARALLEL AND READS THEM OUT SERIALLY WITH THE HELP OF APPROPRIATE CLOCKING SCHEMES. IT HAS TO BE COMPATIBLE WITH THE DETECTOR IN TERMS OF PHYSICAL DIMENSIONS, THERMAL EXPANSION, ELECTRICAL CHARACTERISTICS, OPERATING TEMPERATURE AND HYBRID FOCAL PLANE FABRICATION.

BY PROVIDING A REFLECTING SURFACE ON THE FRONT SIDE OF THE DETECTORS, THE IR RADIATION CAN BE REFLECTED TO PROVIDE A SECOND PASS THROUGH THE DETECTORS AND INCREASE QUANTUM EFFICIENCY.

ALL THESE ASPECTS HAVE BEEN SATISFACTORILY RESOLVED AT ROCKWELL INTERNATIONAL.

MULTIPLEXED BACK ILLUMINATED BIB DETECTOR ARRAY

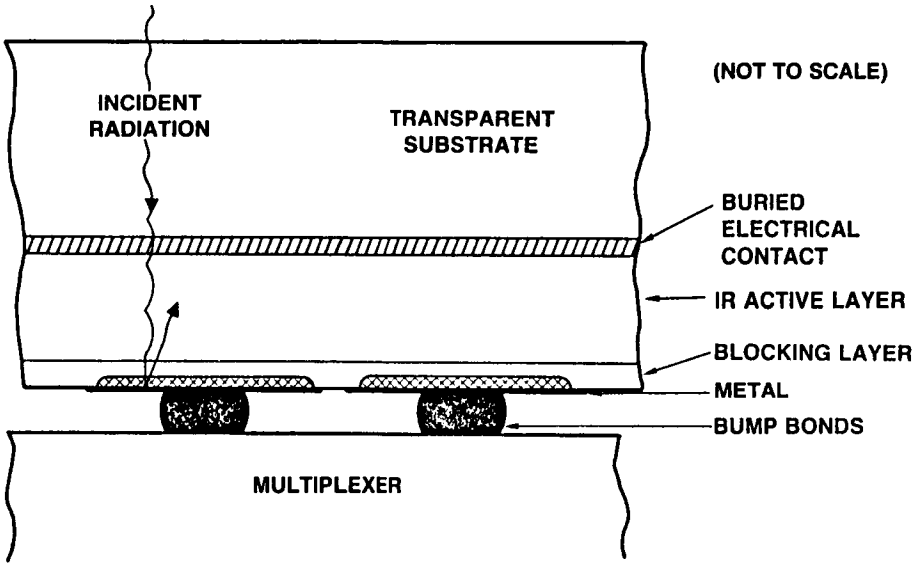

BIBIB DETECTOR/SWIFET MULTIPLEXER HYBRID FOCAL PLANE ARRAY

THIS PHOTOGRAPH SHOWS A HYBRID FOCAL PLANE ARRAY CONSISTING OF A BIBIB DETECTOR ARRAY BUMP-BONDED TO A SWITCHED MOSFET (SWIFET) MULTIPLEXER. THE HYBRID ARRAY IS MOUNTED ON A PACKAGE, AND THE LEADS ARE BROUGHT OUT FROM THE MULTIPLEXER BONDING PADS. THE CENTRAL RECTANGLE IS THE BACK SURFACE OF THE 10x50 DETECTOR ARRAY WHICH OBSCURES THE MAJOR PART OF THE MULTIPLEXER CHIP.

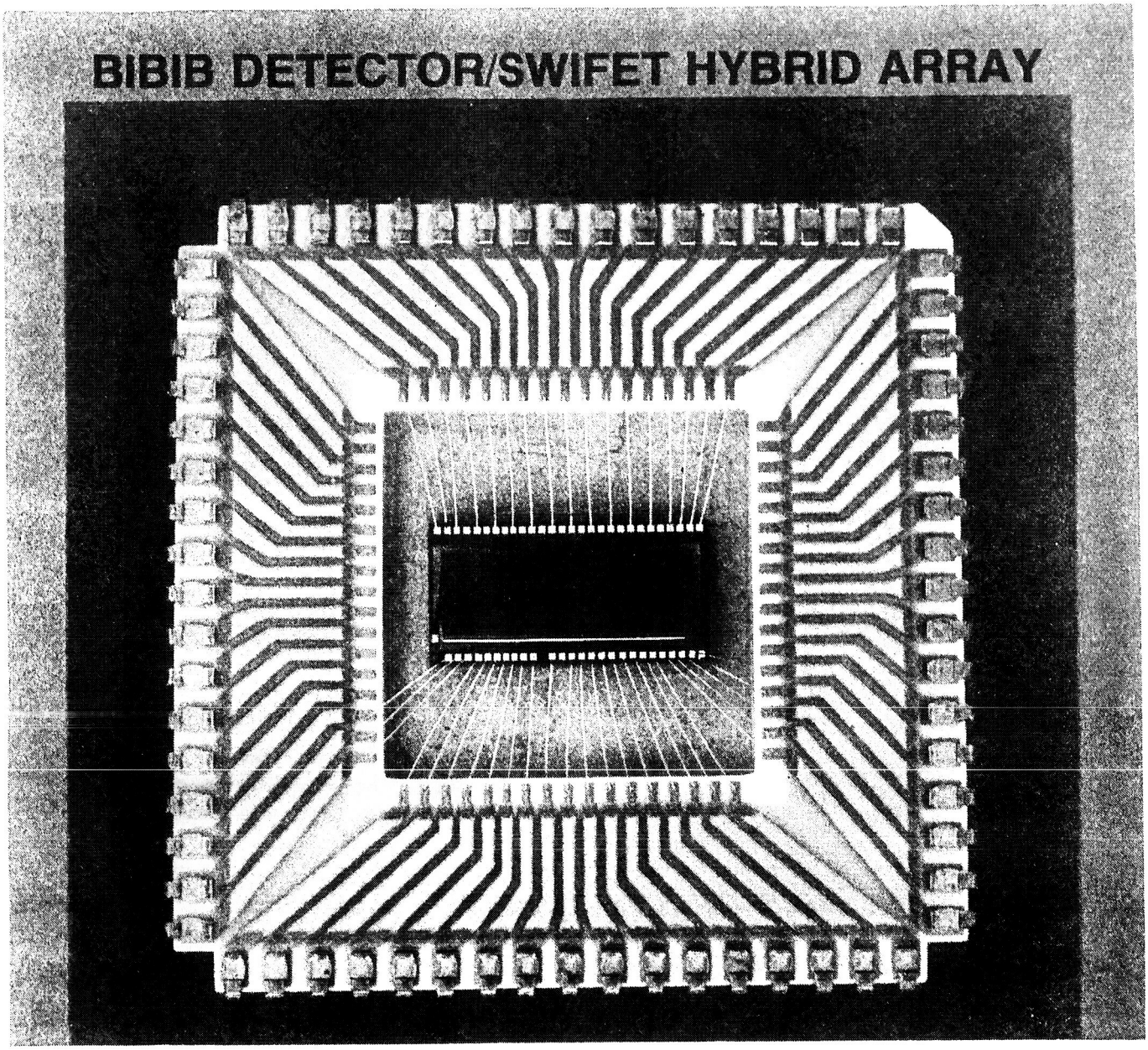

BIBIB/SWIFET HYBRID ARRAYS

SEVERAL HYBRID FOCAL PLANES HAVE BEEN FABRICATED WITH ALL 500 INTERCONNECTS OPERATIONAL. A VARIETY OF MEASUREMENTS THAT HAVE BEEN USEFUL BOTH FOR CHARACTERIZING ARRAYS AND FOR COMPILING STATISTICAL DATA ON LARGE NUMBERS OF DETECTORS HAVE BEEN MADE. RESULTS OF THESE MEASUREMENTS WILL BE PRESENTED ELSEWHERE.

BIBIB/SWIFET HYBRID ARRAYS

- **BIBIB/SWIFET HYBRIDS SUCCESSFULLY FABRICATED**
- **EXCELLENT INTERCONNECT YIELD (~100%) ACHIEVED**
- **OPTICAL AND ELECTRICAL CHARACTERIZATION MEASUREMENTS CONDUCTED**
  - — DARK CURRENT
  - — RESPONSIVITY, NOISE, NEP
  - — CROSSTALK
  - — WAVELENGTHS - 10μm AND 20μm
  - — SINGLE ELEMENT AND ARRAY MEASUREMENTS

SUMMARY

BIB DETECTORS HAVE BEEN SHOWN TO HAVE EXCELLENT PERFORMANCE AND TO EXHIBIT SEVERAL ADVANTAGES COMPARED TO EPC DETECTORS FOR LOW BACKGROUND APPLICATIONS.

FRONT- AND BACK-ILLUMINATED ARRAY STRUCTURES WITH INDIVIDUAL AND MULTIPLEXED READOUTS HAVE ALSO BEEN DEMONSTRATED.

SOME OF THESE DETECTORS AND ARRAYS HAVE ALSO BEEN TESTED AT NASA-AMES, NASA-GODDARD, KITT PEAK OBSERVATORY AND MT. LEMMON OBSERVATORY.

BIB DETECTORS AND ARRAYS ARE OBVIOUS CANDIDATES FOR LOW BACKGROUND INFRARED ASTRONOMY MISSIONS LIKE COBE AND SIRTF.

Si:As BIB DETECTOR ARRAYS

SUMMARY

- **EXCELLENT LWIR DETECTION DEMONSTRATED**
  - — SPECTRAL RESPONSE
  - — RESPONSIVITY
  - — NEP
  - — FREQUENCY RESPONSE
  - — CALIBRATABILITY
  - — CROSSTALK
  - — ARRAY UNIFORMITY
- **SEVERAL ARRAY STRUCTURES DEMONSTRATED**
  - — 10 × 1, FRONT ILLUMINATED, INDIVIDUAL READOUT
  - — 6 × 6, FRONT ILLUMINATED, INDIVIDUAL READOUT
  - — 10 × 50, BACK ILLUMINATED, MULTIPLEXED READOUT
- **SUPERIOR PERFORMANCE FOR LOW BACKGROUND IR ASTRONOMY APPLICATIONS**

A STUDY OF Si:In HYBRID SURFACE CHANNEL IRCCD DEVICES

Eric Tollestrup and Richard W. Capps

University of Hawaii, Institute for Astronomy
2680 Woodlawn Drive, Honolulu, Hawaii 96822

I. INTRODUCTION

Hybrid silicon IRCCDs are one of several different technologies being evaluated for use as viable astronomical detectors. We report on a continuing effort to characterize an experimental IRCCD made by Rockwell International. This detector was described earlier by Pommerrenig et al. (1983) at the first NASA-Ames Workshop on Infrared Detector Technology. The device is a Si:In photoconductor array which is bump-bonded to a silicon multiplexer. The multiplexer is a 32 x 32 pixel, four-phase surface channel CCD with 88 μm separation between pixel centers. The CCD has overflow protection, and electrical fat zero (FZ) can be injected at various locations along the signal's clocking path. A summary of the device parameters is given in Table 1.

Table 1. Typical 32x32 IRCCD Performance

Parameter	Minimum	Typical	Maximum
Spectral response (μm)	2.0		7.5
Operating temperature (K)	10	30	45
Array configuration (pixels)		32 x 32	
Cell size (μm)		88	
Dynamic range		10^4:1	
CTE (f = 500 kHz, FZ = 0)		0.98	
CTE (f = 500 kHz, FZ = 2V)		0.9998	
Noise (electrons, rms)	750	5000	10,000
Integration time (sec)	1.0×10^{-3}		30.0
Charge capacity/pixel (electrons)		20×10^6	
Clock rate (KHz)	250	500	1000
Power dissipation (mW)	1.0×10^{-2}		5.0
Bias Voltage	0	50	100
Responsivity (A/W at 4.5 μm)		5.0	
Output FET (μv/electron) sensitivity		0.4	

A camera system was made by placing the IRCCD in a standard up-looking dewar. One-to-one transfer optics reimage the telescope focal plane onto the IRCCD. Bandpass filters are located on a 77 K filter wheel. The exit pupil is matched to a cold Lyot stop, and the optical path is further baffled by a 4 K shield. The IRCCD is thermally isolated so its temperature can be controlled from ~12 to 300 K.

The IRCCD is operated by a microprocessor-controlled electronics system. This system controls all the CCD gate voltages, timing sequences, integration times, FZ levels, and other options. The output signal is fed into an amplifier/ADC subsystem. Eight gains are available, and either a 12-bit or a 16-bit ADC may be selected. The fastest conversion times for a single correlated double sample of one pixel is 4 μsec at 12-bit resolution and 20 μsec at 16-bit resolution. The digitized signal is stored in a 24-bit-deep high speed memory. Incoming frames can be co-added or subtracted on the fly from the stored frames. The digitized image is also displayed on a TV monitor which views a selectable 8-bit slice of the 24-bit deep image. The control system is interfaced via a CAMAC module to a host computer which can control the IRCCD operations and parameters, store images on magnetic tape or disks, and perform data analysis. In addition, the camera system interfaces to the telescope to control the chopping secondary and beam switching.

The testing and the evaluation was done on a dozen unmated CCD multiplexers and three mated IRCCDs. The most extensive testing was performed on the best IRCCD. The devices were tested for transfer efficiency, quantum responsivity ($G\eta$), linearity, dark current, and noise as a function of the temperature, CCD clock voltages, timing sequences, and detector bias voltage. The tests were done both in the lab and at the 3-m IRTF telescope.

II. TRAPPING STATES & TRANSFER EFFICIENCY

In a surface channel CCD, the charge is physically stored and transferred along the interface layer between the Si substrate and the SiO_2 insulator. The crystal structure of the Si-SiO_2 interface is not perfect though, and many crystal lattice defects are present. These defects cause the formation of trapping sites that have energy states located in the valence-conduction band gap region. When a charge packet is clocked into a CCD well, these energy states trap electrons which would otherwise be in the conduction band. Later, when the main charge packet is clocked out of the CCD well, the trapped electrons are retained in what are now excited states. These excited states eventually decay to release the trapped electrons. Each trapping site has a different emission time constant, so some electrons are released in time to rejoin the main charge packet while the remainder are released later to join following charge packets. The trapping of electrons will affect the CCD multiplexer in three ways. First it affects the response linearity as will be discussed in section III-iv. Second, the capture and release process causes fast interface state trapping noise. This will be discussed in section V-iii. Finally, the amount of trapped charge determines the charge transfer efficiency and how much FZ is required. This will be discussed below.

To better understand all of the above phenomena, it is necessary to measure the amount of trapped charge as a function of signal size. The signal charge was electrically injected into the multiplexer by the fat zero mechanism. The results are shown in Figure 1. Measurements at both 40 and 300 K are shown.

For the 40 K results, three main features are apparent. First, for signals less than about 0.5 million electrons, the trapped charge is roughly proportional to the signal. In fact, the amount of trapped charge is almost equal in size to the signal. For this situation, there are more trapping sites than signal electrons. Also the effective gate area is increasing rapidly with signal size (see Figure 9-15 of Dereniak and Crowe, 1984), which increases the number of trapping sites. Therefore, most of the signal electrons are captured when they are clocked into a well and only about two-thirds are emitted in time to be clocked forward. This region has very poor transfer efficiency. Second, for the region between ~1 to 10 million electrons, the amount of trapped charge is constant. This happens because all the trapping sites are filled and the effective gate size is increasing only very slightly so no new trapping sites become available. The transfer efficiency is correspondingly very good. In fact, within the read noise, the amount of trapped charge is constant for signals between 1.5 to 7 million electrons. Finally, at about 10 million electrons of signal, the amount of trapped charge rises rapidly. This feature is due to a very rapid increase in the effective gate size near full well and causes a very rapid increase in the number of new exposed trapping sites.

Figure 1 shows that if there are between 1 to 2 million electrons of FZ in the multiplexer, then all the trapping sites are filled. If signal electrons are added to this, the amount of trapped charge is still the same. Therefore, effectively no signal electrons are trapped. The transfer efficiency in this case is about 0.9998.

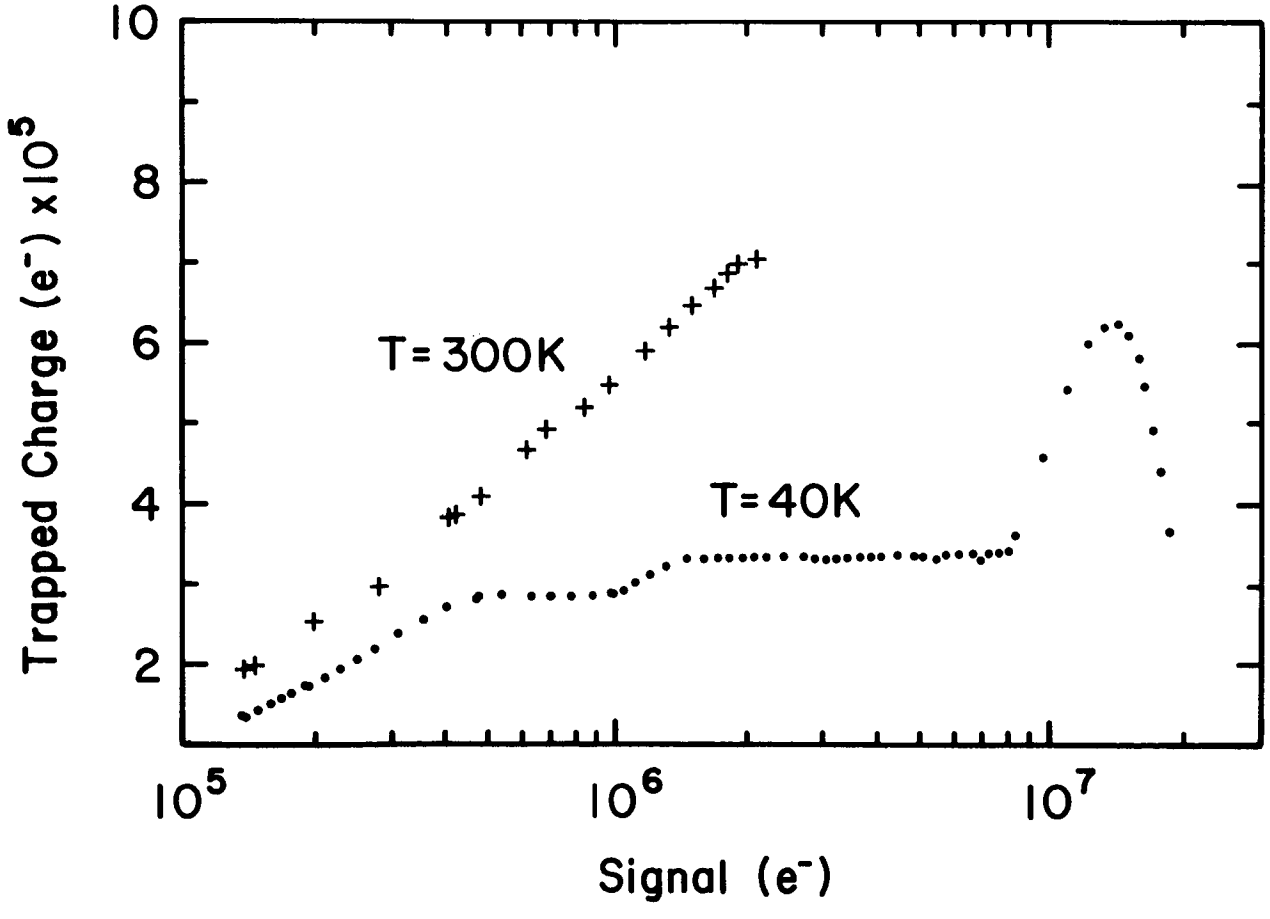

Figure 1. The amount of trapped charge versus signal at 40 and 300 K.

III. DEVICE RESPONSIVITY

Two methods were used to measure the quantum responsivity, $G\eta$, where G is the photoconductive gain and η is the quantum efficiency--flood illumination in the lab and intercomparison of standard star outputs at the telescope. In each case, the photoconductor was biased by approximately 50 volts, and the IRCCD was operated at a temperature of 30 K. The quantum responsivities were calculated with a pixel size of 88 μm squared so that the effects of the dead space are included. However, as will be illustrated in section iii below, the size of the active area of a pixel depends on both its location and the voltage of the multiplexer gates which lie directly below the interpixel dead spaces. The actual active area is probably closer to 55 μm square. Therefore, to characterize the quantum responsivity of the photoconductive material itself, the results should be increased by a geometric scale factor. This correction produces approximately 2.6 times higher quantum responsivity.

1. FLOOD ILLUMINATION

For the first method, a 600 K blackbody illuminated the IRCCD focal plane and enabled the $G\eta$ product to be determined for each pixel. A histogram of the quantum responsivity of all 1024 pixels is shown in Figure 2. The average quantum responsivity is 35% with a range from 25% to over 100%. About 100 pixels have $G\eta = 0$. These "dead pixels" are probably the result of insufficient attachment between the photoconductor and the CCD multiplexer. Most of these dead pixels are located in the last three columns and the bottom row.

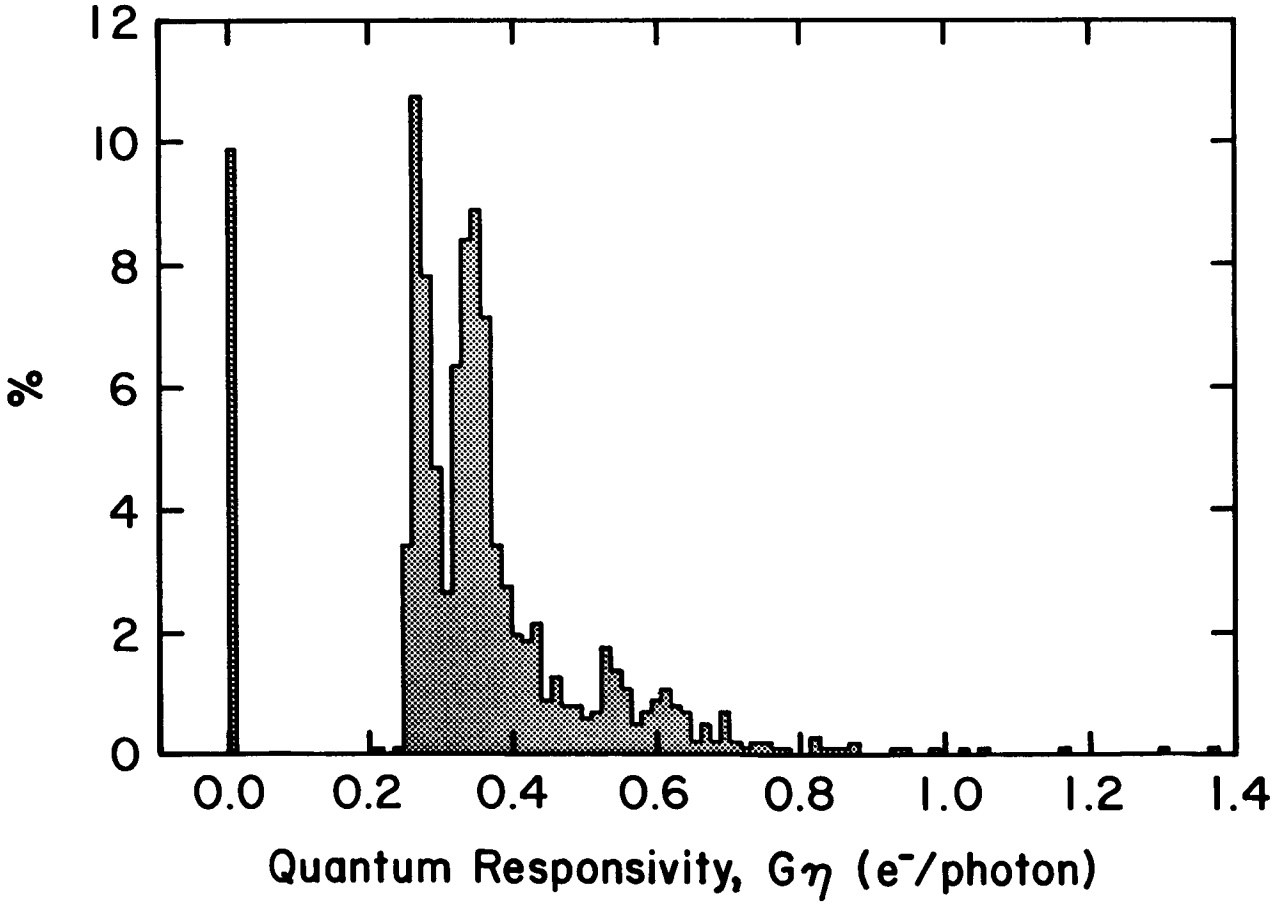

Figure 2. Histogram of the quantum responsivity at 3.5 μm.

ii. CHOPPED IMAGE ILLUMINATION

For the second method, the quantum responsivity was measured at the telescope using infrared standard stars. The telescope secondary mirror was chopped between the standard star and the sky so that the final image contained only the flux from the standard star. The quantum responsivity was defined as the total number of electrons out of all 1024 pixels divided by the total number of photons from the standard star that hit the detector. The quantum responsivity was 35 ± 5% at 3.5 μm and 32 ± 5% at 2.2 μm.

iii. RESPONSE UNIFORMITY

Two effects cause a larger spread in the response histogram than might be expected. Both of them are easily seen by examining a flat-field image such as Figure 3. It shows a black and white image of a flat field taken at the telescope. Black represents the least responsive pixels and white the most responsive pixels. The first noticeable effect is that the outer-most pixels are more responsive than those toward the center. Fringing of the bias field at the outside edges of the photoconductor probably causes these pixels to have a larger active area than the inner pixels and thus to detect more incoming photons. A spot scan of these pixels would demonstrate this effect.

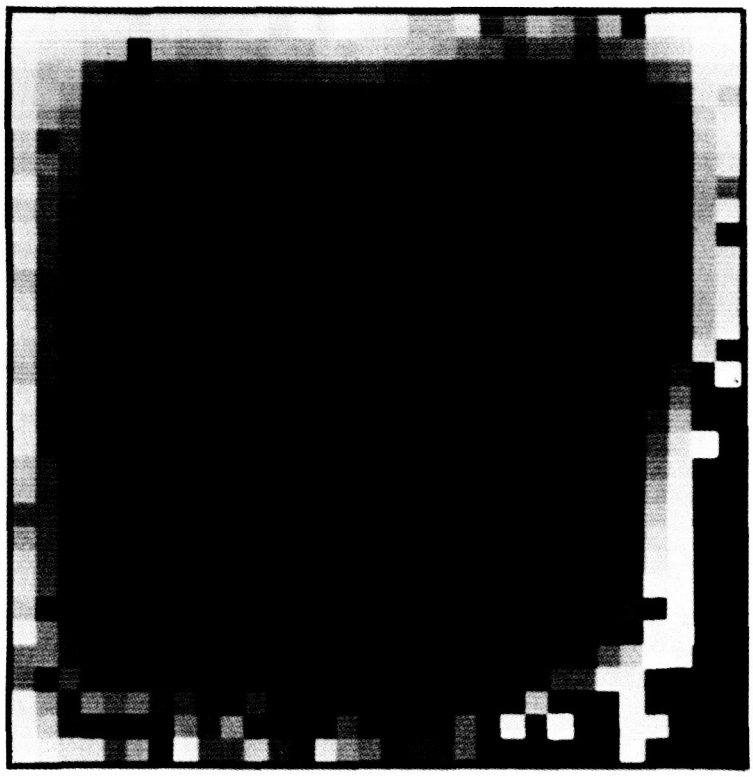

Figure 3. Image of a flat field. Black represents the least responsive and white the most responsive.

The second problem is an odd-even column variation which is caused by an error in the CCD multiplexer masks. This error causes the potential at the input diffusion, V(ID), of the odd columns to have a different value than the pixels in the even columns. This causes two effects. First, since the potential varies from column to column, the potential applied across the photoconductor also varies,

$$V(det) = V(bias) - V(ID),$$

and therefore so does the photoconductive gain, G, because it is a function of V(det). Second, a small transverse bias exists between columns in the detector array and in the multiplexer. This transverse bias allows the odd columns to steal charge from the even columns. The two problems are additive in the sense that the columns which have a larger G also steal charge from adjacent columns.

iv. RESPONSE LINEARITY

The linearity of the IRCCD at 3.5 μm was determined by measuring well-known IR sources and standard stars. The results are shown in Figure 4, where the number of photon/sec onto the IRCCD versus the number of electrons/sec out of the device is plotted for 6 sources. The IRCCD was operated with about 2 million electrons of FZ and at a temperature of 40 K. If the IRCCD is linear then

$$S(out) = G\eta\, S(in)^{\alpha}$$

where $\alpha = 1$ for a linear detector. A best fit to the data yields a value of

$$\alpha = 1.02 \pm 0.02.$$

The device appears to operate linearly in this mode.

However, nonlinearities are possible and under certain conditions are present in this device. The degree of any nonlinearity of the IRCCD will be the result of the nonlinearity in 1) the detector, 2) the CCD input scheme, 3) the transfer process, and 4) the CCD output amplifier. The nonlinearity of the detector material has not been measured. Apparently, though, the above result indicates that the photoconductor has no appreciable nonlinearities and is consistent with photoconductor theory.

The nonlinearities due to the CCD input scheme can be seen by examining individual pixels. Although the whole array is approximately linear in response to stars, individual pixels are not. This is due to the odd-even problem discussed previously. Remember, charge can be stolen or lost to neighboring pixels, and the bias applied across the detector varies from column to column. Both of these effects will introduce nonlinearities. However, the reason the array has a linear response to stars even though individual pixels are not linear is that while some pixels are indeed losing charge, others are receiving it and, over the whole array, the charge is conserved.

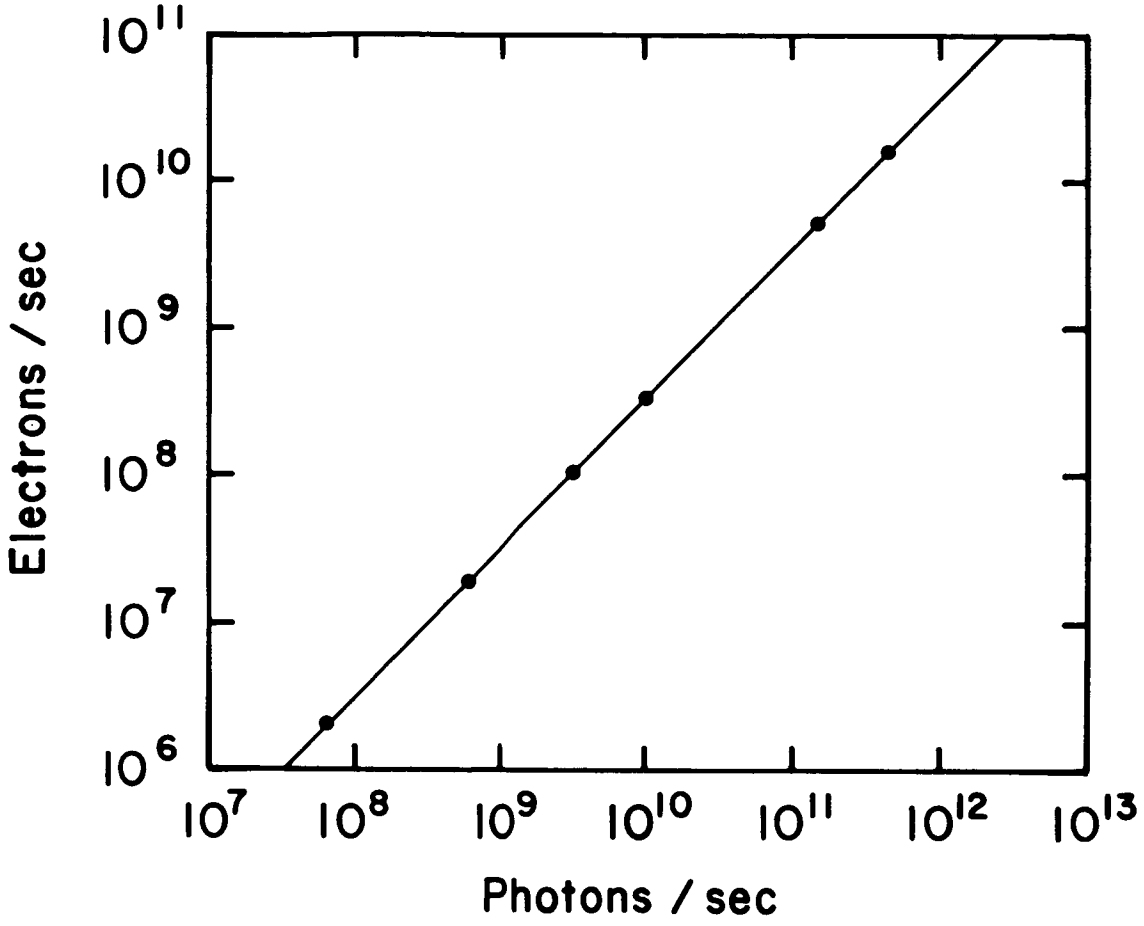

Figure 4. Linearity curve for photons in versus electrons out.

Nonlinearities due to the transfer process are present if no fat zero is used. As Figure 1 shows, the amount of trapped charge is strongly dependent on the signal size. In fact, those signals which are smaller than about one million electrons will have a proportionally much larger fraction of charge trapped than the larger signals. For example, suppose that after some integration time we detect 2 x 10^5 electrons. Only about 10^5 electrons are clocked out; the rest are trapped. If, on the other hand, there are 2 x 10^6 electrons detected, 1.7 x 10^6 electrons are clocked out. Thus, for an object that is only ten times brighter, there is 17 times more electrons read out. But if sufficient amount of FZ is injected, effectively no signal charge is trapped and therefore no nonlinearities occur.

Finally, nonlinearities can occur due to the CCD output amplifier which is a MOS transistor in a source-follower configuration. The output voltage for a source follower amplifier is

$$\Delta V = Q\, g_m R \;/\; C_n(1+g_m R) \qquad (1)$$

where g_m is the transconductance of the MOS transistor, R is the output resistor, Q is the signal charge, and C_n is the node capacitance at the output diffusion. C_n is voltage dependent (Kim, 1979) and could introduce nonlinearities into equation 1. The results of preliminary tests show the output amplifier has no measurable nonlinearities in the voltage range that the IRCCD is operated in.

IV. DARK CURRENT

An investigation of the dark current shows that the spatial dependence of the quantum responsivity is also evident in the dark current. The dark current is higher at the edges and it shows an odd-even column variation. Both are expected because the CCD cannot distinguish a photo-electron from a dark current electron once they are generated in the photoconductor. Therefore, the outer pixels have higher dark current because these pixels have larger areas and thus have a greater volume to generate dark current electrons while the odd-even column problem follows the same discussion as described in section III-iii. Typical dark currents at temperatures between 20 and 40 K are in the range of several 10^5 electrons/second (see right-hand side of Figure 5). One interesting characteristic of the dark current is that it is not constant with respect to integration time. Figure 5 shows a plot of the dark current versus integration time at a temperature of 37 K. The dark current varies from ~3.5 to 7.5 x 10^5 electrons/second over the range of integration times of 0.1 to 10 seconds. Why the variation occurs is unknown, but it may be related to a time-dependent injection efficiency at the CCD input. This hypothesis can be checked by determining if the same thing happens for photo-electron current. If it exists for both currents, it is probably a nonlinearity of the CCD input scheme.

The dark current of the multiplexer alone was measured for one IRCCD. It had an average dark current of 130 electrons/second and 22 dark current spikes which occurred during an integration of 10 minutes (these are pixels which have dark currents much larger, typically an order of magnitude higher or more, than the average pixel). Based on very preliminary tests on other multiplexers, this appears to be a representative dark current for all the multiplexers.

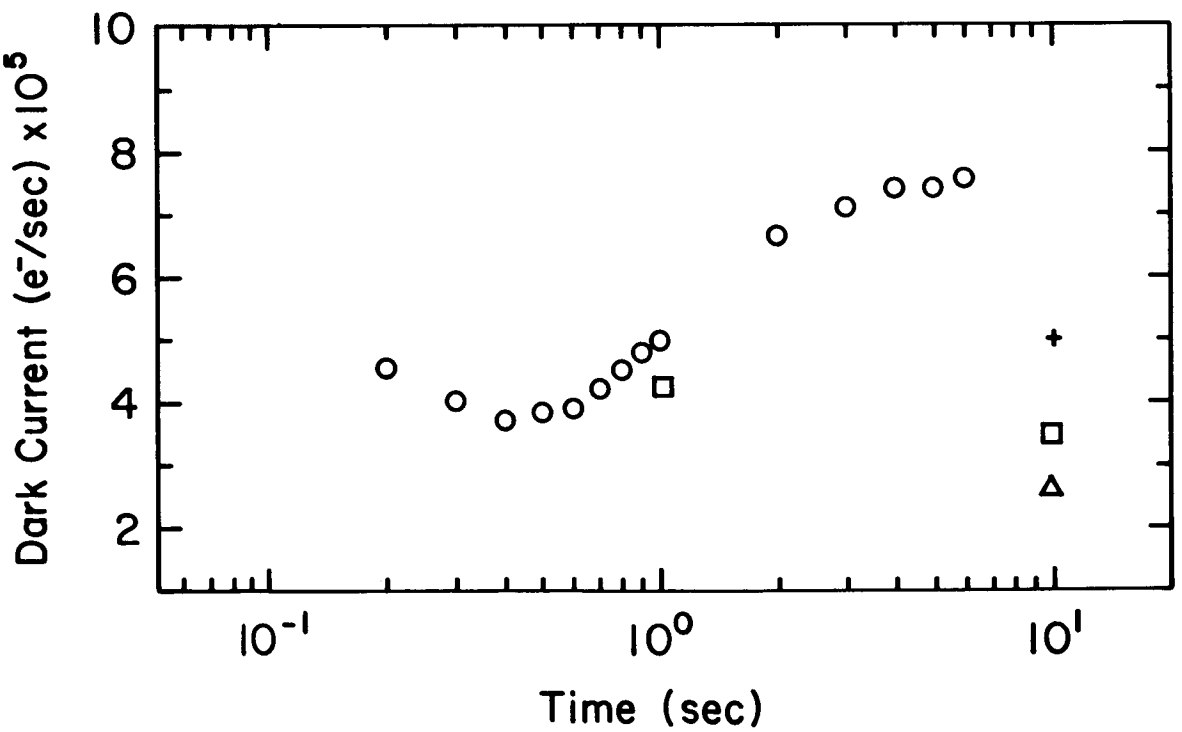

Figure 5. Dark current versus integration time for different temperatures. Symbols are; + T = 40 K, o T = 37 K, □ T = 30 K, Δ T = 25 K.

V. NOISE

There are many sources of noise in an IRCCD which can be broadly classified into detector noise, multiplexer noise, and electronics noise. The first two will be discussed below. The electronics noise will not be, other than to say that it is much less than the total device noise. In addition, fast interface state trapping noise will be discussed separately because it is the most dominate multiplexer noise mechanism.

i. DETECTOR NOISE

The IRCCDs have excess noise in the signal current which originates somewhere in the detector or multiplexer input area. Until more tests are done, the source of the excess noise is unclear. It could be excess noise in the photoconductor material and the associated electrode contacts, or due to a noisy input scheme, or be a consequence of the masking error.

ii. MULTIPLEXER NOISE

For certain situations, the noise of the CCD multiplexer becomes the limiting noise source. As an example, the limiting magnitude achievable for our speckle interferometry program (where integration times are ~0.1 seconds) is determined by the noise of the multiplexer. Therefore the noise was investigated thoroughly so that the IRCCD could be operated at its most optimum configuration.

Five basic noise sources are present in a CCD (Carnes and Kosonocky, 1972; Kim, 1979; Benyon and Lamb, 1980), reset noise, FZ input noise, output FET noise, transfer noise, and fast interface state trapping noise. The first three are small compared to the last. For example, the reset or kTC noise is eliminated through correlated double sampling techniques. The FZ input noise can be shown to be less than kTC noise (Emmons and Buss, 1974) and the output FET noise is thermal channel noise and 1/f noise in the FET (Carnes and Kosonocky, 1972). For our device, these noise sources contribute about 100 electrons at a temperature of 30 K.

Transfer noise is due to small amounts of charge being clocked backward instead of forward. Benyon and Lamb (1980) show that for certain assumptions, the noise is

$$\Delta N = \sqrt{(\varepsilon N_t N_s)} \qquad (2)$$

where N_t is the number of transfers, N_s is the total number of electrons in the well, and ε is the fraction of N_s electrons clocked backwards. As shown in the next section, there is no evidence for transfer noise, so therefore we assume it is not present.

iii. FAST INTERFACE TRAPPING NOISE

As explained in section II, signal electrons are captured and released by trapping sites in the Si-SiO_2 interface. This process causes each charge packet to lose electrons to following charge packets and gain charge from proceeding charge packets and thereby cause fluctuations. The equation for the fast interface state trapping noise, given in terms of the variance, is

$$\Delta N^2 = N_t A_g \int N_{ss}(E) \left[1-\exp(-t\sigma(E)v_{th} N_c \exp(E/kT))\right] \times \exp\left[-t\sigma(E)v_{th} N_c \exp(E/kT)\right] dE. \quad (3)$$

N_t is the total number of transfer, A_g is the area of the gate, $N_{ss}(E)$ is the number of trapping states per unit area per unit energy, E is the energy of the trapping site below the bottom of the conduction band, $\sigma(E)$ is the electron capture cross section, v_{th} is the thermal velocity of the electrons, N_c is the number of electrons per unit volume in the conduction band, k is Boltzmann's constant, and T is the temperature (Tompsett, 1973). To make the problem tractable $N_{ss}(E)$ and $\sigma(E)$ are usually assumed to be energy independent which gives the following results:

$$\Delta N = \sqrt{(1.4kTA_gN_{ss}N_t)}. \quad (4)$$

As discussed shortly, equation 4 accurately describes the relationship between the noise and the gate area, A_g, and the number of transfers, N_t. However, it fails to predict the observed dependence of the noise on signal level. As discussed by Tompsett (1973), we believe that the actual dependence of $N_{ss}(E)$ and $\sigma(E)$ on energy account for this failure. Furthermore, equation 3 should be modified to include the occupation index, which describes how the electrons are distributed in the trapping sites. It is a function of T, N_s, and the Fermi energy. This term is particularly important when the number of electrons is less than the number of trapping sites and when the temperature is high. Otherwise, at low temperatures and large signals, the occupation index is close to unity and may be ignored.

To determine the noise versus signal characteristic, many multiplexers, both mated and unmated to photoconductors, were tested for noise as a function of signal size, gate size, number of transfers, and temperature. The signal charge was electrically injected by the FZ mechanism and could be injected at three sites, the storage gates, the heads of the columns, or the end of the output row. In the case of the mated devices, the detector was disabled and contributed no noise.

In terms of signal size, all the CCDs exhibited the same basic noise versus signal characteristics. A schematic representation of it is shown in Figure 6. Three features are apparent. One feature shows that at about 1 to 2 million signal electrons, the noise becomes constant at about 1 to 2 thousand electrons. Another feature is a general decrease in the noise for signal levels less than ~1 million electrons. The third feature is a dip in the noise which occurs at about 0.5 to 1 million signal electrons. All of these features are probably reflecting the contribution of the occupation index to the noise. In passing,

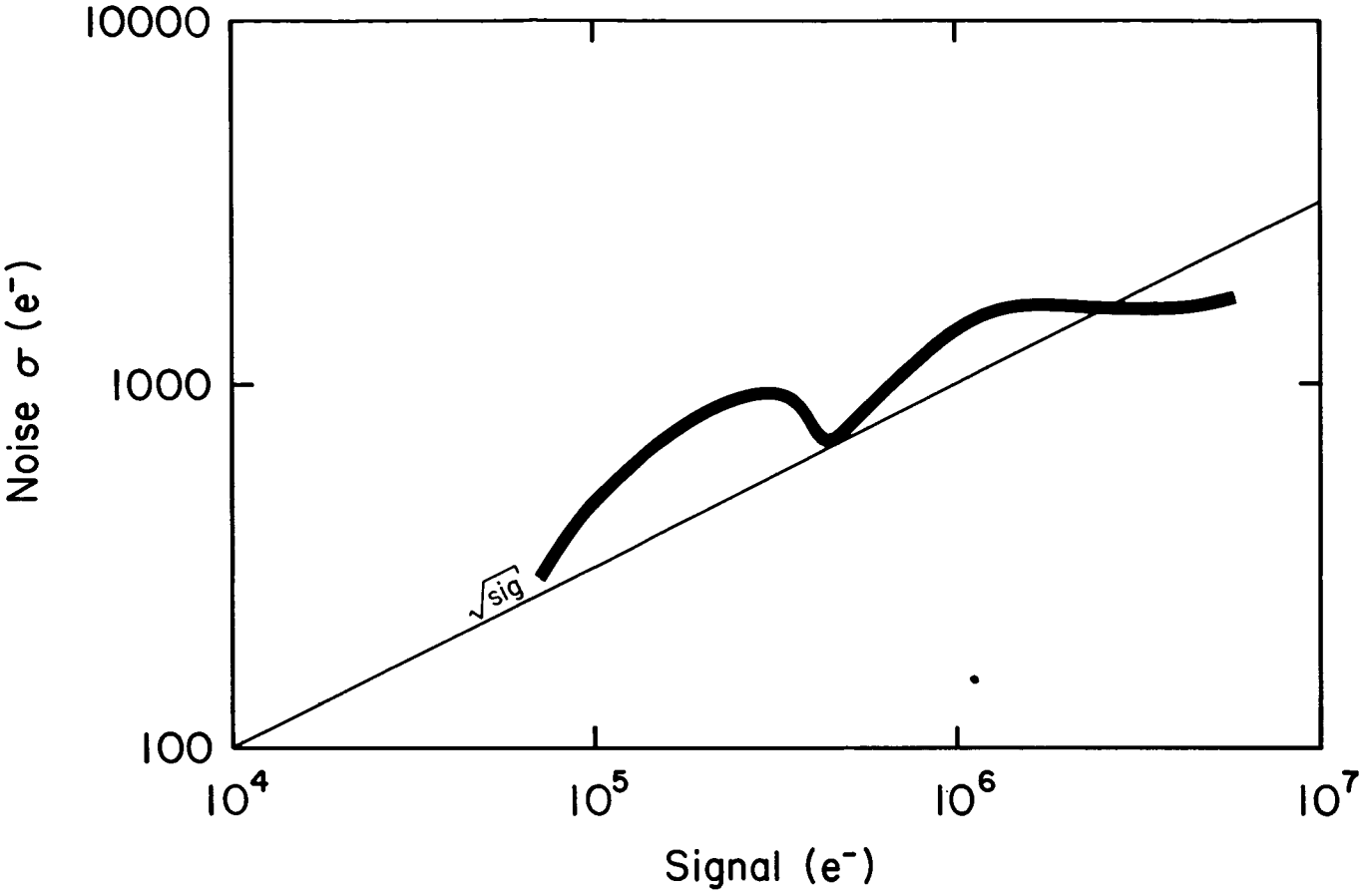

Figure 6. Schematic representation of a typical noise versus signal curve.

note that from equation 2, the transfer noise should exhibit a straight line of slope 1/2 in a log(signal)-log(noise) plot. As illustrated in Figure 6, the noise versus signal is not a straight line and does not parallel the square-root signal line (labeled $\sqrt{sig}$) and is the basis for concluding that it is not a dominate noise source.

In agreement with both equation 3 and 4, the observed noise is proportional to the square-root of both the gate area, A_g, and the number of transfers, N_t. Figure 7a shows the noise versus signal for three different combinations of gate sizes and number of transfers. Although the shapes of the three curves are the same, the absolute level of each one is different. This is particularly evident at $N_s > 1$ million electrons. The three noise curves were normalized to an arbitrary unit gate size and to 100 transfers. The results are plotted in Figure 7b and show how the three normalized curves overlap. It is worth noting that the three curves do not overlap if the noise is corrected only for the number of transfers or only for the gate size.

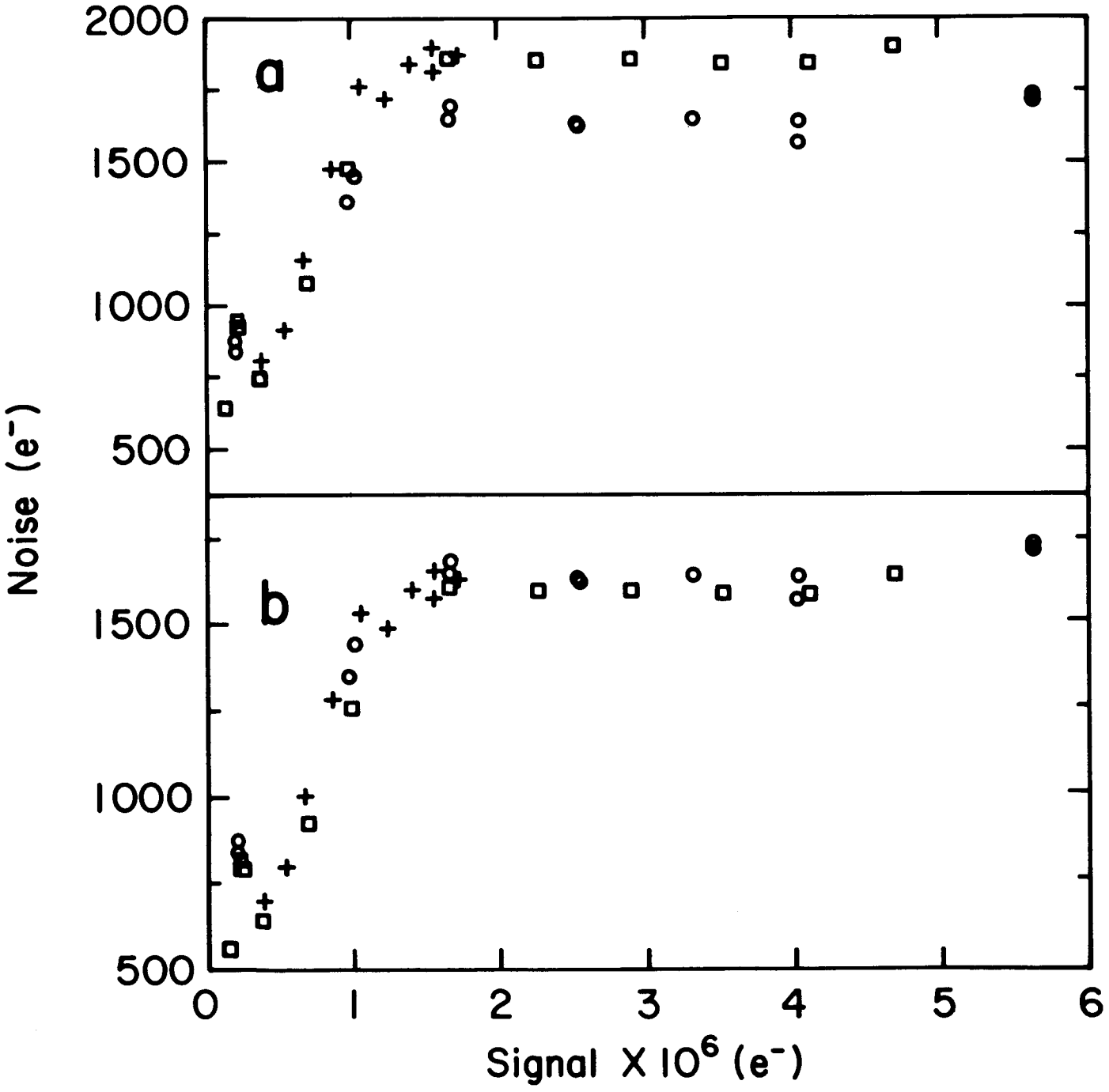

Figure 7. Noise versus signal as a function of gate size and number of transfers, (a) unnormalized, (b) normalized.

Figure 8. Noise versus signal as a function of temperature.

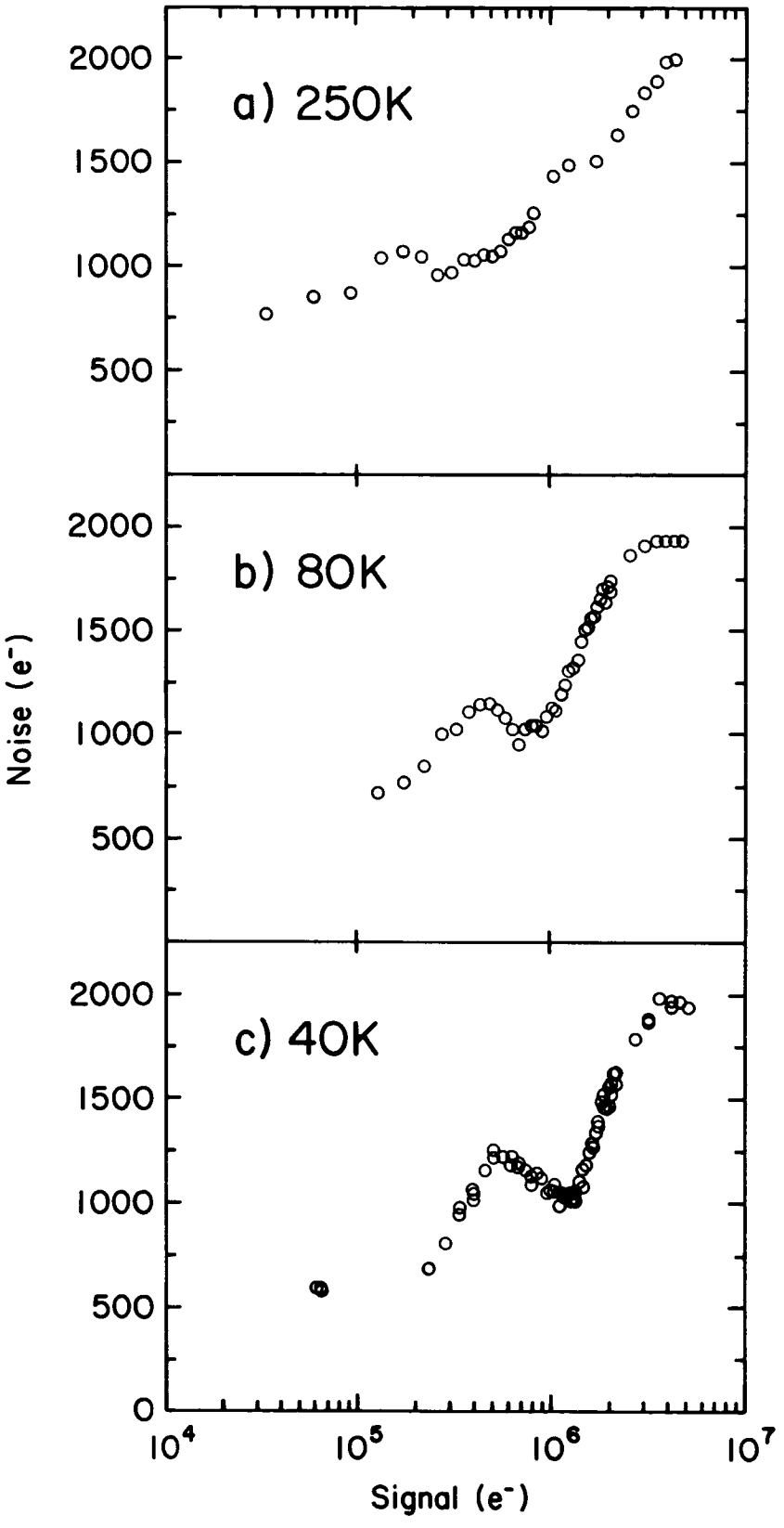

The noise versus signal measurements were repeated for different temperatures ranging from room temperature to 12 K. Figure 8 shows the results from one IRCCD operating at temperatures of 250, 80, and 40 K. Measurements at 30 K were also made and are almost identical to those at 40 K. For signals greater than several million electrons, the noise becomes constant. If equation 4 were correct, the noise would be dependent on the temperature. In fact, the noise at 250 K would be almost 3 times higher than at 30 K. But as Figure 8 shows, the noise has approximately the same value at all the temperatures. However, the location of the noise dip is temperature dependent. At 250 K the dip is relatively wide and the minimum occurs at $N_s \sim 0.5$ million electrons (Figure 8a). With a decrease in temperature, the dip width narrows and the location of the minimum shifts progressively to higher signal levels until at 30 and 40 K it occurs at $N_s \sim 1$ million electrons (Figures 8b and 8c). Although the other miltiplexers were not examined as thoroughly, they confirmed these results.

VI. CONCLUSIONS

Although the IRCCDs were experimental, these devices have been useful astronomical detectors. The kinds of objects that have been observed with standard observing techniques include Jupiter, Uranus, OH-IR stars, and galactic nuclei. The most thoroughly observed object has been the Galactic Center. A 3.5 μm mosaic image made up of 64 overlapping frames is shown in Figure 9. The area covered is 24 x 24 arcsec and is centered on IRS 16 center. The image incorporates two data sets. The first covers the IRS 16 and IRS 1 complex and has a spatial resolution of about 0.7 arcsec. With this resolution, Figure 9 shows that IRS 16 complex consists of at least 5 separate objects. The other data set comprises the rest of the mosaic but is of lower resolution, a little over 1 arcsec. Astrometry was done to determine the location of the nonthermal radio source Sgr A*. The position is marked by a cross about 1 arcsec west of IRS 16-C. No part of IRS 16 coincides with the position of Sgr A*. In addition, a speckle interferometry program was undertaken to obtain very high spatial resolution of young stellar objects. Test results on T-Tau and other double stars shows that this technique can be successfully done with IRCCDs to obtain ~0.3 arcsecond images.

There are a few critical problems that can severely affect the performance of hybrid surface channel IRCCDs. The most important design criteria is to have the potential at the input diffusion, V(ID), exactly the same for all pixels. Without this, the device uniformity and the pixel linearity are degraded. In addition, this may also cause the device to have excess noise and injection efficiency problems. Another design augmentation is to have a guard ring on the perimeter of the detector to prevent field fringing of the bias. The guard ring will insure that all the pixels near the edge will have the same active area as those in the center.

There are several operational criteria to follow. The most important is to use fat zero to fill up the fast interface state trapping sites. There are three reasons for using fat zero. First, the high transfer efficiencies are only obtained when FZ is used. By examining the left-hand side of Figure 1, it is easy to see that the amount of trapped charge is almost equal to the signal size. This corresponds to a very poor transfer efficiency. Second, the use of fat zero insures that the CCD is linear for both very large signals and very small signals. Finally, the noise of the CCD can be adjusted to optimize the signal-to-noise and transfer efficiency for different kinds of observing programs. Usually, the IRCCD was operated with a FZ of about 1 million

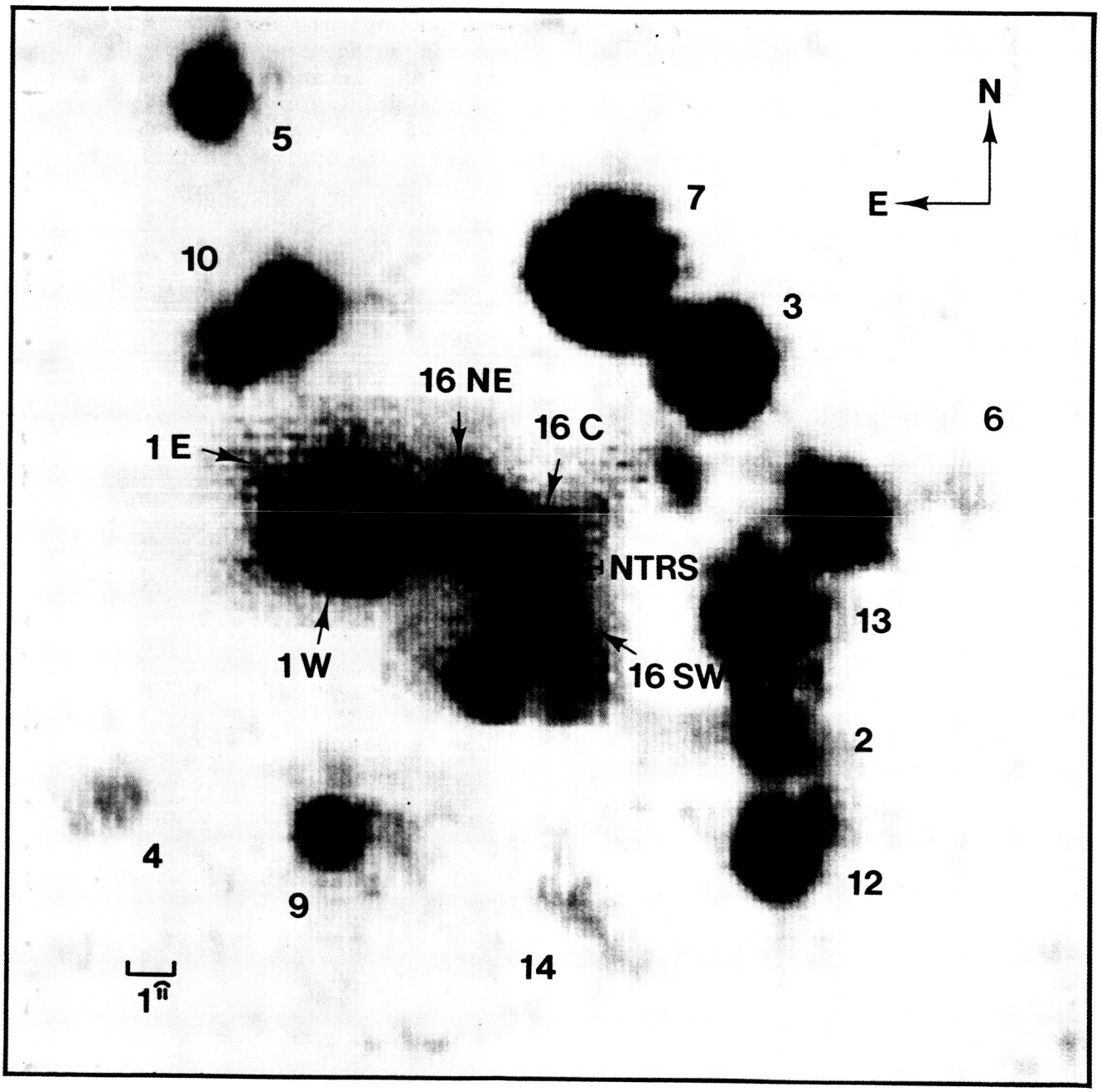

Figure 9. Image of the central 24 x 24 arcsecond region of the Galactic Center. Numbers are IRS source numbers. The cross is the location of the nonthermal radio source (NTRS).

electrons. This optimizes the CCD linearity and the transfer efficiency and keeps the CCD noise multiplexer (~1800 electrons) below the detector noise. For speckle interferometric observations, where the source signals were small, the FZ was readjusted to give lower total noise (~700 electrons) at the expense of a slightly lower transfer efficiency.

In conclusion, IRCCDs offer a promising two-dimensional astronomical detector. Newer devices should obtain excellent spatial uniformity, linear output, reasonable read noise, and high quantum responsivity. In addition, future hybrid IRCCDs should provide larger formats without gaining an unwieldy number of output amplifiers, clocking lines, and associated electronics. Furthermore, a variety of detector materials can be used to cover the entire spectral range from 1 to 20 μm.

REFERENCES

Benyon, J. D. E. and Lamb, D. R. 1980, Charge-coupled Devices and Their Applications. McGraw-Hill, London.

Carnes, J. E. and Kosonocky, W. F. 1972, RCA Review, 33, 327.

Dereniak, E. L. and Crowe, D. G. 1984, Optical Radiation Detectors. John Wiley, New York.

Emmons, S. P. and Buss, D. D. 1974, J. Appl. Phys., 45, 5303.

Kim, C.-K. 1979, "The Physics of Charge-coupled Devices," M. J. Howes and D. V. Morgan, eds., Charge-coupled Devices and Systems, John Wiley, Chichester.

Pommerrenig, D., Enders, D., Trousil, L., Capps, R. W., Irwin, E., Tollestrup, E., and Dereniak, E. L. 1983, in paper presented at the Infrared Detector Technology Workshop, NASA Ames Research Center, July 12-13.

Tomsett, M.F. 1973, IEEE Transactions on Electron Devices, ED-20, 45.

Imagery with a Si:Bi 16 x 16 Array

J. H. Goebel, C. R. McCreight, F. C. Witteborn, and N. Moss

NASA/Ames Research Center
Moffett Field, CA 94035

W. Wisniewski

Lunar and Planetary Lab., Univ. of Ariz.
Tucson, AZ 85721

D. Rank

Lick Observatory, Univ. of Calif. Santa Cruz
Santa Cruz, CA 95064

Abstract

We present a description of the design and performance of an imaging spectrometer intended for operation in the seven to fourteen micrometer wavelength range. It is based upon a sixteen by sixteen element Si:Bi hybrid array, a circular variable filter wheel, and a microcomputer data acquisition system. The spatial-spectral photometric performances have been evaluated in the laboratory as well as field tested at astronomical observatories. The performance characteristics of the system are presented as well as laboratory and astronomical images.

* C-4

I. Review of previous work

In recent years much progress has been made in the field of infrared astronomical imagery. In the 1970's when monolithic detector arrays were unavailable to astronomers, single detector techniques were developed to scan a region of the sky and reconstruct an image of the region from the detector data set. The advocates of the single detector technique have developed procedures for image reconstruction to a high degree of refinement, by employing the maximum entropy algorithms from information theory. As a result regions of space have been mapped down to the limits of the telescope resolution and to the limits of the single detector sensitivity. Grasdalen et al. (1985) have expounded the technique used on ground based telescopes quite skillfully. The IRAS focal plane consisted of an array of single element detectors which mapped the entire sky in the far infrared.

In the 1980's, monolithic infrared detector arrays have become available to astronomers primarily as a spinoff of NASA's OAST programs. These detectors have been under development for many years by industry under government sponsorship. These arrays are demonstrating sensitivities per pixel equaling and exceeding those of the best single detectors available. Recent work by Forrest et al. (1985) has demonstrated an SBRC 32x32 InSb CCD with superb imaging capability. Pommerranig et al. (1983) have been able to demonstrate the astronomical potential of Rockwell developed Si:In CCDs. Arens et al. (1981), Lamb et al. (1983), and Gezari et al. (1985) have been able to demonstrate that Aerojet/General Si:Bi CIDs have astronomical potential. Even now, more arrays are becoming available and in the next few years the field of infrared imagery will explode the number of observations and journal publications. The hot new items in the next few years will be the DRO chips which will have several varieties of detector substrate materials and cover the wavelength range from 1 to 40 microns. BIB detectors will also make a substantial impact with their promise of near unity quantum efficiencies. Some few years later the doped germanium array technology will come of age and imagery will extend out into the several hundred micron range, where as yet only arrays of single element bolometers are working.

We have developed an instrument based upon a monolithic infrared detector array for astronomical applications. The instrument, hereafter called THE INSTRUMENT, it is the prototype in concept of a new generation of instruments for ground based as well as cryogenic space based telescope focal plane instruments Goebel et al. (1983). A similar instrument has been proposed to NASA as a flight instrument for the SIRTF by Gehrz et al. (1983). We use the two dimensional array for imaging with a spectral analyzer to give narrow band wavelength selection. The instrument, called the Photometric Imaging Near Infrared Spectrometer, is capable of directly imaging nebulous objects in the wavelength range from 2 to 17 microns. We present a description of the instrument and its capabilities.

microns), and falls quickly below about half of the peak wavelength (7 microns). A quantum efficiency at 3 microns of less than 1 % is typical. This arises because the quantum yield at an extrinsic dopant site is wavelength dependent. Hence the array is only useful for imaging the brightest sources at wavelengths less than of 5 microns. Astronomically there is a dirth of bright extended sources short of 5 microns, so we have limited our observations primarily to planets and most prominently to Venus. Because of the widespread lack of imaging instrumentation in the near infrared (1-5 microns), even a relatively insensitive array can perform useful science. This will become less true in the future as InSb and HgCdTe arrays become more readily available (Forrest et al. 1985 and Rode 1984). An example of a Venus picture is shown in an accompanying figure. At long wavelengths, reasonable quantum efficiencies are attained. The detectors are then competitive with the best single element photoconductive detectors. A competitive grating array spectrometer, FOGS (Witteborn and Bregman (1984), is capable of observing 4th magnitude sources at 10 microns with a similar radiation bandwidth, on a 1.6 meter telescope. THE INSTRUMENT is capable of 2nd magnitude at the present time. The current limit is not yet set by fundamental processes, but rather by clocking irregularities and pickup. Steps are being taken to reduce these effects.

The well capacity of the CID is not what it should be. 100 Me- are anticipated from the design parameters, but 0.1 Me- have been measured. This difference indicates a fundamental misunderstanding about the design and manufacture of extrinsic silicon CIDs. The well capacity remains a mystery. It limits the application of the detector astronomically to narrowband rather than broadband imagery. Narrowband instruments are much more difficult to build and use than broadband instruments; and there are many more scientific programs which can be pursued broadband.

The detector response of the CID is nonlinear near full well. This causes data taking to be more complex than for a linear system. Flat fields must be acquired at several backgrounds and at several wavelength settings in order to calibrate the nonlinear response. Each pixel has a different near full well response. The flat fielding procedure is further complicated by temperature dependent electronic zeros. Mapping the nonlinear response is most necessary for the brighter sources such as planets. Bright objects fill the wells near the top where there are the greatest variations across the array. An example is Venus which has been observed in the 10 micron range. It has proved difficult to find a bright source which can be used to match the well depth of this planet and fills the telescope beam

II. THE INSTRUMENT

THE INSTRUMENT uses a 16x16 element Si:Bi detector array of the AMCID type. It was manufactured by Aerojet-General and packaged in a dual butterfly case using hybrid packaging techniques Perry (1981). The Si:Bi substrate is processed with metalizations and oxide growth to give a 32x32 array format of which a 16x16 sector is totally active. The last layer of metalization and oxide growth has been deleted in favor of wire stitch bonding for the purpose of improved yield. The chip is epoxied to the butterfly package over a cutout region. Cmos multiplexing chips are wire bonded to the row addresses of the Si:Bi chip, while 3N163 p-channel MOSFET output amplifiers are wirebonded to the column addresses. 100 Mohm bleed resistors are at the MOSFET gate node to transform the detector current to a voltage which is sensed by the MOSFET, and eliminates a reset MOSFET. This genre of detector has been described in the literature by McCreight and Goebel (1981) and McKelvey et al. (1985). Detector performance parameters have been measured for this chip and are consistent with good quality detectors of this kind.

The detector is used in either of two optical configurations, depending upon the wavelength range desired. In the short wavelength range, 2 to 6 microns, the background is low enough to allow reimaging of the full field of view at the field stop onto the detector array. This configuration provides the higher spatial resolution images reported later. In the long wavelength range, 6 to 17 microns, the backgrounds are too high for direct reimaging, so the focal plane is moved outside the dewar and the reimaging lens in front of the field aperture. The field aperture is then a pupil stop, and the telescope secondary is imaged there to block unwanted telescope structural radiation. When used with the 1.5 % bandpass Circular Variable Filter (CVF), the optical system background on an astronomical telescope is sufficiently low to permit operation of the THE INSTRUMENT out to 13 microns. Some demagnification occurs at the long wavelengths because of the positioning of the lens.

The digital electronics used in the data acquisition stream have been described in previous papers by Stafford and Jared (1982). In summary it consists of a dedicated 20 MHz clock rate ALU with supporting ROM and RAM which reduces the information bandwidth product through frame averaging. The data is then transmitted via an RS 232 link to a Heurikon developmental Z80 microcomputer for data collection and processing. A CPM operating system is used with MT+ Pascal language software used for the data acquisition control and analysis programs. The analog electronics consists of gain amplifiers at the dewar and S/H channels in the digital electronics box. The clock and voltage generators are also present in the digital electronics box (Pandora' Box). Pandora's box is within one meter of the dewar, while the microcomputer is within ten meters of the dewar.

The observational forte of the THE INSTRUMENT is mapping of emission line objects at the 1 to 4 arcsec scale over a field of from 15 to 60 arcsec. Because of the use of a CVF, objects can be mapped in atomic and molecular emission features as well as the continuum. However, because of the limited well capacity within the detector itself, it is difficult to do broadband photometric mapping. This limitation, which is imposed by a warm telescope, means only the brightest objects of any class are accessible to the instrument. A space based cryogenicly cooled telescope would not limit the sensitivity of the detector thus, and the instrument would be limited only by fundamental detector parameters. It would be able to make broad band measurements of vastly more objects.

III. Performance characteristics

THE INSTRUMENT has been tested extensively both in the laboratory and in the field. Typical performance parameters are listed in table 1. The detector array has a few peculiarities which are worth discussing. We will concentrate on the limitations of the array rather than its strong points. This does not imply that the array is incapable of producing high quality and scientifically interesting results. The view here is that the capabilities of the array are less than the potential of the AMCID technology. Whatever limitations this array has are not to be taken as a reading of the ultimate capabilities of an optimized technology, and they are indeed impressive.

16 x 16 Si:Bi CID Array Performance
Measurements at Ames

λ = 11 μm at low (about 1E6 ph/s) background

Responsive quantum efficiency	0.25
Well capacity	3E5 electrons
Read noise	600 electrons
Responsivity (17 μm)	4 A/W
NEP	1E-16 W/ Hz or BLIP
Uniformity of responsivity	10%

The quantum efficiency is a strong function of wavelength. It peaks near the cutoff wavelength for the extrinsic dopant (17

in the same manner. The Moon is probably impossible to flat field properly. The wells are running just under full well. A raw data image is presented here which shows the limb of the moon and the vertical striping caused by the array readout procedure.

Amplifier crosstalk reveals itself as an asymmetry in the point source response function in 2 dimensions. Crosstalk in the CID arises from the voltage follower MOSFETs on each of the columns sensing there nearest neighbors. It is substantial in this array amounting to 20% between adjacent rows. There are two ways that the crosstalk can be eliminated. We know that the pixel to pixel crosstalk within a column is 0.1 % and it is suspected that it is entirely optical at that level. Hence we can model the point source response as part of the data reduction process, which we are in the process of implementing. Then the crosstalk can be remove analytically from the images. No AMCID images presented to date by any of the various workers in the field of astronomical imagery have as yet deconvolved the point source response function. Worse yet it has not even been mentioned that the images suffer from the effect, even when it is apparent in the images themselves. A cleaner solution is to use the MOSFETs in a current mode. This TransImpedance Amplifier mode reduces the crosstalk by the open loop gain of the operational amplifier. It is suspected that the point source response deconvolution procedure would then be of little concern.

The amplifier noise (600 e-) for this array limits the ultimate sensitivity in two ways. The noise floor limits the measurement sensitivity in general. The MOSFET read noise is the limit to the CID array used here. The limited well capacity of the detectors forces the readout of the well at just under full well. Under high background conditions, the readout must be at the highest frequencies possible. Hence, it becomes extremely difficult to record sequential frame reads for any study involving transient phenomena such as source variability and atmospheric seeing. The shot noise for a full well readout is about 500 e-, which is nearly the same as the amplifier noise. One is forced to read in the nonlinear region in order to attain a statistical limit. In the linear detector range the detector readout process is decidedly amplifier noise limited. The situation could be improved greatly if selfheated Si:JFETs or Ge:JFETs could be used instead. Then nearly 100 times fewer electrons could be read. The other sensitivity factor is dynamic range, i.e., the ratio of full well capacity to read noise. This factor is particularly important in a space based instrument or when used in any low background instrument. An ideal AMCID with 100 Me- well capacity and a JFET readout amplifier with 10 e- read noise would have a dynamic range of 10 million in one read. The present AMCID has a

dynamic range of 500.

The image acquisition procedures are greatly influenced by the above limitations. These procedures have been developed to reduce the sources of interference to a minimum prior to the recording of data frames. There are however procedures which are necessary after frame recording and require additional data collection, i.e., other than the image frame itself.

The digital electronics is programmed to use a wobbling secondary mirror. On one half of the chop cycle, the detector output is counted up; on the other half, it is counted down. This procedure is repeated some large number of cycles. The large infrared background from warm parts of the instrument appears at the detector output as a large dc voltage or fixed pattern. Nearly all astronomical sources are but a very small fraction of this background. When measuring the large background with the A/D converter, most astronomical sources are found in the least significant bit. So it is necessary to remove this background contribution and this can be done quite handily with a wideband AC coupled amplifier. If the AC component of the fixed pattern is sufficiently small, then the amplifier can have gain. Our CID fixed pattern is determined by clock pickup and not by CID nonuniformity, so we are currently limited to an extra gain of 5-20 depending upon the circumstances. When these pickup sources are eliminated an extra gain of up to 100 should be practicable. Fluctuations in the fixed pattern pickup dominate the noise of all other electronic sources. These fluctuations will scale down linearly with the reduction of the clock pickup. With all astronomical sources so far down in the noise, it is clear that the instrument could take advantage of improved output amplifiers in the near future.

Frames or raw data images are taken in a sequence of quartets + - - +. + means that the star is in, for example, the right field of view, as determined by the wobbling secondary, and - refers to the left. The telescope is moved from + to - beams and the frames are recorded. A source will not necessarily be apparent in the frame + or -, because of the fixed pattern. After one or more quartets are recorded, they can be coadded. Coadding removes all fixed pattern as they are phase insensitive, while the star, or stars, remain. The signal from the star is quadrupled, while any statistical noise is doubled. Nonstatistical interference is unaffected with the last big change usually clobbering the star. Stripe and chevron patterns are certain indications of interference, with dramatically black or white pixel an indication of amplifier saturation. Check patters are an indicator of unstable clock interference. As one might expect, it

is much easier for extented sources to be discerned than point sources near the noise limit. Point sources can actually appear fainter than anticipated because of positioning at the four-corners region of adjacent pixels.

After the combining of quartets, the pixel to pixel variations and column to column variations of gain and offset must be removed. We do all of these corrections with one relatively simple procedure. The DC fixed patterns are observed by looking at the sky nearby the source so that the fixed pattern will have the same value seen by the wells in the source observation. Since the voltage levels are much larger than the stellar signals, this can be done in a relatively short time. By rotating a cold aperture, 4 K, into the array's field of view, the electrical zero background pattern can be measured. These are a sufficient set of measurements to determine the so called flatfield correction to any faint source. Bright sources require DC coupled array patterns to be measured at several background values and a nonlinear interpolation to the appropriate signal level in all the pixels for a precise solution to the image problem. We have not performed so complete of a solution to the image here but have rather used a flat field of very similar voltage level to the bright source. Hence we have some remaining structure in the Venus images at ten microns which we are able to confidently dismiss as an artifact of the data reduction procedure.

Saturation tests of the array and data system have been performed for the brightest infrared source outside the solar system, IRC+10216. It is nearly a point source at our spatial scale and is easily observed in a single pixel at the fastest readout rates. By integrating for long periods of time we were able to overflow the 24 bit words in the coadder RAM. Pixels adjacent to the source position also showed the scattered radiation from the source. Significantly the entire array did not show signal.

The ultimate measure of the value of the instrument is its ability to make infrared images with high fidelity. We have been able to make images of a variety of sources: planets, protostars, HII regions, planetary nebulae, and stars. Infrared mapping is still a novel field so there are few standards with which to compare the images produced by THE INSTRUMENT. Three such objects are presented here and comparisons can be found in the astronomical literature: Venus, BNKL, and Mon R-2.

We have images of Venus in the near infrared at 2.9 microns where it appears as a crescent. Contemporaneous with our observations, maps of Venus were made with a single InSb detector

in a spatial scanning mode at similar wavelengths Allen and Crawford (1984). In addition to the crescent of scattered solar radiation, fainter and anomalous emissions were detected on the dark side of the planet. At the time of our observations, October 1983, the sources of fixed patterns were insufficiently understood in order to soundly arrive at a similar conclusion. Ten micron maps of Venus have been known for years and we have used these as a basis for evaluating the flat fielding procedure. In June 1985, we were able to make observations of Venus at 1.7 and 2.3 microns simultaneously with the Venera balloon expedition at Venus. These images are challenging the data analysis programs because of the large dynamic range required to observe the faint clouds on the dark side of Venus while simultaneously observing the very bright illuminated side.

At 12 microns images of Venus appear nearly circular on the array. However. the point source response of the array has not been removed. Careful examination reveals a greater extension in the horizontal direction than the vertical. The effect is far more obvious on a smaller planet like Mars. A bright star, which is a point source in this case, like Alpha Orionis shows extreme extension horizontally. In fact, the upper and lower vertical edges on the image are quite different. A full point source deconvolution is required to clean up the images. Unfortunately, it is not even obvious that the normal image processing assumption of a spatially invariant point source spread function is reasonable.

For BNKL which is a star forming region in the Orion Nebula, we have images taken at four wavelengths. BNKL has been extensively studied at all wavelengths in the infrared and good comparison maps are available Wynn-Williams et al. (1984). We present these as outputs of the quartet coadding procedure to demonstrate that the corrections necessary to the digital data are subtle indeed. For the most part all features in the images are in general agreement with the existing maps in the literature. Each of the images represents about ten minutes of data collection, including all the telescope overhead time. BN is the northern source, pointlike, but clearly extended east-west due to output amplifier crosstalk. KL is the southern region which is extended in the image. It is relatively colder than BN as is indicated by the decreasing brightness of KL at shorter wavelengths. The quality of this image is more greatly affected by the point source response of the array than by the lack of a flat fielding correction.

Mon R-2 is an HII region with enbedded young stars. The region has been mapped nicely by Hackwell et al. (1982) at a

similar spatial resolution. Their map is spatially matched to the array field of view and the source intensities cover a range of magnitudes suitable for testing the response of the array to multiple sources and intensities. There is also some degree of low surface brightness material present which could be detected if the instrument is really working well. The comparison of the map and image are good with the brightest source IRC1 easily detected, and the fainter sources at the detection limit. There is no clear indication of the low surface brightness material. This image represents about 20 min of observing.

IV. SUMMARY

The instrument described here, THE INSTRUMENT, is a powerful tool for astronomical research. Its capabilities include imaging in a spectro-photometric manner many objects of current astronomical interest. We have presented a detailed description of the instrumental design and operational procedures. Examples of the images produced by the instrument are given which include planets, HII regions, starforming regions, and planetary nebulae. THE INSTRUMENT is the prototype of similar space based instruments to be flown in the 1990's.

V. References

Allen, D. A., and Crawford, J. W., "Cloud Structure on the Dark Side of Venus," Nature, Vol. 307, pp. 222-4. 1984.

Forrest, W. J., Moneti, A. Woodward, C. E., and Pipher, J. L., "The Near-Infrared Array Camera at the University of Rochester," Publ. Astr. Soc. Pac., Vol.97, pp. 183-198. 1985.

Gerhz, R. D., "Mid Infrared Imaging With SIRTF," Wyoming Infrared Observatory, November 1983.

Gezari, D. Y., Tresch-Feinberg, R., Fazio, G., Hoffmann, W. F., Gatley, I., Lamb, G., Shu, P., and McCreight, C., "8.3 and 12.4 Micron Imaging of the Galactic Center Source Complex with the Goddard Infrared Array Camera," NASA Technical Memorandum 86225. 1985.

Goebel, J. H., Witteborn, F. C., McCreight, C. R., Stafford, P., Jared, D., and Wisniewski, W., "Infrared Astronomy Imaging Spectrometer (ISIS) Prototype Instrument," Bull. Amer. Astro. Soc., Vol. 15, p 999. 1983.

Hackwell, J. A., Grasdalen, G. L., and Gehrz, R. D., "10 and 20 Micron images of Star Formation," Ap. J., Vol. 252, pp. 250-68. 1982.

Lamb, G., Gezari, D., Shu, P., Tresch-Feinberg, R., Fazio, G., Hoffmann, W., and McCreight, C. R., "Astronomical Applications of the New Goddard Si:Bi 16 x 16 Array Camera System," Proc. S. P. I. E., Vol.445, pp. 113. 1983.

McCreight, C. R., and Goebel, J. H., "Infrared Charge-Injection-Device Array Performance at Low Background," Applied Optics, Vol. 20, pp. 3189-96. 1981.

McKelvey, M. E., McCreight, C. R., Goebel, J. H., and Reeves, A. A., "Performance of Charge-Injection-Device Infrared Detector Arrays at Low and Moderate Backgrounds," NASA Technical Memorandum 86667, March 1985.

Perry, C., "16 x 16 Element Extrinsic Silicon Detector Array," NASA Contract Report CR-166,285. 1981.

Pommerrenig, D., Enders, D., Trousil, L., Capps, R., Irwin, E., Tollestrup, E., and Dereniak, E., "Hybrid Silicon Focal Plane Arrays," Infrared Detector Technology Workshop, C. McCreight ed., pp. 13.1-9. August 1983.

Rode, J. P., "HgCdTe Hybrid Focal Plane," Infrared Physics, Vol. 24, pp. 443-53. 1984.

Stafford, P. S., and Jared, D. A. "Infrared Astronomical Imaging Using a Microcomputer Data System," AIAA Computers in Aerospace Conference IV, Hartford CT, paper 83-2377CP. October 1983.

Witteborn, F. C., and Bregman, J. D., "A Cryogenically Cooled, Multidetector Spectrometer for Infrared Astronomy," Proc. S. P. I. E., Vol. 509, pp.123-8. 1984.

Wynn-Williams, C. G., Genzel, R., Becklin, E. E., and Downes, D., "The Kleinmann-Low Nebula: an Infrared Cavity," Ap. J. , Vol. 281, pp. 172-83. 1984.

Figure Captions

Figure 1. Venus imaged at 12 microns.

Figure 2. Mars imaged at 12 microns.

Figure 3. Alpha Orionis imaged at 12 microns.

Figure 4. Venus imaged at 2.9 microns.

Figure 5. Venus imaged at 1.7 microns.

Figure 6. IRC +10216 imaged at 11.3 microns.

Figure 7. BNKL imaged at 8.7 microns.

Figure 8. BNKL imaged at 11.0 microns.

Figure 9. BNKL imaged at 11.8 microns.

Figure 10. BNKL imaged at 12.5 microns.

Figure 11. Mon R-2 imaged at 12.5 microns.

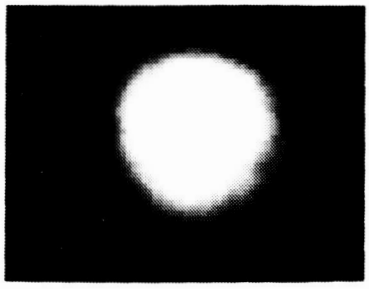

Figure 1

Figure 2

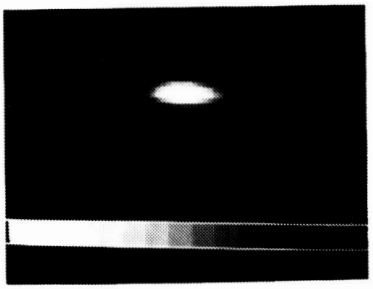

Figure 3

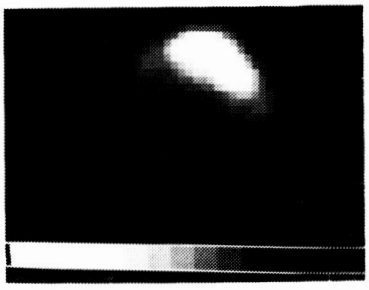

Figure 4

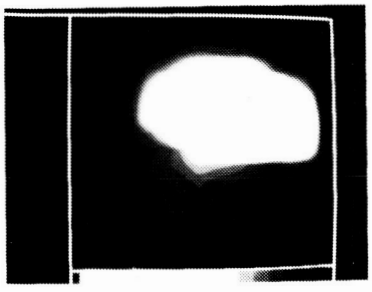

Figure 5

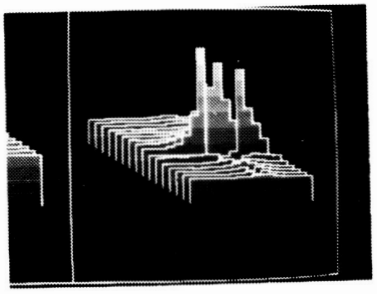

Figure 6

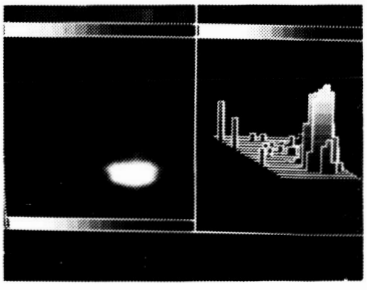

Figure 7

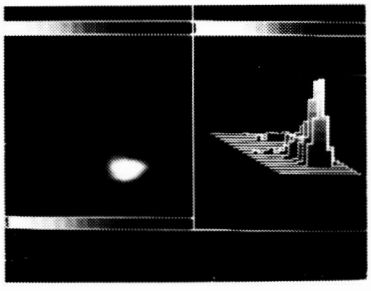

Figure 8

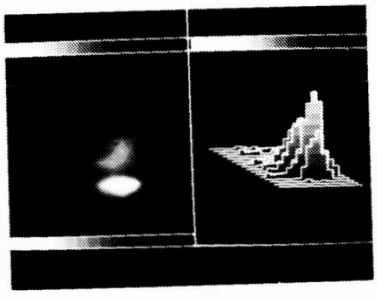

Figure 9

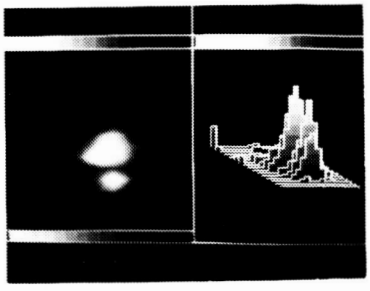

Figure 10

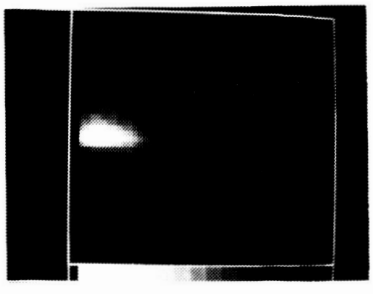

Figure 11

INTERIM REPORT FOR DEVELOPMENT OF 58 × 62 Si:Sb DETECTOR ARRAYS

Prepared for
NASA AMES RESEARCH CENTER
Moffet Field, California

Contract No. NAS2-12110

By
HUGHES AIRCRAFT COMPANY
SANTA BARBARA RESEARCH CENTER
75 Coromar Drive
Goleta, California

and

SEMICONDUCTOR DIVISION TECHNOLOGY CENTER
6155 El Camino Real
Carlsbad, California

6 December 1985

By
STUART WORLEY
STEVE GAALEMA

The paper describes work performed at Hughes IEGTC to fabricate antimony-doped silicon (Si:Sb) detector arrays for use in 30 μm IR imaging applications. A description of the operation of the multiplexer readout circuit which will be used for this application is also included.

This work was performed under contract NAS2-12110 to Santa Barbara Research Center (SBRC) for NASA Ames Research Center, Moffet Field, CA 93117, and under the cognizance of the NASA Ames Technical Director, Craig McCreight.

Detector Fabrication

The Si:Sb detector was fabricated using starting material supplied by SBRC and standard silicon integrated circuit processing techniques. The array is arranged in a format of 58 columns by 62 rows with a 76 × 76 μm pixel size. This format allows the detector array to be used with the CRC228 readout circuit.

Connections to the readout circuit are made for each individual detector pixel using an indium bump hybridization process. This process allows detectors to be processed separately from the readouts to optimize the design and fabrication of each. The detector chip is hybridized to the readout chip by accurately aligning the two chips and then applying pressure to cold weld the detector and readout indium bump.

Detector Measurements

In order to make measurements on individual detector pixels several detector arrays were hybridized to fanout chips where connections to individual pixels can be made to a small number of elements. A limitation of the fanout employed is that connections to adjacent pixels surrounding the detector element under test cannot be made. This limitation prevents measurements of an effective increase in pixel area caused by fringing fields, thereby limiting the degree of certainty of total pixel area function.

Figure 1 depicts the detector current measured as a function of temperature. This measurement was made using an external blackbody for the IR source and an internal 12.5 micron filter to obtain the two backgrounds listed. The BLIP temperatures calculated from this data are 11.5K for the high background measurements and 10.6K for the lower background data.

Figure 2 shows current versus voltage data taken on the same pixel for the same operating conditions. As mentioned above, responsivity cannot be calculated from this data due to the uncertainty in determining the pixel area.

Readout Circuit

Arrays of extrinsic silicon detectors can be read out using a direct integration, source follower per detector circuit as shown in Figure 3. Signal and background currents from the detector are integrated on the detector capacitance and the input capacitance of the readout circuit. The integration is initialized by turning on the reset MOSFET switch to set the sense node potential to V_{RST}. The capacitance is then discharged by its associated detector during the integration period. During the last part of the integration period, the sense source follower amplifier is enabled by the enable transistor, and integration voltage is read out onto the column bus. The sense capacitance is then reset and the cycle repeats. The difference in output voltage before and after the reset pulse is proportional to the infrared energy incident on the detector. By sequentially enabling and disabling the source follower amplifier, only one row of amplifiers is active at any time and power dissipation is significantly minimized.

A series of waveform photographs (Figure 4) shows several multiplexed pixels for integration periods from 1.56 ms to 14 ms. Three levels are seen for each pixel: first, a low level representing the partially discharged sense capacitor, then a short reset feedthrough, and finally a new initial level. As the integration period increases, the voltage change at the sense node increases, and the detector becomes debiased, resulting in saturation at this relatively high background level.

A photograph of a small portion of a particular integrated circuit implementation of the above circuit is shown in Figure 5. This 58 × 62 array of readout pixels has been chosen to evaluate the Si:Sb detector arrays described earlier.

Hybrid Measurements

Measurements made on Si:Sb detector arrays hybridized to readout chips are currently being made and will be reported at a later date.

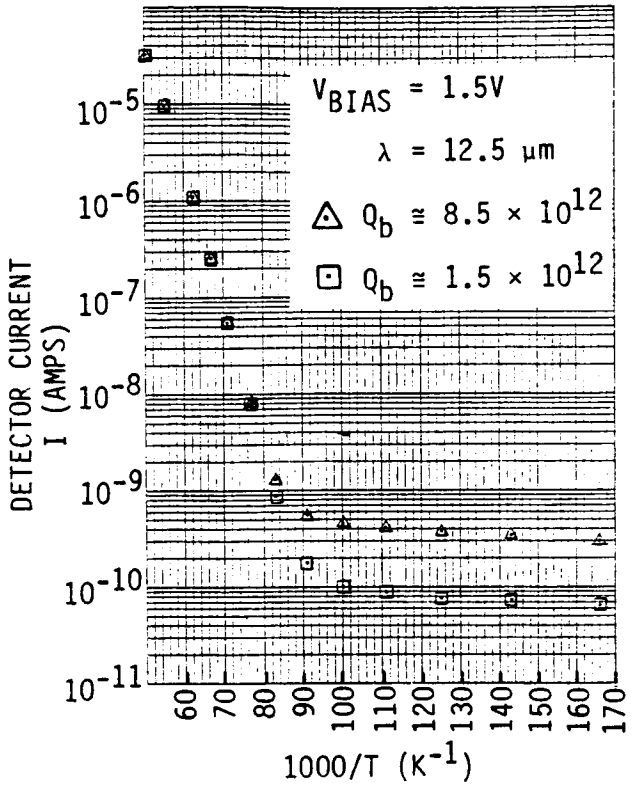

Figure 1. Detector Current versus Temperature

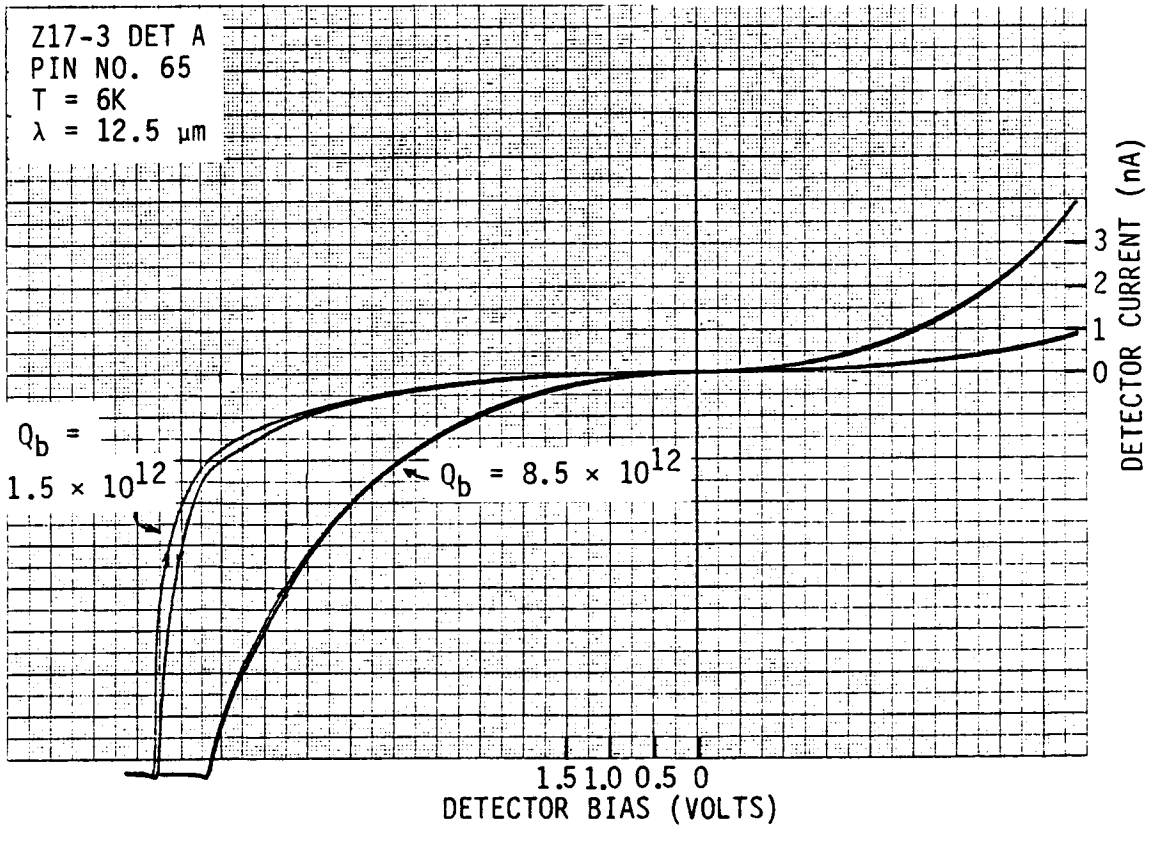

Figure 2. Detector Current versus Bias

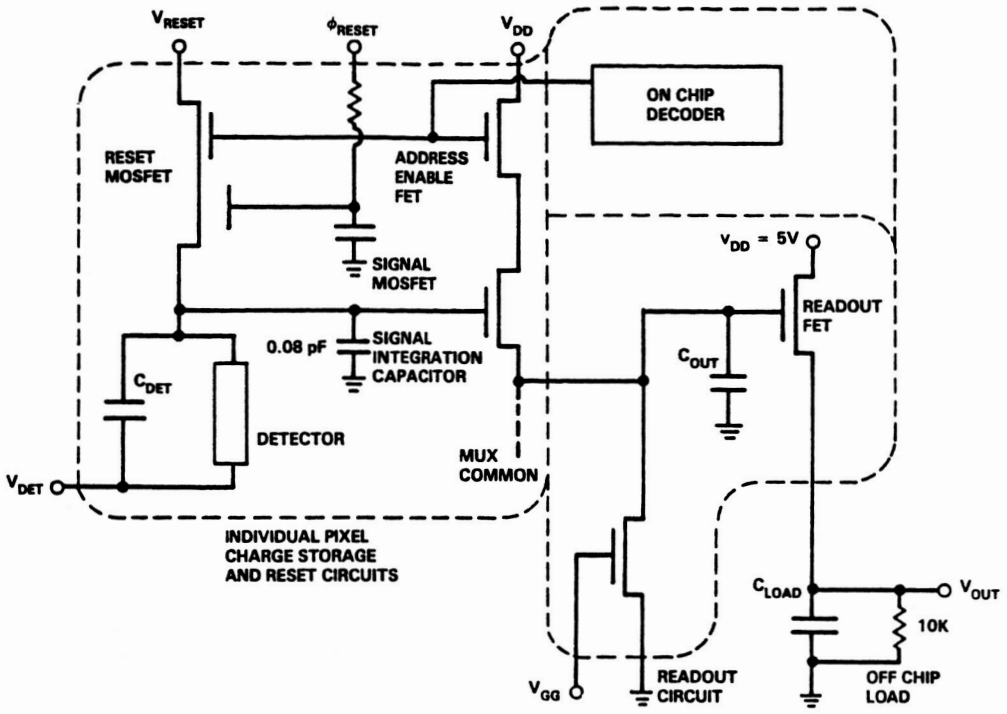

Figure 3. Integration/Source Follower per Detector Circuit Schematic

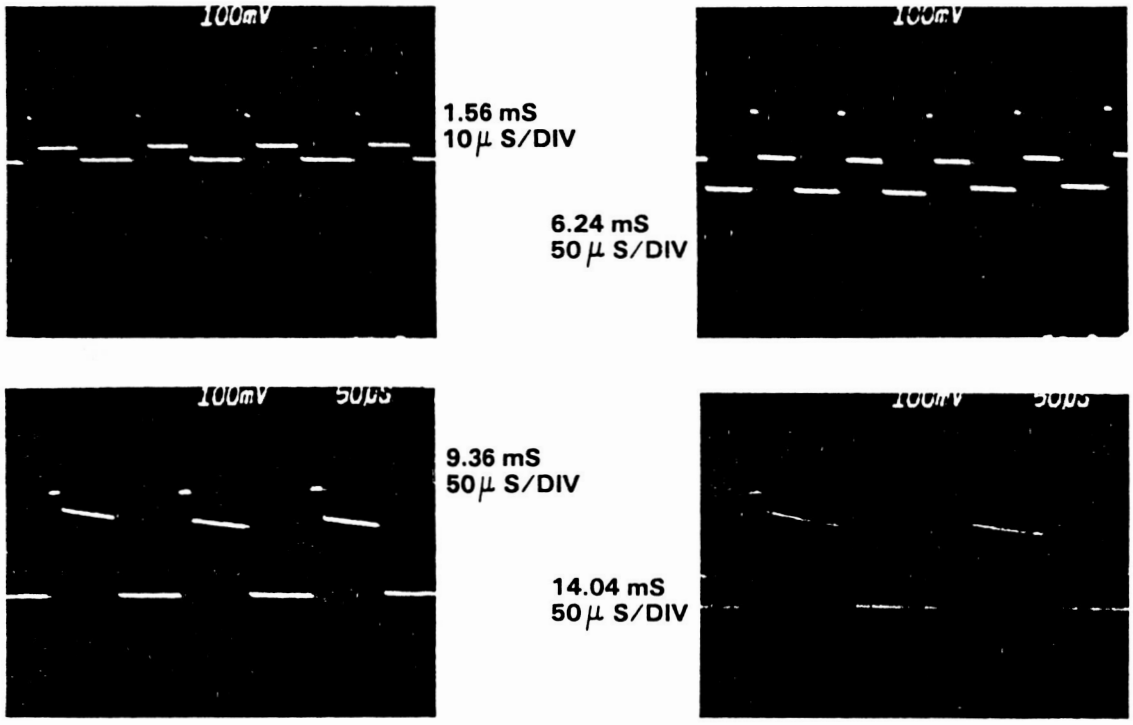

Figure 4. Typical SF/D Output Waveforms

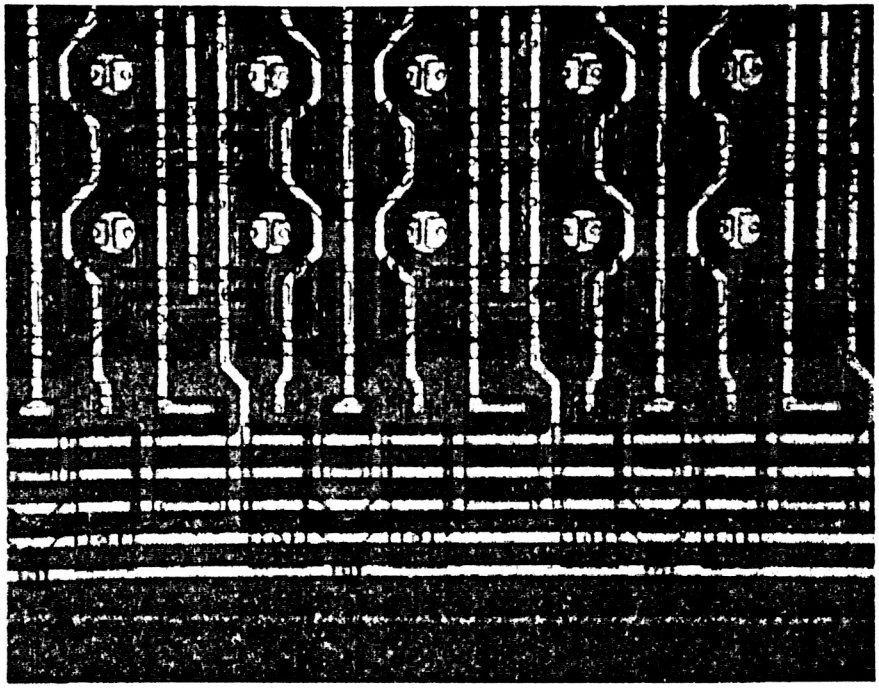

Figure 5. CRC-228 Photomicrograph

Preliminary Test Data Using the MOS DRO with Si:In Detector Material

A. M. Fowler
J. P. Britt
R. R. Joyce
R. G. Probst

National Optical Astronomy Observatories††
Tucson, Arizona 85726

J. L. Gates

Hughes Aircraft Company
Carlsbad Research Center
Carlsbad, Ca.

November 25, 1985

††Operated by the Association of Universities for Research in Astronomy, Inc. under contract with the National Science Foundation.

Preliminary Test Data Using the MOS DRO with Si:In Detector Material

A. M. Fowler
J. P. Britt
R. R. Joyce
R. G. Probst

National Optical Astronomy Observatories††
Tucson, Arizona 85726

J. L. Gates

Hughes Aircraft Company
Carlsbad Research Center
Carlsbad, Ca.

Abstract

In this paper we will describe the initial testing performed at N.O.A.O. by the Infrared Detector R & D group on the Hughes MOS DRO (Metal Oxide Semiconductor Direct Readout) with a Si:In extrinsic infrared array. The testing to date has been of a screening nature and the results are primarily qualitative rather than quantitative. At a later date, we will be getting into the performance optimization phase of our program. An encouraging result is that the detector flux response is very linear over three orders of magnitude. We have also found that this response is strongly dependent on the detector temperature, to the extent that thermal transients introduced during the chip readout will affect the performance. We were able to obtain a responsivity of 1 A/W at 2.2 microns with a bias of 15 volts, which is well below what we feel is the optimum bias.

1. Introduction

Initial screening involved several arrays, but the data presented here were taken on only one array. The test temperature ranged from 13 °K to 50 °K where the detectors became inoperative. The test dewar was a modified Infrared Laboratories (HD-3) dewar fitted with a cooled K band (2.2 micron) filter. This filter was chosen for the convenience of laboratory testing rather than any astronomical significance. The controller used to generate the clocking waveforms and control signals was a fixed state machine which also operated the signal processor. This proved to be a limitation on our ability to try various different operating scenarios. The host computer was a DEC 11/23+ CPU with 500K bytes of memory and an 80 Mbyte Winchester disk.

††Operated by the Association of Universities for Research in Astronomy, Inc. under contract with the National Science Foundation.

We are developing a new dewar which will be used for array evaluation as well as observing at Kitt Peak and Cerro Tololo. This dewar will utilize cold reflective reimaging optics and will have a cold filter wheel with provisions for eight infrared filters. The dewar is now being fabricated, and we expect it to be operational this fall. To operate the new dewar we are also developing improved electronics and a new controller. The controller will be similar to the NOAO CCD controller which utilizes a 2901 uP and RAM memory. In this way the operator can easily change the clocking and processor control signals to evaluate their effect on array performance. In the following section we describe tests of the detector responsivity and linearity as a function of temperature and background flux, at a fixed bias of 15 volts, the maximum permitted by our present test setup. We have made no attempt to optimize bias at this time, but we feel that larger bias voltages should be used for optimum operation.

Block diagrams of the present and planned future test systems are shown in Figures 1 & 2. A more detailed description of the new dewar and operating system will be the topic of a later paper.

2. Test Results

2.1. Responsivity tests

The purpose of these tests was to determine the effect of operating temperature and background flux on responsivity. Figure 3 presents the results of the small-signal (differential) linearity test. This is a critical test of a detector's astronomical utility, since this application requires the measurement of small signals against a large sky background, particularly at longer wavelengths. This test was performed by illuminating the array with a black-body to generate the signal and using a lamp to generate an arbitrary background. There was no attempt to calibrate the background, but it was varied from zero to saturation in reasonably uniform steps as determined by the background count. The data was derived by chopping the black-body and subtracting the results of the blackbody plus background frames from the background only frames. Rows 10 thru 45 of the resultant frame were then averaged to reduce the effect of individual pixels. The slope across the array results from mis-alignment of the blackbody causing some vignetting due to the cold stop in the dewar, as this effect is not seen in other data. The response is encouragingly insensitive to the background flux over a wide range.

Figure 4 is a plot of response versus temperature under fixed signal conditions. Again rows 10 thru 45 were averaged to reduce the effect of individual pixels. Above 30 °K responsivity increases with temperature while there is considerable variation below that temperature. Some of the possible explanations are that the effective gain (volts/electron) is higher below freeze-out (~25 °K) due to reduced capacitance and that the on-chip amplifier gain is higher below 25 °K. In addition the photoconductive gain is probably increasing with temperature due to the increase in material mobility. It is also possible that the detector response may vary with temperature, particularly at a

wavelength well below the peak response at 5 microns. Although we have not had sufficient time to isolate the cause of the effect, it is evident that precise temperature control is of critical importance in operating this array.

2.2. Linearity tests

Again two types of linearity tests were performed. Figure 5 is a plot of linearity versus background flux at various temperatures. This data is similar to that presented in Figure 3 but the form of presentation is different. It shows that the gain decreases slightly with background but that the slope is not a function of operating temperature. There is a considerable change in gain as the temperature is reduced below 25 °K, which has also been seen in transfer function tests run on the DRO with the reset held 'ON'. The decrease may be due to the reduction in photoconductive gain due to reduced detector bias (unlikely) or to gain changes in the DRO due to the shift in the amplifier operating point with signal. The optimum location of the operating point of the amplifier has not been fully evaluated at the time this data was taken.

Figure 6 is a plot of the ratio of measured signal to the ratio of the blackbody aperture at various detector temperatures. With the exception of the one value at 16 °K the array is very linear over three orders of magnitude. Good linearity versus signal flux has also been measured at the telescope during some limited engineering tests performed at the 1.3M telescope on Kitt Peak.

2.3. Power dissipation tests

In order to plan for cryogen consumption we evaluated the power dissipation of the array under various operating situations. The test was performed by turning all power off to the array and setting an operating temperature by using an external heater. The array was then operated and the external heater was adjusted to return to the original operating temperature. The difference in the two external power measurements was attributed to power contributed by the array. With the array operating continuously, at a 28^{+} ms. per frame rate, the array dissipated ~13.5 mw. This could be affected by adjusting $V_{\phi ARST'}$ which controls the 'on' resistance of the address line pull down mosfet. This adjustment could reduce the dissipation by ~3 mw but at the expense of array performance. It should be possible to reduce this effect by using a different clocking scheme without having an adverse effect on array performance. Another source of power was the output source followers which dissipated ~2.5 mw. This contribution could be reduced by decreasing the drain current and the drain voltage. However, it is not a good idea to turn the source follower off during integration for the reasons described below.

During the course of this work we found that the array was very sensitive to its short term operating temperature. Changes in the temperature of the DRO, too small to be measured by the temperature sensor mounted on the cold finger, had considerable effect on the dc level and gain of the array output. These changes were small but frame

to frame changes are a fatal form of 1/f noise. For this reason it is very important to reduce the power dissipated in the chip and, more importantly, to maintain it at a constant level when data is being collected. This requires that the readout be the same in all respects and that delays be inserted before data is taken after changing integration rates to allow the detector to restabilize. This is not a serious problem for ground based work but is an important consideration for long integrations in a low background space environment.

3. Conclusions

These arrays have been used several times at the 1.3 and 2.1 meter telescopes at Kitt peak with favorable results. The performance of the array is illustrated by Figure 7, an image of Comet P/Halley in the H band (1.6μm) obtained on the KPNO 2.1 meter telescope on 7Nov85. The total integration time was 1200 seconds (obtained by co-adding) and the plate scale is 1.5 arcsec/pixel. Although the detector performance was limited by internal background, which limited the integration time to 2 seconds, it was possible to subtract off the very small signal level from the large background level with virtually no fixed pattern noise. The RMS noise in Figure 7 corresponds to H $\sim 15^{mag}$. Much work still needs to be done to optimize performance and to fully understand the effects of thermal transients on the DRO and detectors. SBRC is making arrays using this DRO and InSb detector material. It will be very interesting to compare the performance of Si:In with the InSb when both arrays have been more fully characterized. Certainly the linearity and integration capacity are pluses for the Si:In detectors, while high quantum efficiency, photovoltaic nature, and low dark current are pluses for the InSb detectors.

4. Acknowledgements

We would like to thank Steve Gaalema and Dan Murphy of Hughes Carlsbad Research Center without whose contributions and help this work would not have been possible.

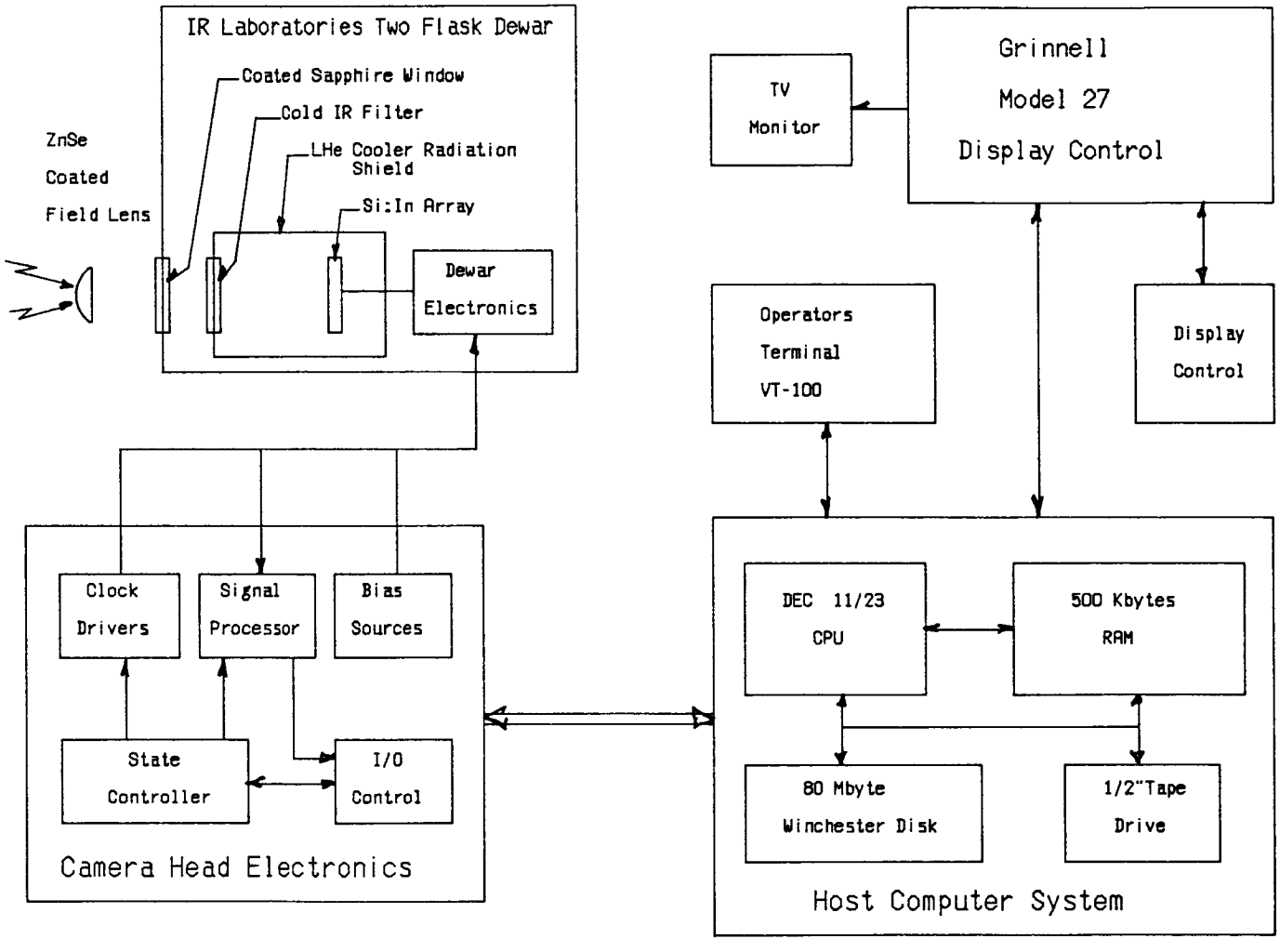

Present Test System

Figure 1

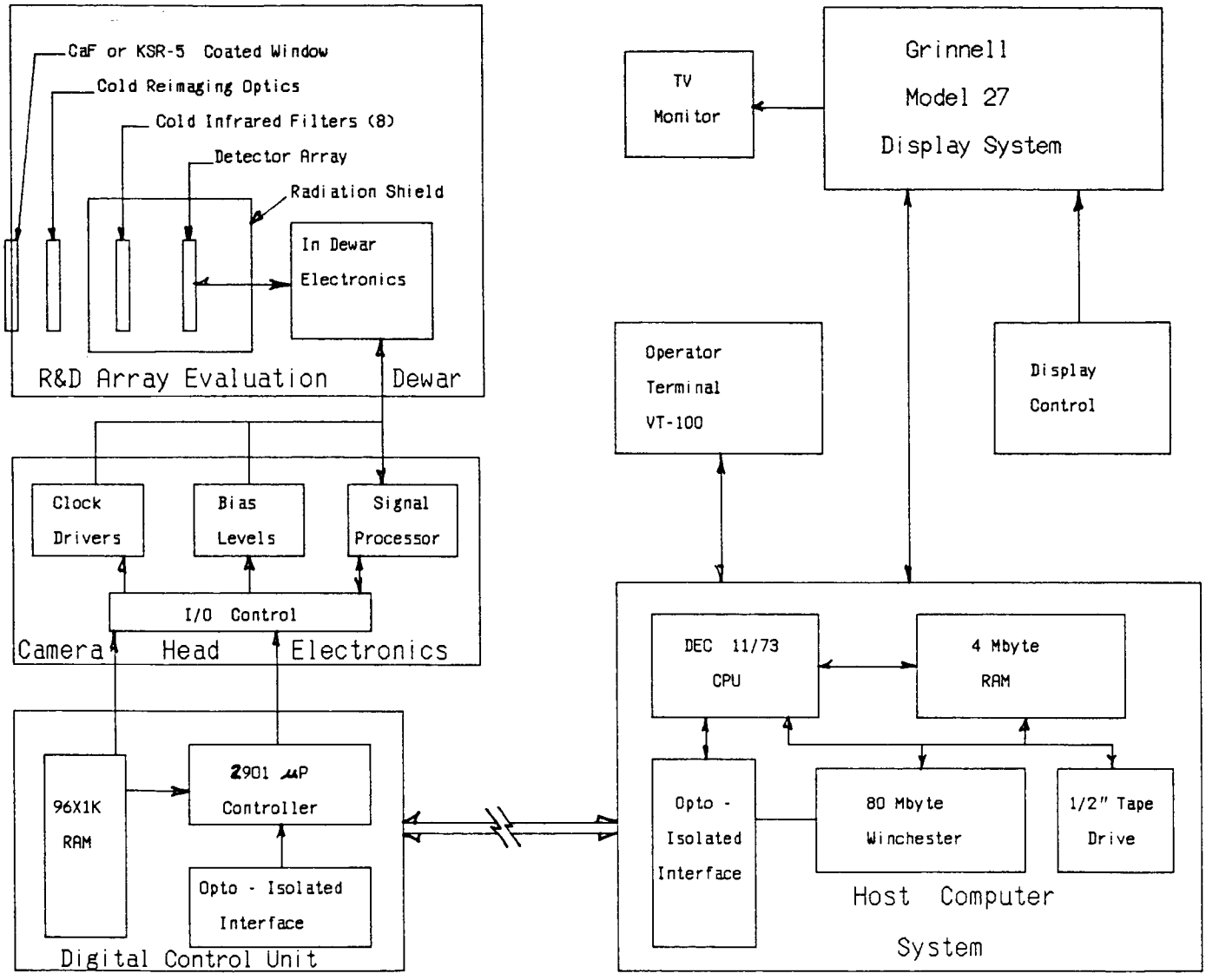

New R&D Evaluation System
Figure 2

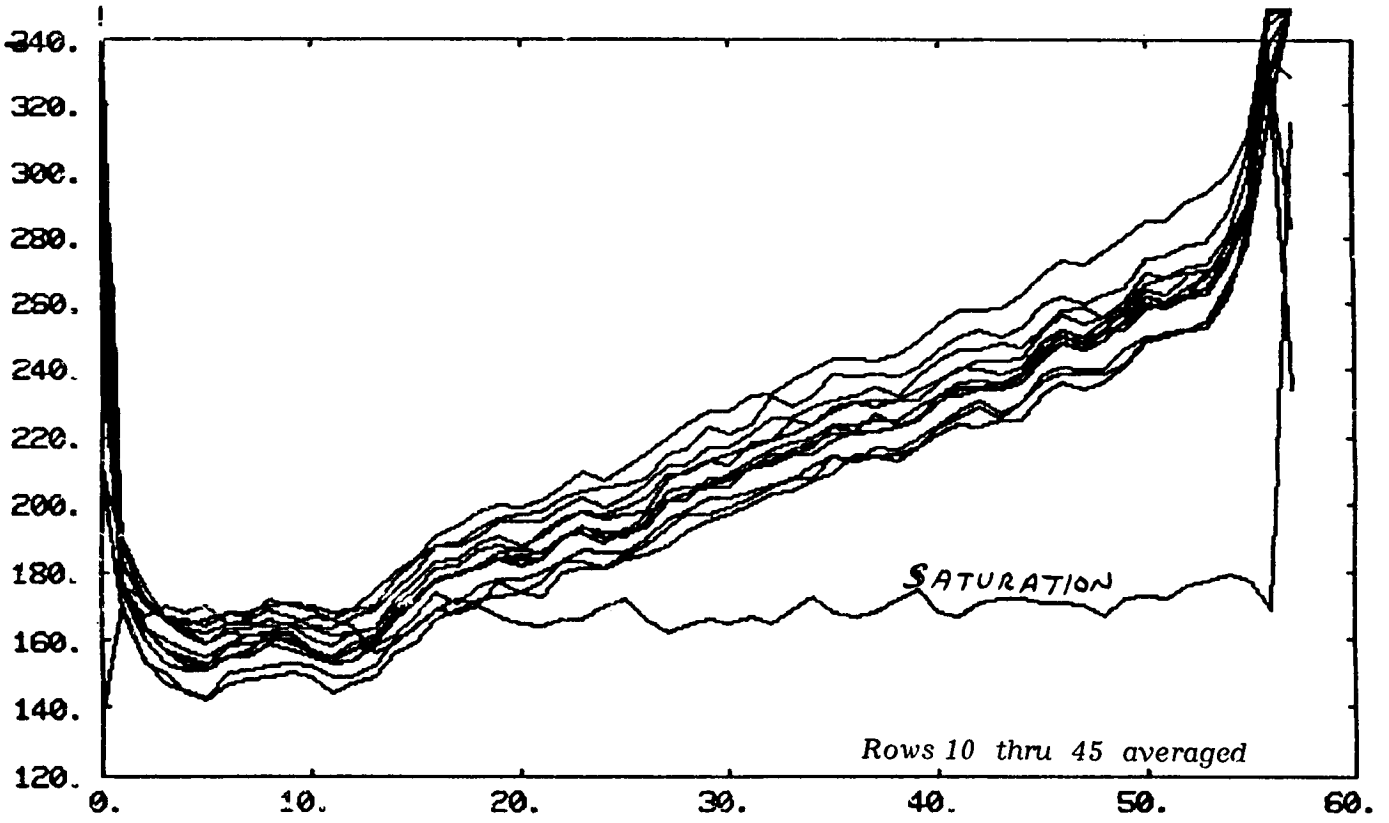

Signal Response Versus Background Flux

Figure 3

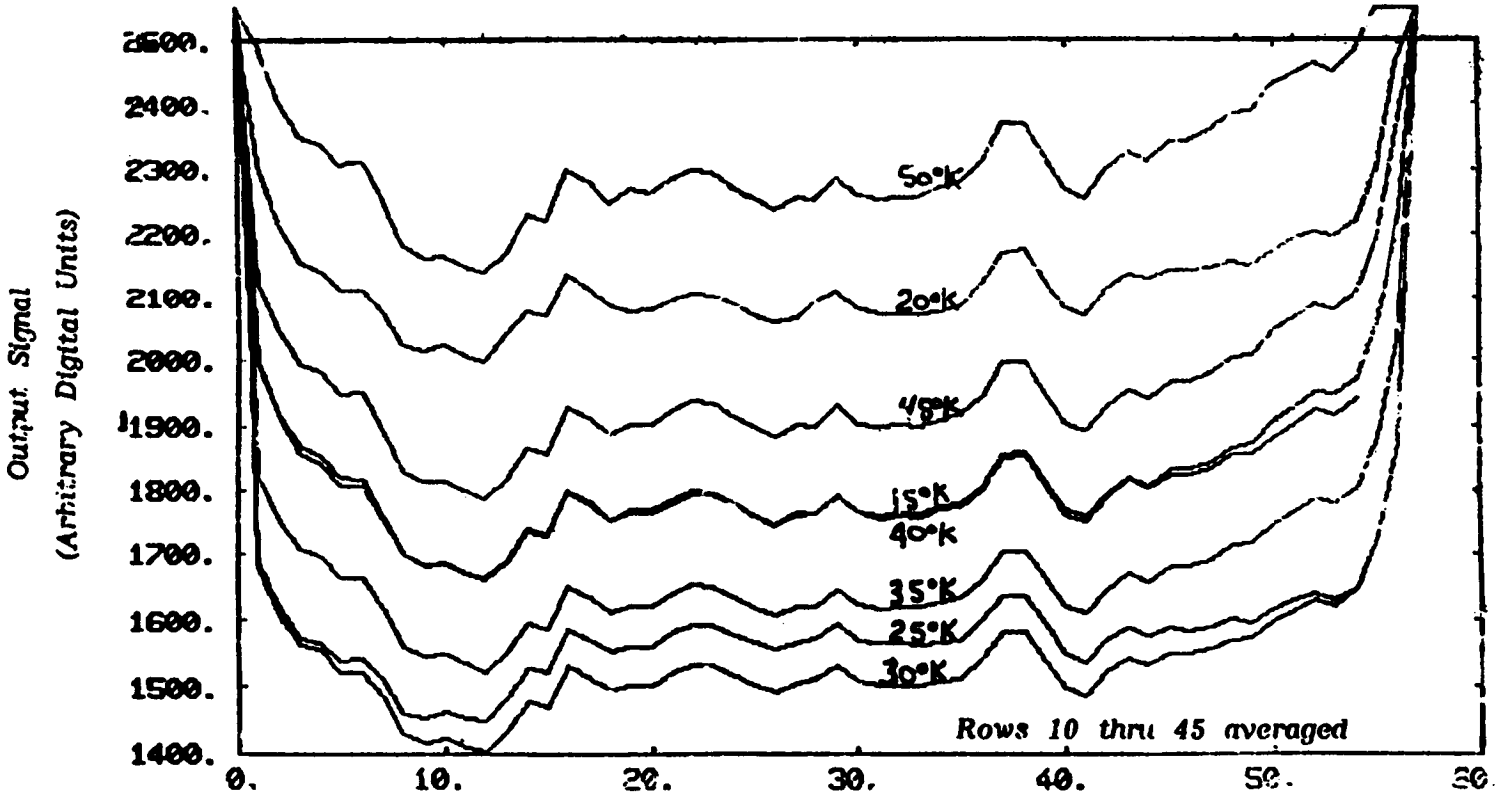

Column Pixel Number

Signal Response Versus Cold Finger Temperature

Figure 4

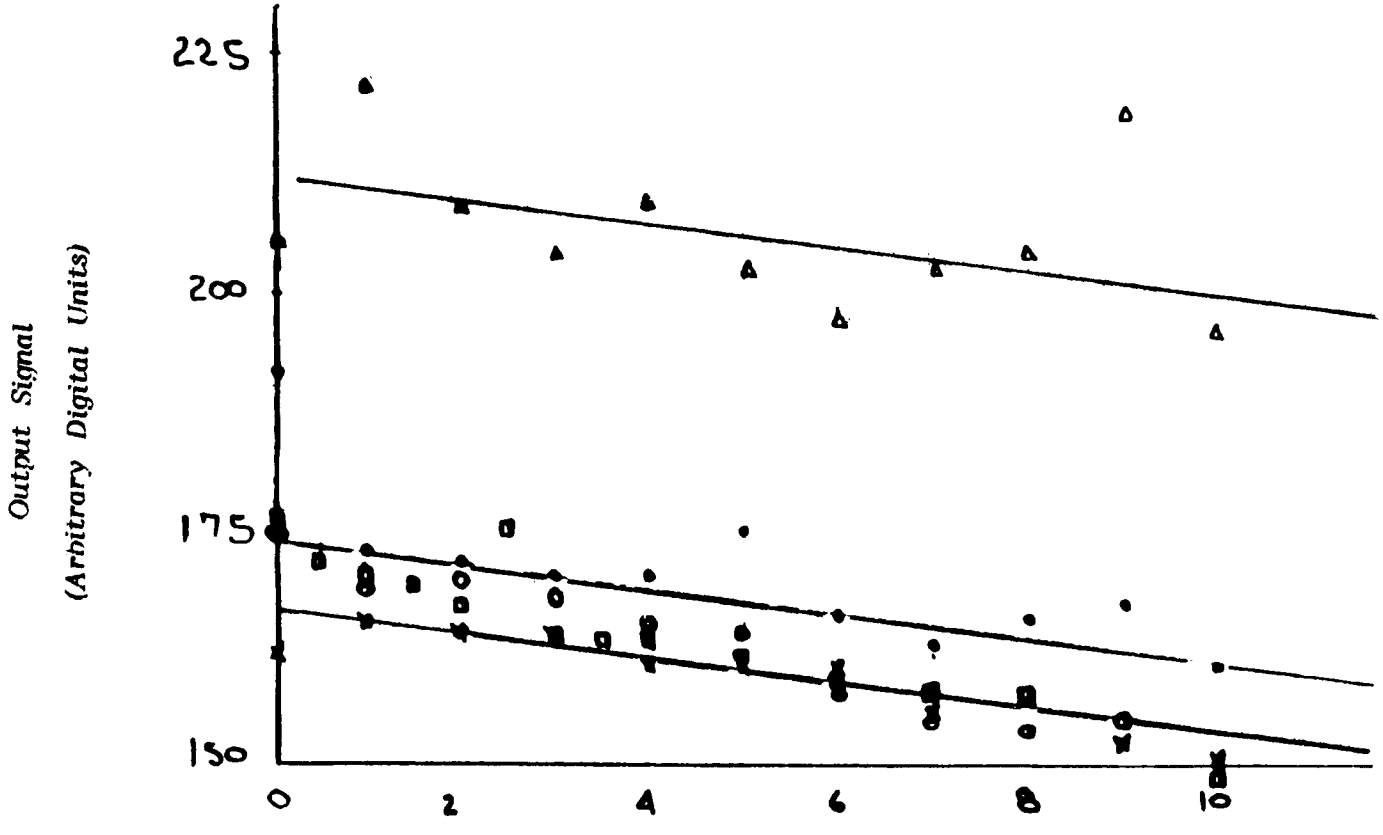

Linearity Versus Background Flux

Figure 5

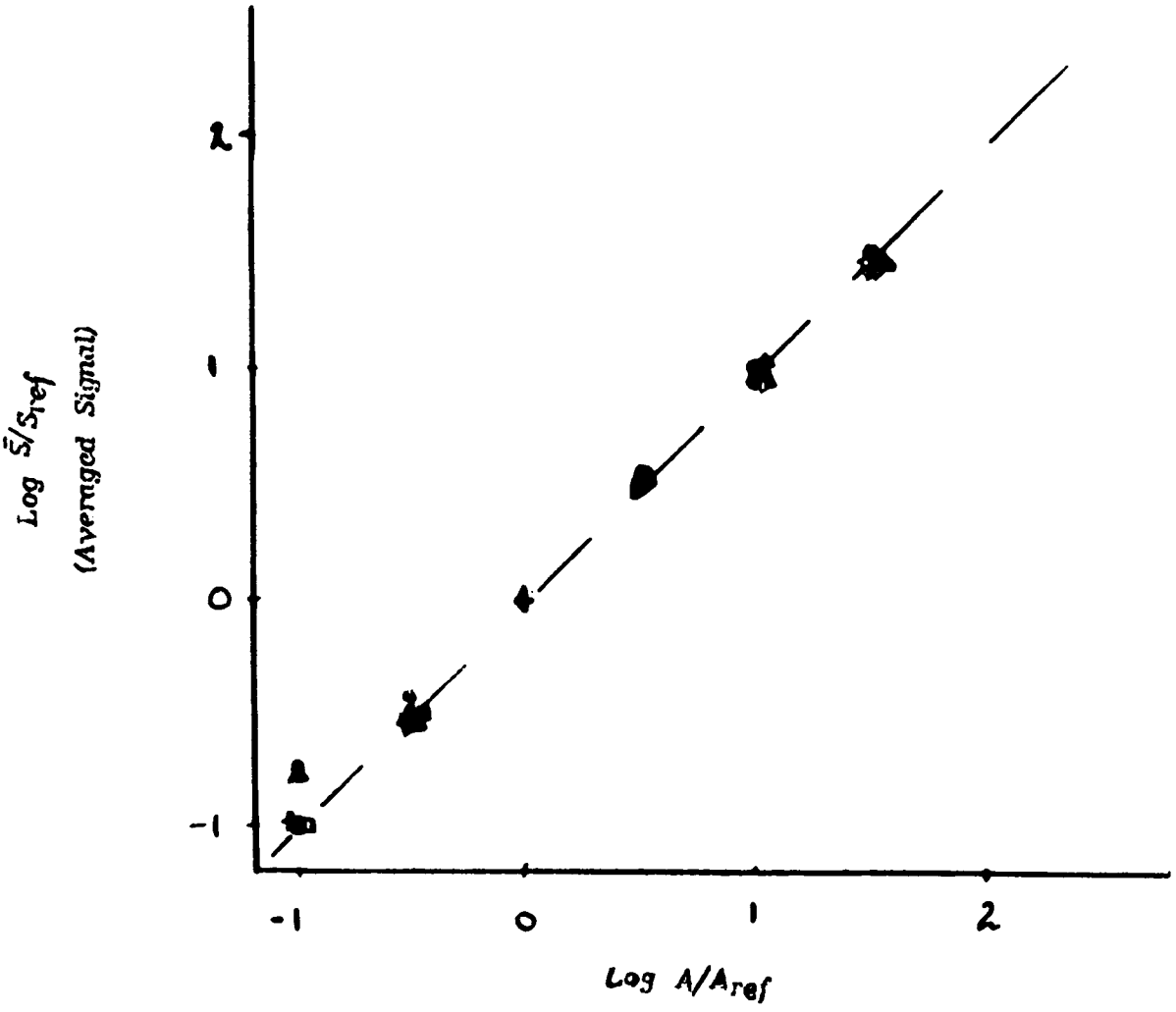

Linearity Versus Temperature

Figure 6

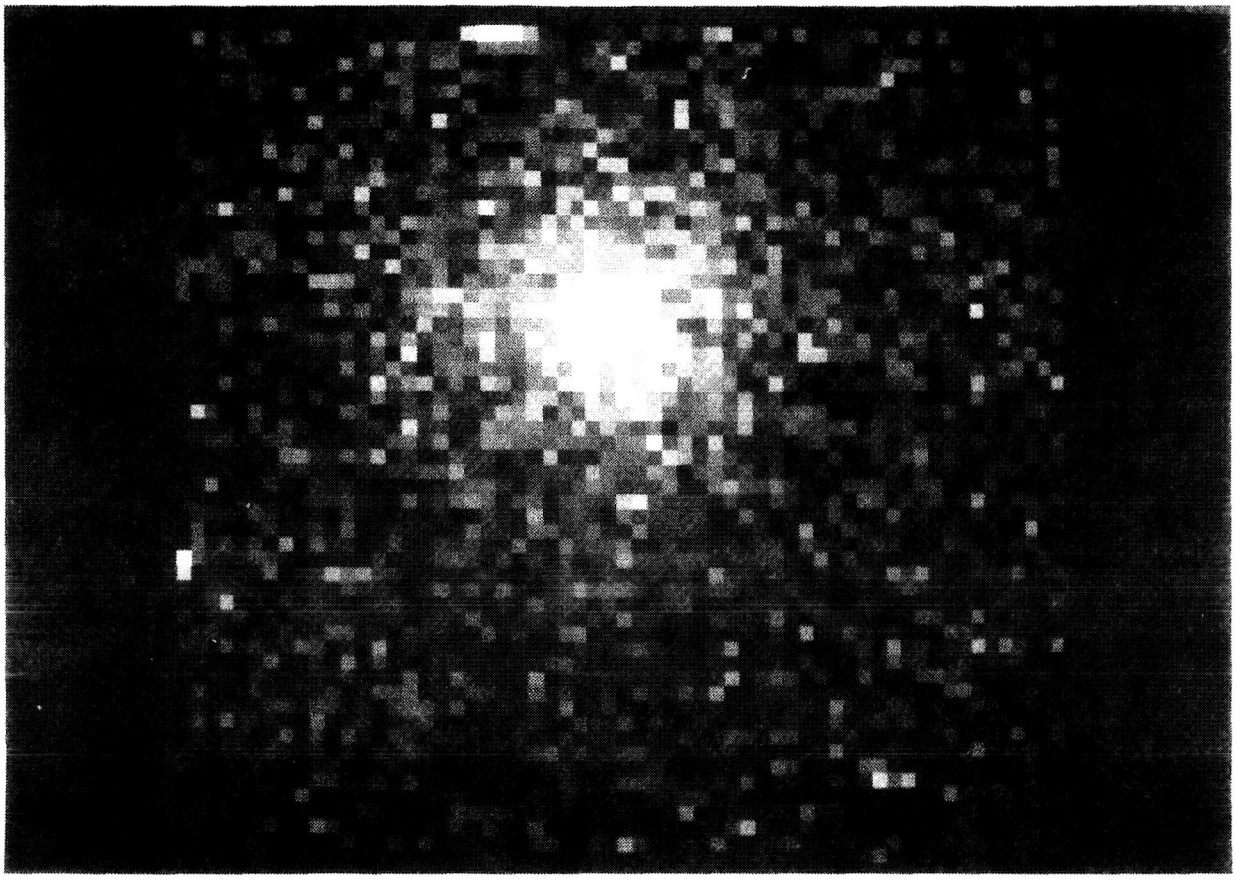

Comet P/Halley
H Band 1.5 arcsec/pixel
November 7, 1985

Figure 7

EVALUATION OF A Si:Ga DIRECT READOUT ARRAY

PRELIMINARY RESULTS

Gerald M. Lamb, Peter S. Shu, Donald C. Lokerson
Instrument Microelectronics and Detectors Branch
Instrument Division
NASA/Goddard Space Flight Center
Greenbelt, Maryland 20771

Daniel Y. Gezari
Infrared Astrophysics Branch
Laboratory for Extraterrestrial Physics
NASA/Goddard Space Flight Center
Greenbelt, Maryland 20771

Jeffrey Bowser
Science Applications Research Corporation
Lanham, Maryland 20706

Introduction:

An infrared array detector evaluation program is in progress at the Goddard Space Flight Center. Array devices are being tested under this effort for the Infrared Array Camera (IRAC) for the Space Infrared Telescope Facility (SIRTF). The three wavelength bands for this instrument cover the range from 2 to 30 micrometers. The instrument goal isw to achieve background limited and diffraction limited imagery over most of the instrument wavelength range. Since the SIRTF telescope is a cryogenic cooled instrument, these requirements place severe performance limitations on the detector.

The state of the art for array detectors has advanced rapidly in the past few years from small format, modest performance, arrays to the current larger format low background devices. As a part of our evaluation program, we are testing one such device, a Hughes Carlsbad Research Center/Santa Barbara Research Center 58 by 62 gallium-doped silicon infrared array.

This device is a hybrid array composed of a detector substrate bump bonded to a direct readout (DRO) silicon multiplexer.

Detector Program Goals:

1. Characterize the performance of existing array devices.

2. Evaluate existing Si:Ga DRO device under anticipated SIRTF/IRAC conditions.

3. Conduct performance evaluations under full-up operating conditions.

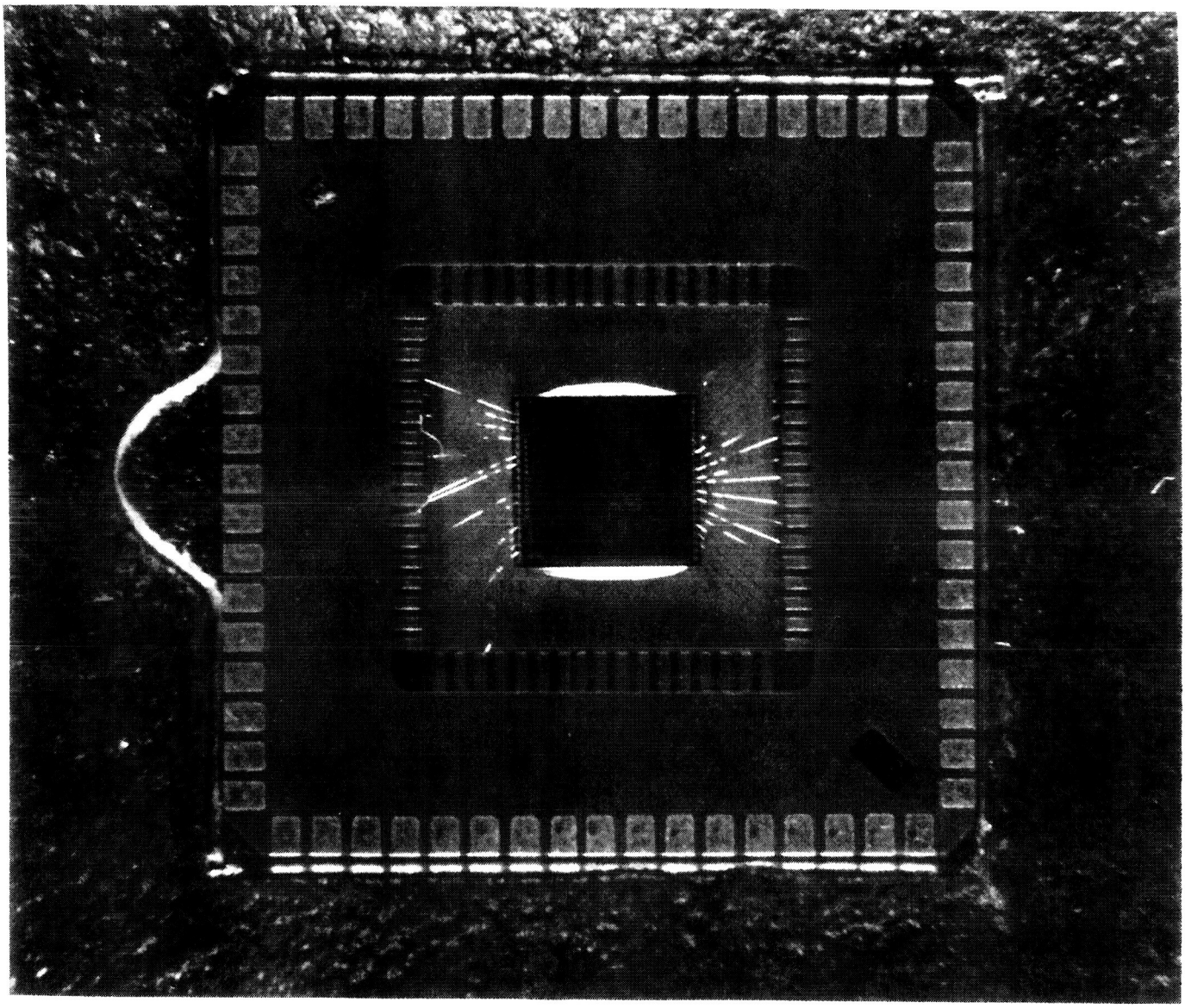

CRC/SBRC Si:Ga DRO Array

This is a photograph of the Si:Ga DRO array in the 68 pad leadless ceramic chip carrier. The array in the center is bonded to the ceramic carrier and electrically connected by the thin wires. This is one of the new generation of devices which uses a cryogenic MOS multiplexer bump bonded to a detector array. This subassembly was furnished to the Goddard Space Flight Center by the Santa Barbara Research Center. This device was not tailored for the SIRTF instrument but was provided as a baseline device representing the MOS direct readout capabilities.

SI:GA CRC 228 DIRECT READOUT ARRAY CHARACTERISTICS

MATERIAL	SI:GA
DOPANT CONCENTRATION	5-6 X 10^{16} GA/CM^3
WAVELENGTH RANGE	3 TO17 MICRONS
MULTIPLEXER	CRC-228
FORMAT	58 X 62
PIXEL AREA	75 µM X 75 µM
PIXEL SPACING	75 µM X 75 µM
MULTIPLEXER GAIN	0.7
SENSE NODE CAPACITANCE	0.1 PF
DRO ELECTRICAL RESPONSE	1.12 µV/E
WELL CAPACITY	3 X 10^6 E

Facing Page: Simplified Block Diagram

This diagram is the simplified schematic for an addressed unit cell of the DRO array through the electronic signal processing used at Goddard. Input photoflux incident on the pixel would follow the solid line diagram in the lower left of the schematic which includes the reset pulses. When operating the array as an imaging device, the output from the common driver includes the signal pulse (shown by the dotted line), the reset pulse, and the reset level immediately following. In the integration time (Ti), the pulse sequence from other addressed unit cells are read out such that a pixel pulse stream is created. For the CRC 228 chip there are two common drivers, one for the even pixels and one for the odd pixels. The signal processor is a double sampling filter which simultaneously differences the unit cell reset and signal levels and suppresses the MOSFET 1/f noise. The unit cell difference is digitized and processed through the data acquisition system.

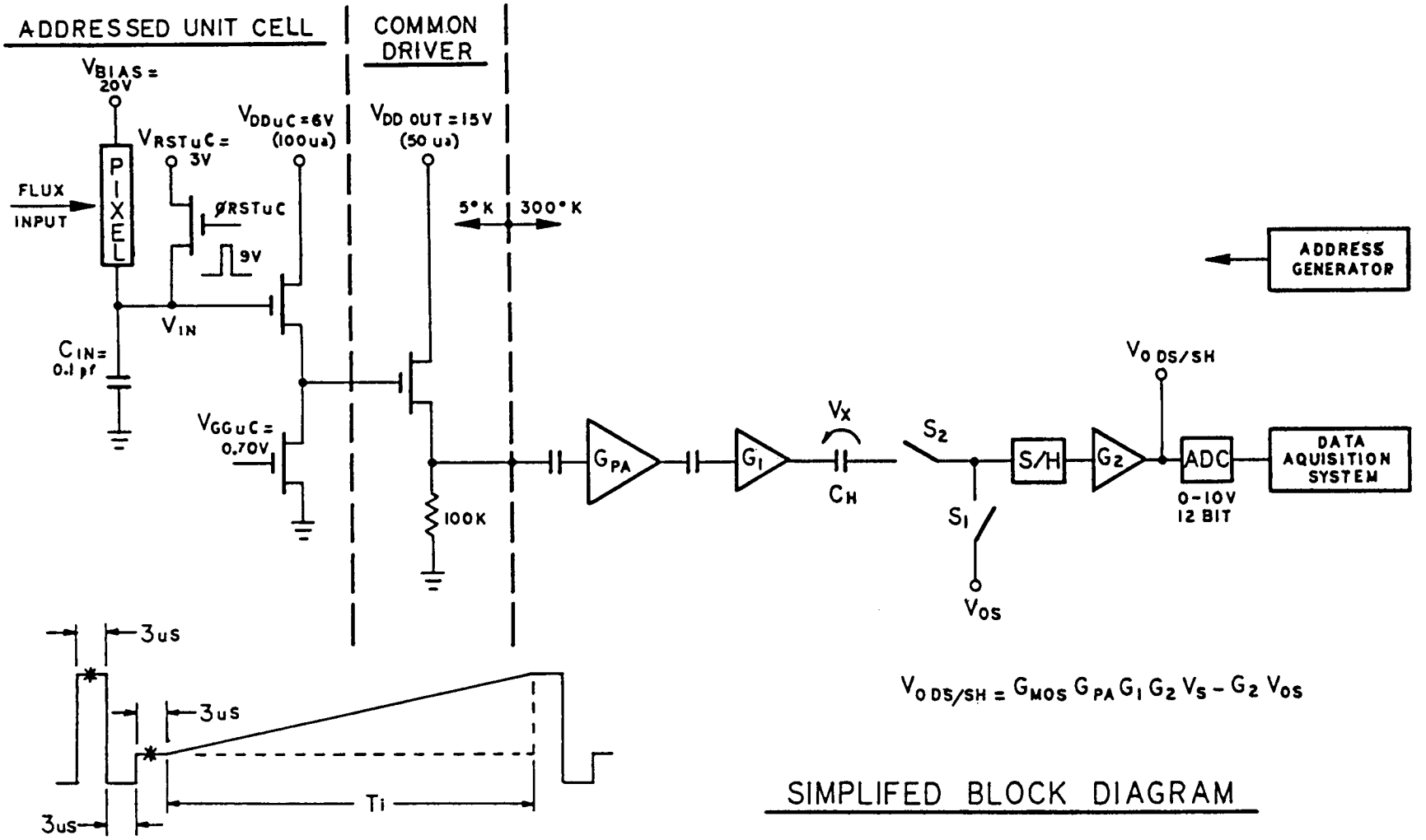

$$V_{O\,DS/SH} = G_{MOS}\, G_{PA}\, G_1\, G_2\, V_S - G_2\, V_{OS}$$

SIMPLIFED BLOCK DIAGRAM

POWER DISSIPATION

TOTAL DEVICE POWER DISSIPATION	4.000 MW
AVERAGE UNIT CELL DISSIPATION	0.984 MW
AVERAGE DRIVER DISSIPATION X2	1.125 MW
ESTIMATED CLOCK POWER DISSIPATION	1.900 MW

FPA TEMPERATURE	5.7 K
TI	0.1 SEC
DET BIAS	14 V
BACKGROUND	MINIMUM

DRO ELECTRICAL TRANSFER FUNCTION

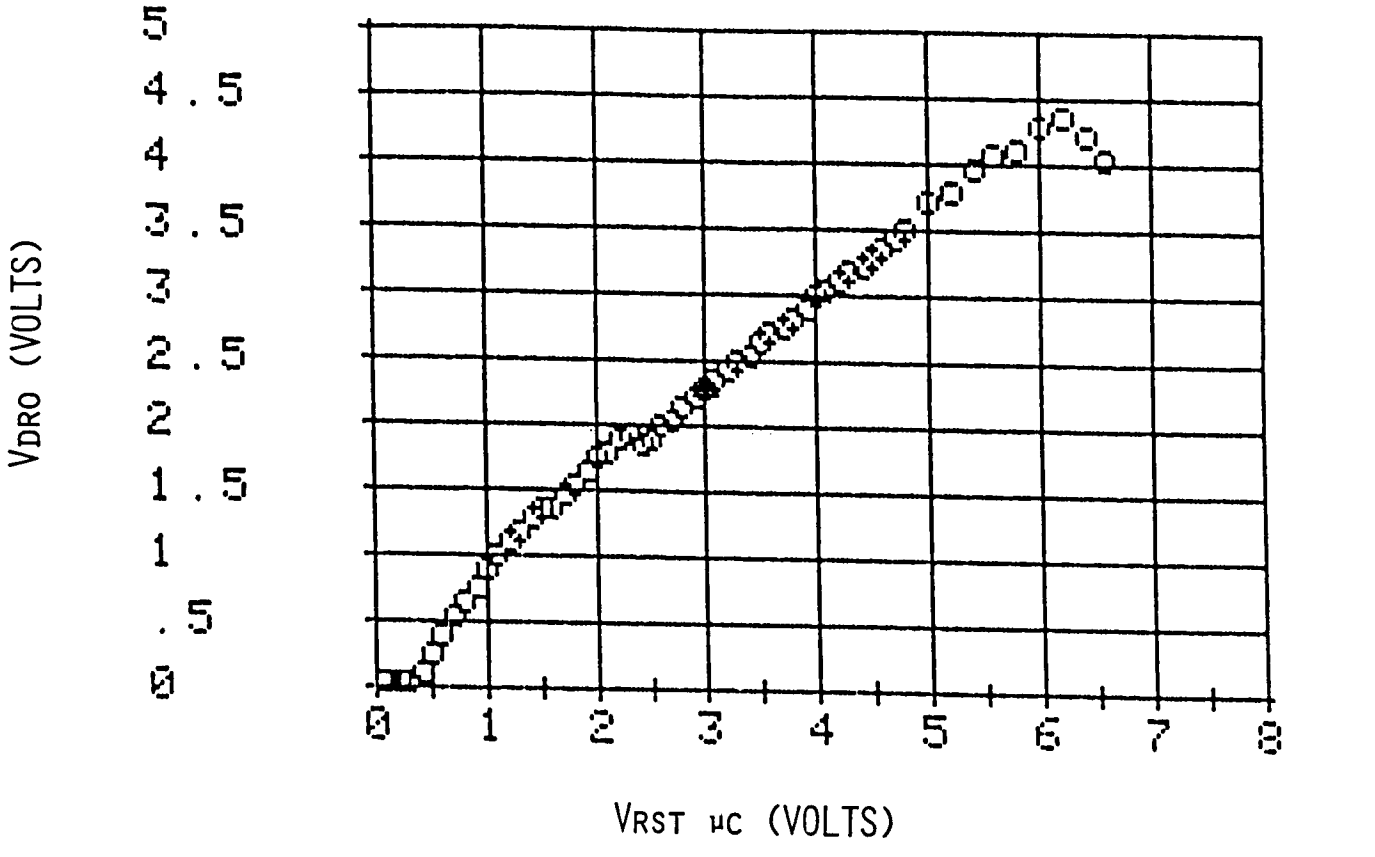

FPA TEMP. = 5.76°K

DRO Electrical Transfer Function

The DRO electrical transfer function highlights the unit cell/common driver operating point. This plot was generated with the detector electric field reduced to zero, the input applied to the reset level and the output recorded at the common driver output. We operate the array at a liquid helium bath temperature and biased above the kink at 2.4 volts.

TEST CAPABILITIES

FOCAL PLANE TEMPERATURE	4.2 K TO 20 K
SIGNAL FLUX RANGE (UNFILTERED)	10^{14} TO 10^{3} P/CM^2
SIGNAL FLUX RANGE (11 μM .5 μM BW)	3×10^{11} TO 3×10^{2} P/CM^2
BACKGROUND (BGND DET)	LESS THAN 1.5×10^{7} P/CM^2
READ OUT FORMATS	7 X 16 16 X 16 29 X 32 29 X 62
SYSTEM GAIN	32 TO 1120
SYSTEM SENSITIVITY	70 TO 2 E/BIN
SYSTEM NOISE FLOOR (DRO INPUT)	60 ERMS
INTEGRATION RANGE	0.025 TO 900 SEC.

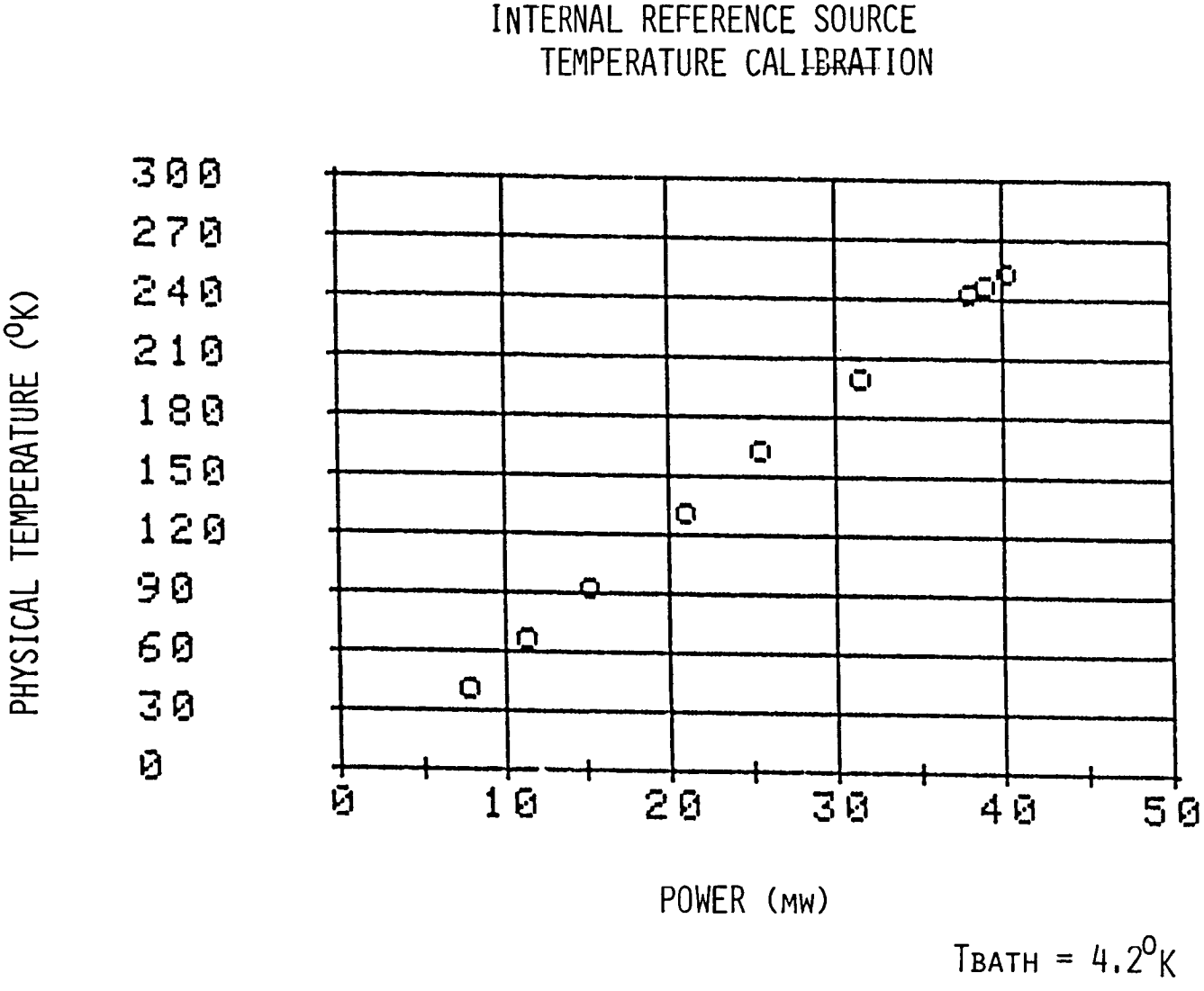

Internal Reference Source Calibration

An internal reference source was placed in the helium temperature enclosure. A temperature sensor was hybridized to the source to record physical temperature. A plot of the power dissipated in the source and the measured physical temperature indicate a useable range from 40 deg Kelvin to about 250 deg Kelvin. The low mass of the source allows modulation at a 1 Hz rate.

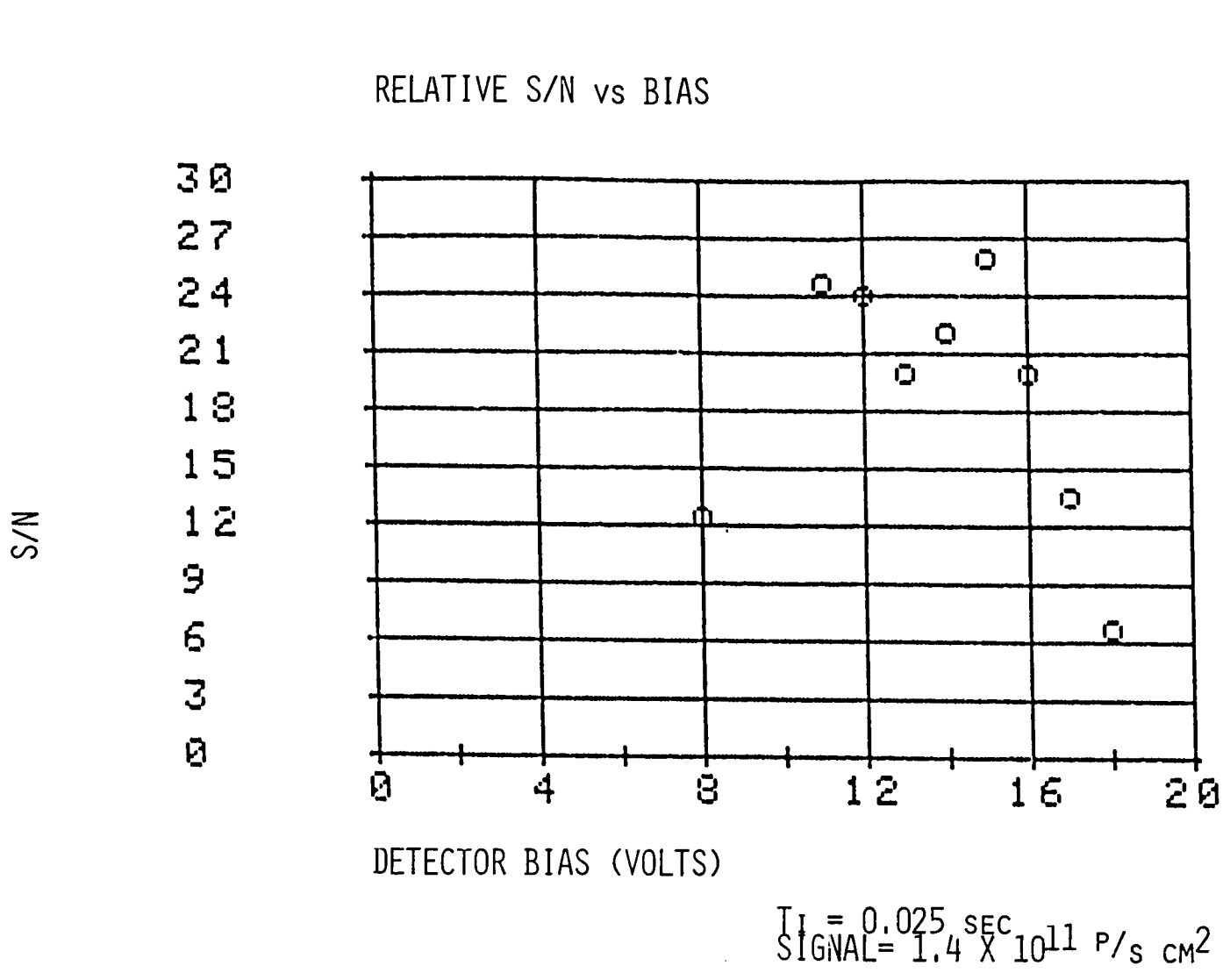

Relative Signal to Noise Versus Detector Bias

The detector bias sensitivity of the present array is highlighted in the plot of relative signal to noise versus detector bias. The rolloff in performance above 15 volts bias is due to detector breakdown at the background tested.

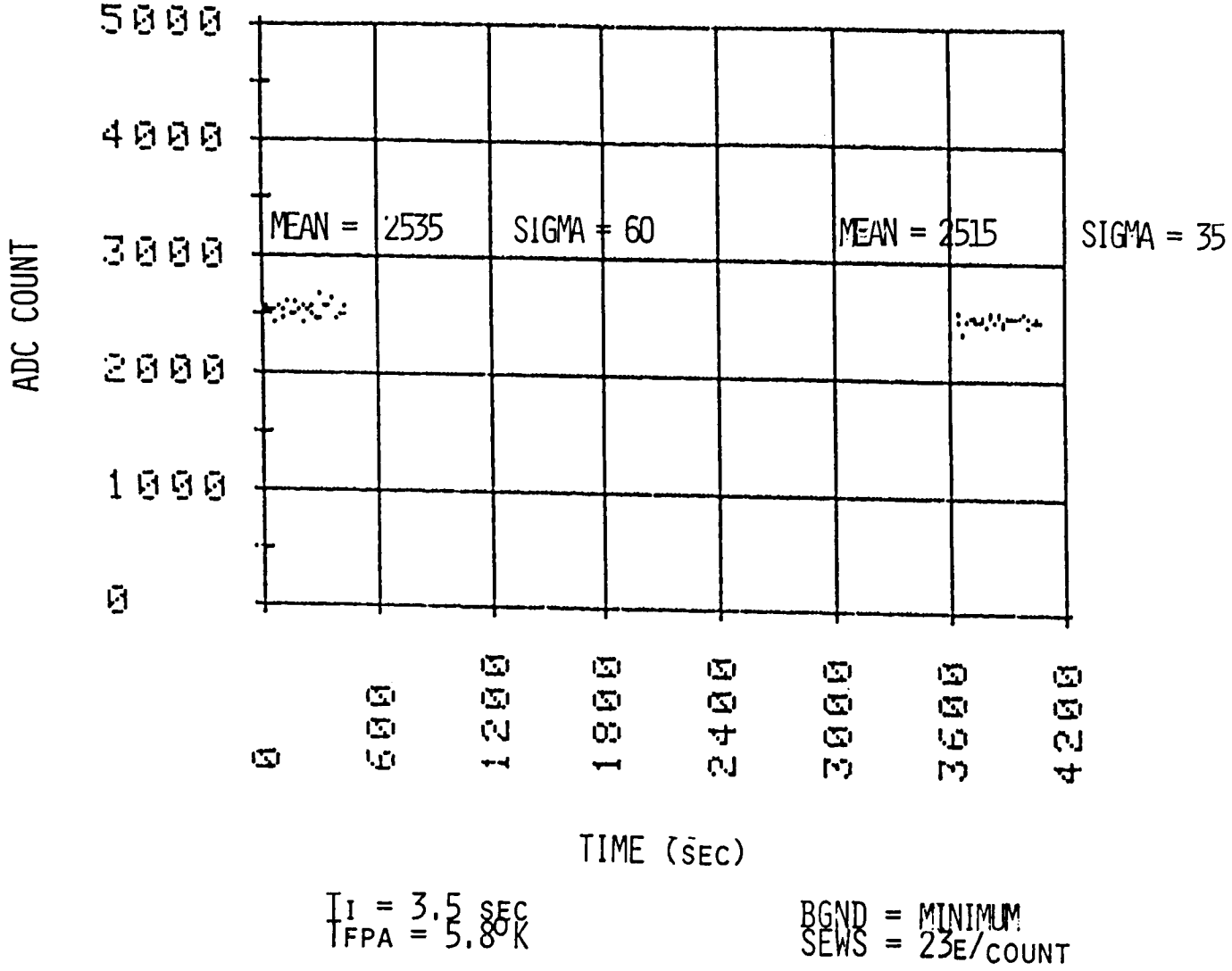

DRO Drift Response

A preliminary evaluation of the drift response was conducted by recording the array output, waiting approximately an hour, and recording again. The results for a detector integration time of 3.5 seconds indicate good drift response under equilibrium conditions for the times considered.

Facing Page: Signal to Noise Improvement with Integration

The facing page pictures a series of integrations showing the signal to noise improvement as a function of the integration time. The vertical axis is arbitrary bin number, the horizontal axis is the frame number. The integration time per frame is shown. Visible in the pictures is the "hook response" frequently seen in conventional photoconductors under low background conditions. The next plot indicates the performance improvement for the current device. To avoid the anomalous effects, equal numbers of frames were compared at the negative going transition to determine the mean and variance.

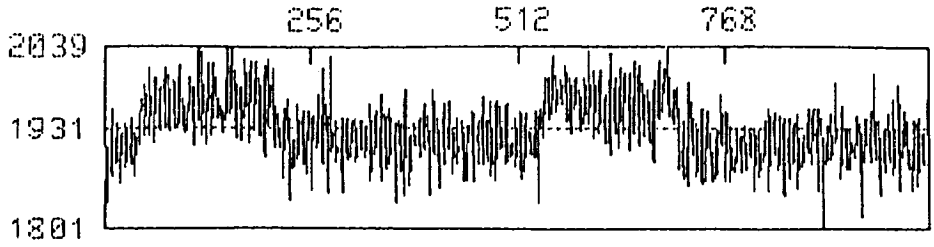

T_I = 0.1s

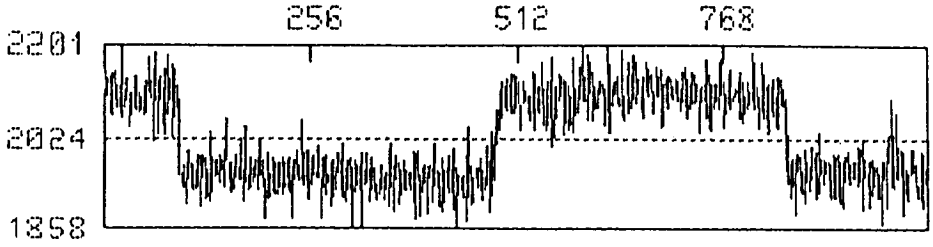

T_I = 0.67s

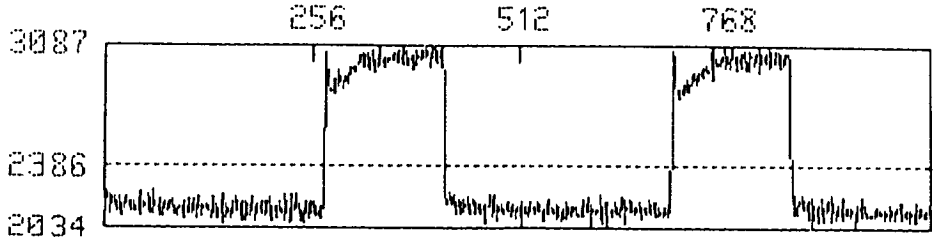

T_I = 1s

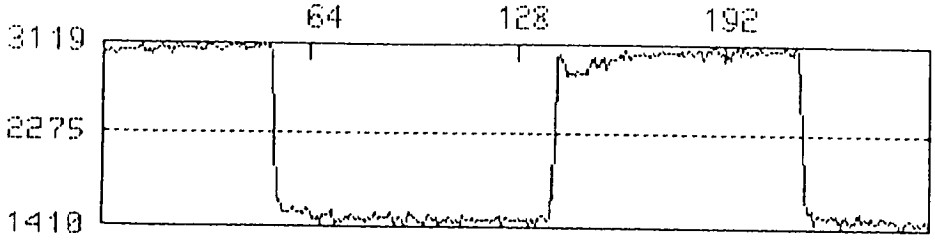

T_I = 2s

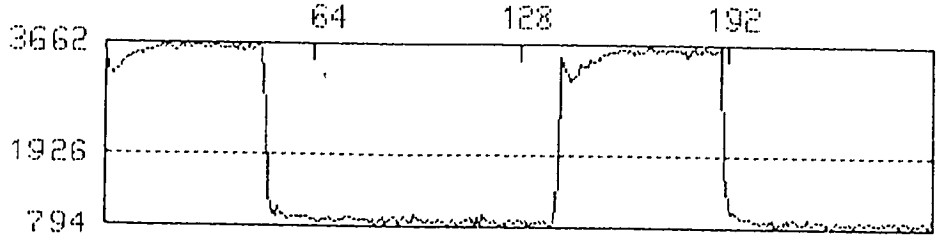

T_I = 3.5s

S/N IMPROVEMENT WITH INTEGRATION TIME

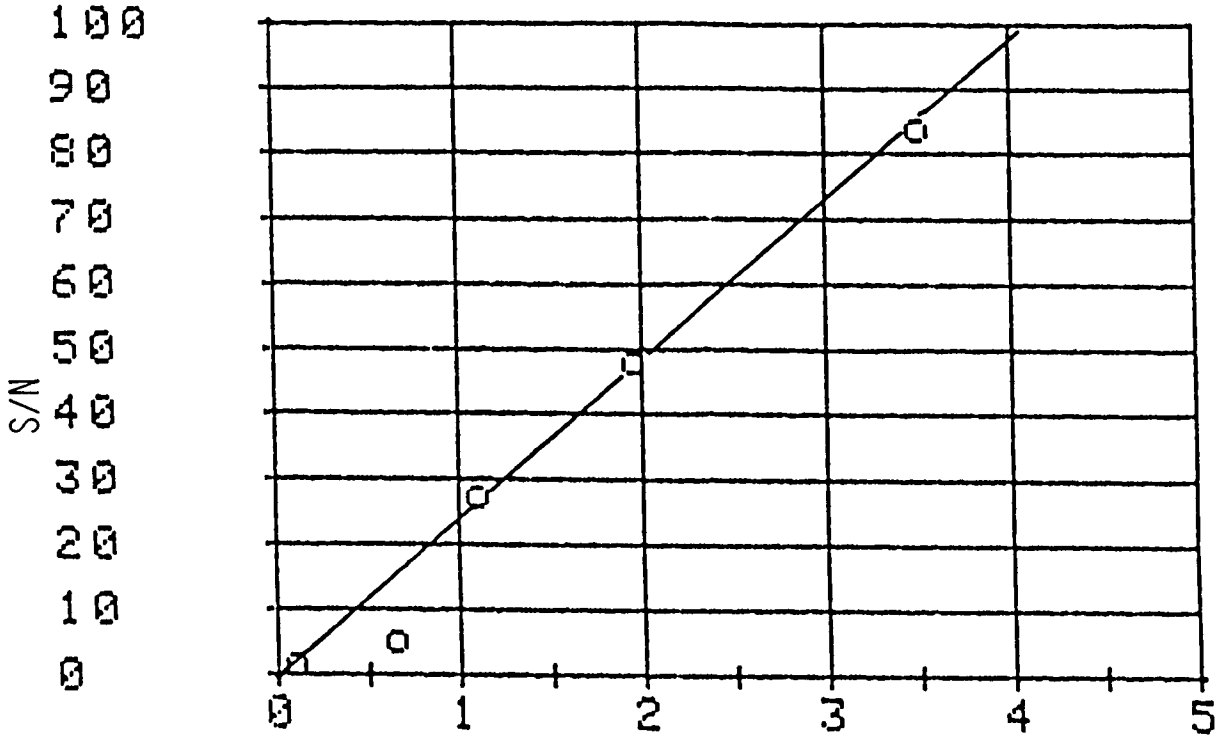

DET. BIAS = 11 BGND = ZILCH
FPA TEMP. = 5.7°K SIG ≈ 10^9 P/S CM^2

PRELIMINARY Si:Ga DRO ARRAY TEST RESULTS

	IDEAL	IRAC GOAL	RESULTS TO DATE
RESPONSIVITY (A/W @ 11μ)	8.87		4.6
READ NOISE (e^- RMS)	18-50	< 100	1400 - 2000 (SYSTEM LEVEL) 180 - 300 (OUTPUT FET)
DARK CURRENT (e^-/SEC PIXEL)		< 200	$< 10^4$ (MATERIAL OR LIGHT LEAK LIMITED, TBD)

TEST CONDITIONS: T = 5.2K, MINIMUM BACKGROUND.

Preliminary Array Test Results

Responsivity as measured with the internal reference source appears to be very good.

The read noise under full up system operation is considerably higher than expected. With the unit cell clocks disabled and sampling the noise from a single unit cell, the noise is considerably improved though not as low as predicted (80-100 eRMS). The effects of the measurement setup and their effect on the noise performance are currently under investigation.

Dark current is considerably higher than desired but not higher than expected for the doping concentration of the device and the operating temperature. Also, at this time we are unable to determine if any of this dark current is due to light leaks in the test system.

FUTURE WORK

- o MINIMIZE CLOCKING AND BIAS NOISE SOURCES
- o CONTINUE INVESTIGATION OF DARK CURRENT
- o INVESTIGATE ARRAY OPERATING TEMPERATURE EFFECTS
- o INVESTIGATE LONG INTEGRATION TIME CHARACTERISTICS
- o VERY LOW BACK GROUND PERFORMANCE
- o REDUCTION OF FOCAL PLANE POWER DISSIPATION
- o LOW BACKGROUND IMAGING CHARACTERISTICS

Summary:

We are very encouraged by the preliminary results from our testing of the Hughes Si:Ga array. The device functioned predictability and repeatibility at the low temperatures needed for SIRTF. The power dissipation was reduced to acceptable levels while still maintaining the device speed. The infrared response was excellent and the degree of "anomalous" effects was comparable to conventional photoconductors. The device dark current will need to be optimized for the SIRTF application and is comparable to conventional photoconductors. The read noise as measured to date has not been minimized, and an excess due to clock coupling is indicated by our tests.

EVALUATION AND CHARACTERIZATION OF HYBRID ARRAYS

John F. Arens, Michael C. Peck

University of California, Space Sciences Laboratory, Berkeley, CA.

Project Summary

An Infrared Camera has been built at the University of California at Berkeley for astronomical observations and for testing arrays for satellite based work. The detectors are sensitive to mid infrared wavelengths. The camera has been tested at the University of Arizona 61" and 90" telescopes and the NASA IRTF. These tests have demonstrated a sensitivity consistent with photon shot noise with an ~10% quantum efficiency for each pixel when the camera was used with a 1.6% spectral filter or when used with a Fabry-Perot having a resolving power of 2000. Initial measurements of read out noise, dark current, cross talk and hysteresis have been made in our laboratory.

The detector chip we are currently using is a hybrid array manufactured by the Hughes Aircraft Company. Because part of our goal was to develop and advance new technology, we decided to work with a switched MOSFET array. This architecture is very promising, and this proposal is addressed to quantifying the detector parameters carefully.

Introduction

An infrared camera sensitive to ~10 micron wavelength radiation has been built at the University of California at Berkeley and has been used for detector testing and astronomical observing at the University of Arizona 61" and 90" telescopes and the NASA IRTF. The detector array is a 10 x 64 element, doped silicon, hybrid chip manufactured by the Hughes Aircraft Company. The use of an array allows all points of an image to be obtained simultaneously and without scanning the telescope. Data acquisition times are thereby reduced by N, the number of pixels; and the relative spatial fidelity of the image is greatly improved by eliminating first order telescope drift effects.

Infrared detector arrays are similar in concept to visible light, silicon CCD's currently being

used in that they are photon counting, charge transfer devices. However, visible light technology has limitations for infrared observations. Narrower electronic bandgaps in the currently less technologically developed infrared detector materials produce larger dark currents than in undoped silicon in spite of cooling the infrared devices. The enormous foreground radiation fluxes from the telescope and atmosphere often dictate very rapid readouts compared with CCD readout times. New technology developments were required for constructing infrared array detector systems.

Several groups are currently developing infrared cameras and spectrometers using microelectronic, multipixel chip detectors. The design of the first camera built was developed by the principal investigator (Arens, 1981, 1983, 1984) and met the criterion of rapid readout needed for the high fluxes of broadband, thermal infrared observations. This camera was tested at several telescopes. An Aerojet Electrosystems Corporation bismuth doped silicon accumulation mode charge injection device served as the detector.

Slightly modified versions of this detector (Parry, 1983) have been used at the Ames Research Center (McCreight, 1981, Goebel, 1983) in very low background tests for space flight applications. This detector is also being built into another NASA funded system (Jones, 1983).

A Rockwell International charge coupled device (CCD) with an indium doped silicon detector layer and Image Information detectors are being built into a system and tested in Hawaii (Pommerrenig, 1983) for IRTF application. NASA is also supporting the construction of a system using a Santa Barbara Research Center indium antimonide-CCD hybrid detector (Forrest, 1983).

A Hughes Schottky barrier array has been built into a camera by Al Fowler at Kitt Peak National Observatory. He has plans to build an InSb array camera.

Other published and unpublished work has been performed in evaluating detector arrays (Infrared Detector Technology Workshop, Ames Research Center, 1983). The above descriptions should serve only to describe the more elaborate systems known to us.

The development of new technology was a partial goal of the project which was originally funded by DARPA, leading us to a complete redesign of the Goddard camera and the inclusion of a detector array of different type from those used by any other astronomical investigators.

Camera Description

The camera was designed around a detector array with multiple parallel outputs and around a computer with good interfaces to external hardware. The system is composed of two parts, the dewar and custom electronics, and the computer. The two parts are connected by optic fibers for carrying the signals and by an IEEE 488 bus for transmitting control and monitor data.

The present detector arrays are hybrid, 10 x 64 element, switched MOSFET, arsenic and gallium doped silicon arrays developed by the Hughes Aircraft Company. The drive electronics has a flexible timing and voltage configuration and is controlled by an IEEE 488 bus from the computer. The output from the array flows in 10 channels, each of which is amplified, correlated double sampled, and digitized to 15 bits. The signals are then sent over the optic fibers to the computer. Depending on the multiplexing configuration, up to 1000 frames/second can currently be read out.

The computer is a Sun Microsystems workstation with additional multibus cards for input and output. The operating system is UNIX bsd 4.2, and the camera control and operations language is MAGIC/L. The Sun central processor as well as four Microbar processors have Motorola 68010 and 68000 chips and are used for control and data acquisition respectively. The system contains a color monitor for data display.

Figure 1 is a diagram of the components of the camera. The dewar assembly allows operation of devices in vacuum at any temperature from liquid helium (4 K) to room temperature and incorporates a set of holder wheels which are controlled by stepper motors for the positioning of filters or sources (Figure 2a). The assembly is electronically controlled by a digital package (Figure 2b) including a flexible method for setting the voltage levels and timing of input signals necessary for operating the Hughes readout chip. All parameters are controlled by a Sun microsystems (Figure 2d) workstation via an IEEE-488 interface connecting the multibus cage of the workstation to a Hewlett-Packard multiprogrammer which operates the digital electronics package.

Outputs from the detector array are processed by the analog package (Figure 2c) which contains several sets of amplifier and analog to digital converter chains. Control signals from the

digital package coordinate the readout chip timing with the switched sampling of the amplifiers and the digitization of the chip outputs. Four optic fiber links (each with a capacity of 20 megabits per second) transfer the digitized signals to the workstation.

The components contained in the multibus cage of the Sun microsystems workstation are indicated in the system diagram (see lower portion of Figure 1). The optic fiber links and IEEE-488 cable connect the workstation with the analog and digital electronics. The IEEE-488 multibus controller enables software in the workstation to control the operation of the facility. Each optical fiber is interfaced to a multibus card containing an independent Motorola 68000 microprocessor with local memory. Several of these processors can receive data in parallel for subsequent transfer to the primary Sun processor card, which executes the UNIX bsd 4.2 operating system. All of these processors execute programs written in MAGIC/L, a threaded code language designed for interactive applications. The workstation incorporates a 400 megabyte disk, 9 track tape drive for data storage, and a color display system.

Figure 3 is a diagram of the MOSFET circuit necessary for operation of the readout chip. The diagram has been divided into several functional portions of the circuit. The pixel selection circuit indicates how a sequence of address lines can select an individual pixel by turning on the gates of the V_{DD} bias MOSFET and the enable gate of the reset MOSFET. Signal charge is generated by the detector portion of a pixel and is fed into the gate of the signal MOSFET. The U_{reset} signal allows the gate of the signal MOSFET to be reset to the V_{reset} level for any pixel that is enabled by the reset MOSFET. The readout MOSFET is connected to the signal MOSFET in a source-follower arrangement providing power for driving an external circuit.

The coordinated sequencing of the reset line and switches S1 and S2 in an external circuit are schematically indicated in Figure 4 illustrating the correlated double sampling technique used for measuring the charge collected on the gate of the signal MOSFET. The times of changes in the states of S1, S2 or U_{reset} during a single cycle are numbered one through six. The voltage difference, dV, across the correlated double sampling capacitor C_{CDS} between time 5 and 6 is determined by the difference in the output, prior to reset (time 1) and after reset (time 5). S1 is

open during reset, insulating C_{CDS} from the large reset pulse. Between times 5 and 6 the voltage across the C_{CDS} can be sampled and held for subsequent digitization by an A/D converter. Analysis time per pixel may be as fast as 10 microseconds to rapidly read out the entire array.

Figure 5b is an oscilloscope trace of the repeated operation of an illuminated single pixel. The upper portion of the trace is the output, V_{out} of the amplifier chain as illustrated in the lower half of Figure 4. The lower portion is the input to the sample and hold with correlated double sample analysis time set to 2 microseconds and reset time interval set to 200 microseconds. Figure 5a is an oscilloscope trace of three different pixels operated sequentially. Note the discontinuity corresponding to pixel advance. The different levels of outputs of the correlated double sample (lower traces of Figure 5a) indicates the different amounts of charge collected on the gates of the three separate signal MOSFETs. The noise labeled "digital pickup" does not affect the output of the CDS. The different voltage levels during and after reset are caused by capacitance coupling and charge transfer from the reset MOSFET. The capacitance at the gate of the signal MOSFET with reset off is 0.08 pF.

This readout design is less susceptible to problems involving incomplete charge transfer or dielectric relaxation effects and to blooming or charge bleeding between pixels. Our tests have so far confirmed these expectations.

Telescope Tests

The most important conclusion from the telescope tests involved the performance of the arrays at various background levels. Through the narrow-band (1.6%) filter near 10μm the array performed essentially as expected and about as well as good discrete doped silicon detectors. From the measured response to starlight, we estimate the product of quantum efficiency (η), photoconductive gain (g), and system transmission (τ) to be $\eta g \tau \approx 6\%$ at $\lambda = 9\mu$m. Estimating the transmission of the telescope, lenses and filters to be $\tau \approx 50\%$, indicates $\eta g \approx 12\%$. From the measured signal-to-noise ratios on stars, summing both signal and noise over a 25 pixel (4" x 4") area, the NEFD was determined to be ~ 7 Jy/$\sqrt{\text{Hz}}$ at $\lambda = 9\mu$m, $\Delta\lambda = 0.15\mu$m. The NEFD of each pixel was then ~ $7/\sqrt{25} = 1.4$ Jy/$\sqrt{\text{Hz}}$. The camera performance can be compared with

other infrared detector systems and the expected photon shot noise. The University of Arizona bolometer system on the same telescope has a NEFD of 0.6 $Jy/\sqrt{Hz}$ at $\lambda = 10.5\mu m$, $\Delta\lambda = 5\mu m$, 5" circular aperture. Scaling by $(\Delta\lambda)^{1/2}$ that system would have an NEFD ~ 3.5 Jy with $\Delta\lambda = 0.15\mu m$. The infrared camera in its first tests was therefore ~ 2 times worse, for detection of a point source, than a very good bolometer system with $\Delta\lambda = 0.15\mu m$. Comparison of the performance of the infrared camera with photon shot noise indicates that it was photon noise limited with $\approx$10% at $\lambda = 9\mu m$, $\Delta\lambda = 0.15\mu m$.

At shorter wavelengths, observations also showed photon noise limited sensitivity, but with a reduced quantum efficiency, $\eta \approx 5\%$ at $\lambda = 5\mu m$. Even through a Fabry-Perot at $\lambda = 4\mu m$, $\Delta\lambda \approx .003\mu m$, nearly photon noise limited performance was achieved by slowing down the array cycle time to 2/3 second. These observations showed that the array worked as expected, with no significant excess noise over more than three orders of magnitude variation in background flux. The only problem (other than cloudy weather) with the observations at $4\mu m$, was that InSb detectors can work at this wavelength and have about ten times better quantum efficiency than doped silicon.

The first device tested was an arsenic doped silicon array which was known to be non-uniform due to contact problems. This array was saturated when used with an 8-13μm filter at the fastest readout rate possible, ~ 1 kHz for the entire array, or 640 kHz pixel rate. Through an intermediate bandwidth filter (10.5-12μm) the array was no longer saturated but showed substantial excess noise which was approximately proportional to photon flux and had a 1/f spectrum. The result of this noise was that the NEFD of the camera was no better with 15% resolution than with 1.5%.

A second device, a gallium doped silicon array, was tested in 1985. It was much more uniform ($\lesssim$10% variations) and did not exhibit excess noise. However, possibly because of improved responsivity, it was sufficiently saturated that it lost most of its responsivity when used with even 1μm bandwidth filters. Tests of its performance at high backgrounds were made by reading out only 1/4 of the array, allowing ~ 4 kHz readout rate. Although still partially saturated, the array

then worked with no excess noise through a 1μm bandpass filter.

Laboratory Measurements

Preliminary work has been started on making accurate laboratory measurements of properties of the arrays. A dewar has been constructed for dark current and low light level measurements and will arrive soon. Software is being written to facilitate the acquisition and analysis of data. However, some measurements have been made, including one using a new technique for measuring hysteresis and pixel-to-pixel crosstalk. The data from these measurements are shown in the remaining figures. Figures 7, 8, and 9 show successive readouts from one pixel and the Fourier transform of the data. 1/f noise can be seen. The data is similar for other pixels.

Figure 10 shows accumulated charge vs. integration time. The charge is caused by dark current, photons that leaked in, on both. Although we used two, nested, fairly light tight LHe enclosures light leaks have existed. The low, horizontal line is the A/D output with the chip disconnected, showing the contribution of electronic noise.

Figure 11 shows the fluctuations of the accumulated charge in a set of measurements vs. the square root of integration time. The straight line is the square root of the difference of accumulated charge and electronic noise in Figure 10. The low, horizontal line is the fluctuation of the electronic noise.

Figures 12, 13, and 14 show hysteresis following an x-ray event. The first two figures, with different ordinates and abscissas, show charge trapping and slow leakage in readouts following the x-ray event. Figure 14 shows a different phenomena, anticorrelation of the following readout.

Pixel-to-pixel cross talk was also measured using x-rays. X-rays primarily ionize silicon atoms rather than dopant and produce charge densities vastly different than typical infrared radiation sources do. However, hysteresis and charge spreading probably do not depend on the mobility of holes or charge concentration and can probably be measured using x-rays. Further work is required to ascertain the validity of this approach. Figure 15 shows the spreading in several x-ray events.

References

Arens, J.F., Lamb, G.M., Peck, M.C., *SPIE Proceedings,* **280,** 61-63, 1981.

Arens, J.F., Lamb, G.M., Peck, M.C., *Optical Engineering,* **22,** 267-268, 1983.

High Spatial Resolution Observations of NGC 7027 with a 10 Micron Camera, Arens, J.F., Lamb, G.M., Peck, M.C., Moseley, H., Hoffman, W.F., Tresch-Fienberg, R., Fazio, C.G., *Astrophysical Journal,* **279,** 1984.

Forrest, W.J., Pipher, J.L., *Infrared Technology Workshop, Ames Research Center,* July, 1983.

Goebel, J.H., Jarred, D.A., Lee, J.H., McCreight, C.R., McKelvey, M.E., Stafford, P.S., *Infrared Technology Workshop, Ames Research Center,* July, 1983.

Jones, B., Puetter, R., Hier, R., Schmidt, A., Casler, J., Nelson, S., Hujsah, J., *Infrared Technology Workshop, Ames Research Center,* July, 1983.

McCreight, C.R., Goebel, J.H., *Applied Optics,* **20,** 3189.

Meyers, P.C. and Benson, P.J. 1983, *Ap. J.,* **266,** 309.

Parry, C.M., *Infrared Technology Workshop, Ames Research Center,* July, 1983.

Pommerrenig, D., Enders, D., Trousil, L., Capps, R., Irwin, E., Tollestrup, E., Dereniah, E., *Infrared Technology Workshop, Ames Research Center,* July, 1983.

Sutton, N.J., 1979, Ph.D. Thesis, University of California, Berkeley.

Townes, C.H., Lacy, J.H., Geballe, T.R., and Hollenbach, D.J., 1983, *Nature,* **301,** 661.

Woolf, N.J., 1982, *Ann. Rev. Astr. Ap.,* **20,** 367.

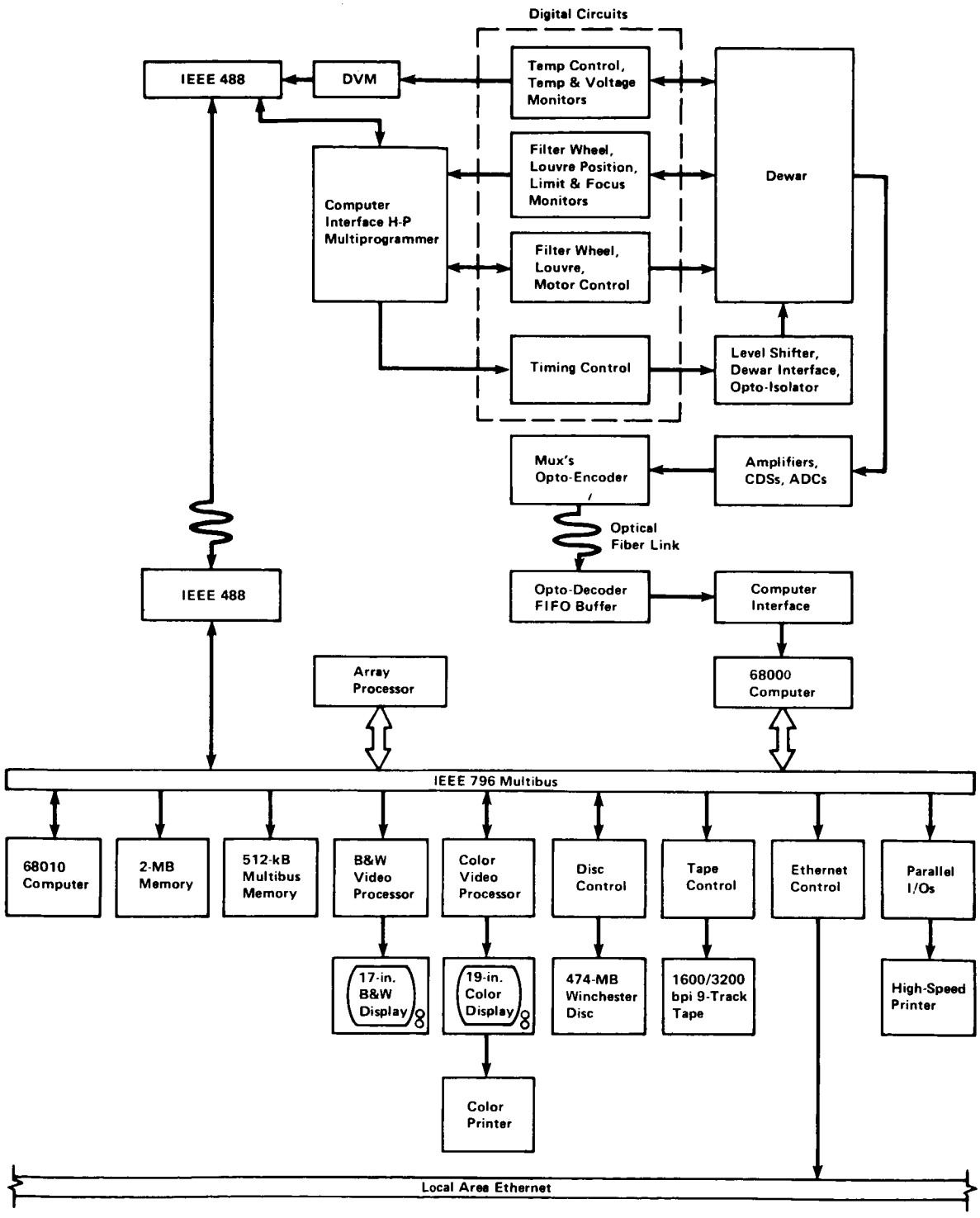

Figure 1. Test Facility Block Diagram

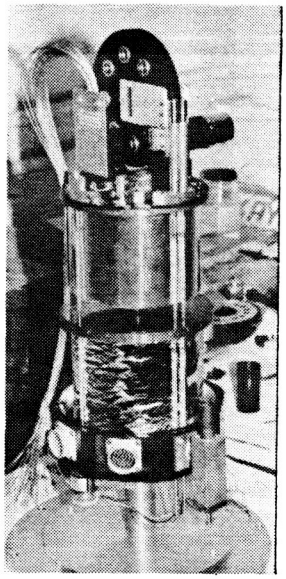

(a) Detector and Dewar

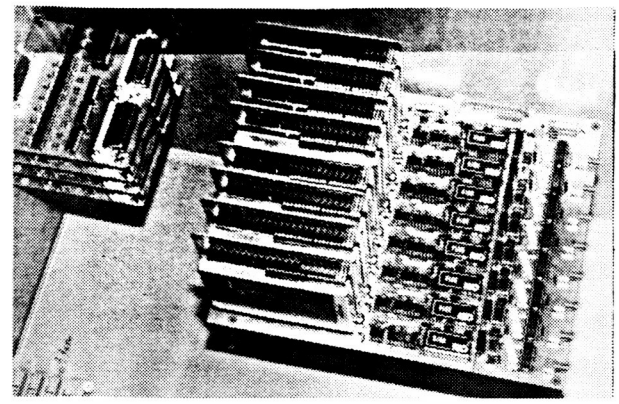

(c) Analog Electronics

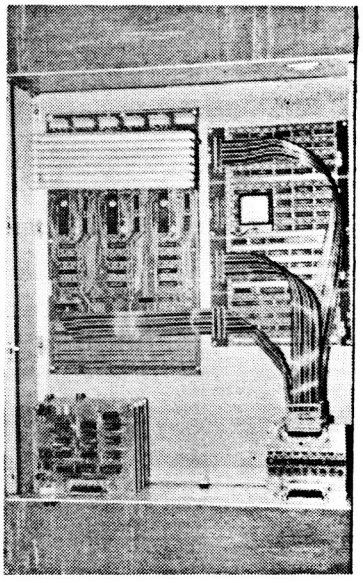

(b) Digital Electronics

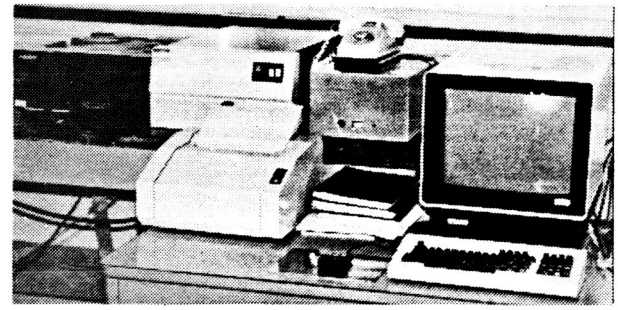

(d) Work Station

Figure 2

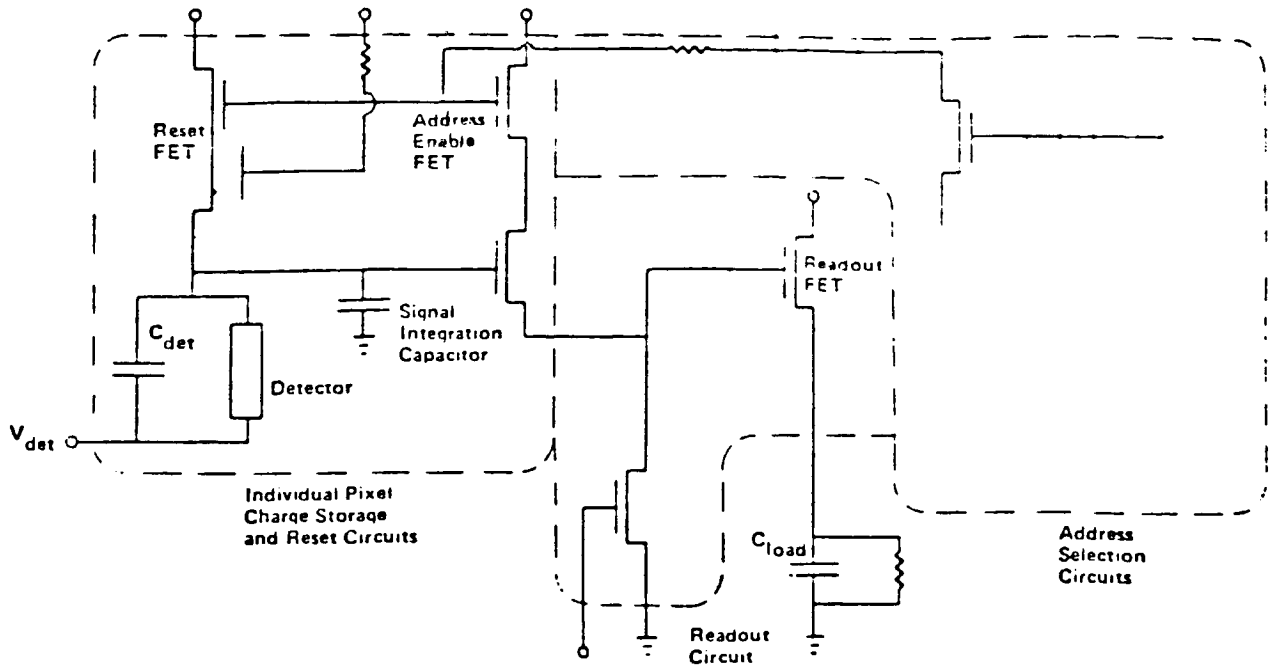

Figure 3 MOSFET Circuit of Hughes Readout Chip

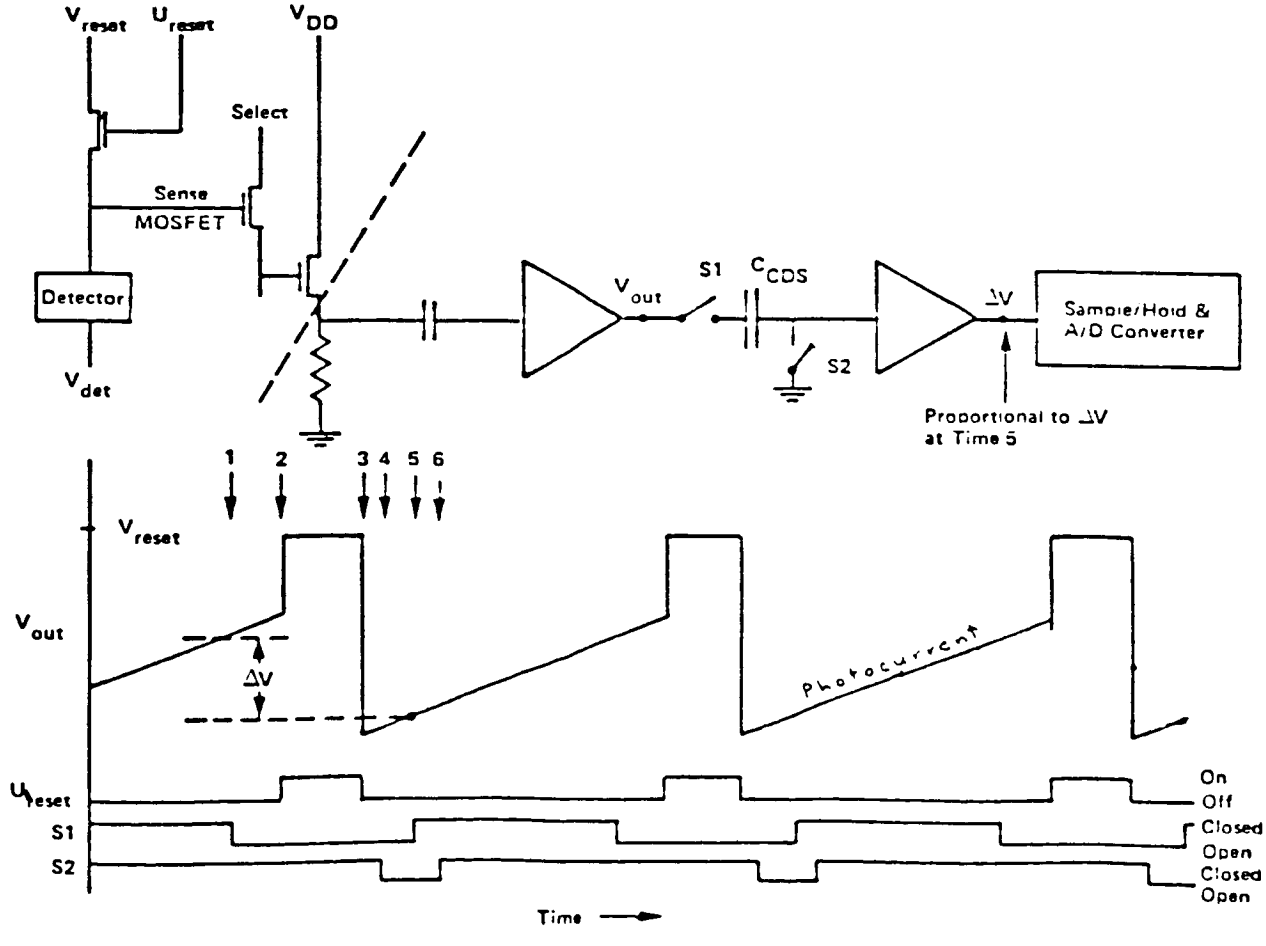

Figure 4 Simplified Schematic of a Correlated Double-Sample and Associated Timing Diagram

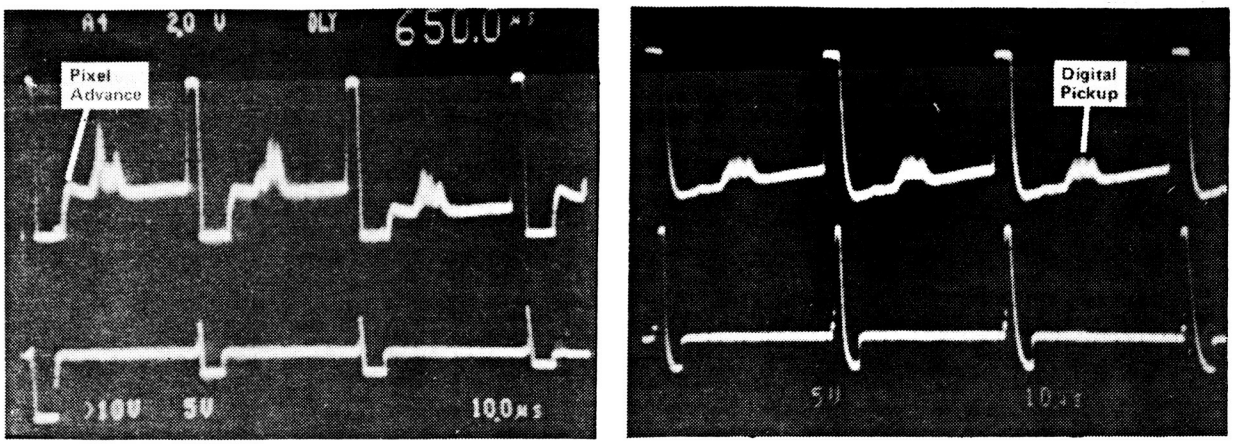

(a) Multipixel, Sequential Sampling

(b) Single Pixel, Repeated Sampling

Figure 5 *Correlated Double-Sampling Timing Traces*

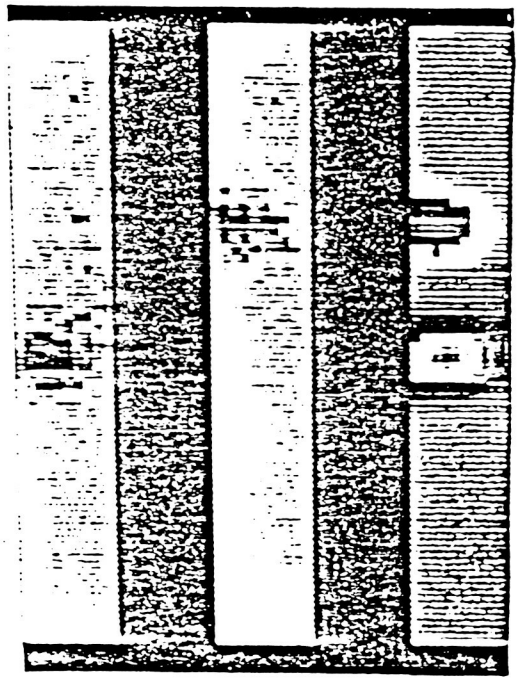

Figure 6 Images of α Ori at λ = 9um. The image on the right is the difference of the other two and has been corrected for pixel-to-pixel gain variations.

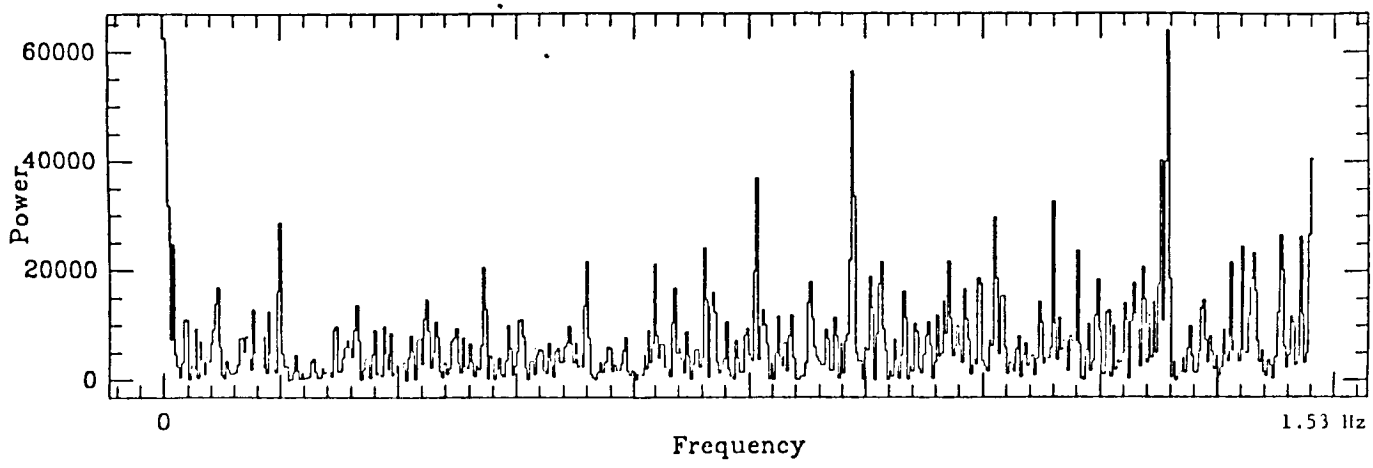
60000
40000
20000
0
Power
0
1.53 Hz
Frequency

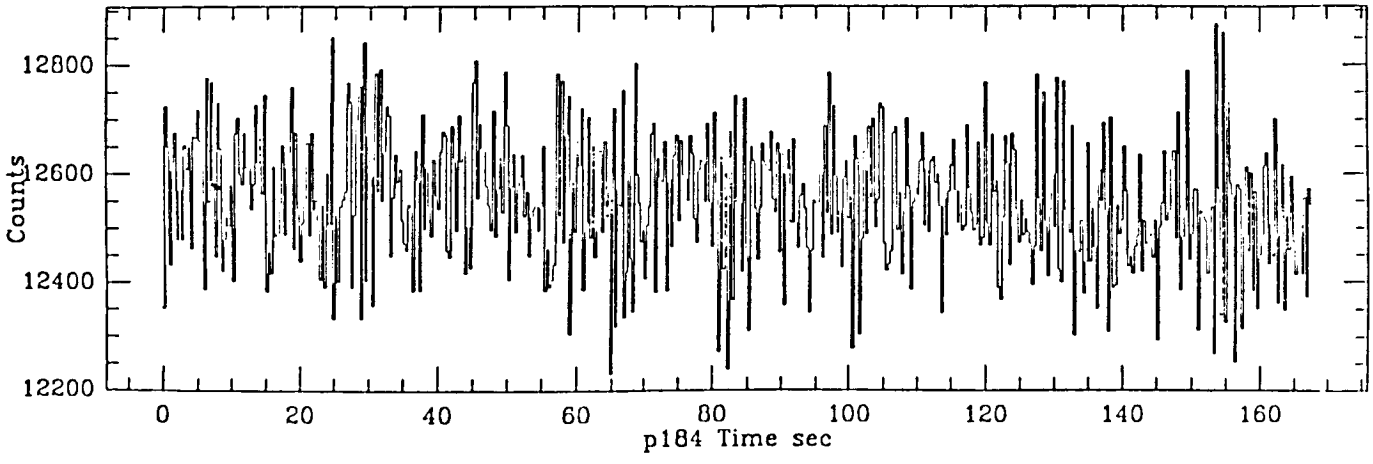
12800
12600
12400
12200
Counts
0
20
40
60
80
100
120
140
160
p184 Time sec

Figure 7

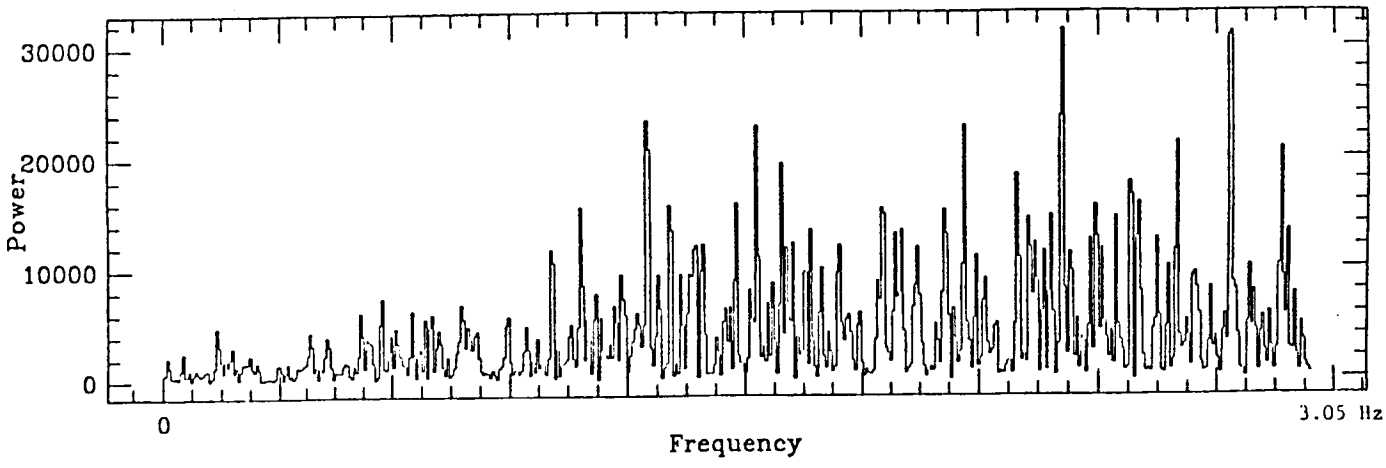
30000
20000
10000
0
Power
0
3.05 Hz
Frequency

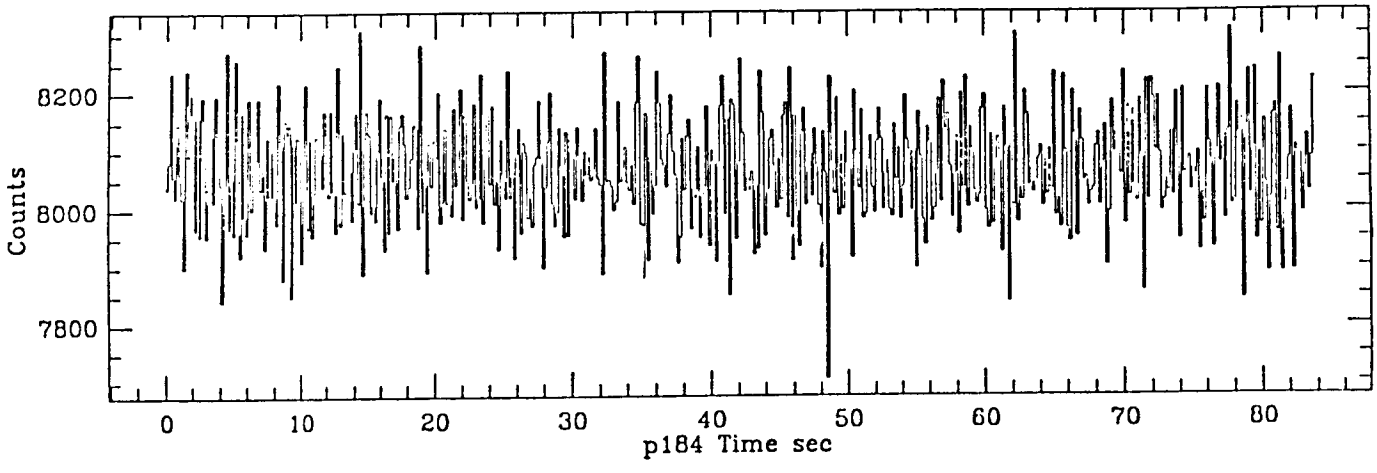
8200
8000
7800
Counts
0
10
20
30
40
50
60
70
80
p184 Time sec

Figure 8

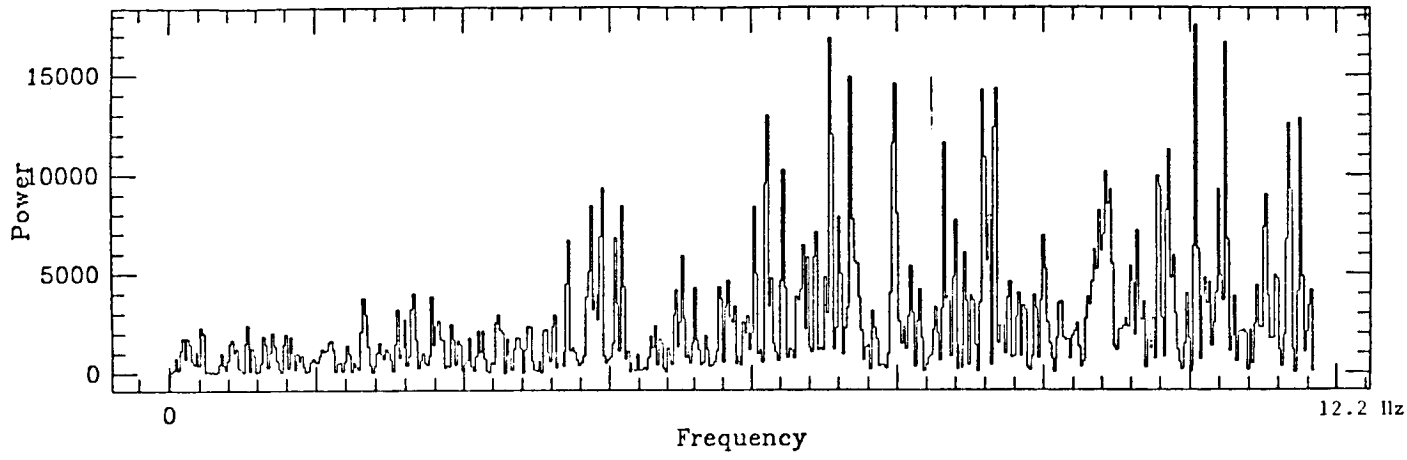
15000
10000
5000
0
Power
0
12.2 Hz
Frequency

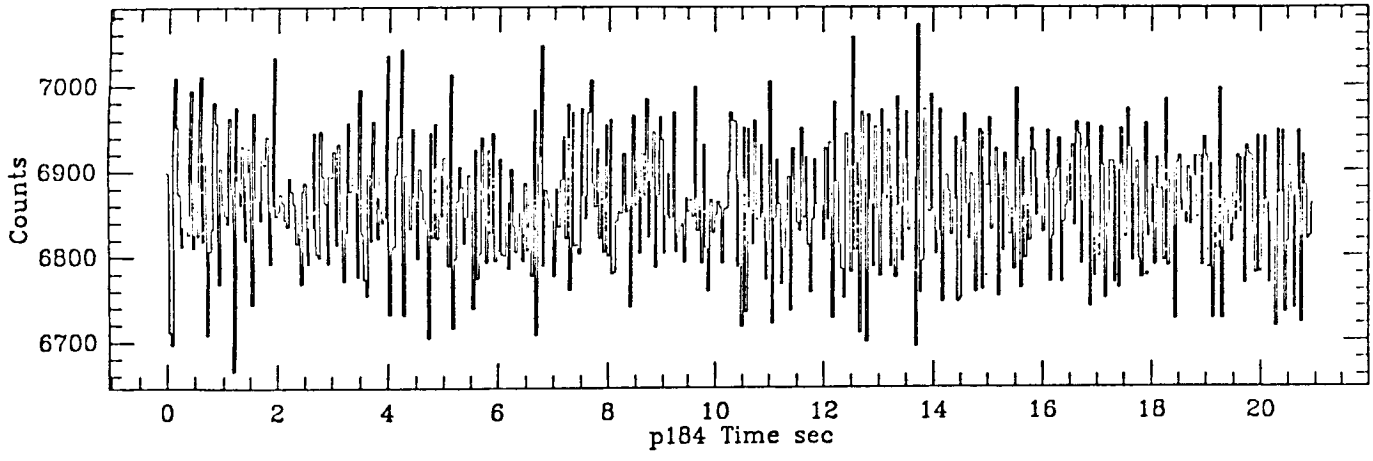
7000
6900
6800
6700
Counts
0
2
4
6
8
10
12
14
16
18
20
p184 Time sec

Figure 9

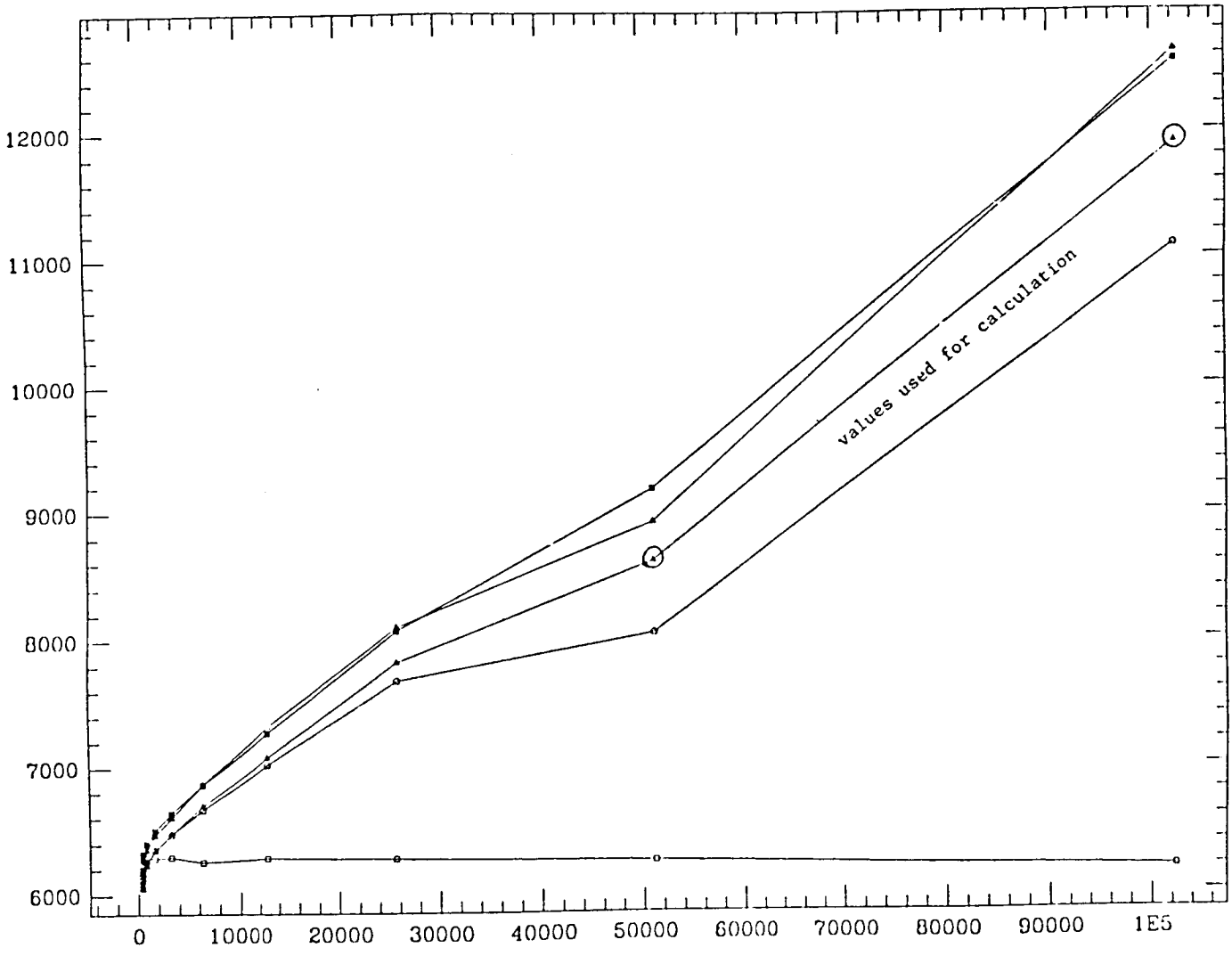
12000
11000
10000
9000
8000
7000
6000
0
10000
20000
30000
40000
50000
60000
70000
80000
90000
1E5
values used for calculation

Figure 10

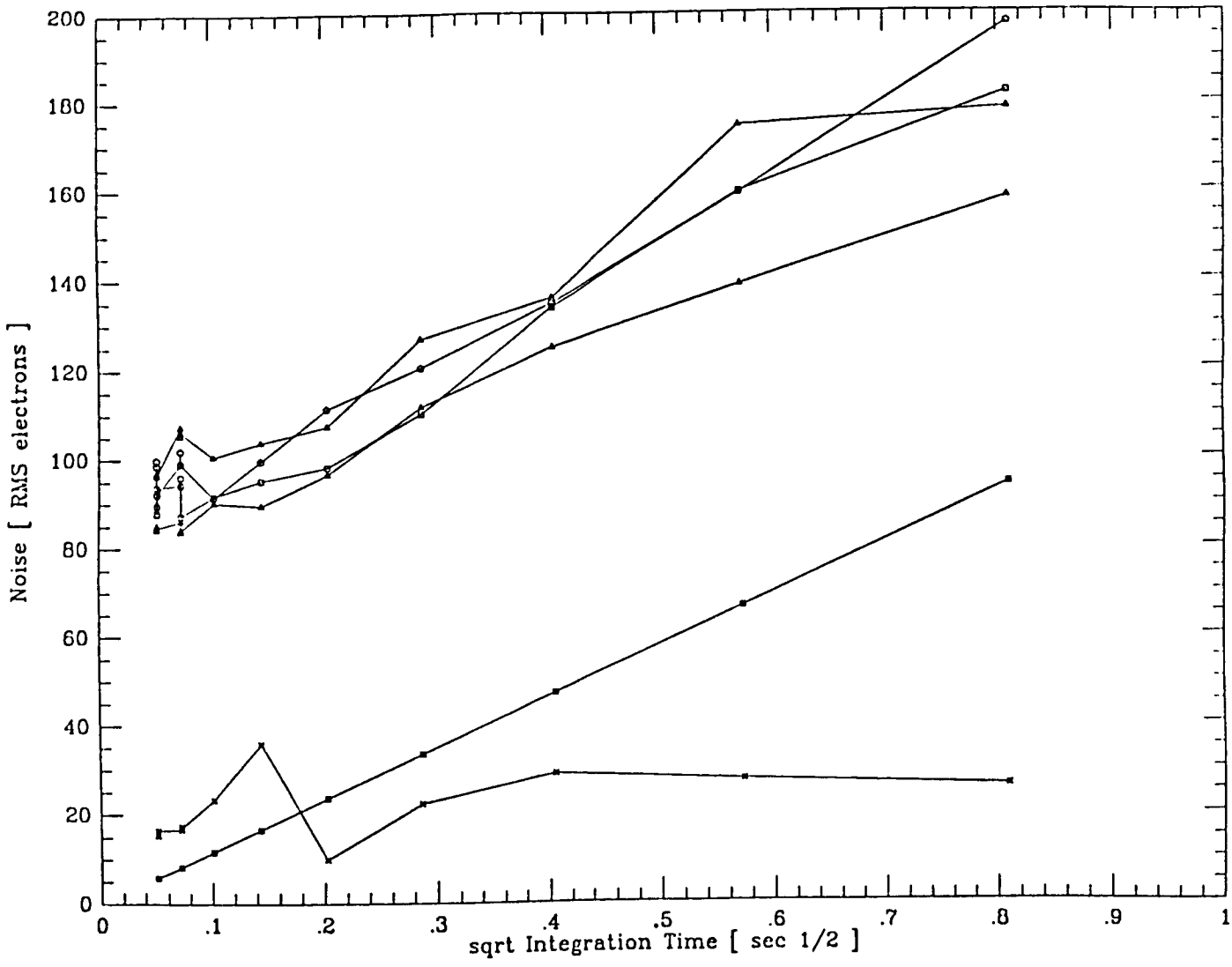
Noise [RMS electrons]
200
180
160
140
120
100
80
60
40
20
0
0
.1
.2
.3
.4
.5
.6
.7
.8
.9
1
sqrt Integration Time [sec 1/2]

Figure 11

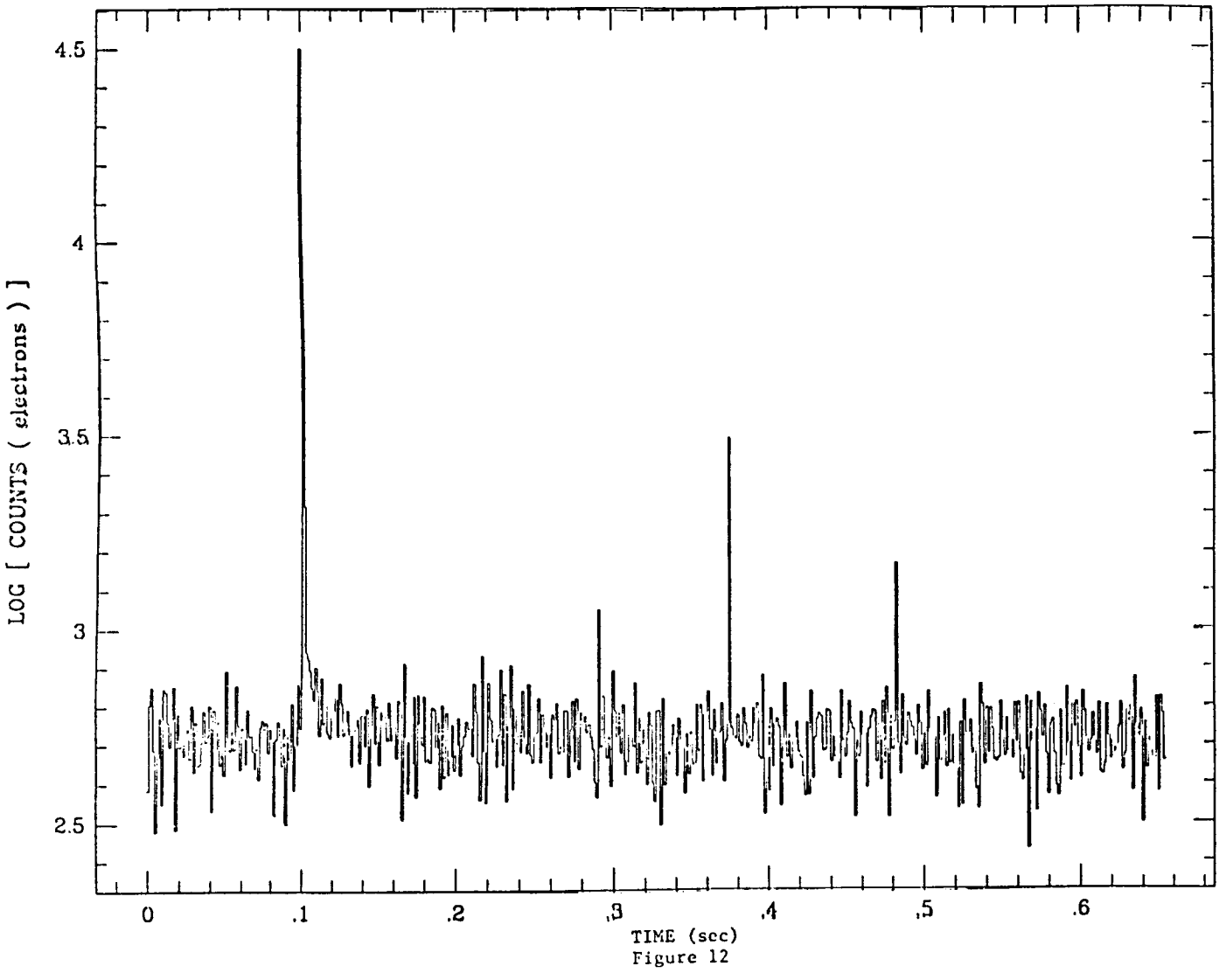

Figure 12

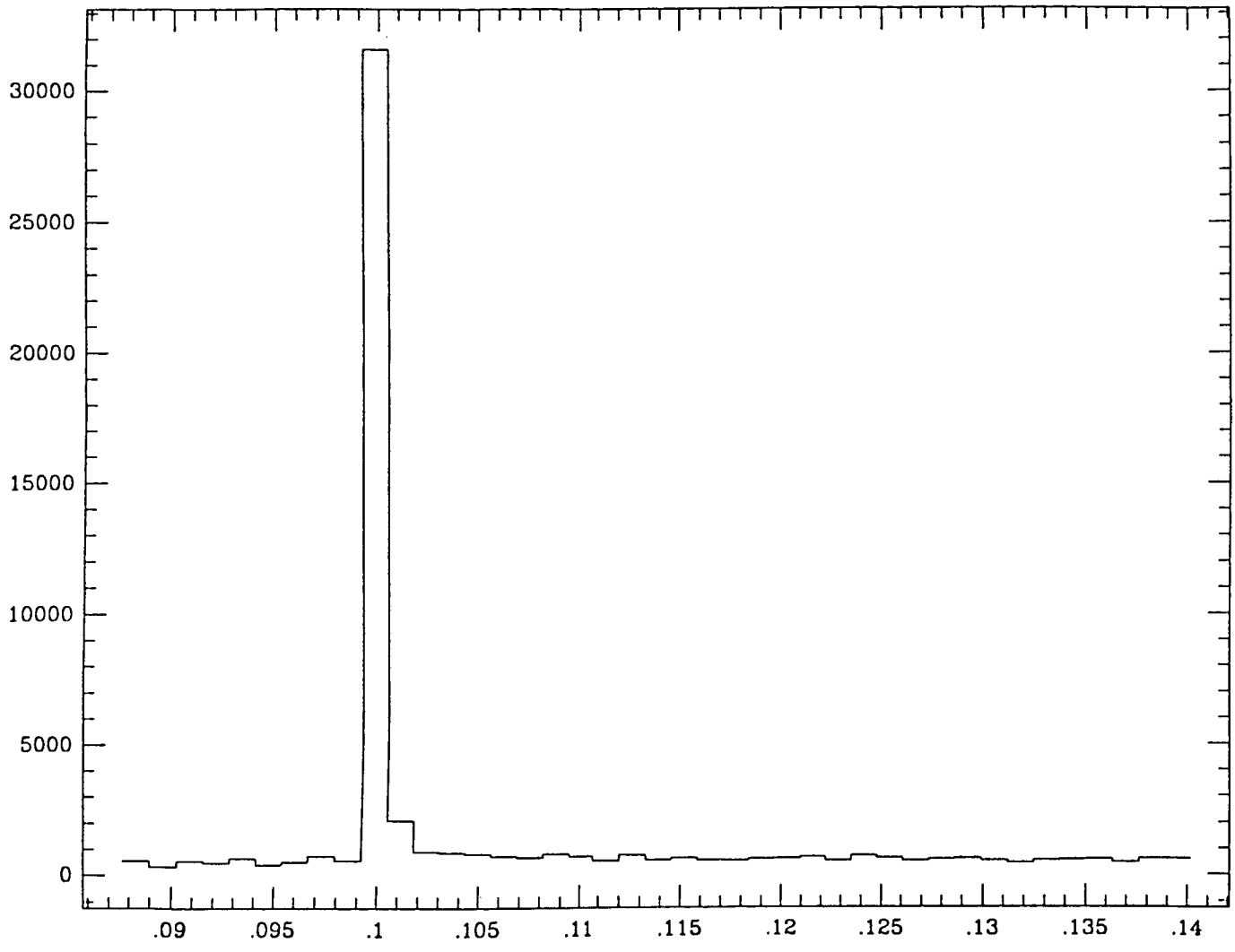
30000
25000
20000
15000
10000
5000
0
.09
.095
.1
.105
.11
.115
.12
.125
.13
.135
.14

Figure 13

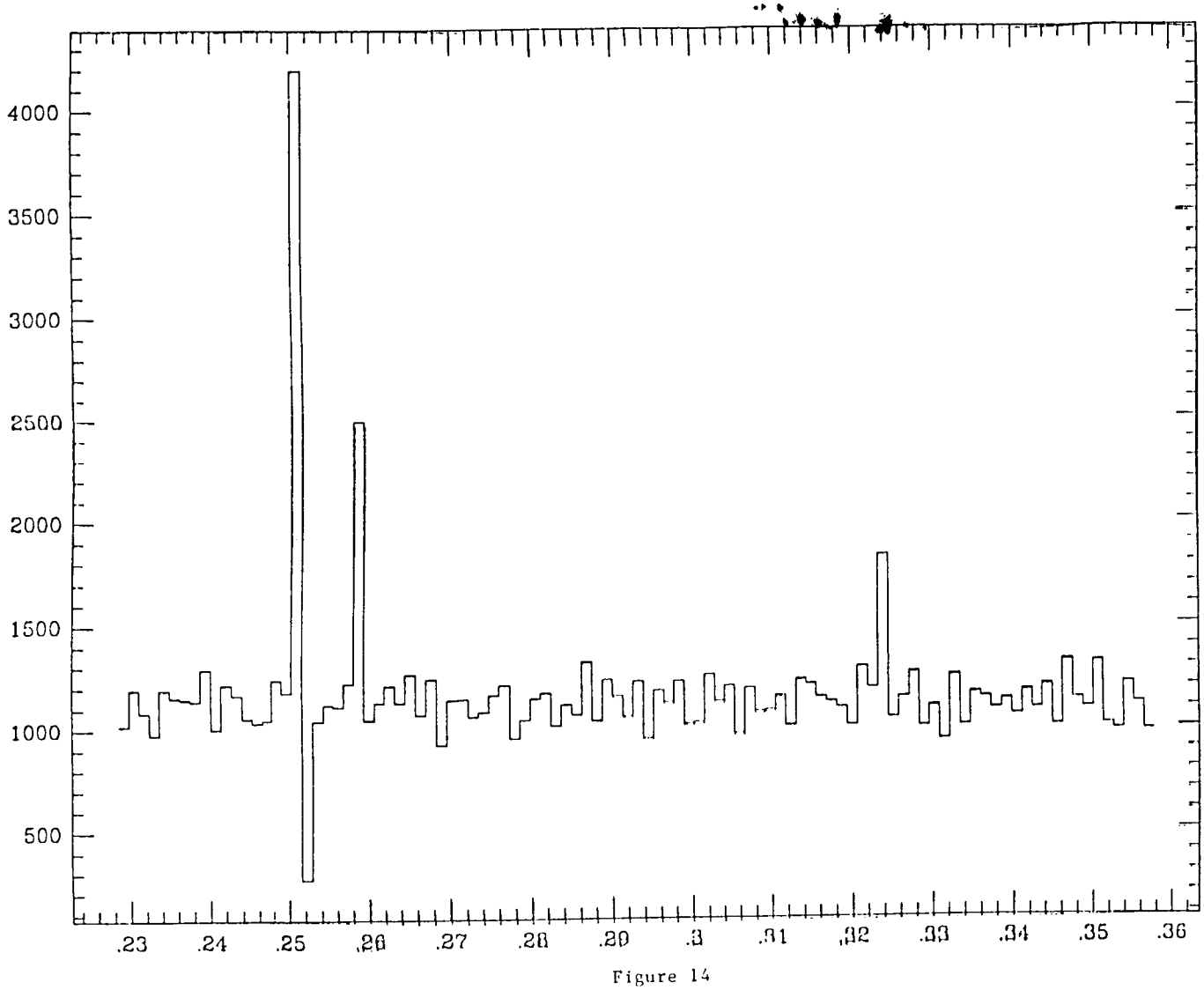
4000
3500
3000
2500
2000
1500
1000
500
.23
.24
.25
.26
.27
.28
.29
.3
.31
.32
.33
.34
.35
.36

Figure 14

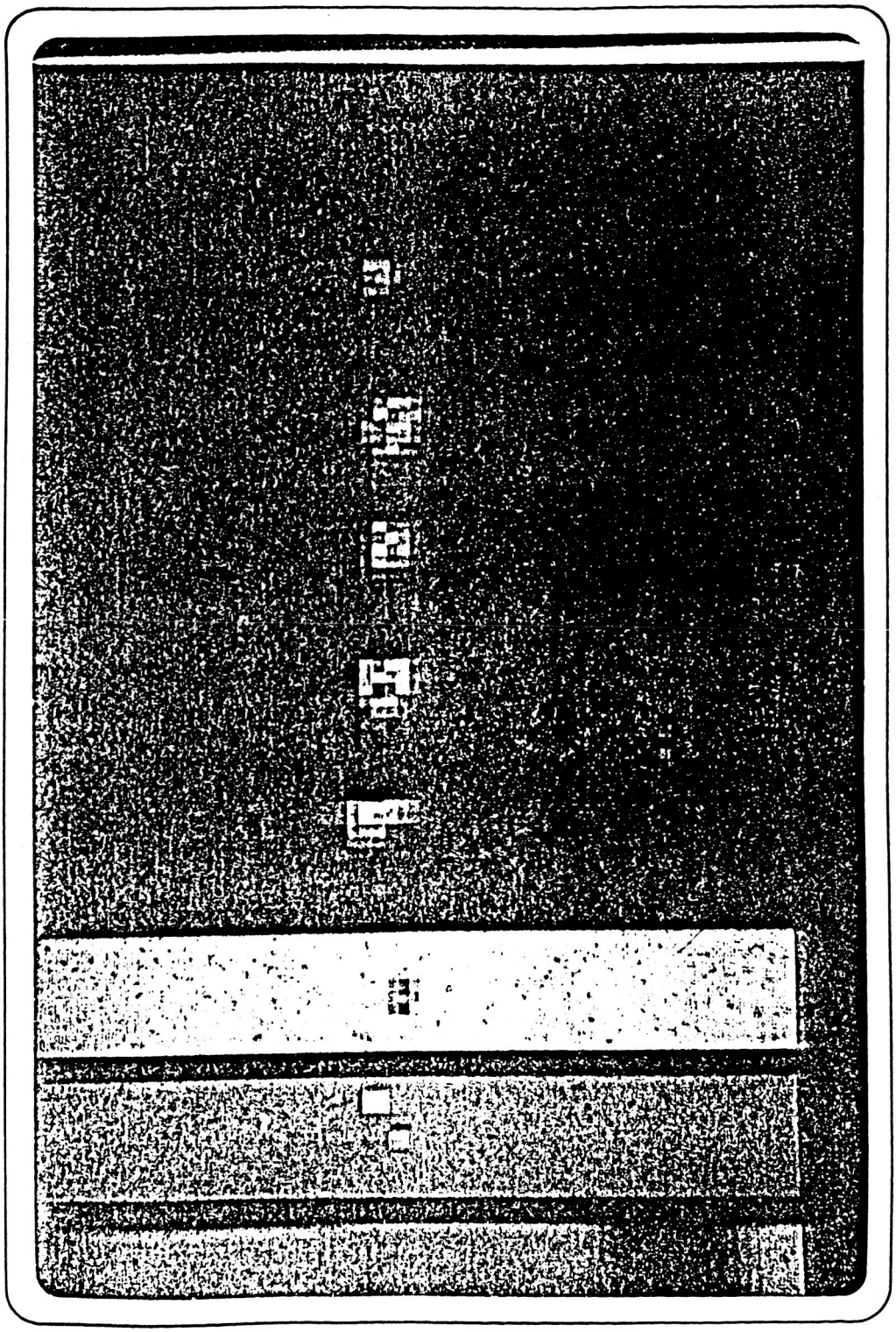

Figure 15

1. Report No.	2. Government Accession No.	3. Recipient's Catalog No.
NASA TM-88213		

4. Title and Subtitle	5. Report Date
PROCEEDINGS OF THE SECOND INFRARED DETECTOR TECHNOLOGY WORKSHOP	February 1986
	6. Performing Organization Code
7. Author(s)	8. Performing Organization Report No.
The authors and their affiliations are shown in the list of attendees	A-86123
	10. Work Unit No.
9. Performing Organization Name and Address	11. Contract or Grant No.
Ames Research Center Moffett Field, CA 94035	
	13. Type of Report and Period Covered
12. Sponsoring Agency Name and Address	Technical Memorandum August 13-14, 1985
National Aeronautics and Space Administration Washington, DC 20546	14. Sponsoring Agency Code 506-45-31

15. Supplementary Notes

Point of Contact: Craig R. McCreight, Ames Research Center, MS 244-10, Moffett Field, CA 94035 (415)694-6549 or FTS 464-6549

16. Abstract

This volume contains a collection of papers summarizing results presented at the Second Infrared Detector Technology Workshop, held August 13-14, 1985, at Ames Research Center. The workshop focused on infrared detector, detector array, and cryogenic electronic technologies relevant to low-background space astronomy. The papers are organized into the following categories: discrete infrared detectors and readout electronics; advanced bolometers; intrinsic integrated infrared arrays; and extrinsic integrated infrared arrays. Status reports on the Space Infrared Telescope Facility (SIRTF) and Infrared Space Observatory (ISO) programs are also included.

17. Key Words (Suggested by Author(s))	18. Distribution Statement
Infrared detectors Infrared detector arrays Cryogenic electronics Infrared astronomy	Unlimited Subject Category - 35

19. Security Classif. (of this report)	20. Security Classif. (of this page)	21. No. of Pages	22. Price*
Unclassified	Unclassified	334	A15

*For sale by the National Technical Information Service, Springfield, Virginia 22161